

**Investigation of Sea Surface
Nanolayer Properties and
Photochemistry Using Modern Laser
Spectroscopic and Surface
Analytical Techniques**

Dissertation

in fulfillment of the requirements for the
degree "Dr. rer. nat." of the Faculty of
Mathematics and Natural Sciences at Kiel
University

submitted by

Florian-David Lange

Kiel 2021

First Referee: Prof. Dr. Gernot Friedrichs
Second Referee: Prof. Dr. Douglas Wallace
Date of the oral examination: 10.08.2021

In Gedenken an meine geliebte Großmutter Adelheid Lange

Abstract

At the interface between natural waters and the sea, an enrichment of surface-active substances can be observed. This has a strong impact on the physical and chemical properties of this system, including the gas exchange. Because of the high local concentration of different organic substances and, in comparison with the bulk, the high intensity of solar radiation, a large number of photochemically induced reactions take place within this interfacial zone.

The scope of this thesis covers both the investigation of natural sea water surface samples and the development synthetic model systems to study such photochemical processes using surface-selective analytical techniques. Out of the different techniques used, Vibrational Sum Frequency Spectroscopy (VSFG) was employed as the primary experimental method.

The first part of the thesis covers the investigation of natural water surface samples by means of VSFG spectroscopy for the semi-quantitative determination of surface-active matter abundance in the so-called Sea Surface Nanolayer (SNL), the direct molecular interface between air and sea. A set of software tools was implemented to allow for an automatized and systematic analysis of large amount of spectral data. These were used to re-examine the data obtained by monthly sampling of natural surface water collected at Boknis Eck time series station over ten years with respect to seasonal variation of the surfactant abundance as well as to correlate surfactant abundance with other oceanographic parameters. A seasonal variation of this SNL abundance through the year could be confirmed. The second part of the thesis describes the synthesis and characterization of a novel class of surface-active photosensitizer molecules based on benzoylbenzoic acid. It was possible to obtain three new substances not yet described in the literature by esterification of the acid with three symmetric diols (hexane, nonane and dodecane diol). Those compounds turned out to be very surface-active and yielded VSFG spectra of remarkable quality and showing pronounced carbonyl peaks. Upon irradiation with artificial sunlight from a xenon lamp, efficient autophotolysis was observed for those molecules, clearly proving their photochemical reactivity. To better mimic the surface of natural waters, in which typically only a small fraction of the interfacial molecules is susceptible to photochemistry, mixed layers of the novel sensitizers and naturally occurring fatty acids (myristic acid, palmitic acid and stearic acid) have been prepared and in-

investigated by means of VSFG spectroscopy, LANGMUIR compression isotherms and simultaneous application of both methods. The mixture of the sensitizer BX12 and stearic acid was identified as the most promising candidate for a model system for future studies.

Kurzzusammenfassung

An der Grenzfläche zwischen natürlichen Gewässern zur Luft reichern sich häufig oberflächenaktive Substanzen an, die einen erheblichen Einfluss auf die physikalischen und chemischen Eigenschaften des Systems einschließlich des Gasaustausches haben können. Durch die besonders hohe lokale Konzentration von verschiedenen organischen Substanzen und der im Verhältnis zum Tiefenwasser hohen Sonneneinstrahlung kommt es in dieser Zone zu einer Vielzahl photochemisch induzierter Reaktionen.

Im Rahmen der vorliegenden Arbeit wurden die oberflächenaktiven Substanzen an dieser Grenzfläche anhand natürlicher Meerwasserproben und synthetische Modellsysteme untersucht. Die dort ablaufenden photochemischen Prozesse mithilfe oberflächensensitiver analytischer Methoden charakterisiert, wobei insbesondere die Vibrations-Summenfrequenzspektroskopie (VSFG) zum Einsatz kam.

Die im ersten Teil der Arbeit beschriebene Untersuchung natürlicher Wasserproben basiert auf der in dieser Arbeit etablierten Verwendung der VSFG-Spektroskopie als geeignetes Mittel zur semi-quantitativen Bestimmung der Menge an oberflächenaktivem Material im sogenannten *Sea Surface Nanolayer* (SNL), der unmittelbaren molekularen Grenzschicht zwischen Luft und Wasser. Mithilfe einer neu implementierten Software konnte eine automatisierte und systematische Auswertung der Spektren sowie eine komfortable Verwaltung großer Datenmengen ermöglicht werden. Diese wurden angewandt, um die über einen Zeitraum von fast zehn Jahren monatlich im Rahmen einer regelmäßigen Ausfahrt gesammelten Oberflächenwasserproben systematisch im Hinblick auf zeitliche Trends und Korrelation mit anderen meereschemischen Parametern zu untersuchen. Eine zeitliche Varianz der Oberflächenkonzentration organischer Substanz konnte bestätigt werden. Des Weiteren wurden während der zwei Ausfahrten (eine im Juni, eine im September 2018) der Baltic GasEx-Kampagne mehrfach täglich Oberflächenwasserproben genommen und zusätzlich zur VSFG mithilfe eines LANGMUIRTroges und tensiometrischer Messungen im Hinblick auf die Menge der oberflächenaktiven Substanzen untersucht und im Zuge dessen ein Satz von einfachen komplementären Parametern definiert, welche die Oberflächenbedeckung quantifizieren.

Der zweite Teil der Arbeit beschreibt die Synthese und Charakterisierung einer

neuen Klasse von oberflächenaktiven Photosensitizermolekülen auf Basis von Benzoylbenzoesäure. Durch Veresterung dieser Säure mit symmetrischen Diolen (Hexan-, Nonan- und Dodecandiol) konnten drei bisher nicht in der Literatur beschriebene Substanzen hergestellt werden, die sich nicht nur als ausgesprochen oberflächenaktiv herausstellten, sondern auch VSFG-Spektren von bemerkenswerter Qualität mit besonders ausgeprägten Carbonylbanden lieferten. Unter Bestrahlung mit dem Licht einer Xenonlampe zur Simulation des solaren Spektrums zeigten die Substanzen erhebliche Autophotolyse, was ein klarer Beleg für ihre photochemische Reaktivität ist. Um die natürlichen Grenzflächensysteme, in denen typischerweise nur ein geringer Anteil der Moleküle photochemisch aktiv ist, besser nachzustellen, wurden gemischte Schichten aus natürlich vorkommenden Fettsäuren (Myristinsäure, Palmitinsäure und Stearinsäure) und den künstlichen Sensitizern hergestellt und mithilfe von VSFG, LANGMUIR-Kompressionsisothermen sowie einer gleichzeitigen Anwendung beider Methoden (VSFG bei verschiedenen Oberflächenkompressionen) auf ihre Grenzflächeneigenschaften und Photochemie untersucht. Bei dieser Untersuchung konnte eine Mischung aus dem künstlichen Sensitizer BX9 und Stearinsäure als vielversprechender Kandidat für ein Modellsystem identifiziert werden.

Declaration

I hereby declare that this thesis is my own work and effort without any help except the guidance of my supervisor Prof. Dr. Gernot Friedrichs. Where other sources of information have been used, they have been acknowledged.

This is my first dissertation and this work has neither been used as a whole nor in parts in any other dissertation attempts. No academic degree has ever been withdrawn from me.

The dissertation complies to the Rules of Good Scientific Practice as proposed by the German Research Foundation (DFG).

Kiel, 28.05.2021

Florian-David Lange

Contents

1	Introduction	1
1.1	The interfacial layer between sea and air	1
1.2	Photochemistry at the air-water interface	4
1.3	VSFG investigation of surface monolayers	8
1.4	Outline of this thesis	10
2	Theoretical Background	13
2.1	Surfactants and interfacial layers	13
2.1.1	Surface tension	14
	The WILHEMY Method of surface tension measurement	15
2.1.2	Surface-active compounds	17
	Surface excess	18
2.1.3	Surface layers and their 2D phase behavior	19
	The LANGMUIR trough and spreading procedure	20
	2D phase behavior of LANGMUIR monolayers	21
2.2	Vibrational Sum Frequency Generation Spectroscopy	24
2.2.1	Generation of SFG and the macroscopic susceptibility	24
2.2.2	Microscopic approach and resonance	30
2.3	Photochemistry	34
2.3.1	General aspects	34
2.3.2	Photochemistry of the carbonyl group	36
3	Experimental Section	41
3.1	Materials and Sampling Techniques	41
3.1.1	Materials	41
3.1.2	Synthesis	43
3.1.3	Characterization of the synthesized substances	43

3.2	SML sampling	43
3.2.1	GARRETT screen	44
3.2.2	Sampling by glass plate	44
3.3	Surface Analysis	45
3.3.1	Tensiometry	45
3.3.2	LANGMUIR trough compression isotherms	45
3.4	VSFG-Spectroscopy	46
3.4.1	VSFG spectrometer setup	46
3.4.2	VSFG spectra acquisition	47
3.4.3	Combination of LANGMUIR trough and VSFG	48
3.5	Photolysis	50
I	Natural surfactant systems	55
4	Automated data processing, storage and management based on Python	57
4.1	Background	57
4.2	Implementation	58
4.2.1	The reusable core: specsnake	60
4.2.2	The thesis-specific package: SFG	62
4.3	Discussion	63
4.3.1	General usage	63
4.3.2	Application: Time series data from Boknis Eck	64
4.3.3	Application: Dataset from the Baltic GasEx cruise	66
4.3.4	Extensibility and re-usability	68
4.4	Conclusion	71
5	The Boknis Eck time series	73
5.1	Introduction	73
5.2	Results from earlier publications	74
5.3	Experimental	76
5.3.1	Sampling	76
5.3.2	VSFG spectroscopy	77
5.3.3	Software	77
5.3.4	Surface coverage	78

5.4	Results and Discussion	80
5.4.1	Typical appearance of the VSFG spectra of a sampling day	80
5.4.2	Comparison with the preliminary time series	81
5.4.3	Long-term trend	82
5.4.4	Difference between SML and bulk water	85
5.4.5	Seasonality	86
5.5	Conclusion	90
6	Contributions to the Baltic GasEx cruise 2018	91
6.1	Introduction	91
6.2	Experimental	93
6.2.1	Time and location	93
6.2.2	Sampling	93
	GARRETT screen sampling	95
	Glass plate sampling	95
6.2.3	Laboratory-based experiments	95
	Surface tension	96
	LANGMUIR compression isotherms	96
	VSFG spectroscopy	96
6.2.4	Software	97
6.3	Preliminary work	97
6.4	Surfactant abundance indices	102
6.5	Cruise data	106
6.5.1	Comparison between the cruises	107
6.5.2	Plate and screen sampling comparison	112
6.5.3	Comparison between zodiac- and ship-based sampling . .	115
6.5.4	SML and bulk water comparison	117
6.6	Inter-comparability of different indices for surfactant abundance	119
6.7	Conclusion and outlook	122
II	Systems of artificial photosensitizers	125
7	BX as surface-active photosensitizers	127
7.1	Abstract	127

7.2	Introduction	127
7.3	Experimental	131
7.3.1	Materials	131
7.3.2	Synthesis of the hydroxyalkyl esters	131
7.3.3	Characterization	131
7.3.4	VSFG spectroscopy and photolysis	132
7.3.5	LANGMUIR compression isotherms and VSFG spectra at constant surface pressure	132
7.4	Results and Discussion	134
7.4.1	Preliminary experiments with Humic Acid and Nonanoic Acid	134
7.4.2	Synthesis and preparation of spreading solutions	136
7.4.3	VSFG spectroscopy	137
7.4.4	LANGMUIR trough Experiments	141
7.4.5	Photolysis experiments	143
	Time-resolved photolysis	145
7.5	Conclusion	146
8	Mixed layers of fatty acids and an artificial photosensitizer	147
8.1	Introduction	147
8.2	Experimental	150
8.2.1	Preparation of the spreading stock solutions	150
8.2.2	LANGMUIR trough measurements	151
8.2.3	VSFG spectroscopy	151
8.2.4	Combined VSFG and LANGMUIR trough measurements	152
8.2.5	Photolysis	152
8.3	Results and Discussion	152
8.3.1	General concept of the experiments	152
8.3.2	SFG spectra	153
8.3.3	Compression isotherms at variable surfactant/sensitizer ratios	157
8.3.4	Combined VSFG/LT experiments	165
8.3.5	Photolysis experiments	173
8.4	Summary and Outlook	177

9 Summary	181
Bibliography	185
Appendix	215
A Python script usage	215
A.1 General remarks and prerequisites	215
A.2 Import	215
A.3 Usage	216
B Boknis Eck Time Series	219
B.1 Baseline correction	219
C GasEx cruise	223
C.1 Statistical tests	223
C.1.1 Results of the MANN-WHITNEY-U test for the enrichment factor	223
D Sensitizers	225
D.1 Analytical data and Synthesis	225
D.2 NMR	227
BX6	227
BX9	228
BX12	228
D.3 Langmuir compression isotherms	234
D.4 Space requirement	234
E Mixed layers	237
Publications	239

Acronyms

Notation	Description
arb. u.	arbitrary units
CDOM	chromophoric (or colored) dissolved organic matter
CMC	critical micell concentration
DFG	difference frequency generation
DMAP	4-dimethylaminopyridine
DOC	dissolved organic carbon
DPPC	dipalmitoylphosphatidylcholine
EDC	1-ethyl-3-(3-dimethylaminopropyl)carbodiimide hydrochloride
EF	enrichment factor
FA	fatty acids
IR	infrared light
KDP	monopotassium phosphate
LBO	lithium triborate
LLG	liquid light guide
Nd:YAG	neodymium-doped yttrium aluminum garnet
NMR	nuclear magnetic resonance
OPG	optical parametric generator
OR	optical rectification
ORM	object-relational mapper

Notation	Description
PTFE	polytetrafluoroethylene
SAI	surfactant abundance indices
SFG	sum frequency generation
SHG	second harmonic generation
SML	sea surface microlayer
SNL	sea-surface nanolayer
SOA	secondary organic aerosols
SQL	structured query language
surfactants	surface-active agents
TEP	transparent exopolymer particles
UV	ultraviolet light
VFSG	vibrational sum frequency generation
VIS	visible light

CHAPTER 1

Introduction

1.1 The interfacial layer between sea and air

As a significant part of the Earth's surface is covered by oceanic waters, the interface between air and sea is an important subsystem of the environment with unique physical, biological and chemical properties that differ significantly from subsurface bulk water.^[1-3] The very border between the two phases is commonly referred to as the sea surface microlayer (SML) defining the uppermost 1 to 1000 μm of the water column.^[4] The SML is inhabited by specific forms of microorganisms (neuston) which are distinct from those populating the rest of the water column^[5]. In addition, this zone is often enriched with amphiphilic organic substances stemming from different origins like biogenic primary production and degradation processes of those products, intake from rivers and anthropogenic sources.^[6,7] These compounds are referred to as surface-active agents (surfactants). Surfactants are usually molecules with both hydrophilic and hydrophobic moieties leading to an energetically favorable orientation at interfaces where the hydrophobic part tends towards air and the hydrophilic part points into the bulk water.

A broad range of substance classes can be found among the surfactants. The most common are several saturated and unsaturated fatty acids, lipopolysaccharides, amino acids and proteins, but also complex macromolecules like chlorophyll and humic substances are present.^[8-12] It has been found that some of those, especially the carbohydrates, are able to form complex aggregates appearing as transparent exopolymer particles (TEP) floating in the SML.^[13-17] Some authors describe the SML as a gelatinous film formed by gels of complex carbohydrates and proteins.^[18-21] When the surface film becomes thick enough that the capillary wave damping is visible to the open eye, such films are referred to as

slicks. The surfactant concentration and chemical composition has been found to vary spatially and temporally.^[22,23] It is suggested that this variability is mainly caused by temporal fluctuations in the primary productivity (e.g. algae blooms) as well as differences in environmental conditions like composition of the microbial communities, wind, solar radiation and temperature.^[3]

It has been shown that at a depth of approx. 50 μm a sudden change in physical and chemical parameters (e.g. pH value and dissolved organic carbon (DOC) concentration) occurs from the bulk water towards the interface.^[24] Besides those intrinsic special physical and chemical properties of the interface itself, the presence and assembly of the surfactants at the interface leads to a change of the physicochemical water properties. With respect to gas transfer, the presence of surfactants can influence the transport rates by two different mechanisms. First, they form a physical barrier which makes it harder for gases to cross the phase boundary. Second, they alter the viscoelastic properties leading to a higher resistance against stress-induced curvature caused by wind resulting in wave damping. Therefore, the presence of surfactants increases the wind speed needed for wave formation. Waves, however, strongly enhance gas transfer because they come along with turbulences and they increase the water surface area.^[25–29] Studies involving artificial surfactants both on the open ocean and under laboratory conditions indicate a significant lowering of gas transfer rates upon the presence of a surface film.^[23,30–32]

The SML is the gateway to the exchange of heat, momentum and matter between ocean and air. The organic matter enriched in the interfacial layer can be transferred to atmospheric aerosols via different mechanisms, for example spray formation through waves and bubble bursting.^[33,34] In fact, bubbles can function as transport vesicles for organic matter by adsorbing it at the surface during ascension through the SML and release it to the marine atmosphere upon bursting. The resulting aerosols are enriched with organic matter, including surface-active species. Those aerosols can be subject to aging caused by reaction with oxidants (such as OH radicals, ozone, etc.) or photochemically induced by ultraviolet light (UV). Primary and secondary aerosols act as condensation nuclei for cloud droplet formation.^[34–39]

A schematic overview of the different depth zones, classes of organic matter as well as transportation and interaction processes with the environment is presented in Fig. 1.1 Actually, the SML covers a huge area and even impacts

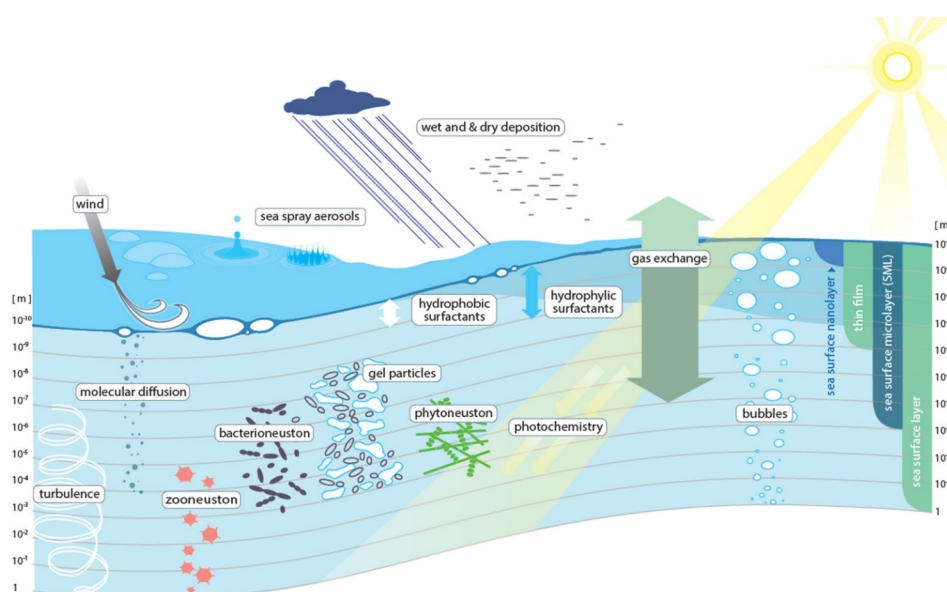


Figure 1.1: Schematic representation of the SML including the different kinds of organic matter, transport processes and interaction with the environment (taken from a recent review by Engel *et al.*).^[3]

global scale processes. Nevertheless, it is rather difficult to probe selectively. The very small vertical dimension requires sampling techniques collecting only the surface water as well as analytical methods with the ability to distinguish between bulk and surface contributions. The importance of this interfacial system lead to high efforts among researchers during the last years in order to establish reliable and reproducible sampling procedures in addition to higher levels of comparibility.^[40] Moreover, a large variety of complementary modern instrumental methods have been employed to improve the understanding of the SML. Those include vibrational sum frequency generation (VSFG) spectroscopy and voltammetry to analyze and quantify the surfactants, BREWSTER angle microscopy to study the morphology of SML films as well as advanced nuclear magnetic resonance (NMR) spectroscopy and high sensitivity mass spectrometry to characterize the substances present in the SML and marine aerosols.^[38,41–44] Considering the SML, it is feasible to distinguish it from the zone at the very interface between the air and the water. This zone is only one to few monomolecular layers thick and commonly referred to the sea surface nanolayer.^[3,45] The distinction between SML and nanolayer is especially useful for those analytic techniques that offer inherent surface sensitivity and directly

target the nanolayer. Nevertheless, besides this rather technical definition, the question arises to what extent the composition and properties of this nanolayer are significantly different from the underlying microlayer is still subject of ongoing research.

Finally, residing directly at the surface the SML is much more exposed to sunlight than the rest of the water column because the intensity of the light is attenuated by passing through the organic-enriched water. In particular, the combination of the presence of several different classes of organic compounds, many of them susceptible to excitation by light and acting as potential photosensitizers, qualifies the SML as an area of active photochemistry.^[4,46]

1.2 Photochemistry at the air-water interface

The boundary between two phases is associated with a sudden change in properties over a small spatial distance. As chemical and photochemical reaction dynamics often strongly depend on the local molecular environment (e.g. polarity, density and pH value), it is to expect that the reaction pathways, rate constants and products differ between processes in the bulk and those at the interface.^[47-49] The photochemistry, especially photodissociation, of adsorbed molecules at metal or semiconductor surfaces has been subject to research for several years. Here, substrates can influence the photophysical properties of adsorbates due to electron transfer from the photoexcited substrate states to the adsorbate (a form of photosensitizing) and opening new pathways for excitation and relaxation.^[47,50,51] Besides these solid/gas interface, boundaries between liquid and gas show remarkable photochemistry as well. Especially interfacial photochemistry between water and air is constantly getting more attention. At the boundary between a gas and a liquid, a potential photoreactant can be accessed by reaction partners from both the bulk and the gas phase, increasing the amount of potential reaction channels. In addition, volatile products of photochemical reactions are not trapped within solvent cages and may escape into the gas phase which can make their formation more favorable and thus leading to reactions different from the bulk. In addition, the high surface energy of water leads to an accumulation of organic material at the interface increasing the local concentration and hence the number of potential reaction partners. As a direct consequence, the presence of surfactants at the air-water interface can lead to accumulation of less surface active materials in the subsurface layer, enabling

them to absorb light and participate at photochemical reactions.^[52,53]

Photochemistry in natural waters includes a variety of complex and strongly interdependent processes, including halide radical formation, direct photoreactions of anthropogenic heteroaromatic pollutants, reactions induced by biogenic chromophores and various reactive oxygen species like hydroxyl radicals.^[54] Seawater contains many compounds which are somehow photoreactive and can act as photosensitizer. One important example is the dissolved organic matter that absorbs light in the visible spectral range, commonly referred to as chromophoric (or colored) dissolved organic matter (CDOM), and consists of a huge variety of different molecules and fluctuates temporally and spatially in its composition. It has been shown that the CDOM molecules can form a photoreactive triplet state upon excitation leading to consecutive reaction forming singlet oxygen formation as well as direct reaction with photochemically inactive substrate.^[55-57] A scheme for the excitation reaction of CDOM and the formation of singlet oxygen is outlined in eqs. 1.1 and 1.2.



Besides the rather unknown and variable CDOM composition, some chromophoric systems in the water are better understood. In particular chlorophyll, being a very efficient photosensitizer, as well as humic acids formed by degradation of dead organic material (detritus) and consisting of huge conjugated aromatic systems including carbonyl groups are contributing to marine photochemistry.^[58-61] In fact, many of the photochemical processes within natural waters are driven by the excitation of various aromatic carbonyl compounds (often derivatives of benzophenone), followed by different reactions including proton abstraction, electron transfer and formation of reactive oxygen species.^[57,62,63]

As the interface is a region with very distinct chemical and physical properties, it was suggested for long that photochemical processes occurring between sea and air might differ significantly from the bulk water. One of the early pioneer

works in the field of photochemistry at the air-water interface is the research conducted by Ehrhardt *et al.* It describes experiments using anthraquinone and similar heterocyclic organic compounds as photosensitizer and different alkyl benzenes and alkanes as reactants under irradiation of both natural and artificial solar radiation, leading to the formation of oxygenated products most probably formed via radical reaction pathways.^[64,65] Even the formation of low molecular weight carbonyls as products of a photosensitized reaction of aliphatic compounds in water has been observed.^[66] In the last few years, a series of studies revealed the formation of unexpected reaction products like unsaturated aldehydes and carboxylic acids from irradiation of surface films, strongly supporting the hypothesis of a difference between bulk and surface chemistry.^[52,53,67-71] An example of a reaction mechanism showing that the proximity to the surface enhances reaction pathways different from those in the bulk is shown in Fig. 1.2. In this example, the influence of the surface leads to the preferential formation of products like unsaturated alcohols and acids which wouldn't be formed in the bulk process. The corresponding experiments conducted by Tinel *et al.* included the usage of different photosensitizers similar to those present in natural systems (e.g. humic acid and benzoylbenzoic acid), applied to both artificial and natural surface samples containing fatty acids. Characterization of the products by means of high-sensitive mass spectrometry did in fact confirm the occurrence of unexpected unsaturated products formed upon radiation and in the presence of an additional photosensitizer. Interestingly, in the case of nonanoic acid, even without the presence of a photosensitizer, an unexpected direct photolysis was observed. Being unsusceptible to sunlight under normal conditions, the authors speculate about a potential red-shift in the absorption spectra of nonanoic acid caused by the formation of a dense interfacial aggregation of the acid as explanation for this behavior. In addition, quantum chemical calculations of the possible reaction pathways indicate the stabilization of some transition states by coordination of water molecules.^[53,72]

For most of the recent studies, the question arises if the photosensitizer was present directly at the air-water interface or if it is dissolved in the water bulk layer near the surface. Actually, surface-sensitive spectroscopy (ATR) has shown that rather soluble photosensitizers can accumulate in the subsurface region if a surface film is present, leading to a situation of a high local concentration of both sensitizer and substrate. In the example presented in Fig. 1.2 (upper left

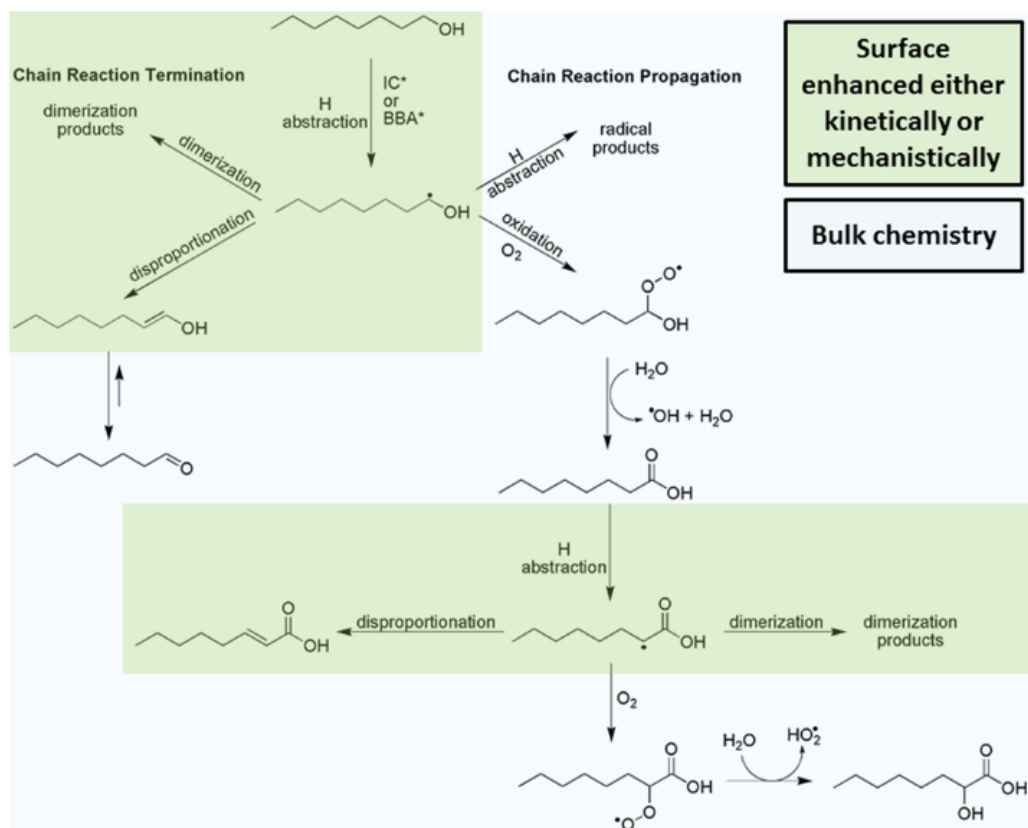


Figure 1.2: Tentative photochemical reaction pathways that may explain the interface-specific formation of unsaturated carboxic acids and high molecular-weight dimerization products (from Tinel *et al.*).^[53]

green box), the photochemical reaction is therefore initiated by H abstraction reaction from an octanol molecule (acting as surfactant) by the photoexcited photosensitizer molecule. In case the substrate concentration is high enough to compete with the fast deactivation of reactive species occurring in the bulk water. Singlet oxygen formed for example by the reaction of excited CDOM molecules (see eq. 1.2) are typically energy transfer reactions and classified as "indirect or type II mechanisms", in contrast to reactions that are based on radical chemistry and happen through electron transfer (type I mechanism).^[49,73] Those processes are described in more detail in chapter 2.3.

Besides model systems of more or less defined chemical compositions, also biological surface samples have been photolyzed. Interestingly, the formation of volatile products was much higher for dead biofilms, indicating that cell lysis and enzymatic degradation of complex biological macro-molecules form species

that accumulate at the interface to form surface layers.^[69] Again, unusual unsaturated compounds arose from interfacial photochemistry that may contribute significantly to the formation of secondary organic aerosols (SOA). So far, it had been widely assumed that unsaturated compounds stem from biological sources exclusively. This finding highlights the importance of understanding those interface phenomena in the context of atmospheric processes on global scale.^[69,74]

1.3 VSFG investigation of surface monolayers

The selective investigation of the interface without getting a significant contribution from the bulk is demanding and requires sophisticated analytical techniques. One of the tools that has been applied successfully to probe surface films down to sub-monolayer sensitivity, is vibrational sum-frequency generation spectroscopy (VSFG). It is a nonlinear laser-spectroscopic technique relying on the phenomenon of resonant sum frequency generation where two laser beams are overlapped temporally and spatially. In order to gain spectral information, usually one of the two beams is tunable within a certain spectral range. As the SFG signal is strongly enhanced if it is in resonance with a molecular transition, the tunability allows to scan the resulting SFG resonance as function of the incident wavelength within a certain spectral range resulting in a SFG spectrum. Note that in case of the vibrational SFG targeting molecular vibrational transitions, the tunable beam is always a laser beam in the infrared range of the spectrum, although in principle SFG experiments with using a tunable visible light (VIS) beam are possible as well and in contrast to the VSFG spectroscopy, would target electronic molecular transitions. The SFG process is related to the hyperpolarizability of the probed medium which is zero for centrosymmetric systems but non-zero for interfaces. Because at interfaces the inversion symmetry is always broken for reasons of symmetry, VSFG is intrinsically surface-sensitive and therefore well-suited to study the chemical properties of surfaces and interfaces.^[75] Finally, SFG also yields information about the chemical structure. The tensor properties of the hyperpolarizability make SFG sensitive to the polarization state of the incident laser beams and provide, supposing that the polarization of the detected signal and the incident fields are known, a way to determine the spatial orientation of the probed molecular transition dipole moment.^[76-79]

Shortly after the discovery of the SFG process by SHEN *et al.*, its potential to

study LANGMUIR monolayers has been identified.^[80-83] As SFG is susceptible to structural effects, highly ordered interfacial layers are particularly well suited to be studied by this technique. Changes occurring in the film upon chemical alteration, e.g. by oxidation processes triggered by ozone or photolysis, as well as declining surface concentration can be monitored in real-time by SFG.^[83] In the past VSFG spectroscopy has been employed to study a variety of interfacial systems and processes such as surfactants, chemically bound to surfaces like gold and silica or directly at the air-water interface. For example, the pronounced 2D phase behaviour of LANGMUIR monolayers and the chemical transformations of surface species of extremely complex interface systems like membrane proteins could be studied.^[84-90] The alteration of the SFG spectrum of pure water in the presence of ions and surfactants has been investigated providing insight in the molecular-level interactions and processes taking place at the very interface.^[91-96] In the context of the investigation of the physical properties of the air-water interface, SFG was successfully used to investigate the structure of pure water surfaces and several model systems of surfactants in water under laboratory conditions as well as naturally occurring surface-active materials.^[41,83,97-100] VSFG spectroscopy has also been applied to investigate of environmentally relevant species and atmospheric reactions at surfaces and interfaces, pioneered by GEIGER *et al.*^[101-104] In context of the cluster of excellence FUTURE OCEAN in Kiel, VSFG spectroscopy was successfully established as a tool to study the presence and relative abundance of surface-active substances in natural sea water samples from the Baltic Sea. This was achieved by measuring the strong VSFG signals of the characteristic stretch vibrations of the surfactant's alkyl chains, proving the feasibility of VSFG as a surface-specific, structure-sensitive technique for SML/nanolayer studies.^[41] Using this tool, in a consecutive study it has been shown that the spectrum of sea water samples exhibit certain distinct spectral signatures of carbonyl vibrations as well as vibrations attributed to the OH network of the water.^[105] Besides that, evidence was found that soluble surfactants (so-called "wet surfactants", typical examples are complex carbohydrates) are dominant rather than insoluble species ("dry" surfactants, typical examples are fatty acids).^[105] Finally, in a long-term time series VSFG analysis based on monthly SML sampling at the Boknis Eck station of the GEOMAR in the Baltic Sea revealed a periodic annual variation in the surfactant abundance that was not in parallel to the pronounced spring algae

bloom. This unexpected finding challenges the paradigm of a direct relation between surfactant concentration in the SML to primary production. In fact, the maximum of the VSFG signal indicating the highest surfactant abundance was typically observed in the late summer, 2-3 months after the main algae bloom. This observation was tentatively ascribed to the presence of molecular species acting as surfactants in the SML that are not direct products of primary production but the result of microbial and abiotic degradation processes.^[106] To get a better understanding and confirmation of this unexpected trend and to further work out details of the seasonal variability of the SML, observations over a longer time have been performed in this work. Moreover, a software tool has been developed to allow for automatized batch analysis of multiple VSFG spectra as well as to analyze (statistical) correlations to other oceanographic parameters obtained during the same cruises.

1.4 Outline of this thesis

The aim of this work was twofold. On the one hand it was to provide a first simple model system for investigating of surface photochemistry by means of surface-sensitive VSFG and LANGMUIR compression isotherms. As the compounds used in the literature for those experiments are typically relatively soluble and tend to equilibrate with the sub-phase to a certain degree, one of the key requirements for a suitable sensitizer is strong surface activity as well as well-known photochemical properties. An ideal model sensitizer system should form a monolayer of the sensitizer, well-aligned at the very interface between air and water in a way that the system is clearly dominated by the properties of the interface rather than the bulk. This would allow for the investigation of true surface photochemistry with the minimum possible bulk contribution. To the best of our knowledge, so far no studies have been performed with photosensitizers with such distinct surfactant properties. Besides that, another goal was to apply the tool set of surface analytical techniques to natural sea water samples in order to improve the understanding of their chemical physical properties with the long-term goal to investigate natural surface photochemistry. This work is structured in five result chapters, each in the form of a publication-like text covering a single topic. They are grouped in two parts, the first describing the tool development and analysis of natural sea water samples, the second covering the development and characterization of the artificial photosensitizer model system.

The necessary theoretical foundations required for all of them are presented in chapter 2. This includes the theory of surface tension, the characteristics and behavior of amphiphilic substances at interfaces with focus on the air-water interface as well as a brief introduction to the theory of VFSG spectroscopy and the photochemistry at surfaces. Following the experimental part (Chapter 3), Chapter 4 describes the custom-made software tools that were implemented and used to support the handling and management of the various interconnected and rather extensive data sets, especially by providing functionality of automated processing and visualization. Chapters 5 and 6 both deal with the analysis of natural sea water samples while the last two chapters focus on purely artificial photosensitizer systems. A time series analysis and overall summary of the SML samples obtained during the monthly Boknis Eck long-term observation station cruise is presented in chapter 5. The results of complementary surface analytical techniques applied to SML samples taken during the Baltic GasEx cruise 2018 are shown in chapter 6. Chapter 7 presents the design, synthesis and VFSG spectra of a novel class of artificial photosensitizers. Besides the basic characterization, first observations of autophotolysis of those systems are reported. The last chapter 8 deals with the 2D phase and chemical properties of mixed layers of naturally occurring fatty acids and the artificial photosensitizer. The ability to form well-mixed monolayers of surfactants and sensitizers is an important aspect for future studies of photosensitized reaction in organic monolayers.

CHAPTER 2

Theoretical Background

The following chapter introduces the basic theoretical concepts that form the foundation of this work. At first, the interface between air and water is characterized from a physical point of view introducing the concept of surface tension and the experimental technique used in this work to measure surface pressure, i.e. so-called WILHEMY plate technique. Subsequently, a brief discussion of the properties of surface-active compounds and their interfacial monolayers is presented. The third part is outline to the underlying theory of this work's primary experimental method, VFSG spectroscopy. Finally, a short introduction of the photochemistry and the specific photochemical properties of carbonyl compounds is given to set the context for the photochemical investigations conducted within this work.

2.1 Surfactants and interfacial layers

An interface is defined as the boundary between two immiscible phases. It must possess a thickness of at least one molecular layer if a molecular theoretical model shall be employed.^[107] Usually, by far the most of the molecules are located in the bulk phase and the interface often has only little contribution to the properties of the system. Examples of matter with very high interface-to-bulk ratios (i.e. surface-to-volume ratio) are very small particles like colloids and aerosol droplets or substances with an extremely high surface area caused by roughness like active charcoal or porous aluminosilicates.

The air-water interface is a zone where the density of water molecules changes extremely rapid within a few molecular layers.

2.1.1 Surface tension

Molecules located in the bulk water underlie strong overall isotropic interactions among each other mediated mainly by strong hydrogen bonds. Compared to them, the molecules at the very interface have substantially less direct neighbor molecules in the direction of the gas phase. Considering the sheer existence of a liquid phase as a proof for dominating attractive forces among the molecules being energetically favorable, molecules located at the surface have to be in a higher energy state due to being surrounded by a lower number of interaction partners. In order to bring molecules from the bulk to the surface and, consequently, in order to increase the surface area, work needs to be performed. Thus, water tends to minimize the surface-to-volume ratio resulting in the formation of spherical water droplets and curved menisci. The work that is required to create a specific amount of surface is called the surface tension σ . It can be defined in terms of simple mechanics considering an experiment where a metal frame of length l is pulled from water by a length dx leading to an increase of surface area equal to the area of water caught within the frame (see Fig. 2.2). This relation is shown in eq. 2.1. The factor of two appears because the frame creates in fact two interfaces (front and back).

$$\sigma = \frac{W}{A} = \frac{F \cdot dx}{2 \cdot dx \cdot l} \quad (2.1)$$

The definition as work necessary to increase the size of the surface area can also be used to express the surface tension in the language of thermodynamics. Assuming the simple case of a system which can only perform pressure-volume work, the reversible change in internal energy can be expressed by

$$dU = \partial Q + \partial W = TdS - pdV + \sigma dA_s \quad (2.2)$$

where dA_s denotes the differential change in surface area. This leads to a definition of the surface tension σ in terms of the free energy F and the GIBBS energy G , respectively:

$$\sigma = \left(\frac{\partial U}{\partial A_s} \right)_{S,V} = \left(\frac{\partial F}{\partial A_s} \right)_{T,V} = \left(\frac{\partial G}{\partial A_s} \right)_{T,p} \quad (2.3)$$

The surface tension of liquids is inherently temperature-dependent and decreases with rising temperature. An empirical relation describing this behavior was found by EÖTVÖS given in 2.4:

$$\sigma_m V_M^{2/3} = k_\sigma (T_{cr} - 6 \text{ K} - T) \quad (2.4)$$

In this expression, σ_m is the molar surface tension, T_{cr} is the critical temperature of the substance, V_M the molar volume. and k_σ the EÖTVÖS constant. The subtraction of 6 K, introduced by RAMSAY and SHIELD, reflects that the linear trend has been found to be valid for temperatures up to six Kelvin below than the critical temperature.^[108,109]

Besides the temperature dependency, solutes in the water and substances at the interface may alter the surface tension significantly. This is especially important because most of the naturally occurring water contains significant amount of dissolved salts. A plot of the surface tension as function of the salinity (for the sake of simplicity set equal to the concentration of NaCl in the water) is depicted in Fig. 2.1 for three different temperatures. It can be seen that the surface tension increases with the salt concentration which is the direct consequence of the difference between the potential energy of the surface water molecules with respect to the bulk phase, caused by the higher charge density inside the water due to the salt ions. This is the opposite of the effect of surface tension lowering by the presence of surfactants as described in section 2.1.2.

The WILHEMY Method of surface tension measurement

The surface tension can be measured by various static and dynamic methods. A very popular technique is the so-called WILHEMY plate method. The setup of this experiment is schematically shown in Fig. 2.2. A plate attached to a microbalance is submerged in the liquid where the surface tension shall be measured. The liquid forms a meniscus around the plate. The additional mass of this meniscus can be measured as a force related to the surface tension by eq. 2.5.

$$\sigma = \frac{F_z}{2(l + z) \cos \theta} \quad (2.5)$$

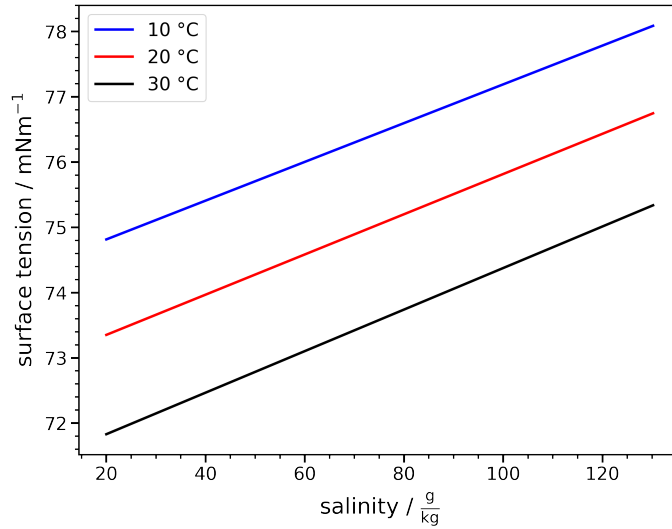


Figure 2.1: Surface tension as function of the salinity (salt concentration in the water) at three different temperatures.^[110]

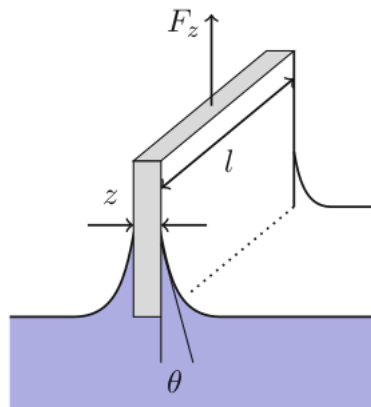


Figure 2.2: Schematic representation of the setup of the WILHELMY method. θ is the contact angle between the immersed plate and the liquid, F_z is the force exerted by the balance in order to keep the plate in equilibrium, z is the thickness and l the length of the plate.^[111]

Here, θ is the contact angle between the plate and the liquid. The geometry parameter necessary to describe the shape of the meniscus is the so-called 'wetted perimeter', defined by two times the length and the thickness of the plate. To avoid the need for knowing the contact angle, in practice rough platin or paper plates are applied. The rough surface leads to a contact angle down to zero, due to complete wetting. Typically, to compensate for the plate's mass and the buoyancy which also act as forces on the balance, a calibration of the system is necessary.

Another widespread and similar method to measure the surface tension is the dynamic DU NOÛY-PADDAY technique.^[112] A metal ring or rod, again with a rough surface to ensure complete wetting resulting in contact angle of effectively zero, is moved up-and downwards a few millimeters into the liquid of which the surface tension is to be measured. The force acting on this probe is measured by an electric or mechanic force sensor. The surface tension is related to the maximum of this force occurring during the movement which acts on the metal probe and can be calculated after careful calibration of the instrument.^[112-114]

2.1.2 Surface-active compounds

Some molecules show a tendency to concentrate and assemble at interfaces or surfaces spontaneously. As spontaneous processes are driven by a decrease in GIBBS free energy, this process of migration from the bulk to the interface must be energetically or entropically favorable. In case of the air-water interface, surfactants possess both moieties with hydrophobic and hydrophilic properties in spatially well-separated parts of the molecule. As the air-water interface shows a gradient of polarity from the gaseous phase with a low density of water molecules towards the bulk water, surfactants can assemble in a way that the hydrophobic parts can avoid the energetically unfavorable position being surrounded by water. This can happen by pointing the hydrophobic parts outside the phase boundary into the air. In addition, the hydrophilic parts can stay inside the water phase. The presence of a surface layer of amphiphiles leads to a reduction of the surface tension of the water. Note that there is an energetically favorable interaction of the hydrophilic groups of the monolayer with water molecules of the interface. The resulting enrichment of the surface-active compound at the interface can be described by the GIBBS isotherm.

Surface excess

The model developed by GIBBS assumes a system consisting of two phases A and B and an interface line with no vertical dimension between them (usually referred to as the dividing surface). If an amount of substance, for example a surfactant, is added to this system, the substance will be distributed among the phases and the surfaces according to its solubility, but the total amount of the i -th substance n_i^{total} will remain unchanged. This is reflected by eq. 2.6.

$$n_i^{total} = n_i^\sigma + n_i^A + n_i^B = n_i^\sigma + c_i^A \cdot V^A + c_i^B \cdot V^B \Rightarrow \quad (2.6)$$

$$n_i^\sigma = n_i^{total} - c_i^A \cdot V^A - c_i^B \cdot V^B \quad (2.7)$$

This means that the amount of substance i present at the interface n_i^σ can be determined by measuring the concentration of it in the phases A and B . As the interface has no thickness in this model (i.e. the concentrations c_i^A and c_i^B can be assumed to be stay constant up to the dividing surface), the measured sum of n_i^A and n_i^B can become bigger or smaller than the total amount of substance n_i^{total} . This is the result of an over or underestimation of the amount of substance in the two phases near the interface, caused by the enrichment or depletion of the compound i in the interfacial region. The ratio of n_i^σ and the area of the dividing surface A , as shown in eq. 2.8, is defined as the **surface excess concentration**.^[115]

$$\Gamma_i^\sigma = \frac{n_i^\sigma}{A} \quad (2.8)$$

GIBBS derived a relation between this excess concentration and the change in surface tension σ as stated in eq. 2.9. Here a_i is the activity of component i , R is the gas constant and T the absolute temperature.

$$\Gamma_i^\sigma = -\frac{1}{RT} \left(\frac{\partial \sigma}{\partial \ln a_i} \right)_{p,T} \quad (2.9)$$

For positive Γ_i^σ , σ decreases with increasing concentration of the surfactant. Note that in contrast to surfactants, it is also possible that substances avoid the interfacial region (negative surface excess concentration) which leads to an increase in surface tension, as it can be derived from 2.9. This is observed for dissolved ions and results from the strong electrostatic interactions between them and the water.

Typical classes of surface-active molecules are long-chain fatty acids, bearing a hydrophilic carboxyl group with the potential to increase the hydrophilicity even more upon deprotonation, long-chain alcohols, phospholipids and complex carbohydrates and glycoproteins. Those compounds are classified by their ionization state as non-ionic, cationic, anionic or zwitterionic surfactants.

Depending on the solubility of the surfactant it is distinguished between rather "soluble surfactants", which enrich in the surface region by adsorption equilibration but do not form a well-ordered film at the very interface, and insoluble ones, which are so hydrophobic that they completely avoid the dissolution in water and aggregation to surface films or, at high concentrations, can form micelles. The latter are referred to as **dry surfactants** whereas the former are known as **wet surfactants**. The dense and well-ordered monolayers formed by dry surfactants are defined as LANGMUIR layers, the sub-phase aggregation adsorption layers as GIBBS monolayers. Substances like long-chain fatty acids behave almost like ideal dry surfactants which is attributed to their very low water solubility, whereas complex biological macromolecules (e.g. lipopolysaccharids) rather show the behavior of wet surfactants. Nevertheless, both models must be seen as extreme cases reflecting the limits of a continuum and it is possible that a real system shows characteristics between those extremes. This becomes clear if the homologous series of carboxylic acids is considered: real dry-surfactant behavior starts at carbon chain length > 12 , the shorter acids are too soluble. The enrichment of surfactant molecules at the surface can reach a maximum value known as the critical micell concentration (CMC). If the concentration is further increased at this point, the interfacial layer collapses and forms micells, multilayers and other forms of aggregates in the sub-phase.

2.1.3 Surface layers and their 2D phase behavior

Besides the rather old experimental procedure of the measurement of compression isotherms, a variety of modern analytical techniques have been applied to study the structural and physical properties of those films in detail. This includes X-ray diffraction structure determination, BREWSTER angle microscopy, polarized fluorescence microscopy and VFSG.

The LANGMUIR trough and spreading procedure

In order to understand the complex 2D phase behavior of LANGMUIR monolayers, it is necessary to introduce the concept of the recording of compression isotherms by means of a LANGMUIR trough. This instrument consists of a trough made from an inert material (often polytetrafluoroethylene, PTFE), equipped with two movable barriers that hold back the surface film, and a probe to monitor the surface tension, usually a WILHEMLY plate. This setup can be used to monitor the change in the surface pressure as function of the area available per molecule by adjusting the barrier position. The trough is filled with a solvent, often water, and the surfactant of interest is introduced by spreading a volatile surfactant solution onto the surface of the substance in the trough. This procedure allows to form films of substances that, under normal circumstances, wouldn't form surface films but insular domains or micelles. The physical quantity determining whether a liquid B spreads spontaneously over another liquid A is the **spreading pressure** $S_{A/B}$ as defined in eq. 2.10.

$$S_{A/B} = \sigma_A - \sigma_B - \gamma_{AB} \quad (2.10)$$

γ_{AB} is the interfacial tension between the two liquids and σ_A and σ_B are the surface tensions between the pure liquids and air, respectively.^[116] A positive spreading pressure indicates a spontaneous spreading. This indicates that, if the surface tension of B is very high, it might not spread spontaneously, making it necessary to apply the volatile solvent as described above. In this case, the surface tension of the solvent becomes relevant for the spreading pressure, hence leading to a spreading of the solvent containing the surfactant. Because of its volatility, the solvent evaporates rapidly, leaving a film of the surfactant behind. The final amount of surfactant present on the surface can be tuned by variation of its concentration in the spreading solvent. In LANGMUIR compression isotherms, usually the **surface pressure** Π is measured as function of the area per molecule in the unit of \AA^2 per molecule. Π , bearing the unit of N m^{-1} , is defined as the difference between the surface tension of the pure solvent σ_s and the actual surface tension measured by the probe that is influenced by the presence of the monolayer σ_{ml} . This relation is stated in eq. 2.11.

$$\Pi = \sigma_s - \sigma_{ml} \quad (2.11)$$

To describe the mechanical behavior of the film, the quantity **surface elasticity** ε is often used. It is defined as shown in eq. 2.12 where A is the area and Π is the surface pressure. The inverse of the elasticity is known as the compressibility of the film and measures the resistance of the film against compression. A high compressibility refers to a small increase in surface pressure upon a large decrease in available area per molecule and *vice versa*.

$$\varepsilon = A \cdot \frac{\partial \Pi}{\partial A} = \frac{\partial \Pi}{\partial \ln A} \quad (2.12)$$

2D phase behavior of LANGMUIR monolayers

The surface pressure is, as it describes the change in the solvents surface tension caused by the surfactant, strongly dependent on the interactions between the surfactant molecules on the surface. Assuming a typical compression isotherm experiment, upon compression of the barriers and therefore reducing the available space for the molecules, the intermolecular interactions increase. An idealized isotherm obtained in this way is shown in Fig. 2.3. Starting at $\Pi = 0$, directly after spreading, the area available for each molecule is large comparing to its size. Thinking in a molecular picture, the surfactant molecules lay coiled and flat on the surface of the solvent, having enough free space between each other that no interaction can occur. As this situation of molecules not interacting with each other is similar to the 3D situation of an ideal gas, this state is called **gaseous**. The influence on the surface tension of the underlying solvent is minimal and usually the surface pressure in this state remains close to zero. As the barriers are moved and the area per molecule is decreased, the molecules start to interact with each other, after lifting up existing alkyl chains from the surface into the air. The horizontal line in the isotherm shown in Fig. 2.3 indicates the coexistence of the gaseous and the **liquid-expanded** region. After this zone of coexistence, the liquid-expanded phase is predominant. Compressing this liquid-expanded phase leads to, after passing an area of coexistence again, another phase transition to a state where the chains are pointing upward from the liquid in an ordered manner, leading to a much higher structured order. This state is, according to HARKINS, referred to as the **tilted-condensed** or **liquid-condensed** phase because a significant tilting angle between the chains and the molecule's surface normal is observed.^[117] As the molecules strongly interact with each other, the

overall structural order is strongly enhanced compared to the liquid-expanded state. Therefore, the terminus “condensed” is justified. The tilt angle is a degree of freedom with respect to further compression until reaching the next transition point where the compressibility becomes lower, resulting in a steep rise of the isotherm. This region is called **untitled-condensed** or **solid**, following the HARKINS nomenclature.^[117] The hydrophobic chains are well-aligned and structured and the tilt angle with respect to the surface angle is minimal, although not necessarily equal to zero.

If the compression is continued, after reaching a specific critical surface concentration, the monolayer collapses. This is a chaotic process, leading to the formation of micells, multilayers and partial dissolution into the sub-phase. Furthermore, monolayer collapse is irreversible, meaning that upon expansion of the barriers and repeating the compression the surface pressure as function of the area per molecule will not be reproducible. An extrapolation of the surface-pressure isotherm to the abscissa, starting at the collapse point as illustrated by the dashed red line in Fig. 2.3, yields the molecular cross-sectional area. It is a measure for the minimal space requirement of a single surfactant molecule within the compressed monolayer.

The phase behavior, especially the position of the phase transition points and its temperature dependence, is specific for each type of surfactant. Structural properties of the compounds like chain length, degree of chain branching, polarity and size of the hydrophilic head group as well as the presence and configuration of double bonds are factors that have strong influence on the appearance of the isotherm. However, external factors like temperature and ionic strength of the system as well as the presence of other surface-active contaminants often change the isotherms drastically. This makes it necessary to conduct those kind of experiments under well-defined and preferably clean-room conditions.

The described 2D phase phenomena are typically observed for dry surfactants forming LANGMUIR monolayers. Considering wet surfactants that are enriched in the sub-phase, up to very high concentration no measurable effect on the surface pressure is observed. However, this does only hold true for compression speeds which are slow compared to the equilibration time of the surface adsorption equilibrium. Under typical compression speeds used in LANGMUIR trough experiments the upconcentration by reducing the available area exceeds a certain critical point, both changes in surface pressure and phase transitions

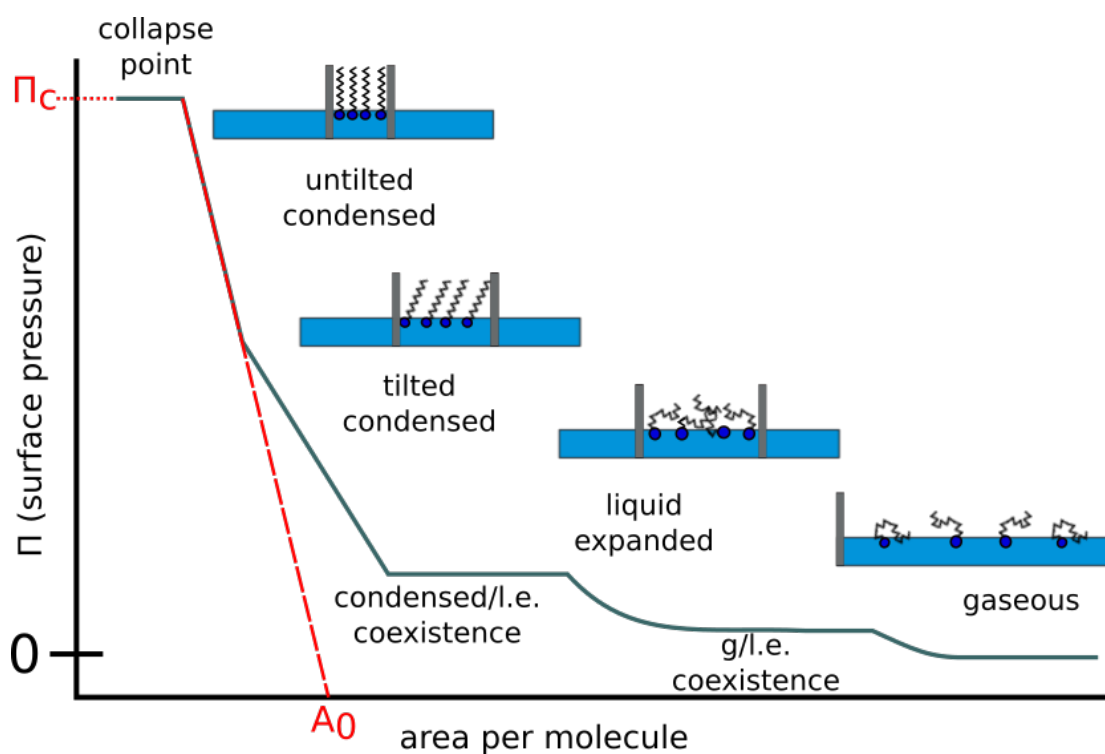


Figure 2.3: Idealized isotherm reflecting the 2D phase behavior of a LANGMUIR monolayer. Π_c is the surface pressure at which the collapse of the layer occurs and A_0 indicates the cross sectional area of the molecule. The phase naming convention follows the suggestion of Kaganer *et al.*^[118] Note that different nomenclatures of the phases are present in the literature with the one of HARKINS being used frequently for historical reasons.^[117]

may be observed. In the case of high compression speed, the equilibration with the sub-phase is too slow to keep up with the upconcentration at the surface. If the compression is stopped, the dissolution will then lead to a decrease of the surface pressure until the equilibrium is restored. The solubility of wet surfactants is dependent on the temperature, the pH-value and in particular to the presence of other species in the system. This can become relevant in natural systems if the presence of dry surfactants at the interface may lead to an upconcentration of rather wet surfactants in the underlying sub-phase. In natural systems, such wet surfactants like for example humic compounds can act as photosensitizers, especially if they are enriched in the proximity of potential photochemical reaction partners.

2.2 Vibrational Sum Frequency Generation Spectroscopy

2.2.1 Generation of SFG and the macroscopic susceptibility

Electromagnetic fields induce a polarization in susceptible media by displacement of valence electrons. For low field strengths, the response of the medium is linear, giving rise to phenomena like refraction and reflection. The induced polarization, defined as the dipole moment per unit volume, can be expressed as follows:

$$\vec{P} = \epsilon_0 \chi^{(1)} \vec{E} \quad (2.13)$$

Here, ϵ_0 is the dielectric constant, \vec{E} is the driving electric field and $\chi^{(1)}$ is the first-order susceptibility of the medium. If the external field strength is of the same order of magnitude as the field the electrons of the medium experience by their nuclei, the response of the material is no longer linear.^[79,119] The expression for the polarization must be extended by nonlinear terms, yielding the power series shown in eq. 2.14.

$$\vec{P}_{total} = \sum_{i=1}^n \vec{P}^{(i)} = \epsilon_0 \sum_{i=1}^n \chi^{(i)} \vec{E}^i \quad (2.14)$$

In this equation, $\chi^{(i)}$ represents the i th order susceptibility. The electric field strength required to observe significant nonlinear contributions can be achieved by employing pulsed lasers. In the case of optically anisotropic materials $\chi^{(n)}$ is a tensorial quantity of rank $n + 1$, mapping the components of the electric field vectors of the incident fields oscillating at ω_1 and ω_2 to the resulting SFG vector, using the sum convention of EINSTEIN:

$$E_{\omega_1+\omega_2,i} = \chi_{ijk} E_{\omega_1,j} E_{\omega_2,k} \quad (2.15)$$

It is obvious from eq. 2.15 that sum frequency generation is a second order nonlinear process occurring when two intense laser beams overlap temporarily and spatially. In the exponential form, the time-dependent electric field generated by those two beams of the distinct frequencies ω_1 and ω_2 can be expressed as the

sum denoted in eq. 2.16.

$$\vec{E}(t) = \vec{E}_1 e^{-i\omega_1 t} + \vec{E}_2 e^{-i\omega_2 t} + c.c. \quad (2.16)$$

In this term E_i denotes the amplitude of the electric field, i the imaginary unit and $c.c.$ the complex conjugate of the electric field expressions. As sum frequency generation is a second order process, only the second order susceptibility is taken into account.

$$\vec{P}^{(2)}(t) = \epsilon_0 \chi^{(2)} \vec{E}(t)^2 \quad (2.17)$$

Substituting the square of eq. 2.16 into eq. 2.17 yields the following expression:

$$\begin{aligned} \vec{P}^{(2)}(t) = \epsilon_0 \chi^{(2)} [& \\ \vec{E}_1^2 e^{-2i\omega_1 t} + \vec{E}_2^2 e^{-2i\omega_2 t} & \quad \text{SHG} \\ + 2\vec{E}_1 \vec{E}_2 e^{-i(\omega_1 + \omega_2)t} & \quad \text{SFG} \\ + 2\vec{E}_1 \vec{E}_2^* e^{-i(\omega_1 - \omega_2)t} & \quad \text{DFG} \\ + c.c.] & \\ + 2\epsilon_0 \chi^{(2)} (\vec{E}_1 \vec{E}_1^* + \vec{E}_2 \vec{E}_2^*) & \quad \text{OR} \end{aligned} \quad (2.18)$$

As it can be seen, the resulting electric field has several contributions oscillating at different frequencies which are referred to by special termini, as indicated at the right-hand side of eq. 2.18. The frequency-independent part is called the optical rectification (OR) and describes a static polarization induced by the external fields. The two contributions oscillating at the double frequency of both incident waves refer to a process known as second harmonic generation (SHG). The difference frequency generation (DFG) and the sum frequency generation (SFG) terms describe components oscillating at the sum and the difference of the two incident frequencies ω_1 and ω_2 . The following considerations will focus on the sum frequency generation.

In order to find an adequate formalism to describe the dependence of the SFG process on the direction, polarization and intensity of the lasers, a sequence of transformation steps is necessary. A schematic representation of the simplified system that is used to describe SFG is shown in Fig. 2.4. The polarization of the incident beams is defined with respect to the plane of incidence, a theoretical

plane that is spanned by the incident beam, the surface normal and the reflected SFG beam. If the plane in which the electric dipole of the incident beam oscillates is perpendicular to the plane of incident, the polarization state is defined as **s** (derived from German "senkrecht"), if it is parallel the state is referred to as **p**. In Fig. 2.4, the polarization of the IR beam is p and the VIS beam is s-polarized, as this combination is used most frequently in the experimental scope of this work. The beams overlap on the surface and induce a surface field, giving rise to a surface polarization and finally leading to the generation of SFG. The angles of incident θ_{IR} and θ_{VIS} as well as the SFG reflection angle θ_{SFG} are measured with respect to the surface normal. As example, one palmitic acid molecule is depicted to symbolize the presence of a surfactant at the probed interface. Two coordinates coexist in this model: the laboratory coordinates x,y,z which are used to express the macroscopic susceptibility and the molecular coordinates a,b,c of each molecule which are related to the first hyperpolarizability, i.e. the microscopic analogy of $\chi^{(2)}$.

The picture shows that a series of transformations is necessary to relate the incident electric fields with the generated SFG signal. The steps for this connection are illustrated in Fig. 2.5. Beginning from the incident laser beams in s/p polarization, the first step is the generation of a surface electric field, including the mapping to the surface coordinates. This can be achieved by employing the **K-factors**. This relation is expressed in eq. 2.19 where \vec{E}_i is the resulting surface electric field in i -direction, $E_{s/p}^I$ is the incident electric field in s or p polarization, \hat{i} is the corresponding unit vector in i -direction and K_i is the K-factor for the i direction of the surface field.^[120]

$$\begin{aligned}\vec{E}_x &= K_x E_p^I \hat{x} \\ \vec{E}_y &= K_y E_s^I \hat{y} \\ \vec{E}_z &= K_z E_p^I \hat{z}\end{aligned}\tag{2.19}$$

It can be seen that the different polarizations contribute to different components of the surface field. Comparing the direction of the y -coordinate and the direction of the s-polarization in Fig. 2.4 indicates clearly that the y direction of the surface field can only be induced by s-polarized light whereas p can be separated in a x and a y component. The K-factors are expressions derived from the

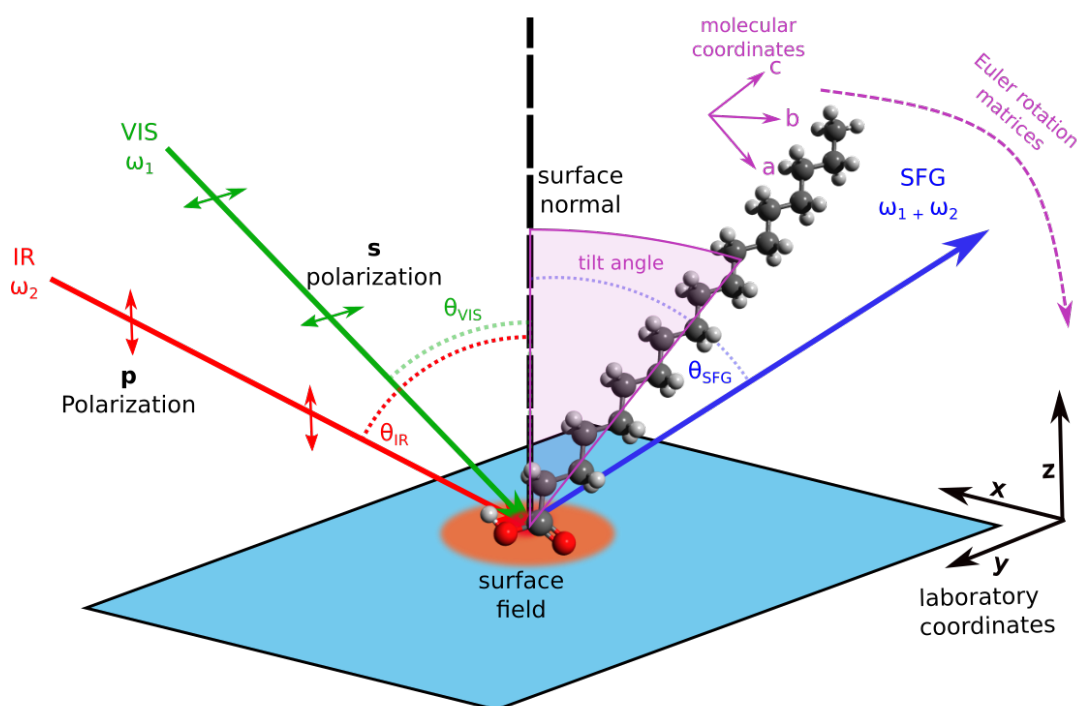


Figure 2.4: Illustration of the model system commonly employed to derive the theoretical description of the SFG response. The red and green arrows indicate the incident laser beams of frequency ω_1 and ω_2 , respectively. The blue arrow depicts the generated reflected SFG field. The corresponding angles of incidence and reflection θ_i are defined with respect to the surface. Note that the reflected incident beams as well as the transmitted beams are omitted for reasons clarity. All the experiments in this work were conducted in reflection geometry. Indicated in purple, a well-aligned all-*trans* molecule of palmitic acid at a tilt angle of the alkyl chains with respect to the surface normal is shown to visualize the molecular and laboratory coordinate systems.

FRESNEL equations. As example, the term describing K_x is given in eq. 2.20.

$$K_x = \pm \cos \theta_I (1 - r_p) \quad (2.20)$$

Here, the θ_I is the angle of incidence relative to the surface normal and r_p is the FRESNEL factor, defined as the ratio of reflected to incident light for p-polarization. This factor has to be taken into account because the total electric field of the interface is the sum of incident and reflected beam's fields. It can be obtained as stated in eq. 2.21, where $\vec{E}_p^{R/I}$ is the reflected/incident field in p-polarization, respectively, n_T and n_I are refractive index of the medium where the beams are transmitted (T) to and occurring from (I) and $\theta_{I/T}$ the respective angles of transmission and reflection.^[120]

$$r_p = \frac{\vec{E}_p^R}{\vec{E}_p^I} = \frac{n_T \cos \theta_I - n_I \cos \theta_T}{n_I \cos \theta_T + n_T \cos \theta_I} \quad (2.21)$$

Having found the relation between incident fields and surface electric field, the sum frequency polarization $\vec{P}_{i,SF}^{(2)}$ of the medium caused by this field can now be expressed in the following form:

$$\vec{P}_{i,SF}^{(2)} = \epsilon_0 \chi_{ijk} \hat{j} K_j E_{p/s,\omega_1}^I \hat{k} K_k E_{p/s,\omega_2}^I \quad (2.22)$$

Here, \hat{j} and \hat{k} are the unit vectors in the three space dimensions of the respective field components of both incident waves. To relate this polarization generated by the surface field with the resulting SFG, a set of expressions called the **L-Factors** (non-linear FRESNEL factors) has been derived.^[121] This connection is shown in eq. 2.23 where the index i represents the three cartesian coordinate and $\vec{E}_{i,SF}$ the resulting SFG field in i direction.

$$\vec{E}_{i,SF} = L_i \vec{P}_{i,SF}^{(2)} \quad (2.23)$$

For each direction in space and for both reflection and transmission, one L factor is defined. This allows one to express the intensity of the emitted SFG field as proportional to the sum over all components of the surface polarization, generated by the two incident beams, multiplied by the respective L factor. This

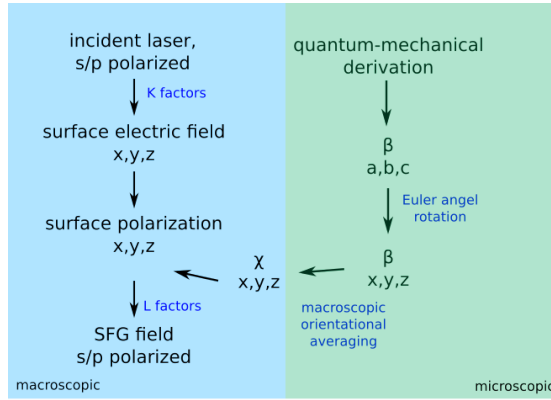


Figure 2.5: Schematic representation of the calculation steps to relate the incident laser intensities in s/p polarization with the resulting SFG response, including the transformation from the microscopic molecular system to the laboratory bulk system.

is shown in eq. 2.24 for the p-polarized SFG beam.^[120]

$$\begin{aligned}
 I_{p,SF} &\propto \left| L_x \vec{P}_{x,SF}^{(2)} \right|^2 + \propto \left| L_z \vec{P}_{z,SF}^{(2)} \right|^2 \\
 &\propto \left| L_x \sum_j^{x,y,z} \sum_k^{x,y,z} \epsilon_0 \chi_{xjk}^{(2)} K_j E_{p,\omega_1}^I K_k E_{p,\omega_2}^I \right|^2 \\
 &+ \left| L_z \sum_j^{x,y,z} \sum_k^{x,y,z} \epsilon_0 \chi_{zjk}^{(2)} K_j E_{p,\omega_1}^I K_k E_{p,\omega_2}^I \right|^2
 \end{aligned} \tag{2.24}$$

This expression relates the two incident fields with the emitted SFG wave. However, this is not yet sufficient to explain the frequency-dependence of the generated SFG signal which allows the SFG spectroscopy. To describe this in detail, the connection of the macroscopic susceptibility to the corresponding microscopic properties of the molecule is essential. Besides this frequency-dependent resonant part of the SFG signal arising from molecular transitions, the substrate (chemical environment the species of interest is located, typically a gold, quartz or water interface) may contribute to the overall SFG intensity in a resonant or non-resonant way. For surfactants bound to gold surfaces, the non-resonant signal can be significant and influence the signal shape and intensity drastically.^[122] In case of the water surfaces that are they key focus of this work, however, the

non-resonant contribution of the water to the overall SFG signal is so small that it can be neglected. However, it has been shown quite recently that even for water surfaces charges in the proximity of the interface, as induced for example by dissolved ions, may contribute a significant third-order susceptibility term ($\chi^{(3)}$) which can alter the appearance of the spectral line shapes.^[123] This means that especially for high ion strength, high surfactant concentrations at the surface and charged surfactants (e.g. deprotonated carboxylic acid residues), special attentions has to be taken to such effects if a sophisticated modeling and simulation of the SFG lineshapes is intended.

2.2.2 Microscopic approach and resonance

The response of a single molecule to an external electric field, hence the microscopic analogue to the susceptibility a power series expansion is as shown in eq. 2.25 is employed.

$$\vec{\mu} = \vec{\mu}_o + \alpha\vec{E} + \beta\vec{E}^2 + \gamma\vec{E}^3 \dots \quad (2.25)$$

In this expression, $\vec{\mu}_o$ is the permanent dipole moment of the molecule and μ the overall induced dipole moment as induced by the driving electric field. As SFG is a second-order nonlinear process, the physical quantity governing this phenomenon is β , the so-called first hyperpolarizability. In analogy to the changes in linear optical properties occurring if the incident wavelength is close to the energy of a molecular transition, β strongly depends on the frequency of the incident electric field. Large values are obtained if one (single resonance) or both (double resonance) incident laser beams match the transition energy between two molecular states. This is reflected by the form of β given in eq. 2.26. It holds true for a single resonance experiment with a LORENTZIAN-type line shape of the underlying molecular transition.

$$\beta_{\alpha\beta\gamma} = \frac{1}{2\hbar} \frac{M_{\alpha\beta}A_{\gamma}}{\omega_{\nu} - \omega - i\Gamma} \quad (2.26)$$

β , being a tensor quantity as χ , also has three indices named $\alpha\beta\gamma$ that refer to the molecular coordinates abc as depicted in Fig. 2.4. The frequency of the incident field is ω , the frequency of the molecular resonance is ω_{ν} , \hbar the reduced PLANCK constant, A_{γ} the infrared transition moment, $M_{\alpha\beta}$ the RAMAN tensor

and Γ the mean lifetime of the excited state that determines the linewidth. This indicates that an SFG-active transition with a nonzero value for β (being SFG-active) must be both IR and Raman active. Actually, the resonant SFG process can be characterized as a simultaneous Raman-and infrared transition as it is illustrated in the schematic energy state diagram depicted in Fig. 2.6. In the resonant case illustrated in the left schema, the IR photon matches the energy between the ground state and an excited vibrational state, leading to absorption and vibrational excitation. At the same time, the visible photon induces an anti-Stokes Raman process connecting the vibrationally excited state with the ground state via an virtual energy level S . In the non-resonant case, both transitions correspond to virtual states and occur with a much lower probability. Based on this model, it is clear that the hyperpolarizability strongly depends on the incident frequencies. This allows, if one or both of the incident beams are tunable in their frequency, to measure the arising SFG signal as function of frequency and obtain spectral information about the probed system. In most setups, a fixed-wavelength laser in the near-IR or visible range is used as the upconversion light pulse and a tunable IR laser is overlapped and the spectral range of molecular vibrational transitions is scanned, resulting in a VFSG spectrum.

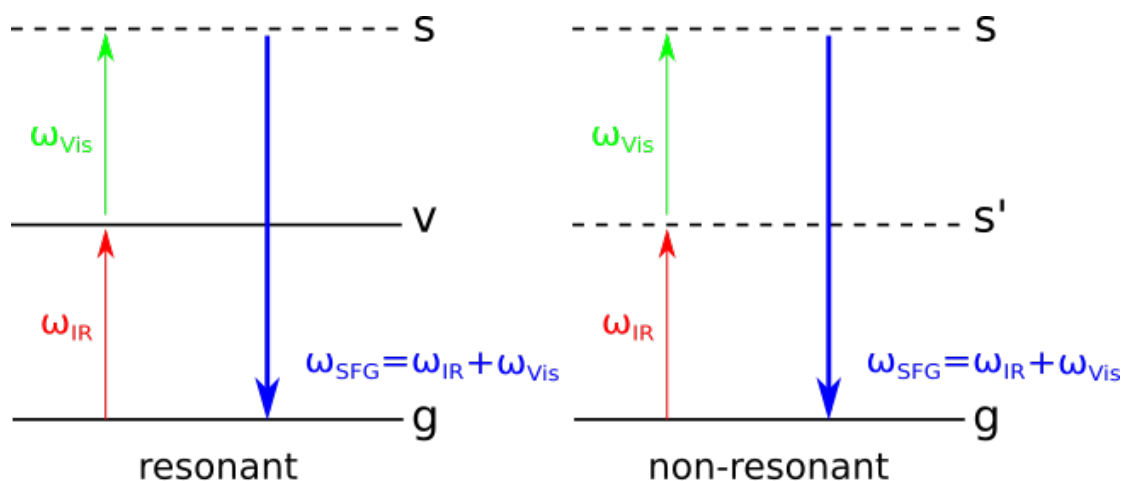


Figure 2.6: Schematic representation of the involved states in the resonant (left) and non-resonant (right) SFG process. g indicates the ground state, v an excited vibrational state and s/s' virtual energy levels not corresponding to molecular eigenstates.

In order to calculate the macroscopic susceptibility from β , first one has to take into account that a transformation from the molecular coordinates, in which the hyperpolarizability is defined, to the laboratory coordinate system defined by xyz is necessary. Those coordinates are interrelated by three rotation angles between their coordinate axes, usually referred to as the EULER angles. The EULER transformation allows to transform from one to the other system by applying a sequence of three rotation matrices, each corresponding to one of the angles. Second, χ may be expressed as the macroscopic average of β within a unit volume. Therefore, it depends on the average orientation expressed by the gross average of the EULER angles depicted in eq. 2.27:

$$\chi_{ijk} = \frac{N}{\epsilon_0} \sum_{\alpha\beta\gamma} \langle R(\psi)R(\theta)R(\phi)\beta_{\alpha\beta\gamma} \rangle = \beta_{\text{eff}} \cdot N \quad (2.27)$$

Here, $R(i)$ is the matrix transforming the molecular coordinate system by rotation about the EULER angle i to the laboratory coordinate system and N the number of molecules per unit volume. The average angular distribution of a given set of molecules in a system can be obtained, for example, by molecular dynamic simulations which, in combination with quantum-chemical calculation of the transition moments, allows a prediction of the susceptibility in principle. However, this approach was found to be difficult in practice and is a subject of ongoing research.^[124] As the average orientation of the molecules relative to the laboratory coordinate system influences the signal, SFG intensity is not only depending on the square of the number of molecules at the surface but exhibits an additional orientation-dependence related to β_{eff} as shown in eq. 2.28:

$$I_{\text{SFG}} \propto (\beta_{\text{eff}} \cdot N)^2 \quad (2.28)$$

Hereby, N is the number of surface oscillators, β_{eff} the average (and therefore orientation-dependent) hyperpolarizability. Note that for a surfactant monolayer β_{eff} is a function of N itself. As shown in section 2.1.3 the overall molecular orientation is strongly dependent on the surface coverage. In case of a complete isotropic distribution of surface transition dipole moments of the molecule, the SFG signal completely vanishes because of destructive interference. This is due to the fact that in the ideal isotropic configuration for each molecular vibration

in a certain direction, another one with the exact same intensity and phase but in the opposite direction will occur.

Several studies have been published investigating molecular orientation by means of VSFG, however, usually a set of assumptions and approximations is applied to reduce the immense complexity of the system.^[125,126] A common model is to assume the molecules exhibit a certain small range of tilt angles with respect to the surface normal while the azimuth angles are distributed isotropically, leading to a C_∞ -symmetry of the surface. In combination with a symmetric environment of the probed functional group, e.g. C_{3v} for a terminal methyl group in alkyl chains, the number of independent tensor elements is significantly reduced and the evaluation of the SFG intensities at two different polarization combinations can be sufficient to determine the molecular tilt angle.^[127,128] A more recent approach to determine the molecular orientation relies on the so-called *polarization null angle* method. This method utilizes a p-polarized tunable IR beam in combination with an upconversion beam with a polarization state between s and p, usually -45° . The detected SFG polarization is then varied until a minimum of the signal is found. This SFG angle can then be related to the molecular orientation.^[129,130]

The total macroscopic susceptibility usually consists of both a resonant and a non-resonant part. Non-resonant susceptibilities often arise from contributions of the substrate. In case of surfactants at the air-water interface the non-resonant background signal from water is relatively weak. In such a case and assuming a specific vibration being in phase with the non-resonant background signal it is possible to simply subtract the non-resonant contribution by taking the difference between the square roots of the SFG signal intensity I_{SFG} and the background I_{BG} . (eq. 2.29) This corrected signal is still proportional to the number of surface oscillators and the effective susceptibility.^[131]

$$\sqrt{I_{SFG}} - \sqrt{I_{BG}} \propto \beta_{\text{eff}}(N) \cdot N \quad (2.29)$$

In practice, in and out of phase interaction of the background and the resonant signal can occur. Therefore, care should be taken in cases where the background intensity correction becomes comparable to the resonant signal contribution. In such cases, a simple relation of the SFG intensity with the total number of surface oscillators may not hold true at all.

2.3 Photochemistry

2.3.1 General aspects

The absorption of light in the UV and VIS region of the spectrum by chromophoric species, such as molecules and semiconductors, initiates photochemical reactions and allows a very large variety of reactions to take place that are almost impossible by simple thermal excitation. The most important photo-physical processes that can occur upon excitation of a susceptible system are shown in the JABLONSKI diagram in Fig. 2.7. In most cases, the first step is the excitation from the ground state to the first excited state of the same multiplicity, that is $S_0 \rightarrow S_1$. From this state of high energy, the system can undergo various pathways of relaxation. One possibility is returning to the singlet ground state by converting the excess energy into thermal energy. This mechanism is called vibrational relaxation, often going along with the a transition of the vibrational state of the electronically excited state to a highly vibrational excited state of the electronic ground state (internal conversion). From the latter, again a fast relaxation due to thermal energy dissipation by the surrounding environment (e.g. solid matrix or solvent) takes place. Another way of relaxation is the direct emission of a photon corresponding to the energy difference between S_0 and S_1 , commonly referred to as fluorescence. Those two mechanisms are often rather fast and lead to a deactivation of the excited state too fast for consecutive photochemical transformations. However, in some chromophoric systems it is possible that a radiationless transition between the excited singlet state and an excited triplet state of similar energy takes place. This process is called intersystem crossing, leading to a significantly enhanced lifetime of the excitation because the transition back to the ground state S_0 is spin-forbidden. The radiative relaxation from such an excited triplet state leads to a relatively long-lived emission of light known as phosphorescence.

If the photochemical system is in an electronically excited state it has electrons with an energy much higher than at thermal equilibrium. This is the driving force for consecutive photochemical transformations. The most simple case of a photochemical reaction is the direct homolytic bond cleavage by absorbing a UV photon leading to highly reactive radical products. For example, this happens in the upper parts of the atmosphere and plays an important role in the photochemistry of gases. In condensed matter, the spatial proximity between

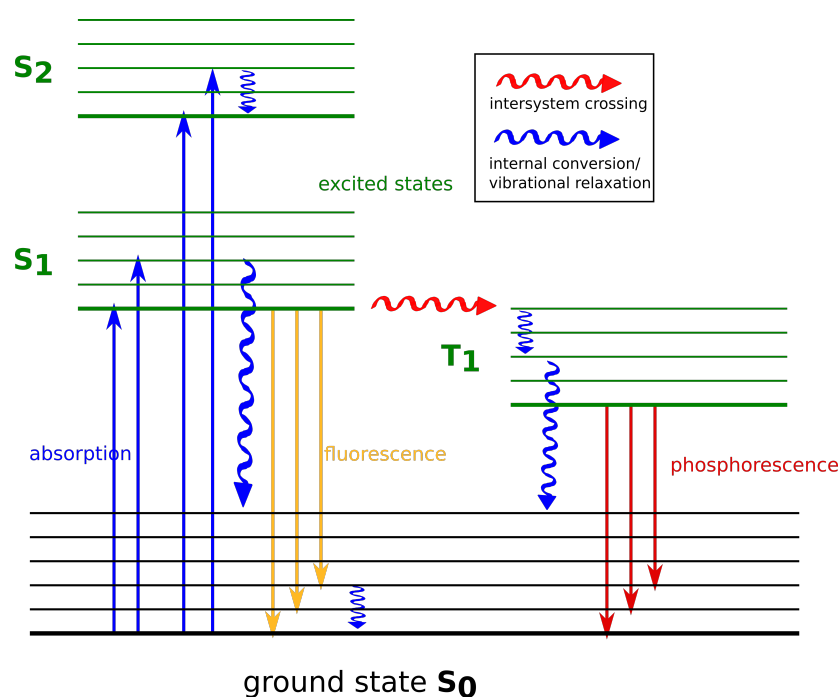
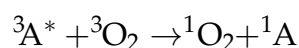


Figure 2.7: JABLONSKI diagram showing the different possible relaxation pathways an absorber can undergo after photoexcitation.

molecules and atoms opens a variety of other reaction possibilities. A measure to determine the probability of a specific photophysical event or photochemical reaction is the **quantum yield** ϕ . It is defined in general for all processes involving light absorption, as shown in eq. 2.30, by the number of occurring events per absorbed photons.^[132]

$$\phi = \frac{\text{number of events}}{\text{number of absorbed photons}} \quad (2.30)$$

In the case of photochemical reactions, the number of events refers to the amount of reactant formed or product consumed, whereas in the case of intersystem crossing it refers to the number of molecules reaching the triplet state. In general, the reaction can either happen through the transfer of energy (indirect photochemistry) or the transfer of electrons (direct photochemistry) between the reactants. Energy transfer describes in this context the quenching of the excited state by a reaction partner that receives the energy, leading to its excitation. The formation of singlet oxygen by deactivation of excited photosensitizers



is probably the most important example for such a photochemical energy transfer reaction.

Even species without absorbance in the UV or VIS may undergo reactions by photochemistry. This is possible if a so-called **photosensitizer** acts as receiver and mediator of photon energy. Per definition, a photosensitizer is a species with the ability to absorb light and transfer the energy to photo-inactive reactants. Ideally, the photosensitizer should act as a catalyst and remain unchanged after the overall reaction. Photosensitizers undergo intersystem crossing with a very high quantum yield (e.g. $\phi \approx 1$ for acetone), forming a long-lived triplet state. An efficient photosensitizer is characterized by the following set of properties:

- high absorption coefficient
- high quantum yield of the triplet state
- higher energy of the excited state than the potential acceptor
- long lifetime of the excited state

Of course, a maximum absorbance of the available light is desirable in terms of energy efficiency. As only the triplet state is long-lived enough to be involved in photochemistry, a maximum conversion rate from singlet to triplet is very important. For a spontaneous energy transfer from the sensitizer to the substrate it is necessary that the sensitizer's excited state is higher in energy than the one of the substrate. In addition, a long lifetime increases the probability for a reactive encounter with a substrate species before relaxation to the ground state. Some examples of typical, widely used natural and artificial photosensitizers are shown in Fig. 2.8.

2.3.2 Photochemistry of the carbonyl group

Carbonyl groups are present in many different classes of biological systems and other organic matter and possess remarkable photochemical properties, making them key functional groups for the understanding of environmental photochemistry. Most of both artificial and natural photosensitizers utilized in the investigation of surface photochemistry in aqueous systems receive their photochemical properties by light absorption of a carbonyl group. Besides the omnipresence of carbonyl compounds in typical natural photosensitizers (e.g. humic acids, curcumin, ...), the reason for this is the detailed knowledge of their

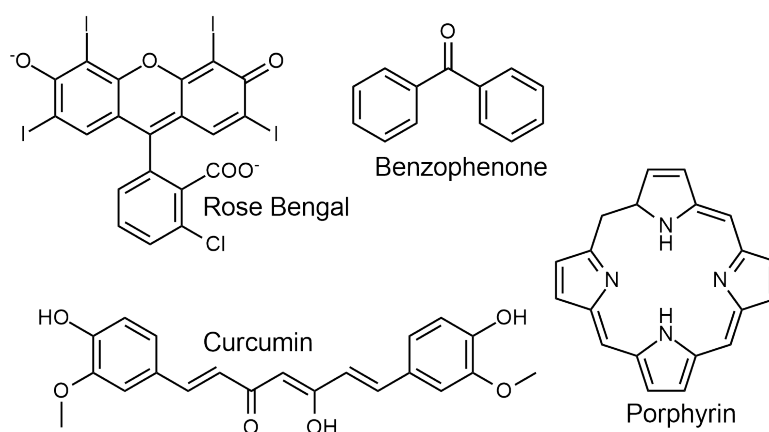


Figure 2.8: Some examples for widely used artificial (benzophenone, rose bengal) and natural (porphyrine, curcumin) sensitizers. Porphyrine ring derivatives often appear coordinated with a metal ion inside the aromatic ring, for example in chlorophyll (Mg) and heme (Fe).

photophysics and specific photochemical reaction pathways that has been in the focus of research for decades.^[133]

Saturated, conjugated and aryl carbonyls can be excited and undergo efficient intersystem crossing from singlet S_1 to triplet T_1 , although the exact involved states and excitation wavelength vary (see tab. 2.1). The excitation leads to a shift of electron density from the oxygen center to a carbon atom, leading to a decrease of the dipole moment with respect to the ground state, a negative partial charge at the carbon and a positive partial charge at the oxygen atom. The excited state shows biradical character and the unpaired electron located at the oxygen is considered to be the reason for its high reactivity. The mesomeric resonance structures of this excited state are shown in Fig. 2.9. Initiated from this excited state, hydrogen abstraction, cycloadditions and rearrangement reactions may occur. However, for photochemistry in the proximity of organic matter in the subsurface region in aquatic systems, the hydrogen abstraction reactions are probably the most relevant. The excited carbonyl species can abstract a hydrogen

Table 2.1: Wavelengths and states of photochemically significant transition for conjugated and saturated carbonyls.

	saturated	conjugated
wavelength/ nm	270-280	310-330
transition	$\pi \rightarrow \pi^*$	$n \rightarrow \pi^*$

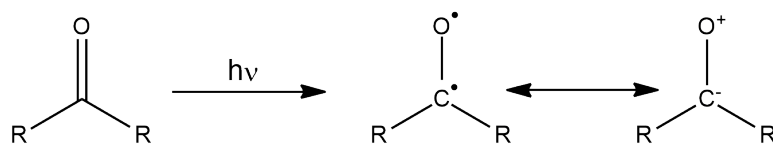


Figure 2.9: Schematic representation of the two limiting mesomeric structures of the excited state of carbonyl compounds.

either from a donor molecule like an amine, alcohol or an aliphatic chain or undergo intramolecular abstraction. Those reaction pathways are depicted in Fig. 2.10. Abstraction of a hydrogen atom from a donor leads to the formation of a radical bearing a hydroxy group which can undergo further reactions. In aqueous systems, a regeneration of the initial molecule is possible by reaction with dissolved molecular oxygen, initially yielding peroxy- or hydroperoxyradicals. A scheme of this reaction is shown in Fig. 2.11. Because of this, carbonyl photochemistry can act as source for reactive oxygen compounds. Besides this sensitizing path with the carbonyl compound remaining unchanged after reaction, the excited state may also undergo NORRISH type I or II reactions. A NORRISH type I reaction begins with a homolytic cleavage of the bond between the carbonyl carbon and the adjacent α -C atom. The two formed radicals may react further through different reaction channels, including the release of carbon monoxide and radical recombination. In contrast, a NORRISH type II reaction occurs typically in systems with a hydrogen atom in γ position to the carbonyl group. Via a cyclic transition state, an intramolecular H abstraction leads to a biradical which then either undergoes fragmentation by homolysis yielding two unsaturated products or, by intramolecular radical recombination, forms a cyclic product. The latter reaction is known as YANG cyclization.

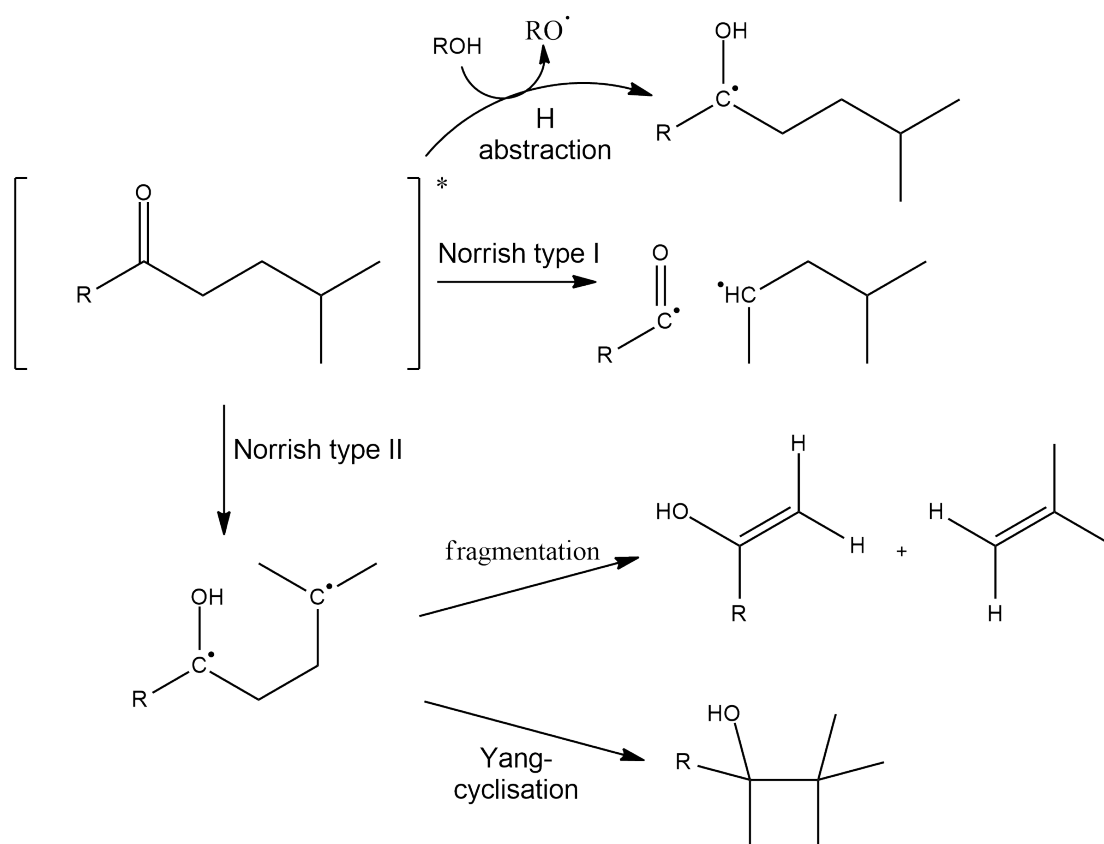


Figure 2.10: Schematic representation of the carbonyl photochemical pathways beginning with an initial hydrogen abstraction. This schema is reproduced from Canonica *et al.*^[62]

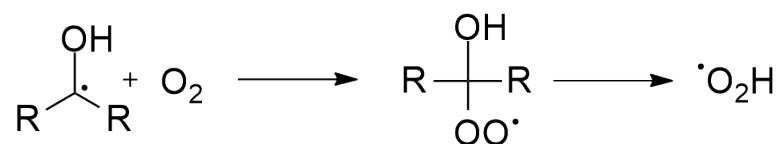


Figure 2.11: Reaction scheme of the reaction of a possible reaction between carbon radicals and dissolved oxygen.

CHAPTER 3

Experimental Section

3.1 Materials and Sampling Techniques

3.1.1 Materials

A list of the compounds and substances used for the synthesis of the artificial model sensitizers and the preparation of the spreading solutions with their respective purities and manufacturers is provided in tab. 3.1. The table column "purpose" specifies the particular application context of the respective substance. Compounds that were used to carry out the synthesis are labeled as "reagents", solvents to prepare the spreading solutions with "solvents", surfactants for surface-sensitive experiments have the purpose "surfactant", photoactive substances for photosensitization or photochemical reaction are labeled with "sensitizer". Solvents used for column chromatography are labeled with the tag "chromatography". All purchased chemicals have been used without further purification. The ultrapure water used for different kinds of experiments and calibration procedures was obtained from a laboratory purification system (PURELAB ULTRA by ELGA) with a specified resistance of 18.2 M Ω .

Table 3.1: List of used reagents and chemicals.

Retained name	Systematic name	Manufacturer	Purity	Purpose
Arachidic Acid	eicosanoic acid	Sigma-Aldrich	≥ 99 %	surfactant
Benzophenone	diphenylmethanone	Sigma-Aldrich	99 %	sensitizer
Benzoylbenzoic Acid	benzophenone-4-carboxylic acid	Sigma-Aldrich	99 %	reagent, sensitizer
Chloroform	trichloromethane	Sigma-Aldrich	≥ 99.5 %	solvent
DCM	dichloromethane	Walter CMP	98 %	solvent
DMAP	<i>N,N</i> -Dimethylpyridin-4-amine	Sigma-Aldrich	≥ 99 %	reagent
EDC	<i>N</i> -Ethyl- <i>N'</i> -(3-dimethylaminopropyl)carbodiimide-hydrochloride	Carbolution	99 %	reagent
Dipalmitoyl-phosphatidylcholine	1,2-dipalmitoyl-sn-glycero-3-phosphocholine	Sigma-Aldrich	99 %	surfactant
Dodecanediol	1,12-dodecanediol	Sigma-Aldrich	99 %	reagent
Ethyl acetate	ethyl acetate	Walter CMP	n/a	chromatography
Hexanediol	1,6-hexanediol	Sigma-Aldrich	99 %	reagent
Humic Acid	-	Sigma-Aldrich	technical	sensitizer
Myristic Acid	hexadecanoic acid	Fluka	> 99 %	surfactant
Nonanediol	1,9-nonanediol	Sigma-Aldrich	98 %	reagent
Pelargonic Acid	nonanoic acid	Sigma-Aldrich	≥ 99.5 %	surfactant
Pentane	pentane	Walter CMP	n/a	chromatography
Stearic Acid	octadecanoic acid	Sigma-Aldrich	≥ 99.5 %	surfactant
Triton X-100	<i>t</i> -octyl-phenoxypolyethoxy-ethanol	Sigma-Aldrich	99 %	reagent, sensitizer

3.1.2 Synthesis

In the course of this theses, three novel surface-active compounds have been synthesized by the procedure described below. A more detailed description of the synthesis strategy and procedure is given in chapter 7. The reaction schema was the same for all three variants as only the length of the symmetric diol was different. 4-dimethylaminopyridine (DMAP) (0.2 mmol,) and the respective diol (5 mmol) were dissolved in 30 mL of dichloromethane. 4-benzoylbenzoic acid (1 mmol) and 1-ethyl-3-(3-dimethylaminopropyl)carbodiimide hydrochloride (EDC) (1.5 mmol) were dissolved in 20 mL of ice-cooled dichloromethane. This mixture was added to the diol/DMAP solution and stirred for 4 h at room temperature. Afterwards, the reaction was quenched with sat. aqueous NaHCO₃ solution. The phases were separated and the organic phase was washed with brine (sat. aqueous NaCl solution), dried over anhydrous magnesium sulfate and evaporated. The crude product was purified by column chromatography using pentane/ethyl acetate as the mobile phase. Afterwards, the product was dried *in vacuo*.

3.1.3 Characterization of the synthesized substances

The novel sensitizers have been characterized by a set of standard analytical techniques. The instrumental details of those methods are provides in tab. 3.2.

Table 3.2: Standard analytical techniques.

Method	Instrument manufacturer	Model
CHNS	ELEMENTAR	Micro cube
IR	BRUKER	Alpha-P ATR IR
NMR	BRUKER	AvanceNeo 500
MALDI	BRUKER	MALDI-TOF Autoflex
UV/Vis	SHIMADZU	UV-1800
Raman	BRUKER	FRA 106

3.2 SML sampling

As the small dimensions of the SML makes it necessary to employ special methods of sampling, the following paragraph describes the utilized sampling procedures that were applied to collect natural SML samples from the Baltic Sea. Sampling by GARRET screen was the default mode of operation whereas the plate sampling was applied during the Baltic GasEx cruise in 2018 to comply

with the standard sampling procedure of the other cruise participants. All sampling procedures followed the best-practice-guide established by Wurl *et al.*^[40]

3.2.1 GARRETT screen

All SML samples were collected in PE bottles with a volume of 500 mL. The stainless steel screen (30 cm diameter, ASTM 16 mesh, LINKER INDUSTRIES) was attached to a stainless steel chain that was then connected to a long rope, submerged under the water surface from the ship's deck and moved aside to avoid uptake of bubbles and foam caused by the perturbation during the dipping process. Before the first sample was taken, the bottle and funnel were rinsed with surface water gathered by the screen. If not otherwise stated, seven consecutive dips of the screen followed by slightly tilting it and allowing the water to flow via a stainless steel funnel into the sampling bottle were taken. Typically, seven consecutive yielded 250- 300 mL water. The samples were transferred into the lab for the measurements. After usage, all metal parts were thoroughly rinsed with fresh water to avoid corrosion. Cleaning of the funnel and the screen was carried out with a laboratory dishwasher employing a strongly alkaline cleaning agent at a temperature of 85 °C for the metal parts and 55 °C for the plastic bottles, respectively.

3.2.2 Sampling by glass plate

The glass plate was made of borosilicate and had a dimension of 500 mm in length, 250 mm in width and a thickness of 5 mm. To collect the SML samples, typically from a zodiac, the plate was submerged into the water perpendicular to the surface. Afterwards, the plate was withdrawn from the water at a slow speed. The SML samples were collected in PE bottles with a volume of 500 mL which were cleaned by means of a standard laboratory dish washer using a strong alkaline cleaning agent at 55 °C. To transfer the water into the samples, the plate was inserted into a slit formed by two Teflon wipers attached in a manner that the water flew into a funnel. Typically, 10 consecutive dips yielding yielded 250-300 mL were conducted. Before sampling, the glass plate and wiper were cleaned by washing with aqueous HCl (10 mol-%) and rinsed subsequently with ultrapure water.

3.3 Surface Analysis

3.3.1 Tensiometry

Measurements of surface tension were carried out using a AQUAPI+ tensiometer by KIBRON at laboratory ambient temperature (21 °C). Suitable polytetrafluoroethylene (PTFE) sample holders by KIBRON were used. The instrument was calibrated with ultrapure water according to the manufacturer's manual. Briefly, the dish was filled with the water and the automatic calibration routine was started from the instrument's control software. The surface tension of this sample is then interpreted by the software as the surface tension of water at 20 °C (72.8 mN m⁻¹). To check the stability, another sample of ultrapure water was measured to ensure the same surface tension reading is reproduced. During a set of consecutive measurements, stability of the calibration was checked after each sample by measuring the surface tension of ultrapure water again and the calibration routine was repeated if a drift from the expected reference tension value occurred. The manufacturer states an accuracy of 0.1 mN m⁻¹ for this method.

3.3.2 LANGMUIR trough compression isotherms

Compression isotherms were recorded using a RIEGLER & KIERSTEIN LANGMUIR trough with a surface area adjustable between 190 cm² and 27 cm² by two step motor-controlled movable PTFE barriers. Surface pressure was measured by means of a WILHELMY film balance (accuracy ca. 0.5 mN m⁻¹) equipped with a custom-cut filter paper attached to a stainless steel hook. For a regular measurement, the trough was filled with approx. 100 mL of ultra-pure water. Afterwards, a chloroform solution of the surfactant to measure was dropped from an EPPENDORF pipette held at a flat angle. The typical spreaded volume was in the range of 30-60 µL. After evaporation of the solvent, the surface pressure was recorded upon compression and expansion of the barriers with an acquisition interval of 0.5 s per data point. The compression speed was typically in the range of 0.3 - 3.2 Å² min⁻¹ molecule⁻¹. After finishing the measurement, the water was removed from the trough using a vacuum tube. To clean the trough, few drops of a special cleaning agent (TICKOPUR R 33, DR. H STAMM GMBH) were added, followed by consecutive rinsing with hot, then ultrapure water until the surface pressure upon rapid compression remained below 0.8 mN m⁻¹.

3.4 VSFG-Spectroscopy

3.4.1 VSFG spectrometer setup

VSFG spectroscopy was performed using a commercially available, user-modified spectrometer by EKSPLA. The pump laser was a passive-active mode-coupled neodymium-doped yttrium aluminum garnet (Nd:YAG) laser operating at a wavelength of 1064 nm with a pulse duration of 30 ps, a repetition rate of 10 Hz and a pulse energy of 30-40 mJ. To achieve tunable IR radiation, a combination of an optical parametric generator (OPG) and difference frequency generator (DFG) was employed. To feed this OPG, the spectrometer contains a Harmonic Unit built around a non-linear monopotassium phosphate (KDP) crystal converting the pump laser into its second (532 nm) and third (355 nm) harmonic. The energy of the second harmonic had a pulse energy of 600 μ J per pulse. The OPG, equipped with a lithium triborate (LBO) crystal, was pumped by the third harmonic, generating a signal (420-680 nm) and the corresponding idler (740-2300 nm) beam. The output wavelength can be tuned by rotating the nonlinear crystal. The idler output in the range of 1210-1980 nm is sent to the DFG sub-unit, containing an AgGaS₂ nonlinear crystal, to generate tunable

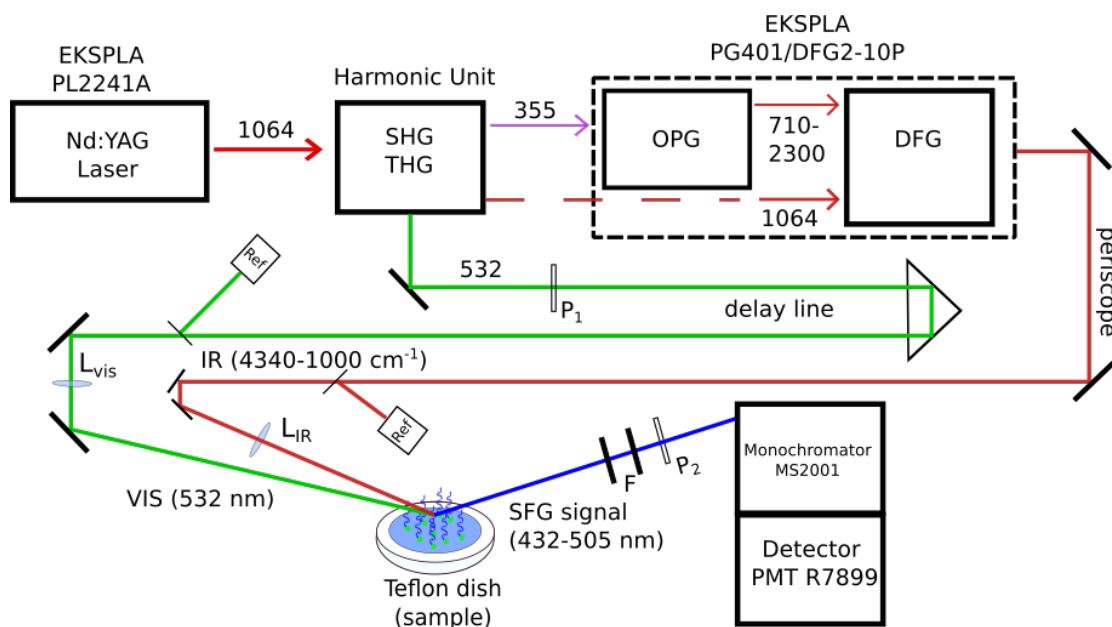


Figure 3.1: Schematic, simplified representation of the VSFG spectrometer. The symbol P represents a polarizer, L a Lens, Ref a reference detector and F a filter. Reflected VIS and infrared light (IR) beams are omitted for clarity.

coherent IR radiation with an energy of approx. 200 μJ per pulse and a spectral band width of 3.5 cm^{-1} . The spectral tuning of this IR output was 2300-10000 nm ($4350\text{-}1000\text{ cm}^{-1}$). The polarization of the visible upconversion beam can be adjusted using a half-wave plate as polarizer P_1 . Temporal overlap of the IR and the Vis beams is achieved by employing a tunable delay line. To reach the sample holder, which is located at a different height than the incident beam path, the IR beam was guided through a periscope. The energy of both IR and Vis beam was monitored using two reference detectors. Care was taken that the beam path length from the beam splitter to the reference detector and the sample was the same to allow for proper normalization of the SFG signal with respect to CO_2 and H_2O absorption in air. Spatial overlap was attained by two adjustable mirrors guiding the IR beam to the sample. Both incident beams were focused on the sample using a set of lenses (L_{VIS} and L_{IR}). The angles of incidence for the IR and the Vis beam were 53° and 59° , respectively. The SFG beam was emitted at an angle of approx. 58° . After spatial separation of the beams and removing the remaining green scattered light by a combination of an iris, low-pass and a notch-filter (F), the polarization of the SFG was selected by a glan prism polarizer P_2 . After passing a monochromator, the SFG beam intensity was detected by a gated high-sensitivity photomultiplier tube with a detection limit of about two photons per pulse.

3.4.2 VSFG spectra acquisition

In a usual experiment, a certain volume (typically 10-50 μL) of a solution ($c = 1 - 5\text{ mmol L}^{-1}$) of the surfactant was dropped from an EPPENDORF pipette held at a sharp angle onto a water surface in a teflon dish. The diameter of the dish was 5.1 cm for artificial samples and 14 cm for sea water samples. Before measurement, the solvent was allowed to evaporate and the system to equilibrate for approx. 5-20 minutes.

The spectra were recorded either in ssp or ppp polarization with ssp as the default, so all reported spectra without additional information about the polarization state were measured in ssp. To obtain one data point, 100 pulses were averaged. The spectral step width between two adjacent points was typically set between 2 cm^{-1} and 5 cm^{-1} in the spectral region of interest and more coarse-grained in the other parts of the spectrum where no signals were expected. An overview about regions of the spectrum that were probed and the corresponding

molecular vibrations and applied step widths for SML analysis are summarized in tab. 3.3.

For spectra analysis, the obtained intensity values were divided by the product of the VIS and IR intensities as recorded on the reference detectors and reported in "arbitrary units (arb. u.)" as function of the IR wavelength given in reciprocal centimeters. At the beginning of each day of measurement, the setup was adjusted and controlled by preparing a fresh sample of DPPC (40 \AA^2 per molecule) by the procedure described above, setting the wavelength to 2880 cm^{-1} corresponding to the ν^+ band of the CH stretch vibration and optimizing the overlap of the upconversion beam and the IR beam as well as the guidance of the SFG beam towards the detector in order to maximize the SFG signal intensity. A DPPC reference spectrum was recorded before and after a day of measurement to allow normalization to the average of those spectra in order to correct for daily spectrometer performance fluctuations. In thus way it was possible to obtain reliable and comparable intensity readings for time-series studies spanning months to years. Analysis of the repeatability of the setup can be found in the supplement of a past publication of our group. The direct repeatability of SF measurements was found to be about 8%, the long term stability $\pm 11\%$.^[105]

3.4.3 Combination of LANGMUIR trough and VSFG

In addition to separate SFG and LANGMUIR trough measurements, the customizable setup allowed for a combination of those techniques by placing the trough on a height-adjustable mount inside the laser's beam path, as it is demonstrated in Fig. 3.2. For those experiments, the trough was operated in the constant surface pressure mode, so the pressure was set to a certain value at the beginning of the experiment and the electronic trough control adjusted the barriers

Table 3.3: Spectral regions probed during VSFG measurements of the SML samples.

range/ cm^{-1}	typical step width	spectral region
1600-1800	5	CO (carbonyl)
2750-3050	5	CH (alkyl)
3050-3150	5	CH (aryl)
3050-3600	20	OH, bulk
3650-3840	5	dangling OH

automatically to hold on to this surface pressure during the SFG measurement. In this state of constant pressure, SFG spectra were recorded to probe the spectral features of the sample at a given state of surface coverage. Before the beginning of a set of combined VSFG/LT measurements, a DPPC sample was prepared in the trough as described in 3.3.2, a surface pressure of 38 mN m^{-1} (assuming a dense monomolecular layer of the substance) corresponding approx. to an area per molecule of 40 \AA^2 was set and the height of the mount and the laser setup were adjusted in order to achieve maximum signal intensity, exactly like for regular samples. A DPPC reference spectrum was recorded to ensure the setup was working correctly and to allow for normalization between the days of measurement

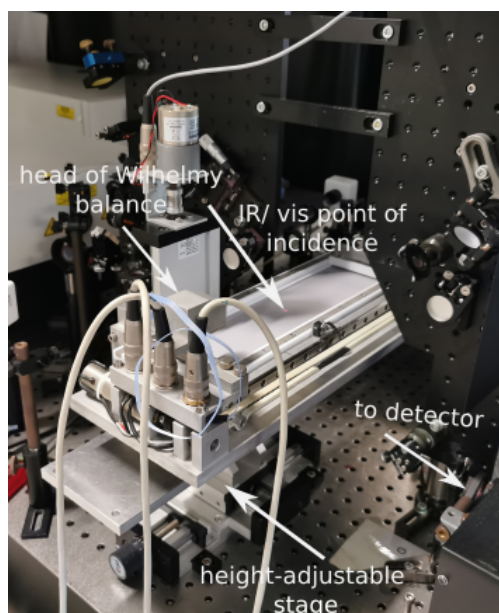


Figure 3.2: Photograph of the combined SFG/ LANGMUIR trough setup.

3.5 Photolysis

In this thesis, a new photolysis setup has been installed for combined photolysis/SFG measurements. The photolysis experiments were carried out using a 150 W Xenon arc lamp manufactured by NEWPORT. Bundled with the lamp, a set of accessories was used to allow a direct coupling of the lamp with the SFG experiment. This accessories included a filter utility to cut off the IR part of the spectrum consisting of a transparent chamber filled with water and attached to an external cooling circuit, a focusing lens assembly to lead the output of the lamp into a flexible fiber filled with a light-guiding liquid (liquid light guide (LLG)) and an output collimator to refocus the highly divergent output of the LLG. A custom-made hemispheric stainless steel reactor that has been built in the past for SFG monitoring of oxidation experiments has been modified to allow a direct connection of the LLG. Its lid was equipped with a plug allowing to fit the LLG directly into it. A detailed description of the reactor is given elsewhere.^[131] For the photolysis experiments, different configurations to irradiate the sample were possible, depending on the exact set of utilities connected to the lamp:

- plug the LLG directly into the SFG reactor
- illuminate the sample from above with the LLG without collimator
- illuminate the sample from above with the LLG using the collimator

An overview about all those accessories, including the corresponding NEWPORT product identifier is provided in tab. 3.4. For the experiments in this theses, only

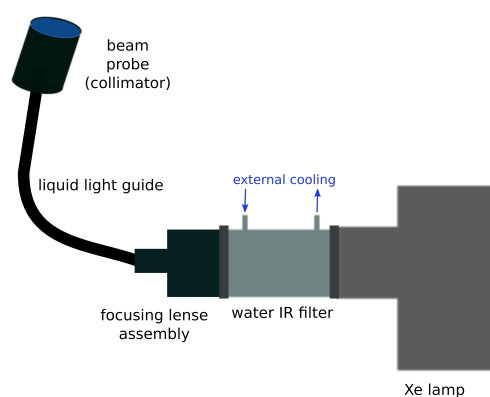


Figure 3.3: Schematic representation of the Xe lamp setup used for photolysis. The IR filter is a transparent water-filled chamber attached to an external cooling circuit driven by a small water pump.

the LLG capable of transmitting near UV radiation has been utilized for all the employed sensitizers possess absorption maxima in this region. The influence of both the LLG and the water filter on the appearance of the lamp's spectrum is depicted in Fig. 3.4. It shows that infrared radiation is reliably removed but the spectral region of interest remains unaffected.

Typical photolysis time was in the range of a few minutes for most of the experiments but up to three hours in some cases. As the output of the liquid light guide was spatially divergent, the intensity was determined with a calibrated power meter. Those values are provided in tab. 3.5. The typical distance of the probe output from the sample was 1-5 cm, ensuring that the lighting field of the beam did not exceed the sample surface, so the loss in energy was minimized. This was necessary. Note that the intensity distribution of the resulting light spot was spatially non-uniform with a maximum in the middle of the lighting field. This can be seen from the increase of the calculated $I_{\text{total}}^{\text{max}}$ in Tab. 3.5, where the values at high distance of the detector from the LLG are systematically too high (447 mW represents the correct value).

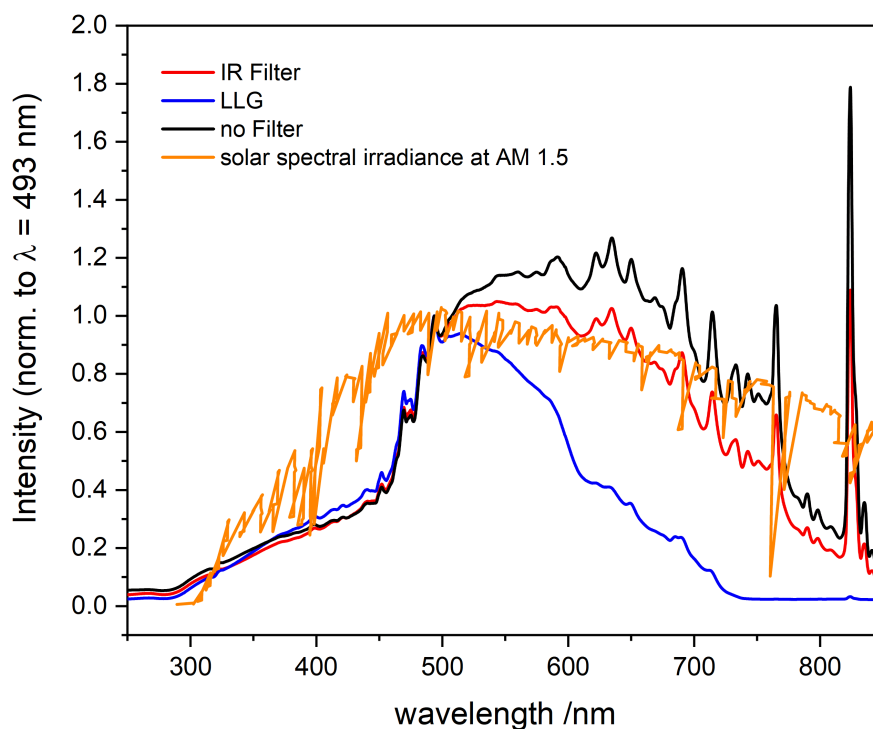


Figure 3.4: Transmission curves of the lamp setup with and without the liquid light guide and the water filter. For comparison, the AM 1.5 standard spectrum (ASTM G-173-03) showing the terrestrial solar spectral irradiance is shown (normalized to $\lambda = 493$ nm) , reproduced from ISLAM,^[134] is included.

Table 3.4: List of accessories for the photolysis setup.

component	NEWPORT identifier	comment
lamp	66907-150XF-R1	ozon-free Xe lamp
liquid light guide (UV/VIS)	7759	for VIS and near UV
liquid light guide (VIS)	7757	for VIS
infrared filter	61945	water filter to remove IR
beam probe	76600	collimator to focus LLG output
focusing lens assembly	77800	connect lamp to LLG

Table 3.5: Lamp output power per area as function of the distance from the sensor of the powermeter. It was always ensured that the middle of the lighting field hit the middle of the detector.

distance from sensor/ cm	power/ mW cm ⁻²	spot diameter/ cm	A/ cm ²	I _{total} ^{max}
0	447	-	-	447
1	311	1.4	1.5	479
5	53	3.6	10.2	541
11	14	8.5	56.8	795

Part I

Natural surfactant systems

CHAPTER 4

Automated data processing, storage and management based on Python

4.1 Background

Managing and analyzing big amounts of experimental data obtained by different instrument operators over a long time and, with the necessity of preceding steps of preparation like normalization and baseline correction, can easily become a tedious and error-prone task. Also, the handling of those data in a central database simplifies exchange between cooperation partners and within working groups. Therefore, it is highly desirable to employ auxiliary software tools to simplify and unify this procedure. Ideally, the underlying programming language needs to offer simplicity, readability and concise syntax to avoid a steep learning curve for scientists who are typically not trained software engineers. Furthermore, the availability of reliable libraries for recurring tasks in scientific programming as well as open source availability of the software involved are key ingredients, allowing for reliable and freely available software. The programming language Python is a dynamically typed, interpreted language with drastically growing popularity during the last years.^[135,136] Python is especially popular in the scientific community because the language is beginner-friendly and has a concise and readable syntax while being much less verbose than other popular programming languages in science and engineering like for example C/C++, Java or Fortran. Besides that, a set of very useful and popular scientific libraries are available: *numpy* for high.-performance numerical computation and handling of typed arrays, *pandas* for data analysis as well as handling of tabular-like data and *matplotlib* for scientific plotting and data visualization.^[137–139] In this work, two reasonable use cases for automatized analysis tools are described. The first is the analysis of VSFG spectra of Natural sea water samples, obtained during a time

series running over almost ten years. The other case are related measurements of different analytical techniques applied to the same samples taken during a research cruise. The second example deals with the need that the VSFG spectra need to be properly normalized to the intensity of the IR and VIS laser intensities as well as the ro signal of with respect to the reference samples recorded at exactly the same day. Faced with the initial situation of several hundreds of spectra distributed over a manifold of directories, named with different naming conventions and by different operators, it was decided to develop a software tool to support, automatize and accelerate the process of data handling.

4.2 Implementation

The architecture of the software, indicated in fig. 4.1, intends the separation of the data import logic from the analysis, evaluation and visualization, as usually the import occurs once shortly after acquisition, whereas data processing and analysis is an ongoing process. In addition, this allows the distribution of the database yielded during import to others without the necessity to deal with a huge amount of raw data files. To simplify the selection of data according to certain criteria, it was chosen to use a structured query language (SQL) database as output of the import sequence. However, to avoid sticking to a specific database implementation and, keeping in mind that the target audience might not be familiar with SQL, simplify the query syntax the object-relational mapper (ORM) *sqlalchemy* was used.^[140] During import, metadata of the measurements is extracted from the file (timestamp of creation) as well as its name (by parsing using regular expressions). Of course, correct parsing of the file names requires the experimentalist to follow a strict naming convention. The sub-package ORM contains classes to manage the file import and the mapping of the spectral data on database tables as well as expose convenience query functions to the user in order to access the data. This design is extensible, it is simple to add new types of spectra and additional metadata tables. The sub-package **natural_samples** uses this extensibility to add information about the sampling time and conditions, the relation of multiple complementary measurements applied to the same water sample as well as providing simple functions to select data by those new parameters (see sections 4.3.2 and 4.3.2).

The functionality to work with spectra is isolated in a separate package as this part is so general that it might be used by other researchers and for dif-

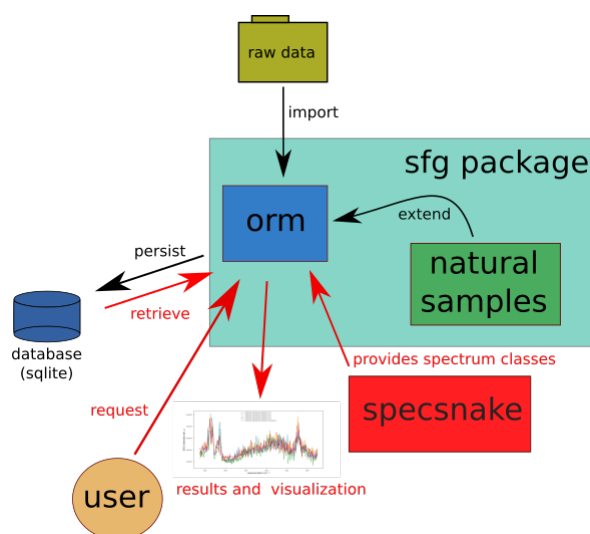


Figure 4.1: Schematic view of the organization and working steps involved in the `sfg` package. Black arrows indicate the import routine, red arrows show the regular analysis interaction. `specs snake` is an external package that contains the classes representing spectral data and that is intended for reuse by others.

ferent applications as well. Because of this, it is a stand-alone project that can be installed and shared. This package called `specs snake` (available at GitHub under <https://github.com/Darkskald/specs snake>) follows an object-oriented approach, representing each measurement as a spectrum object containing the data, metadata and methods to operate on them. In general, a spectrum is considered to be an entity with an array of x and y data with the same dimension. In addition, they need to have a `LATEX` string `x_unit` and `y_unit` defining the axis labels upon plotting. To ensure no spectrum object can be instantiated without those four essential properties, the metaclass `MetaSpectrum` is used for all types of spectra. The mechanism preventing instantiation of malformed spectra is demonstrated in listing 4.1. If the spectrum does not have the four essential properties, an exception will be raised.

All spectra objects, no matter if they are UV/Vis absorption spectra, VSFG spectra or LANGMUIR compression isotherms, need a set of common functions to operate on them. These are, for example, functions returning the spectral range (maximum and minimum x values including step widths), splitting the spectrum in a given interval, normalize the dataset either to an external value or its maximum as well as numerical integration of the whole or parts of the spectrum. To avoid redundancy, this shared behavior is implemented in an base

```

class MetaSpectrum(type):
    """Metaclass responsible for the correct runtime behaviour of
    ↪ spectrum objects derived from it."""

    def __call__(cls, *args, **kwargs):
        """This methods ensures that no spectrum may be instantiated
        ↪ without the required properties that are
        essential for plotting."""
        temp = super().__call__(*args, **kwargs)

        for attr in ("x", "y", "x_unit", "y_unit", "name"):
            if not hasattr(temp, attr):
                raise InvalidSpectrumError(f'Tried to
                ↪ instantiate spectrum object without
                ↪ suitable attribute {attr}!')

        return temp

```

Listing 4.1: Demonstration of the code that prevents malformed spectrums from being instantiated.

class **BaseSpectrum** from which all specific types of spectra classes are derived. In conclusion, the interplay between the data management sub-packages (**orm**, **natural_samples**) and the bundled analysis capacities in the **specsna** packages reflect the initial architectural intention that makes the code easy to use, maintain and extend. The documentation and usage guide of this package is available under <https://specsna.readthedocs.io/en/latest/>. The following sections will provide an overview about the core functionality and features of the software utilities.

4.2.1 The reusable core: specsna

The **specsna** package abstracts the logic of dealing with spectral data to a set of reusable interconnected classes and functions that are able to accomplish reoccurring tasks like, for example, batch import of files from a folder and their visualization.

Interaction with the framework and extensibility

The design of the package allows new types of spectra with specific functionality, names for x and y units and file extraction routines to be added with ease. This can be done *on-the-fly* by applying a set of convenience function and using a modified version of an existing spectrum class or by extension of the package

and registering the new class to the existing logic. A concrete example is given in section 4.3.4.

BaseSpectrum as general-purpose data structure for spectra

The *BaseSpectrum* class is the most general representation of a simple x/y data set and the base class for all other spectrum types. It needs representations for the x and y units as strings to be used as axis labels. It offers comparison to other spectra by the underlying file's timestamp of creation, so it is possible to sort a list of spectra by their time of measurement. In addition, it allows file export to JSON and CSV format, integration of parts or the whole data set and provide information about the maximum and minimum x values and step widths and spectral range used to record the spectrum was recorded (spectral range).

Representation of VSFG spectra

The functionality for SFG spectra covers the automatic normalization of the spectra to the intensity of the infrared and visible laser intensities, automatic integration of specific spectral regions (as they are typically of relevance for SML samples), automatic baseline correction and export to common data formats like CSV and JSON. In addition, an auxiliary class is able to average any desired number of spectra including preceding interpolation of them to a common x-scale. As it can be necessary to normalize the spectra with respect to a reference spectrum. This reference was typically measured at the same day, but as it is not guaranteed that all spectra were recorded at one day, the averager applies an effective normalization value c_{eff} for all spectra, which is calculated by the equation

$$c_{eff} = \sum \frac{n_i}{n} \cdot c_i \quad (4.1)$$

where n is the total number of spectra to average, n_i is the number of spectra recorded at one specific day and c_i is the reference value (in the usual case, the average dipalmitoylphosphatidylcholine (DPPC) integral over the CH stretch vibration spectral region) obtained at this day.

Representation of Langmuir compression isotherms

Dealing with isotherms obtained during LANGMUIR trough measurements is

supported by the *langmuir_isotherm* module which includes the handling of multiple data columns (area, area per molecule, time, surface pressure) allowing a simple switch between them for plotting, calculation of the compression factor (area divided by max. available area), calculation of the surface elasticity (as defined in eq. 2.12) as well as averaging over multiple isotherms.

4.2.2 The thesis-specific package: SFG

The **SFG** package contains the code that is specially tailored for this thesis. This means that the direct re-usability might be restricted but nevertheless, some concepts might be useful to others. This code is hosted at GitHub under <https://github.com/Darkskald/SFG>.

Data import and database generation

This package is responsible for the bundling of raw data into a relational database. A core feature is the extraction of the measurement data, population of the single-file database and building the relations between its tables. The final *SQLite* database contains 2400 SFG spectra, 520 compression isotherms, metadata for the Baltic GasEx cruises and the Boknis Eck time series campaign as well as minor amounts of UV, Raman and IR spectra. The file is only about 33 megabyte in size and the complete procedure of generation takes about 14 seconds on a standard PC equipped with an INTEL i7-8565, quad core CPU (4.6 GHz). For everyday use, only this single file is required.

Database access

For the purpose of interacting with the data, a convenient wrapper class¹ *DbInteractor* is provided. This allows the user to fetch data from the database without the need for explicit SQL query strings and convenient generation of spectrum objects as implemented in the **specsnake** package. As the database is built with many relations between the entities, it is easy to access the objects that "belong" to each other, for example all SML SFG spectra that belong to a specific station of the Baltic GasEx cruise. Filtering of the data to match certain criteria (e.g.

1 A wrapper in the context of programming is a piece of code "wrapping" another, usually more complex, class or function. Often it is used to allow a simpler usage of complex library functions.

a certain data of sampling or measurement, containing a specific compound, being of a certain type) is included.

Calculation of relevant data from natural samples

The sub-package **natural_samples** contains the classes and functions that have been used to calculate the data for the Baltic Gas Ex cruise (chapter 6) and the Boknis Eck time series (chapter 5) directly from the values stored in the database in a transparent way, hence the logic of calculation is separated from the import and database construction. Those classes make heavy use of the relations of the database tables as it is demonstrated in section 4.3.3.

4.3 Discussion

4.3.1 General usage

To achieve maximum convenience, a lot of the database interaction functionality is wrapped in classes designed for every day usage while working with the data. In order to use the tools to work on the data, import and database construction have to be done. This is handled in the ORM module and the details depend on the concrete shape of the data, so the discussion is beyond the scope of this section. Assuming the database exists and contains all data, the workflow is the following:

1. Instantiate of the database interaction class, usually the **DbInteractor**
2. Call query functions to retrieve the data of interest
3. Convert the data to spectrum object representations
4. Operate on this spectrum objects
5. Visualize the results

A typical use case for this approach is demonstrated in fig. 4.2. Here, all spectra recorded on the first of August shall be retrieved. As these are natural samples from the Boknis Eck sampling site and the inclusion of the reference samples from the same day shall be avoided in the plot, the type of spectra is restricted. The **DbInteractor** collects the desired spectra by invoking SQL queries filtering by date and converts them to **SfgSpectrum** objects as defined in the **spectrum** sub-package. In the next step, the spectra shall be averaged. This can be achieved

by invoking the **SfgAverager** class which takes a list of SFG spectra objects as argument and calculates the average spectrum. If the spectral ranges and step widths do not exactly match, it is able to interpolate the input spectra to achieve a common x/y scaling. The result of this process is visualized using a plotter class. In Fig 4.2, the partly transparent lines and data points refer to the input spectra, the red line the resulting average. This demonstration shows the interaction between the sub-packages of the program. A more sophisticated demonstration and explanation of the program's features is provided in the appendix A.

Different query functions are available to filter the spectra not only for measurement date and type but also for the substances and the operator of the experiment. Of course, this applies to all kinds of spectral data, not only the SFG example. Averaging is a typical task in the scope of spectra analysis, but many other features are also included in the spectrum classes. The following list names the most important:

- apply a baseline correction
- pick peaks
- slice the spectrum in a user defined interval
- integrate the spectrum
- export the spectrum to CSV or JSON files

4.3.2 Application: Time series data from Boknis Eck

The Boknis Eck campaign included collecting SML samples each month over a time span of almost ten years, performed by different researchers. Thus the initial situation was a variety of raw measurement and reference data distributed over many directories and named according to different conventions. A central EXCEL spreadsheet served as sample and metadata (e.g. temperature, wind speed, depth...) register. The capabilities of the Python package were enabled to interpret the name of the measurement files using different regular expression patterns for each naming convention and map them to their date of sampling, their date of measurement and their entry in the spreadsheet. The tracking of both the day of sampling and measurement, obtained automatically by evaluating the file creation timestamp, is very important because each sample is normalized to the reference signal obtained on its day of measurement to achieve

```
In [6]: 1 import matplotlib.pyplot as plt
2 %matplotlib inline
3
4 from SFG.orm.interact import DbInteractor
5 from specsnake.sfg_spectrum import DummyPlotter, SfgAverager
6 from datetime import date
7
8 plt.style.use("qt.mplstyle")
9
10 # create an instance of the interaction class
11 ita = DbInteractor()
12
13 # get all Boknis Eck spectra measured at 2017/08/01
14 exp_day = ita.session.query(ita.measurement_days).filter(ita.measurement_days.date == date(2017,8,1)).one()
15 spectra = [ita.construct_sfg(spectrum) for spectrum in exp_day.spectra if spectrum.type == 'boknis']
16
17 # apply a baseline correction and average the spectra
18 average = SfgAverager(spectra, baseline=True).average_spectrum
19 spectra.append(average)
20
21 # visualize the average spectrum and the underlying original ones
22 DummyPlotter(spectra, special='AV').plot_all()
23
```

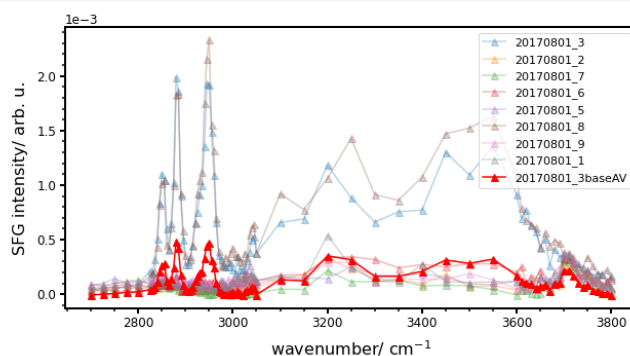


Figure 4.2: Demonstration of the workflow of the program for fetching data from the database, averaging and plotting of selected data using a browser-based Jupyter notebook environment.

comparability between different spectra. But as in many cases not all samples of one sampling day have been measured on the same day, the normalization has to take this into account. This is, if not automatized, tedious and error-prone. The Python package writes all metadata from the spreadsheet to a database table, maps the measurement data table to the correct sampling date and calculates several parameters like the average surface coverage in advance. Automatic look-up of the corresponding reference spectra, normalization and calculation of average spectra specified by selection conditions (e.g. include all samples from the SML, only the bulk, with a certain number of dips...) are provided as functions. The result is a comprehensive and related set of database tables which makes it possible to find all spectra belonging to a certain cruise date, differentiate between bulk water and surface samples and keep track of additional data from other sources like the chlorophyll and oxygen concentration, temperature and wind speed. Tasks like getting all samples taken during a specific time

of the year, normalize them to the annual maximum and investigate seasonal variation is just a matter of a few nested query functions and simplifies time series analysis significantly.

4.3.3 Application: Dataset from the Baltic GasEx cruise

During the cruise, many of the samples were probed with different analytical techniques. In addition, the samples were collected under different conditions. The software toolset was used to keep track of the interrelated measurements and especially the metadata. The first step was to apply a naming convention to make sure that measurements of the same sample are recognized. This was ensured by generating an unambiguous sample hash¹ from the filenames. As all samples were taken during a certain station of the cruise registered in the cruise log, also a station hash was extracted from the file names. Those hashes were used to create and populate a database table, mapping the measurements to the samples and the samples to the stations. The metadata of the stations (e.g. geographical coordinates, temperature, salinity...) were loaded from a spreadsheet produced by the ship information system, the sample meta information like sampling tool and location were generated from the systematic name. A schematic overview of the database is shown in fig. 4.3. It can be seen that the actual measurement data (raw x/y values as obtained from the instrument) is still resting inside the `sfg` and `It` tables. Only the metadata and the relation between measurements, samples and stations is constructed from the systematic names. The SFG and LANGMUIR trough data are mapped via a foreign key relation² to the tables `gasex_sfg` and `gasex_It`, respectively. Those contain the sample id which points as foreign key to the samples table. This table does not only point to the station table but does also contain additional information about each sample, like, for example, the value of the measured surface tension. Because of this relational structure, one can easily perform tasks like obtaining all SFG spectra belonging

1 A string that is generated from the systematic name of the sample to identify the corresponding sample. All measurement file names of the same sample yield the same sample hash. In general, a hash function in computer science maps a sequence of bytes to another and the exact purpose and algorithm can be very different.

2 In databases, primary keys are unique identifiers for each database record. In the case of SQL, this comparable to a row in a table. If one record has a relation to another, it can contain its primary key as field to model this relation. From the perspective of the containing item, this primary key of the other is a foreign key.

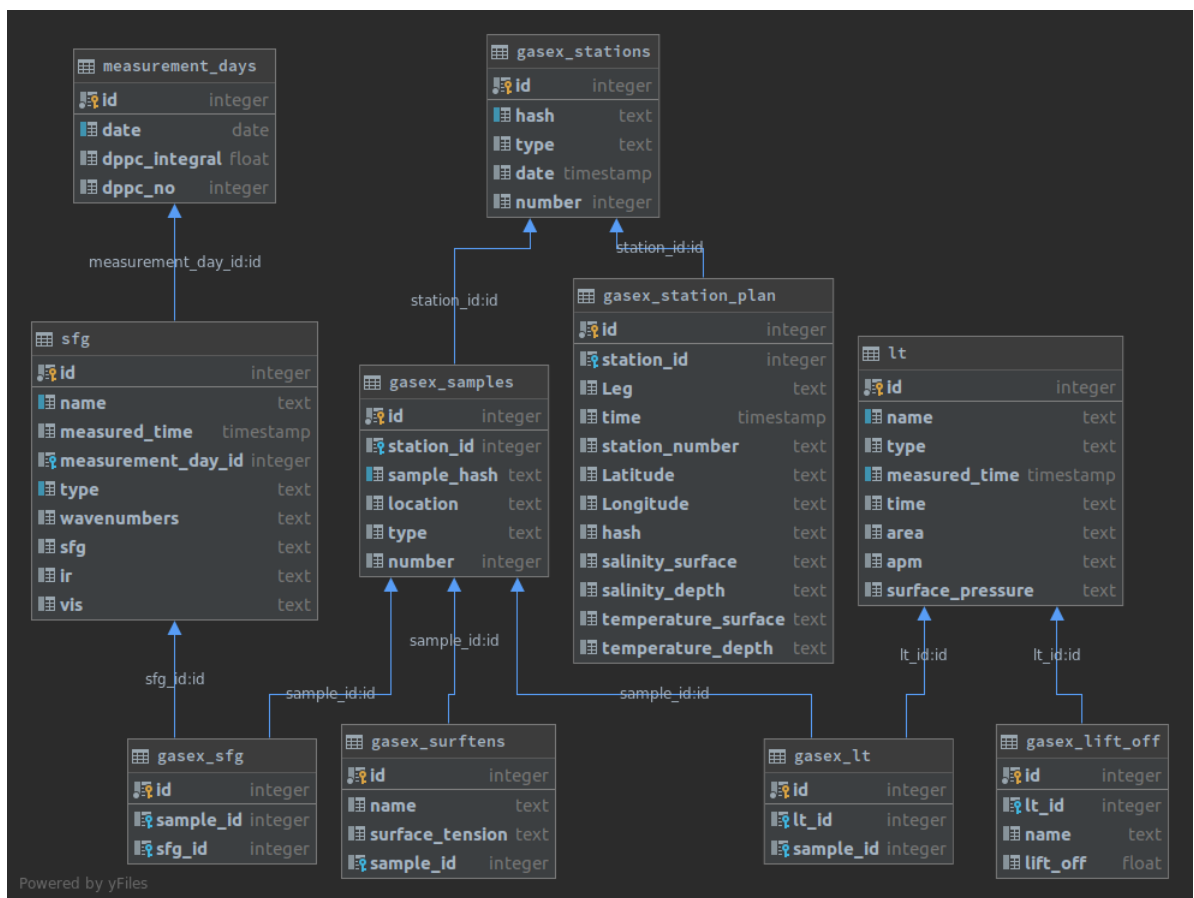


Figure 4.3: Database scheme of the columns used to map the GasEx data.

to a certain station via SQL queries wrapped in convenience functions of the **orm** package database interaction classes. Invoking the functionality of the **spectrum** package in the next step, it is possible to calculate parameters of interest (surface coverage, max. surface pressure ...) from the raw measurement data, average them and visualize the results. A map from the station to the day of the year is predefined, so time trend analysis can be performed with few lines of code. The software toolset prepares some calculations of station characteristics in advance and stores it in another database table called **station_stats** which is not included in the figure due to lack of space. This includes different average values, based on the sampling device type, sampling depth and location. This ensures that the data of interest is available ahead of time without the need of time-consuming computation.

4.3.4 Extensibility and re-usability

This section demonstrates how a new type of spectra can be added *ad-hoc* and make use of the framework capabilities. As use case, a scenario is assumed where a number of UV/Vis-spectra are located in a target directory (called 'uv') and the goal is to visualize them all in one plot. The way how this can be achieved is shown in listing 4.2 and the resulting plot is depicted in fig. 4.4. The general procedure for this is to define a function which extracts the data from the files (extractor), a function that produces the instances of the spectrum class (constructor) and optionally a function that converts the file name in a meaningful string that can appear in the legend of a plot (name transformer). As many files resulting from measurements are somehow column-based, with a variable number of lines to skip at the beginning and different separators, the framework has a way to provide customized extractor functions based on those parameters (ExtractorFactory), so no explicit implementation of the extractor is necessary. Similarly, the **BaseSpectrum** class is so generic that it can fit many typical application cases for spectra. Because of this, the spectrum has a built-in function called **provide_spectrum_constructor**, which can be used to pass custom values for the `x_unit` and `y_unit` parameters and to specify which data columns to use, that returns a pre-configured **BaseSpectrum** constructor. Finally in this example a name transformer which removes the file ending and everything after the first underscore is passed. With those three functions, the **CustomSpectrumFactory** can be called to create a spectrum factory object which is able to extract all files in a given directory and converting them to spectrum objects that can be passed to a plotter to visualize.

```
from pathlib import Path
from specsnake.plotting import Plotter
from specsnake.builtin_loaders import ExtractorFactory,
    ↪ provide_spectrum_constructor
from specsnake.spectrum_factory import
    ↪ CustomSpectrumFactory

# spectra are located in the directory 'uv' and obey the
    ↪ scheme <name>_<nr>.csv
base_dir = Path('uv')
# configure the new spectrum type
col_names = ("wavelength", "absorbance")
extractor = ExtractorFactory(columns=(0, 1),
    ↪ column_names=col_names, skip=2, sep=',').build()
config = {'y_unit': 'absorbance', 'x_unit': 'wavelength/
    ↪ nm'}
constructor = provide_spectrum_constructor('wavelength',
    ↪ 'absorbance', **config)
name_transformer = lambda x: x.stem.split('_')[0]
factory = CustomSpectrumFactory(extractor, constructor,
    ↪ name_transformer)
# extract and plot
spectra = factory.build_batch(Path(base_dir))
p = Plotter(spectra)
p.show()
```

Listing 4.2: Demonstration of how to use the **specsnake** framework to quick-plot a set of spectra of a custom type *on-the-fly* from a directory.

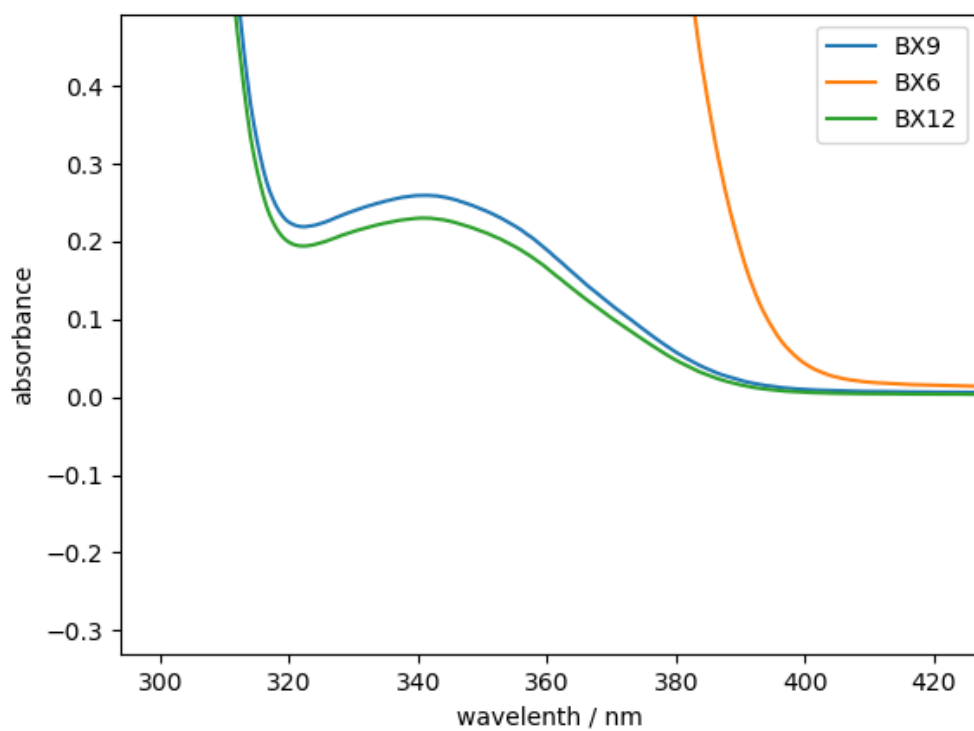


Figure 4.4: Framework extension demonstration, see text.

4.4 Conclusion

In summary, this Python software toolset provides a convenient way to manage data obtained by physicochemical methods and analytical techniques in general. However, as it becomes clear from the listings provided in this chapter, a basic understanding of Python and SQL is needed to take advantage of the full functionality of the software tools. In addition, a detailed description of the tools as provided in the documentation is required to allow a new user to make use of the software's full capabilities.

Storing the data inside a relational database, including the metadata, instead of the traditional way of having several directories with single measurement files profits from the fast optimized table look-up of modern database implementations, reflects the internal connection between much better and allows the user to make use of the very elaborated filter and query methods of SQL. From the scientist's perspective, automated processing makes it possible to handle significantly larger amounts of data compared to manual approach. It is possible to generate several hundreds of high-quality plots in a few minutes. In addition, data processing steps by means of an algorithm prevents a possible bias, which may happen if humans with previous knowledge and experience work with experimental data (thinking of, for example, setting the anchor points for a baseline correction by eye). The extensible approach of the spectrum representation makes it possible to add new kinds of spectral data without too much effort.

The next step of software development is to implement a generic way of adding new types of spectra in the form of configuration text files and the generalization of the package, decoupling it from the special requirements of this work. Looking towards a future where web-based applications become more and more important, connecting the functionality of this package and database with a web front end is feasible, opening the road for cooperation and sharing data in a very convenient way. In addition, this kind of application layout makes it easy to pass the spectral data to machine learning and big data libraries, which has become an important tool in scientific data analysis, especially for amounts of data which are beyond human capabilities. For the future, it might be useful to migrate the core part (mainly the specsname package) to a modern statically-typed language like Rust, Julia or Kotlin to enforce type correctness for the spectrum data structures and to further increase the performance for situations where huge amount

of spectra needs to be processed.

CHAPTER 5

The Boknis Eck time series

5.1 Introduction

The Earth's surface is vastly covered by the oceanic waters. The sea-air interface between sea and air is therefore one of the most important interfaces. It couples the ocean to atmospheric processes on global scale. Because exchange of mass, heat and momentum must necessarily occur through this border.^[2,4,141] Several chemical and biological processes occurring in the sea water column yield chemical substances containing both moieties with hydrophilic and hydrophobic properties, the interface is enriched in organic material. Typical classes of such substances (known as surfactants) that have been found to be present in the ocean's surface microlayer (SML) include complex carbohydrates, proteins, humic substances and fatty acid compounds.^[3,4,16] The uppermost water layer, is also the part of the sea which has the strongest exposure to solar radiation. Therefore, the SML is not only a place of intense exchange of matter and interfacial chemical reactions but also a dynamic environment for interface-specific photochemistry. In general, the presence of surface-active matter can change the physical and chemical properties of the interface significantly. Examples are the reduction of surface tension and the alteration of gas transfer coefficients.^[45] This phenomenon has been confirmed by laboratory experiments and field studies conducted with artificial and naturally occurring surfactants.^[18,26,27,32,142-146]

The outermost boundary between air and water which is in the order of magnitude nanometer thickness, and often only consisting of one molecular layer, is referred to as sea-surface nanolayer (SNL). In comparison to the SML, the nanolayer is assumed to be dominated by surface-active species, thus exhibiting a certain degree of structural order. A detailed understanding of the processes at microscopic level is highly desirable. For example, it has to be examined

whether the nanolayer is really a well-confined layer that needs to be considered separately from the microlayer. For sure, there is in constant exchange of organic matter between SNL and SML, but it is yet unclear, if the dominating kinds of surfactants are rather soluble or insoluble ones. Though much effort was spent on investigation and understanding of the SML, studies specifically targeting the nanolayer are scarce because of the challenge to selectively probe the nanolayer. Its exploration requires at least analytical methods that are able to distinguish between the signal contribution of this layer with its small vertical dimension from the underlying bulk water and being still sensitive enough to trace the very low amounts of organic surface-active matter. Only few methods fulfill those requirements. Examples are some electrochemical method such as AC voltammetry, BREWSTER angle microscopy and VSFG, the technique used in this study.^[41–43]

The composition and structure of the highly dynamic and complex SML and SNL are subject to seasonal and spatial dynamics. However, until today quantitative information about the seasonal and spatial changes within the SML (and, even more valid for the SNL) is very limited.^[3] Therefore, a time series analysis of the SML were accompanied by other oceanographic experiments in order to keep track of the kind and magnitude of those variability is highly desirable. The Boknis Eck time series station, since 1957 a well-established observation point in the Baltic Sea^[147], provides a well-suited spot for a long-term analysis of the SML by means of surface-sensitive analytical techniques because other important parameters such as temperature, salinity or chlorophyll concentration are measured on a routine basis as well. Besides the easy-to-access physical and chemical parameters, an interesting property of the Bocknis Eck site is the seasonal occurrence of pronounced algae blooms leading to a significant and seasonal increase in biomass. To understand the mutual relationship of the SML/SNL state and the rate of primary production of phytoplankton in the underlying water column, a time series VSFG analysis can provide valuable insights in the SML/SNL formation mechanisms.

5.2 Results from earlier publications

The Kiel research group of Friedrichs has successfully established VSFG spectroscopy as a tool to investigate the SNL directly on natural samples obtained by GARRETT screen sampling, resulting in semi-quantitative measure of the surfac-

tant abundance.^[41,105,106] VSFG spectroscopy is a nonlinear laser spectroscopy based on the second-order nonlinear effect of sum frequency generation. A detailed description of this process is provided in Chapter 2.2. Due to the selection rules of the underlying quantum chemical process, the technique is inherently surface-sensitive. VSFG spectra are obtained by varying the frequency of tunable incident IR beams and measures the SFG more or less resembles an IR spectrum of the surfactant residing at the air-water surface.

The evaluation of SNL spectra showed that the presence of surfactants in the samples leads to a reduction of the intensity of the dangling OH bond (i.e. the "free" OH bond of water).^[148] Apart from that, the surfactant signal is dominated by alkyl signals, probably stemming from lipid-like compounds arranged to surface films with a certain degree of order. Interestingly, as it was deduced from the similarity of the spectra at low and high surface coverages, the structural order seems to be retained even at low organic SNL abundance of surface coverage.^[105] Moreover, indications have been found that soluble (wet) surfactants are dominant over insoluble (dry) surfactants within the SML samples. In stirring experiments, it was found that the reformation of the film upon disturbance occurs immediately (within seconds).^[41] Hence such surface films may form quickly, even under harsh weather conditions and strong winds. In addition, remarkable spectral features at $3400\text{-}3500\text{ cm}^{-1}$ and 2920 cm^{-1} appeared which were tentatively associated with the presence of carbohydrate-rich matter. A very interesting finding of the early time-series data from Boknis Eck was that both the appearance and intensity of the VSFG spectra exhibited a low spatial, but high seasonal variability. As the Baltic Sea is known for having three algae blooms per year with the spring bloom (typically taking place end of March) being most pronounced, it was an obvious assumption to investigate a possible correlation between the primary productivity (which is typically quantified by utilizing the chlorophyll concentration as a proxy) and the surfactant abundance measured by VSFG spectroscopy. The results of the Boknis Eck data up to mid 2013 have already been published.^[106] An annual trend of the SFG intensity with a maximum in the summer months (June/July) was observed. With a typical offset to the aforementioned spring algae bloom of about 2.5 months and no clear correlation to the measured chlorophyll intensities, the common paradigm of a direct relation of SML/SNL abundance and primary productivity going along with high organic surfactant abundance could not be confirmed. As a

possible explanation, it was postulated that sloppy feeding of zooplankton and microbial degradation of macro-molecules resulting from primary production might be the most important sources for surface-active compounds.^[106] Directly building on these first findings, the main goals of this study can be summarized as follows:

- Continuation of the monthly time series sampling measurements to allow a longer time-trend analysis
- Validation of the preliminary results of the 2013 paper^[106] with respect to the reported annual trend of the surfactant abundance, based on a prolonged time series and supported by automatized batch spectra analysis
- Validation of the observation made in the previous study^[106] indicating the presence of a distinct spectral feature appearing at 3400-3500 cm^{-1} , based on a prolonged time-series and semi-automatized gross averaging and spectra analysis

5.3 Experimental

5.3.1 Sampling

SML sampling was performed using a GARRET Screen sampler made of stainless steel (30 cm diameter, ASTM 16 mesh, Linker industries) attached to a chain. The screen and the steel funnel used to transfer the sample into the bottle was rinsed with sea water before sampling.^[40] The sampling was performed from the side of the ship facing towards the wind and the incoming waves. To sample the SML, the screen was submerged under the water surface from the ship's deck and moved aside to avoid uptake of bubbles and foam caused by the perturbation during the dipping process. After pulling it back on board and allowing the excess water to drain, the screen was tilted to fill the SML water via a steel funnel into the PE sampling bottle. This procedure was repeated until the desired volume (typically 150 - 250 mL for 7 dips) of water was collected. The samples were transferred to the lab for the actual measurements. Cleaning of both the metal parts and the plastic bottles was achieved in a lab dishwasher using a strongly alkaline cleaning agent.

5.3.2 VSFG spectroscopy

The detailed description of the experimental setup can be found elsewhere^[106] and in chapter 3. Briefly, the VSFG measurements were performed using a spectrometer by EXPLA. A Nd:YAG laser with a pulse duration of 30 ps at a repetition rate of 10 Hz served as the primary light source. Tunability of the infrared beam is achieved by employing an optical parametric generator (OPG), generating coherent infrared generation in the wavelength range of 2300-10000 nm ($4350\text{-}1000\text{ cm}^{-1}$) with a maximum pulse energy of 200 μJ . For upconversion, the second harmonic of the pump laser (532 nm) was used, typically operating at a maximum pulse energies of 600 μJ . The samples were filled in Teflon dishes with a diameter of 14 cm and were allowed to rest for half an hour before measurement. SFG spectra were recorded in the range of $2750\text{-}3840\text{ cm}^{-1}$ with a step width of 5 cm^{-1} , for covering the spectral range of the aliphatic CH stretch vibrations ($2750\text{-}3050\text{ cm}^{-1}$) and the dangling OH bond ($3650\text{-}3840\text{ cm}^{-1}$) and a step width of 20 cm^{-1} for the region of the hydrogen-bonded water network signals. For each set of measurements, a dense se DPPC monolayer with a surface coverage of 40 \AA^2 area per molecule served as the referencne sample for day-to-day spectrum normalization.^[105] Small day-to-day changes of SFG intensity are inevitable and are caused by adjustment of the optical setup and light beams alignment and laser performance.

5.3.3 Software

Analysis of the new data and revision of the already published data has been performed using a newly-developed Python software package (see chapter 4). Assuming the initial situation of the raw SFG measurement files being present in folders corresponding to their respective day of measurement and accompanied by an Excel sheet with the sample metadata (geographical location, wind speed, ambient and water temperature, sampling depth ...), the script performs the following tasks:

- map the table entries to the corresponding raw data file
- write the data to an SQL database
- fetch the measurement day's DPPC reference spectra CH integral for normalization purposes

- compute average spectra for specified time intervals (e.g. each sampling day or different months), differentiating between bulk and SML samples
- perform automatic baseline correction and calculate surface coverage for each of those spectra (according to eq. 5.1)
- yield a compiled table for each day of measurement including number of SML and bulk samples and the corresponding surface coverage values
- provide different convenient functions to visualize the generated data

5.3.4 Surface coverage

The term "surface coverage" is used in the sense of a proxy that reduces the information contained in the spectra to a single number. It is a raw measure of the fraction of the surface that is covered by surfactants, sc , with the purpose to share this value with other researches investigating surfactant properties of the SML without the need to input the complete spectral information. It is operationally defined as the integral over the CH region of the SFG spectrum normalized to the average DPPC reference integral measured the same day. Before, the intensities of both the reference and the samples are divided by the product of IR and Vis intensity (to correct for laser intensity fluctuations) and baseline-corrected to remove additional background SFG intensity caused by non-resonant interfering signal stemming from water (indicated by $I_{\text{H}_2\text{O}}$ in eq. 5.1). Because of the square dependence of the SFG signal on the surface concentration (see Chap. 2.2), it is necessary to take the square root of the integral ratio.^[41,120] As it is not absolutely sure if the interference with the background is strictly constructive or destructive, this equation is a practical compromise to provide a consistent way of background subtraction.

$$sc = \sqrt{\frac{\int_{2750}^{3000} (I_{\text{Sample}}(\tilde{\nu}) - I_{\text{H}_2\text{O, sample}}(\tilde{\nu})) d\tilde{\nu}}{\int_{2750}^{3000} (I_{\text{Reference}}(\tilde{\nu}) - I_{\text{H}_2\text{O, reference}}(\tilde{\nu})) d\tilde{\nu}}} \quad (5.1)$$

This relation is based on the assumption that alkyl surfactants dominate the signal and structural changes of the monolayer that could affect the signal are negligible. For sure, the latter assumption may fail at low surface coverage, yielding too low signal and surface coverage values due to the loss of structural order. Moreover, also the assumption that surfactant coverage is always going

along with CH signal may be flawed. Therefore, it should be emphasized that over-interpretation of the calculated relative surface coverage should not be over-interpreted. More research is needed to fully recognize the relationship between VSFG signal and abundance of surface active material. Note that alternative baseline correction, accounting for the situation of constructive interference between sample signal and background by subtracting the root of the background from the root of the signal yielded the same trend (see Appendix, Fig. B.2).

A demonstration of the data processing that was done for each day of sampling is depicted in Fig. 5.1. Here, the spectra are first grouped by their category (either SML or bulk water), second the average spectrum of each category is calculated and baseline-corrected and third the coverage calculated using the reference integrals according to 5.1.

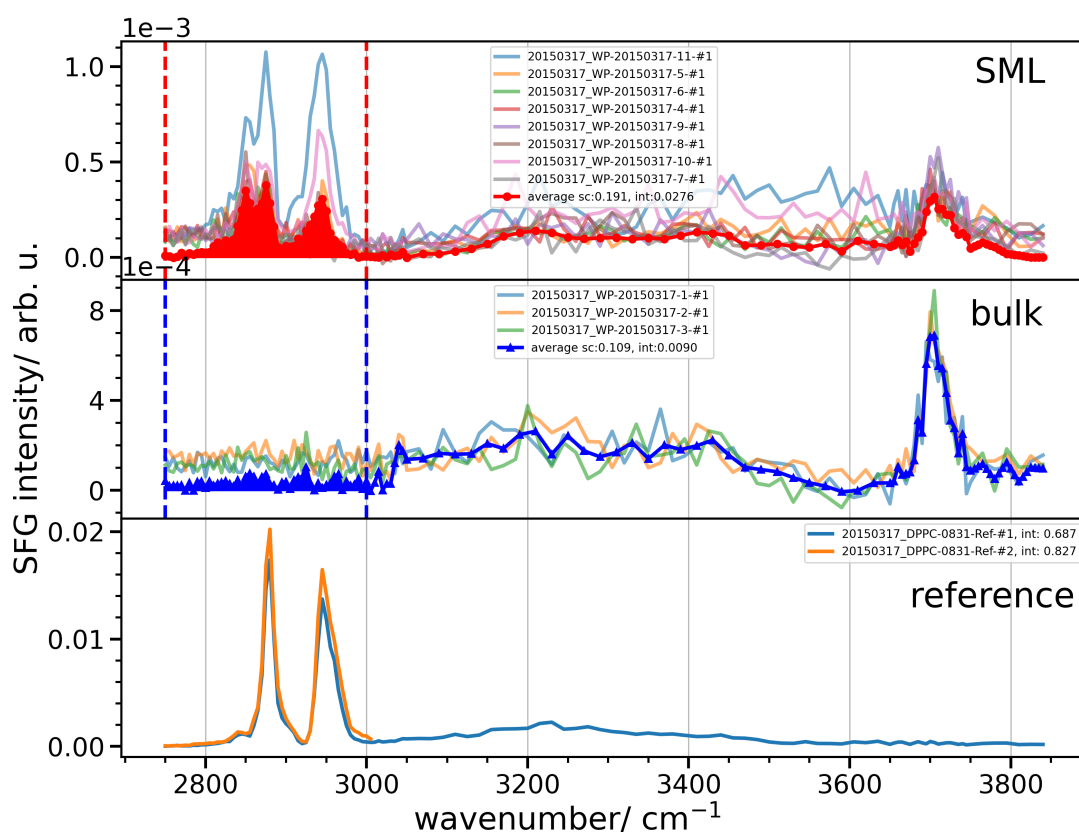


Figure 5.1: Demonstration of the analysis procedure performed for each Boknis Eck sampling day. Here, the dataset of 2015-03-17 is shown as example. The SML spectra and the resulting average spectrum (indicated in red) are shown at the top, the bulk water samples and the resulting average spectrum (indicated in blue) are indicated in the middle and at the bottom the DPPC reference spectra from the corresponding day of measurement are displayed. The filled area under the average curve indicates the region over which the integral is calculated. In the legends, the values for the resulting integral and surface coverages are provided.

5.4 Results and Discussion

5.4.1 Typical appearance of the VSG spectra of a sampling day

Fig. 5.1 shows many of the most important spectral features present in the spectra of SML and bulk water samples. The SML spectra exhibit the typical signals of an aliphatic group: a peak at 2850 cm^{-1} , corresponding to the symmetric stretch vibration of the methylene group (d^+) and a pronounced peak at 2880 cm^{-1} belonging to the symmetric stretch vibration of the terminal methyl group (r^+). At about 2950 cm^{-1} , the spectra show a broad peak which corresponds to signals stemming from the FERMI resonances of both the d^+ and r^+ mode. The bulk

water samples do not show those aliphatic CH signals but a pronounced peak at approx. 3750 cm^{-1} which is usually attributed to the so-called "dangling OH bond", an OH bond reaching out of the water surface towards air. Typically, this signal is observed only if no significant amount of surfactant is covering the surface.^[148] The example of this sampling day shows significant CH signal for the SML samples, indicating a high surfactant abundance, and no CH signal and, in addition, the prominent dangling OH bond as indicator for a more or less surfactant-free water sample. Note, however, that the amount of signal present in the SML samples was, in comparison with other sampling days, rather high, as well as the extreme difference to the underlying bulk water spectra, and this ideal example was chosen for reasons of clarity here.

5.4.2 Comparison with the preliminary time series

A comparison of the VSFG surface coverage data as function of the respective day of the year from samples collected between 2009 and 2012 on the one hand and the complete data set (2009-2018), both analyzed with the new automatic routines, is shown in Fig. 5.2. The blue line indicates the rolling mean with a window size of 8 data points. It can be seen that, in general, the maximum values occur in the middle of the year rather than in early spring or winter. This holds true for both the old and full data, but the trend is less pronounced for the larger data set. This can be explained by two factors:

1. In the later years, the overall surface coverage was very often very low
2. The variance among the different sampling days was quite big, resulting in a blurring of the trend

In addition to the surface coverage data, chlorophyll and oxygen concentration measures are depicted as well. The chlorophyll data exhibits the pronounced spring algae bloom and a second, less prominent bloom occurring in autumn. Both are typical features of the Boknis Eck sampling site. The annual oxygen maximum coincides with the spring algae bloom and follows a clear trend during the year. It can be seen from those figures that the findings published in the past^[106], i.e. that the annual maximum of the surfactant abundance determined by VSFG does not coincide with the algae bloom indicated by the chlorophyll concentration, holds still true for the new analysis based on a larger data set. All

in all, although the seasonal trend is not so clear like in the previous published results, the general findings remain valid.

5.4.3 Long-term trend

The long-term trend of the surface coverage as function of sampling date is shown in the lower sub-figure of Fig. 5.3. The green dots indicate the average surface coverage obtained per day of sampling from the SML samples, the blue squares show the average coverage of bulk samples taken from the ship's CTD in a depth of 1, 5 and 25 m. Although the variation is quite pronounced among the month, two observations can be made: in most of the cases, the detected surface coverage for SML samples is higher than for the corresponding bulk water samples which is in agreement with the expectation of enrichment of surface-active substances at the interface. Second, the detected coverages are usually lowest in the late autumn and winter months, although the annual maximum occurs in different months. The seasonal trend of a re-occurring annual maximum in the early summer months, as reported in the preceding analysis,^[106] which was obtained by using a sinusoidal fit with a period length of one year to the data of the coverage, cannot clearly be observed in the data based on the customized data analysis routine. This is probably the result of the gross averaging, taking into account also spectra that were considered of not having any peak in the preliminary way of analysis, as well as the automatic baseline correction routine which may lead to different results than a manual analysis by an experienced VSFG researcher.

To compare the long-term variation of the surface coverage of the SML and bulk and visualize the annual trends more clearly, Fig. 5.4 depicts the coverages normalized by their corresponding annual maxima. In addition, the figure shows annually normalized data for the temperature, chlorophyll and oxygen concentration measured at one meter depth to detect possibly occurring correlations between those parameters. A clear seasonal trend with distinct annual maxima in spring and summer is obvious for the oxygen and temperature, respectively. The (unfortunately not that dense) chlorophyll data also exhibit an annual "up and down" but with seemingly varying dates of the annual maximum. The same holds true for the coverage data: There is a fluctuation during the year, typically with rather low values in late autumn and winter, but the maximum is not re-occurring at about the month. The strong scatter of the coverage data

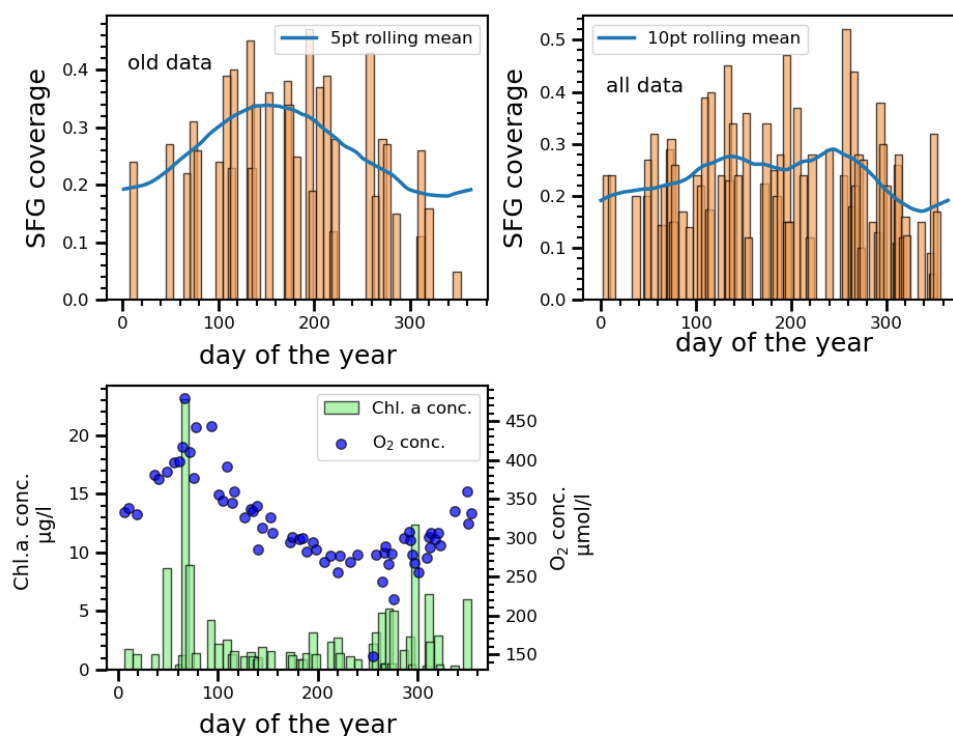


Figure 5.2: Comparison of the VSG surface coverage data obtained during the phase reported in the first publication^[106] (2009-2012) and all collected samples (2009-2017). For comparison, also the oxygen and chlorophyll a concentration is displayed.

among the month as well as the absence of a clear periodicity makes it difficult to identify any direct correlation between those parameters. The only observation that may be reported with some confidence is that the annual maxima of the SML and bulk water coverage appears after the maximum in oxygen (appearing typically in March). For the chlorophyll data, this is in agreement with the observations published before^[106] and confirms the assumption that there is no direct correlation between primary production (for which chlorophyll concentration acts as proxy; actually a much debated issue as well)^[149] and coverage of the sea surface with surfactants. In the following, this general statement will be analyzed by a more rigorous statistical analysis.

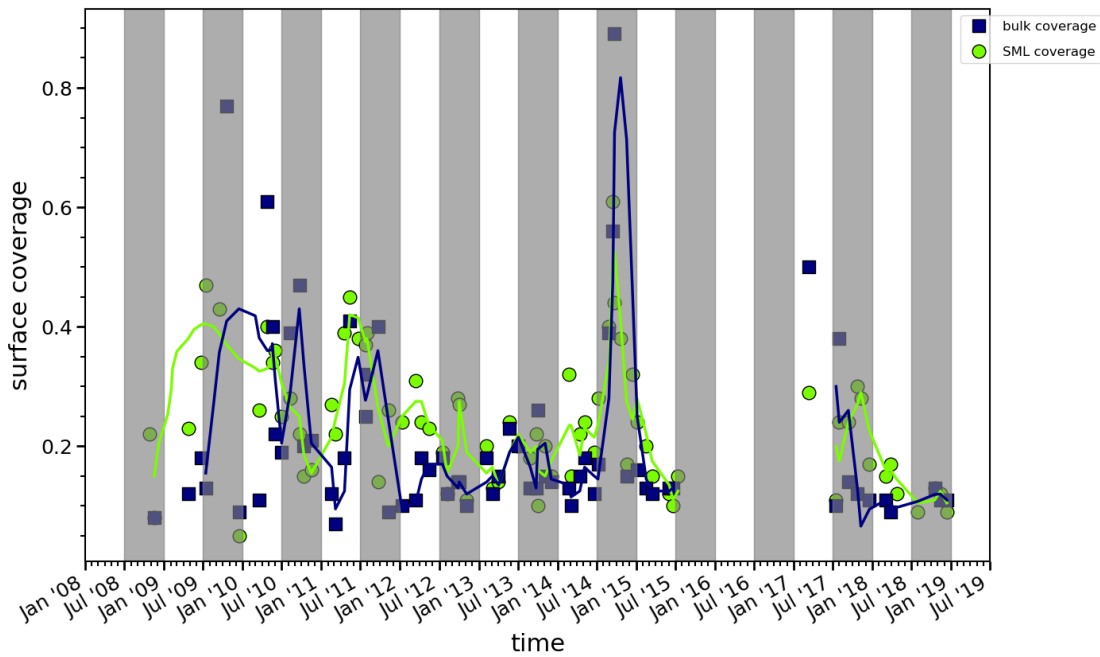


Figure 5.3: Time series of the SML and bulk surface coverage of the monthly Boknis Eck samples calculated according eq. 5.1.

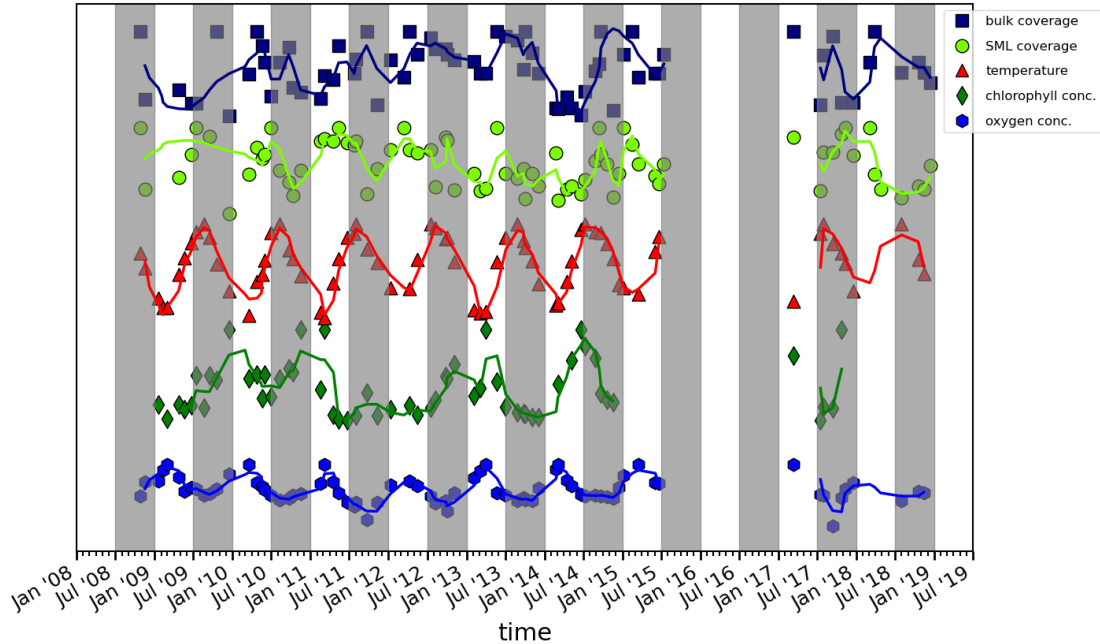


Figure 5.4: Time series of the SML and bulk surface coverage of the monthly Boknis Eck samples calculated according eq. 5.1 and other oceanographic parameters^[147], all normalized to their corresponding annual maximum.

5.4.4 Difference between SML and bulk water

To evaluate a possible correlation between the measured surface coverages of the SML samples with water samples from 1 m depth, or from higher depth (usually 5 and 25 m depth) have been compared by calculating the pairwise PEARSON coefficient. This statistical value describes the degree of linear correlation between two data sets and takes values from -1 (strong negative) to 1 (identical, so strong positive). A coefficient of 0 indicates that the data sets are totally uncorrelated. The results of this calculation as well correlation scatter plots of the categories and histograms showing the coverage value distribution of each category are presented in Fig. 5.5. The category "bulk" contains all bulk water samples, including the ones from 1 meter depth, the category "> 1" contains the coverages of all samples collected at sampling depths greater than one meter. The correlation between SML samples and samples from 1 meter depth is, with a PEARSON coefficient of 0.46, relatively weak whereas the correlation between samples with sampling depth > 1 m and 1 m is slightly higher (0.6). Surprisingly, the correlation between SML and samples from depth > 1 m is nearly the same like SML and 1 m depth (0.48). This indicates a clear difference between the SML and depth = 1 m or > 1 m on the one hand, but also for the samples from 1 m and greater depth on the other hand. This finding may suggest that the 1 meter depth might be considered as a kind of transition zone. The different character of the sample depth categories is also reflected in the histograms at the main diagonal of Fig. 5.5. Whereas for the bulk samples > 1m the vast majority of coverage values is between 0.1- 0.2, the SML values are wider distributed with a center inbetween 0.2 and 0.4. The distribution of the samples collected at 1 m sampling depth exhibit, similarly to the deepest sampling depths, but occasional occurring of clusters at higher coverage values. All those findings are supported by the result of pairwise MANN-WHITNEY-U for equality of means between the different sample categories (see the results of the SHAPIRO-WILKS testing for required normal distribution are provided in Tab. B.1 in the Appendix). Those results are shown in Tab. 5.1. The null hypothesis of equal means cannot be accepted for any of those pairs, meaning that the one meter sample is significantly different from both the surface layer samples and the deep water samples. Comparing the p values, again it is reflected that the one meter sample is somewhere in between the SML samples and those stemming from greater

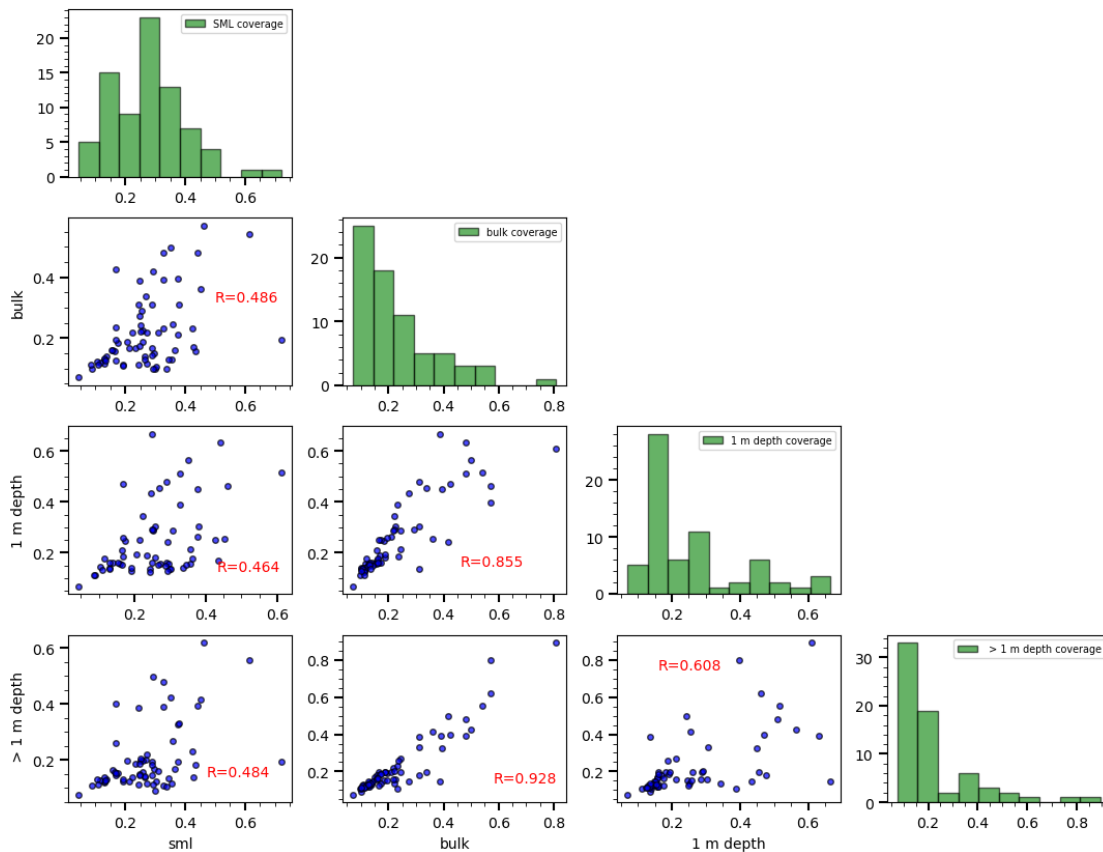


Figure 5.5: Scatter matrix plot of the SML and bulk samples, the samples taken from 1 m depth and the samples taken from depth > 1m. The pairwise PEARSON correlation coefficients are depicted in red in the corresponding scatter plots, histograms of the distribution of the single categories are displayed on the main diagonal.

depths, as the value is extremely low for the pair SML/greater one but closer to the significance level of 0.05 for SML/one and greater one/one. This clearly supports the hypothesis that the one meter samples reflect a zone of transition between two clearly distinct zones.

5.4.5 Seasonality

To approach the question of a potential seasonal variation in the SML signal in a more quantitative way, the samples belonging to each quarter of the year have been analyzed together. This division scheme has been chosen because the results of preliminary studies indicated a relatively low surface coverages during spring and the winter months but a high surface coverage during summer and early autumn.^[106] All spectra were mapped to the corresponding quarter, normalized to the reference integral of the day they were measured and afterwards

Table 5.1: Results of the MANN-WHITNEY-U test for equal mean for the surface coverages from SML samples, samples from 1 meter depth, greater than 1 meter depth and "bulk" which contains both the latter. The null hypothesis H_0 of equal mean is accepted if the p value is higher than the significance level of 0.05.

category 1	category 2	statistics	p -value	H_0 accepted
SML	bulk	39774	$1.02 \cdot 10^{-8}$	n
SML	one	16263	0.034	n
SML	greater one	23510	$1.08 \cdot 10^{-9}$	n
greater one	one	3272	0.009	n

all spectra of a quarter were averaged. The resulting averaged spectra are shown in Fig. 5.6. The number of spectra used for each average spectrum is indicated in the legend. The intensities in the CH region are significantly lower in late autumn and early winter (quarter 4, Oct-Dec.). The CH intensities from the first quarter is only slightly lower (if at all) than in quarter 2 (Apr-Jun.) and 3 (Jul-Sept.). A significant difference can be seen in the spectral region of the water OH network signal ($3000-3650 \text{ cm}^{-1}$). Here, the signals from quarters 1 and 4 are lower whereas those from quarters 2 and 3. The highest values for both the CH region and the OH network appear in late summer/early autumn (quarter 3). With increasing intensity of the OH network signal, the dangling OH bond that appears typically at clean surfaces about 3700 cm^{-1} becomes more and more blurry. However, it is still visible as a distinct peak, even in the quarter averages with high CH and OH network intensities. Overall, it is most prominent in winter and early autumn (quarter 4 and 1), indicating a general lower presence of surfactants in the corresponding spectra. These findings confirm a seasonal variation in the shape of the spectra with a maximum in CH and OH hydrogen network signals in samples taken between late spring and early autumn and a minimum in late autumn till early spring. However, due to averaging of spectra with a rather high variability in the single spectra, the resulting overall trend is not very pronounced.

The OH signals appearing in VSFG spectra of natural aqueous systems are significantly influenced by the presence of a surfactant monolayer. In general, the surfactant layer that changes the order and orientation of the underlying water interacting with its polar head groups, often causing a strong increase in VSFG signal intensity.^[148] This is consistent with the observed seasonal trend

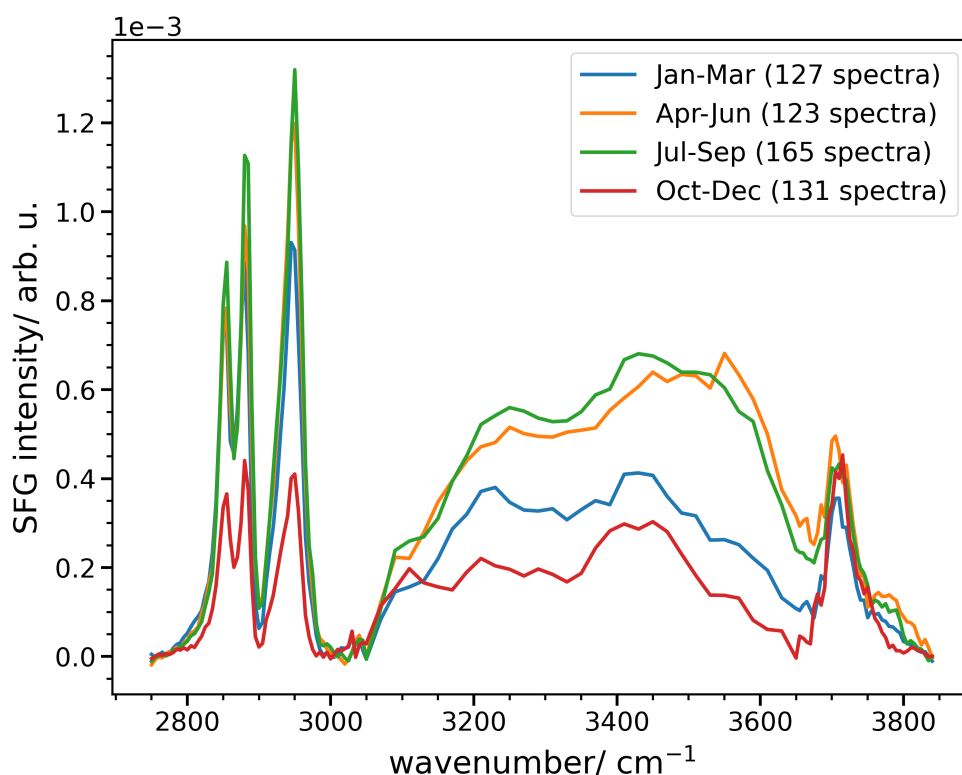


Figure 5.6: Average SFG spectra calculated for four quarters of the year. All spectra were divided by the DPPC reference integral of the day before averaging. The number in brackets inside the legend indicates the total number of spectra included in this average.

of the shape of the spectra in this example. A higher presence of surfactants indicated by a high signal intensity in the aliphatic CH region coincides with a high intensity in this OH region. The distinct peak at approx. 3450 cm^{-1} that has been reported in the previous studies and was attributed to the presence of carbohydrate species^[105,106], typically appearing in late summer or early autumn, is not clearly visible in this batch average. This may be the result of the averaging process which can lead to the loss of individual spectral shape features if they are not present in many of the averaged spectra. Note, however, that the intensity of the broad peak at about 3500 cm^{-1} is higher than that at about 3250 cm^{-1} . This is quite unusual for a surfactant (see for example the DPPC spectrum included in Fig. 5.1)

One of the biggest pitfalls in the automatized gross averaging over defined

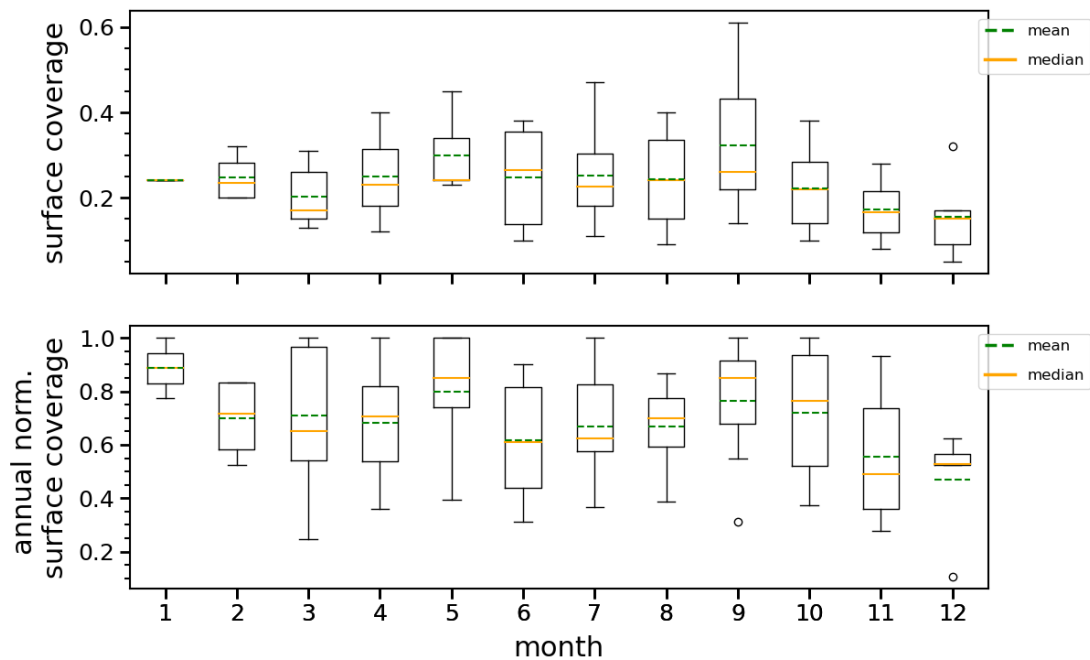


Figure 5.7: Boxplot of the monthly averages of the SML surface coverage as determined by VSFG in total and normalized to the annual maximum.

time intervals is the high variance among the CH integrals of SML samples obtained during a single day of sampling (see Fig. B.1) This variance remains visible if the surface coverage averages per sampling days are grouped by the corresponding months, as it is shown in the boxplots in Fig. 5.7. The surface coverage is strongly varying in between the data from different years for the same month (upper plot). This holds true even if all values are normalized to their corresponding annual averages to account for differences between different years (lower plot). In fact, many months exhibited the highest value of surface coverage in one of the years and, using this kind of analysis, no obvious annual trend of the relative surface coverage can be seen in Fig. 5.7. Moreover, for January and February, only few sampling days were in those month, leading to a strong influence of those individual values on the result and thus being not fully statistically reliable. To this ends, the only obvious finding from Fig. 5.7 is a remarkably low coverage for November and December which is in agreement with the previous findings from the 2013 publication.^[106] This shows that the result batch analysis is sensitive to individual samples with coverages far above

or below the average.

5.5 Conclusion

All in all, the analysis and re-evaluation of the Boknis Eck time series sampling data confirmed a difference in the appearance of the spectra and the amount of surfactant coverage during the course of the year. Spectra from the winter months and early spring show a higher presence of surfactants in their average spectra, although fine spectral features may disappear upon rigorous mass-averaging. What is absolutely clear is that here is a significant difference in the amount of surfactants present in the bulk water samples compared to the SML, which complies with the model of surface enrichment. However, using this way of analysis, the seasonal trend was not following a clear pattern peaking in the early summer month with some delay to the spring algae bloom as it has been reported earlier.^[106] The scatter among the individual day of measurements is significant. Here, the automatized data analysis routine, has the clear advantage of being able to process huge amounts of data in an unbiased manner. However, a disadvantage of such an automatic data evaluation in comparison to a manual analysis, in particular for noisy data, is that data of bad quality may enter the analysis that have been easily identified by an experienced physical chemist to be unreliable.

CHAPTER 6

Contributions to the Baltic GasEx cruise 2018

6.1 Introduction

The interface between air and sea is a place of permanent exchange of heat, matter and momentum between the two phases. As the ocean can act as important sink and source for many environmentally relevant gases such as CO₂ and N₂O, a detailed and microscopic understanding of the interfacial phenomena related to gas transfer is essential for the investigation and prediction of global-scale atmospheric processes.^[2–4,12,149]

Because of the bipolar nature of this interface, bordered by the highly polar solvent water in the one and the apolar medium low-density medium air in the other direction, amphiphilic organic matter tends to accumulate in this region. This matter is produced by biological primary production and anthropogenic entry and altered by consecutive photochemistry and biological degradation.^[1,6,19,46,150] The surface-active material is composed of several classes of substances, for example complex carbohydrates, fatty acids and proteins.^[10,13,17,151] The presence of these substances as well as the sudden change in molecular density in the interfacial region gives rise to a remarkable alteration of the surface layer's physical and chemical properties in comparison with the bulk phase.^[16,152] Because of this distinct properties, the uppermost millimeter or nanometer of the sea is referred to as the SML or surface nanolayer (SNL) and is subject to ongoing interdisciplinary research.^[3,45]

Theoretical considerations, laboratory experiments in tanks and wind channels as well as field studies with artificial surfactants have shown that the surfactant layers assembled at the air-water interface can influence the gas transfer mainly by two different mechanisms: by forming a physical diffusion barrier and by changing the viscoelastic properties of the water which lead to a higher

resistance against wind-driven wave formation and therefore a reduction in turbulent gas transfer.^[18,26,27,32,142–146]

Examples for surface-sensitive techniques found to be suitable for the measurement of surfactants in the SML are laser spectroscopic technique like VSFG, electrochemical methods like AC voltammetry and indirect techniques targeting the surface tension which can be significantly reduced in the presence of surface-active substances.^[41,42,105] VSFG, being a vibrational spectroscopy, holds the advantage of providing additional information about the surfactant composition whereas the other techniques yield only information about the amount of surfactants. As bioproduction is considered as one of the most important sources of the surfactants, there have been several attempts to correlate the surfactant abundance with indicators for the level of primary production (e.g. chlorophyll concentration) but until now no non-ambiguous correlation between such indicators has been found, indicating that the relation is rather complex and might involve biotic and abiotic decomposition of the matter generated by primary production.^[106,153] The concentration and composition of the surfactants has been found to vary spatially and temporarily. For example, in long-term SML VSFG experiments with samples collected from the Boknis Eck time series sampling station in the Baltic Sea an annual variation of the surfactant concentration with a maximum in the late summer months was observed (see chap. 5). This finding was interpreted as a consequence of the annual cycle of alga abundance, starting with a strong bloom in spring with drastically enhanced primary production.^[106] The observed delay of the surfactant concentration maximum with respect to the bloom indicates that at least a significant part of the surfactants are secondary products formed by degradation of organic matter built up during the bloom.

The purpose of the Baltic GasEx cruise 2018 was the simultaneous measurement of gas-transfer rates and amount of surfactants present at the interface to obtain a direct correlation between these physical parameters and to eventually proof and quantify the influence of surfactants presence on gas exchange in a field setting. To measure gas exchange rates, two complementary techniques (dual tracer release experiment and eddy covariance measurement) have been applied. The surfactant abundance in the SML was determined by AC voltammetry, VSFG, surface tension and Langmuir compression isotherm measurements. As the preliminary time-series studies at the Boknis Eck time series station of SML

samples by means of VSFG spectroscopy indicated an annual variation of the surfactant abundance it was decided to schedule one cruise at a time where usually a low surfactant concentration could be expected (early summer) and the other later in the year when the concentration is typically higher.^[106]

6.2 Experimental

6.2.1 Time and location

The first cruise took place from 06/03 - 06/15, the second from 09/12 - 09/22 in 2018. As the Baltic Sea around Kiel and the Bay of Eckernförde has been studied in detail during the last years, especially due to the Boknis Eck time series station,^[147,154] the gases for the dual tracer experiments have been released in this region after a suitable spot was found. After the release of the tracers, the vessel followed the tracer patch. Stops to take samples (stations) were scheduled in a systematic way. This procedure was the same for both cruises. The geographical location of those cruise stations as well as the position of the Boknis Eck time series station are displayed in Fig. 6.1. The stations of the first cruise are indicated in green, the ones from the second cruise in red.

6.2.2 Sampling

During the cruise, the ship stopped at certain times during the day to perform a variety of sampling procedures. These "stations" were subdivided in "big" and "small" stations. During a small station, the vessel stopped only for a short period of time to allow for GARRETT screen SML sampling from the ship's deck. In contrast, a big station typically took up to several hours and included the launching of a zodiac to perform SML sampling in a bigger distance from the ship, avoiding possible contamination caused by the ship. In addition to the SML sampling, bulk water samples were collected during big stations by the CTD rosette sampler of the ship. These samples were always taken from the station's sampling depth, hence in proximity to the seabed. An overview of the number and types of samples collected during big and small stations is given in Tab. 6.1. In both cruises, each day two big stations (one in the morning, one in the afternoon) were scheduled. During the first cruise, one small station took place at 12 pm and one at midnight. During the second cruise, the midnight station was omitted. The zodiac was positioned as far upwind of the ship as possible and away from the path taken by the ship. During sampling, the outboard

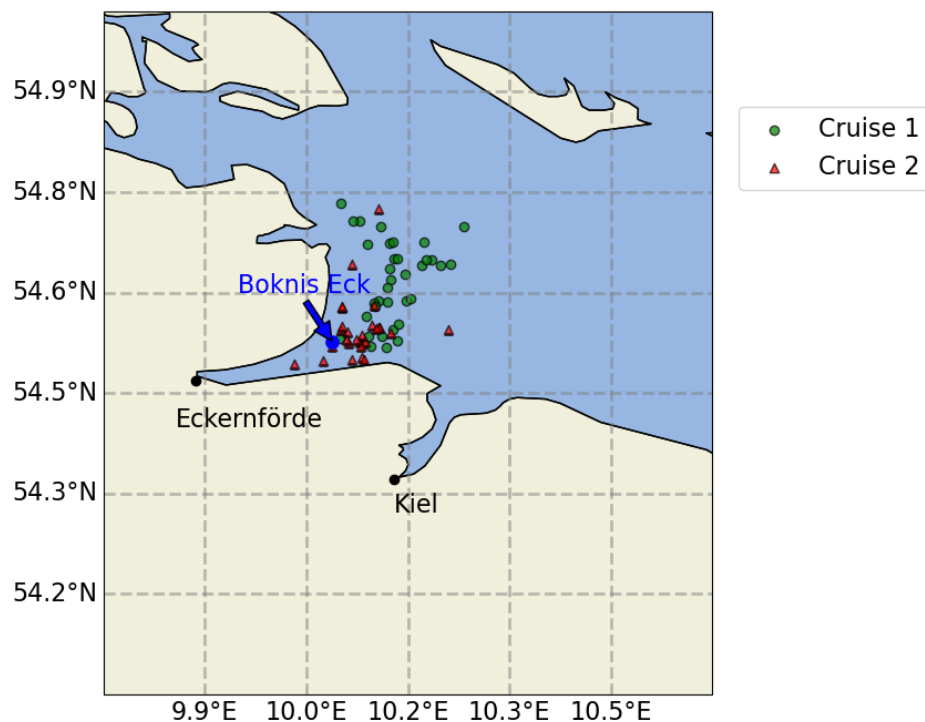


Figure 6.1: Stations of both the GasEx cruises, located in the Baltic Sea (Bay of Eckernförde). The Boknis Eck time series station is indicated with a blue arrow. The plot was generated using the *cartopy* Python package.^[155]

Table 6.1: Number and type of samples taken during the Baltic GasEx cruise 2018.

(a) Big station		(b) Small station	
type	no. of samples	type	no. of samples
plate	3	screen	2
screen	2		
CTD	1		

motor was switched off. Samples were collected in upwind clean waters with the waves moving towards the boat using both screen and glass plate sampling. PE bottles for SML and bulk water sampling with a volume of 500 mL were cleaned before the cruise by means of a conventional laboratory dish washer with a strongly alkaline cleaning agent. The samples were stored at -18 °C until performing the laboratory measurements.

GARRETT screen sampling

This sampling procedure has first been described by GARRETT.^[156] From the edge of the zodiac, the screen was submerged into the water, moved away from the position where it was dipped in and withdrawn from the water. After slightly tilting the screen to remove bulk water from the gap between the sieve and the mantle, the surface water was transferred from the meshes into a metal funnel by tilting the screen strongly. The water was collected in clean PE bottles. After sampling, all metal parts were washed immediately with fresh water to prevent corrosion. Before the next usage, the screen was treated with a neutral detergent, washed repeatedly with hot freshwater and finally rinsed with ultrapure water (MilliQ).

Glass plate sampling

The borosilicate plate of 500 mm length, 250 mm in width had a thickness of 5 mm. A teflon wiper was used to remove the water from the glass surface. Before sampling, the glass plate and wiper were cleaned by washing with aqueous HCl (10 %) and rinsed subsequently with ultrapure water. To collect the SML samples the plate was submerged into the water perpendicular to the surface and withdrawn slowly. Afterwards, the wiper was used to transfer the water into a clean PE bottle.

6.2.3 Laboratory-based experiments

The deep-frozen samples were allowed to thaw. VSFG spectroscopy was performed first. To record the surface tension, the PTFE sample holder of the tensiometer was immersed into the big SFG teflon dish carefully to fill it. In case a compression isotherm was recorded as well, after finishing the SFG measurement, the SML sample was poured from the big teflon dish into a clean glass beaker. From this, about 100 mL were filled into the LANGMUIR trough.

Surface tension

The surface tension was recorded at 21 °C ambient laboratory temperature using a commercially available AQUAPI+ tensiometer by the manufacturer KIBRON. Suitable teflon sample cups with a volume of 3 mL by KIBRON were used. The tensiometer was calibrated to the surface tension of ultrapure water several times a day using the built-in automatic calibration routine. Stability of the calibration was checked after each sample. After measurement, the teflon cups were cleaned by applying few droplets of TICKOPUR detergent, washing with hot water for about a minute and subsequent rinsing with ultrapure water.

LANGMUIR compression isotherms

The compression isotherms were obtained by using a LANGMUIR trough by RIEGLER & KIRSTEIN. The trough had two movable teflon barriers allowing to vary the sample's surface area in between 190 cm² and 27 cm². The surface pressure was measured by a WILHEMY film balance attached to one of the movable barriers. SML samples were poured into the trough and compressed at a speed of 0.3 $\frac{\text{cm}^2}{\text{s}}$ until the lowest possible area has been reached. If a significant increase in surface pressure was detected, the barriers were reset to the initial position and the compression experiment was repeated at 3.5 $\frac{\text{cm}^2}{\text{s}}$ compression speed.

Cleaning of the trough was achieved by adding few drops of TICKOPUR detergent and subsequent cleaning with hot water. Finally, the trough was rinsed with ultrapure water. The success of the cleaning procedure was checked by recording an isotherm of clean water afterwards. If the surface pressure at full compression was below 0.8 mN m⁻¹, the instrument was considered clean.

VSFG spectroscopy

The exact procedure is described in detail elsewhere.^[41,105] Briefly, the VSFG measurements were performed using a modified VSFG spectrometer by EKSPLA, which was based on a mode-coupled Nd:YAG laser emitting at a wavelength of 1064 nm. For upconversion, the second harmonic of the laser (532 nm) was used. The sample was poured into a teflon dish with a diameter of 14 cm, placed on the sample holder table of the spectrometer. The tunable IR, generated by an optical parametric generator, and the fixed-wavelength VIS beam were overlapped on the sample's surface by adjusting the height of the sample holder. The samples

were measured within the spectral ranges stated in tab. 6.2. At the beginning and the end of a measurement day, a VSFG spectrum of the reference substance DPPC was recorded. The initial reference sample was also used to adjust the optical components of the spectrometer setup to yield maximum SFG intensity.

Table 6.2: Spectral regions probed during VSFG measurements of the SML samples.

range/ cm^{-1}	step width	spectral region
2750-3050	5	CH (alkyl) stretch vibrations
3050-3600	20	OH stretch vibrations, bulk hydrogen-bonded network
3650-3840	5	dangling OH stretch vibration

6.2.4 Software

The analysis and calculation of all data was performed using a custom Python package that is available at GitHub and described in detail in chapter 4. Briefly, the raw measurement data is loaded in a relational database to map the relation *experimental data* \mapsto *sample* \mapsto *station*, so each station object is aware of the samples that belong to it and each sample has access to the measurements of surface tension, SFG and compression isotherms (if performed). The surface tension values have been normalized to reference salinity of 17 PSU according to an empiric equation derived from a systematic set of surface tension measurements published in the literature (see also section 2.1.1).^[110] The values of the different measures for surfactant abundance were calculated for each sample and the samples are either averaged per station or categorized by their type (e.g., plate or screen) for further analysis. Note that all statistical tests utilized have been performed using the Python implementations bundled in the *scipy.stats* module.^[157]

6.3 Preliminary work

To prepare for the sampling and data analysis of the GasEx cruise, a set of laboratory experiments was conducted within the scope of the Bachelor thesis of Nhat-Thao Ton-Nu associated with this work and was co-supervised by the author of this thesis.^[158] The most important findings are summarized here. The aim of this thesis was the investigation of LANGMUIR compression isotherms of pure and mixed samples of both soluble (wet) and insoluble (dry) surfactants. This set included artificial and natural samples. The natural SML consist of a

complex mixture of multiple compounds. Earlier experiments in the context of the Boknis Eck time series SFG studies revealed that a significant fraction of the surfactants is rather soluble. Dry and wet surfactants may influence sea/air gas transfer by slightly different mechanisms. Whereas the dry surfactants are in principle able to form a physical diffusion barrier by forming a well-ordered surface monolayer in addition to the change in the viscoelastic properties, the wet surfactant's contribution is based on the latter effect only. An illustration of those surfactant effects is depicted in Fig. 6.2. However, to get a better understanding on how dry and wet surfactants and a mixture of both behave and which of the variants is more representative for the behavior of the natural SML samples, a systematic measurement series of compression isotherms has been performed. Experiments have been conducted both for natural SML samples from the Baltic Sea and humic acid as laboratory proxy compounds. Here, arachidic acid has been selected as a dry surfactant known to form well-structured monolayers and Triton X, a polythelene glycole derivate which is frequently used as wet surfactant. The molecular structures of both compounds are depicted in Fig. 6.4. Finally, experiments have been performed with humic acid, a complex mixture of compounds with varying amount of polyaromatic groups.

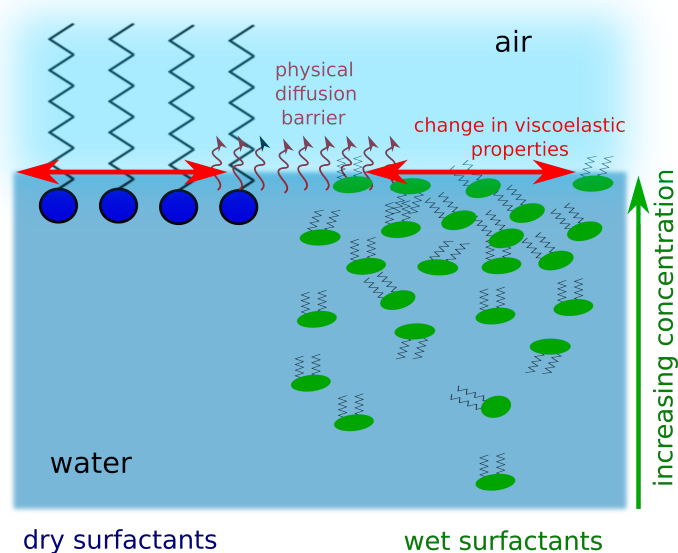


Figure 6.2: Schematic representation of dry and wet surfactants and the mechanisms by which they are able to influence air-sea gas exchange. Red arrows indicate a location of reduced gas exchange rate due to surfactant presence.

Comparison of the isotherms of natural SML samples and both dry and wet surfactants clearly showed that the SML isotherms are more similar to the isotherms measured for the wet surfactant proxies, as they do not exhibit a 2D phase transition and the appearance of the isotherm is more strongly dependent on the selected compression speed. To illustrate this, Fig. 6.3 shows isotherms of the soluble surfactants Triton-X and humic acid, the insoluble surfactant arachidic acid, and a freshwater sample collected using a GARRETT screen from a pond on the Kiel university campus at three different compression speeds. This complies with the hypothesis mentioned above that a significant fraction of natural surfactants is rather soluble.

The compression experiments were conducted at three different compression speeds. In general, a higher compression speed led to an earlier lift-off point and a higher value for the maximum recorded surface pressure (see Fig. 6.5). This is due to the necessary equilibration of the 2D structure and (in case of wet surfactants) surface adsorption equilibria, which may be too slow compared to the compression at high compression speeds. Moreover, another interesting observation was a hysteresis phenomenon occurring when performing multiple consecutive compression experiments of the same sample, as it is shown in Fig. 6.5. After each repetition, the lift-off point was observed at slightly higher area values. This unexpected observation could indicate an accumulation of the soluble surfactant in the proximity of the surface induced by the compression. If this accumulation is faster than the equilibration of the excess surfactant with the sub phase, the resulting sequential increase in surfactant surface concentration could cause the observed shift in lift-off points and surface pressure.

Spreading a monolayer of arachidic acid on a sub phase with dissolved Triton X led to a change in the compression isotherms with respect to those of the isolated compounds, manifested in an earlier lift-off point and a higher maximum surface pressure. The pronounced phase behavior of the arachidic acid became blurred, especially for low surface concentrations. However, for increasing surface concentrations of arachidic acid the isotherm became more and more similar to the isotherm of pure arachidic acid. A qualitative interpretation of this effect could be the following: on the one hand, it could be the result a possible interaction between the surface monolayer and the wet surfactant in the sub phase can lead to an exchange of molecules. At low concentrations of arachidic

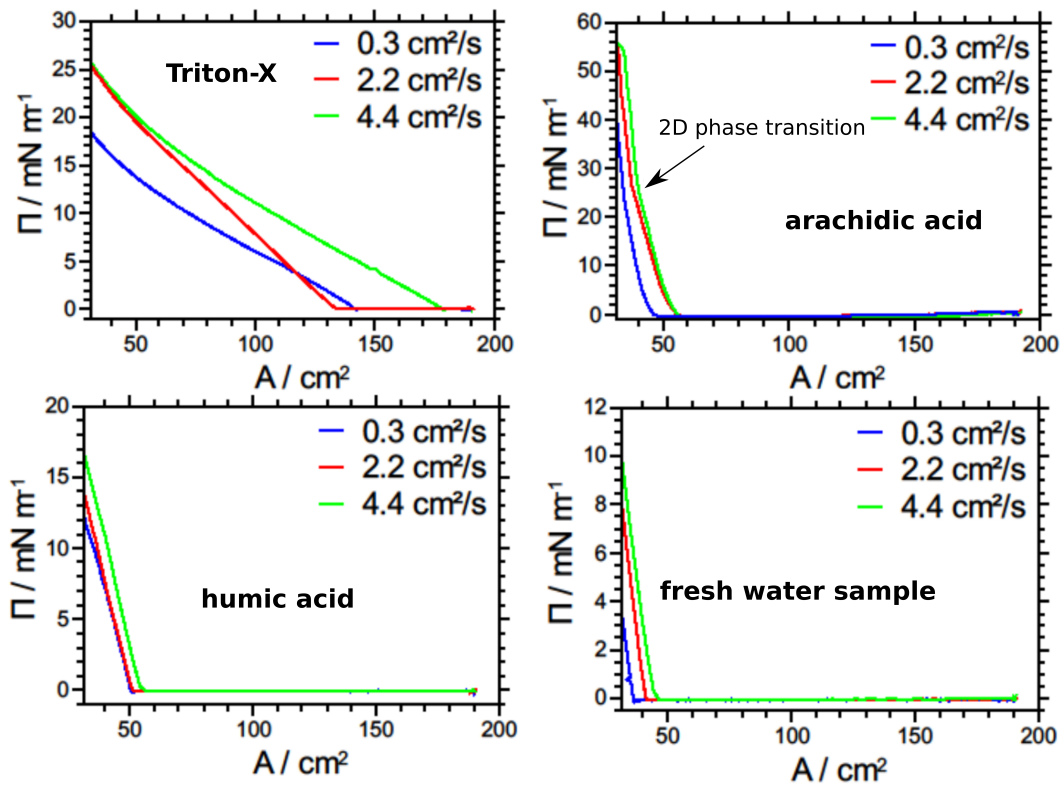


Figure 6.3: Comparison of compression isotherms of different surfactants (soluble and insoluble) and a fresh water sample collected from a pond located on the Kiel university campus. Adapted from Nhat-Thao Ton-Nu's thesis.^[158]

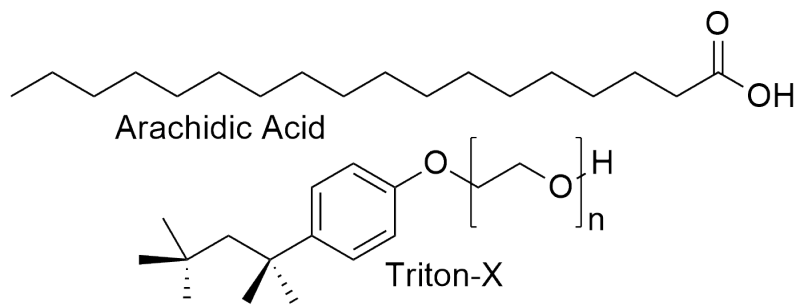


Figure 6.4: Molecular structure representations for the dry surfactant arachidic acid and the wet, polymeric surfactant Triton-X. Humic acid consists a complex and varying amount of polyaromatic compounds and is omitted for simplicity.

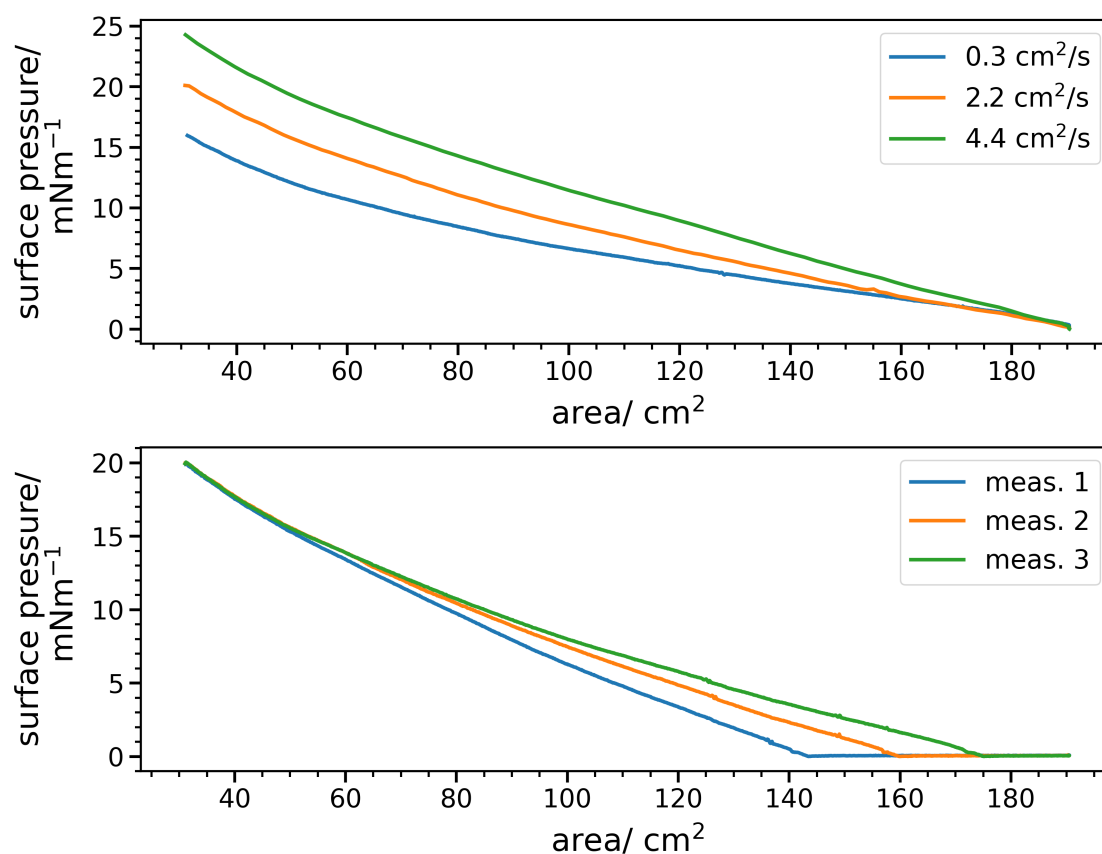


Figure 6.5: Visualization of the behaviour of the artificial wet surfactant Triton-X upon compression at different compression speeds (top) and consecutive compressions at the same speed, here $0.3 \text{ cm}^2 \text{ s}^{-1}$ (bottom).

acid, this exchange with the sub phase might prevent the formation of a dense monolayer and therefore explain the absence of the typical 2D phase transition. On the other hand, the diffusion of the Triton-X molecules from the surface into the bulk may be much slower than the enrichment effect induced by the fast compression, leading to an overall increase in the surface concentration and the formation of a highly compressed mixed layer.

All in all, the preliminary experiments can be summarized as follows:

- Isotherms of natural sea samples are more similar to isotherms of wet than of dry surfactants.
- For wet surfactants, consecutive compression at the given speeds yields a hysteresis effect, showing that the system's equilibration time is rather long.

- Isotherms of mixtures of dry and wet surfactants appear significantly different from isotherms of the pure substances indicating the formation of mixed monolayers or strong near-surface interactions of those compounds.
- Although quite unexpected, wet surfactants yield compression isotherms, even at low compression speeds. This shows that the equilibration with the sub phase is indeed a very slow process such that the accumulation of wet surfactants can be induced by the mechanical compression. In consequence, this effect allows the determination of a lift-off point in analogy to the dry surfactants which can be used as an indicator for the total amount of surfactants present at the surface. Moreover, as the lift-off point is typically related to a surface concentration that corresponds to a fully covered surface, the compression ratio at the lift-off point can be taken as a simple indicator for the surface coverage of the (uncompressed) organic layer- no matter if dry, wet or a mixture of both surfactant classes are present.

6.4 Surfactant abundance indices

Index from VSFG measurements

As the employed analytical techniques are rather complex and a cruise in the context of ocean science is a very interdisciplinary project with the requirement to exchange data between researchers frequently, it is highly desirable to reduce the complexity of the data as much as possible while keeping the most important aspect of information detected from a specific analytical technique. However, the question arises how the VSFG and Langmuir trough measurement results can be related to the presence and amount of surfactants in natural samples. In this context, it is beneficial to reduce the rather complex VSFG spectra and compressions to simple numeric quantities that carry information about the surfactant abundance in the corresponding samples. Therefore, the next paragraphs describe how such surfactant abundance indices (SAI) were obtained from the raw measurements. From VSFG spectra, an index termed the surface coverage sc was calculated according to the following equation:

$$sc = \sqrt{\frac{\int_{2750}^{3000} (I_{\text{Sample}}(\tilde{\nu}) - I_{\text{H}_2\text{O}}(\tilde{\nu})) d\tilde{\nu}}{\int_{2750}^{3000} (I_{\text{Reference}}(\tilde{\nu}) - I_{\text{H}_2\text{O}}(\tilde{\nu})) d\tilde{\nu}}} \quad (6.1)$$

This equation defines the surface coverage as the integral over the CH region of the SFG spectrum normalized to the average DPPC reference integral measured the same day. This definition of the coverage relies on the assumption that a DPPC film with an area per molecule of 40 \AA^2 corresponds to full surface coverage (one monolayer), thus the ratio of the integrated SFG intensities for the DPPC reference and the natural seawater sample reflects the degree of surface coverage ranging from zero (no coverage) to one (full coverage). The intensities of both the reference and the samples were first divided by the product of the corresponding IR and Vis intensity to correct for laser intensity fluctuations (not included in eq. 6.1 where I corresponds to the already corrected intensities) and baseline-corrected to remove additional background SFG intensity caused by the water (indicated by $I_{\text{H}_2\text{O}}$). Because of the square dependence of the SFG signal on the surface concentration, it is necessary to take the square root of the integral ratio. By directly referencing the VSFG intensity to the intensity measured for a well-ordered monolayer, this definition does not account for surface structure effects (i.e the alignment and distribution of the probed surface oscillators with respect to surface normal, see chapter 2). A justification for this rather crude simplification comes from previous work where the VSFG signal has been examined in dependence of the surface coverage for several characteristic peaks, yielding a surprisingly linear correlation.^[105] However, in general VSFG intensity is known to diminish at low surface coverages because of the increased disorder of the interfacial molecules (compare section 2.1.3). Therefore, the surface coverage as defined by eq. 6.1 is prone to a bias towards too low calculated surface coverages at least in the case of very low surface concentrations.

The region of the spectrum which is integrated in order to get the coverage as well as the automatic baseline correction being performed by the Python routine (see chapter 4) is shown in Fig.6.6 for a typical signal.

Index from Langmuir trough measurements

To use Langmuir compression isotherms as indicator for the amount of surfactants, the maximum surface pressure of the measurement and the so-called "lift-off point" can be used. On the one hand, the maximum surface pressure is simply the highest value the surface pressure reached during the compression.

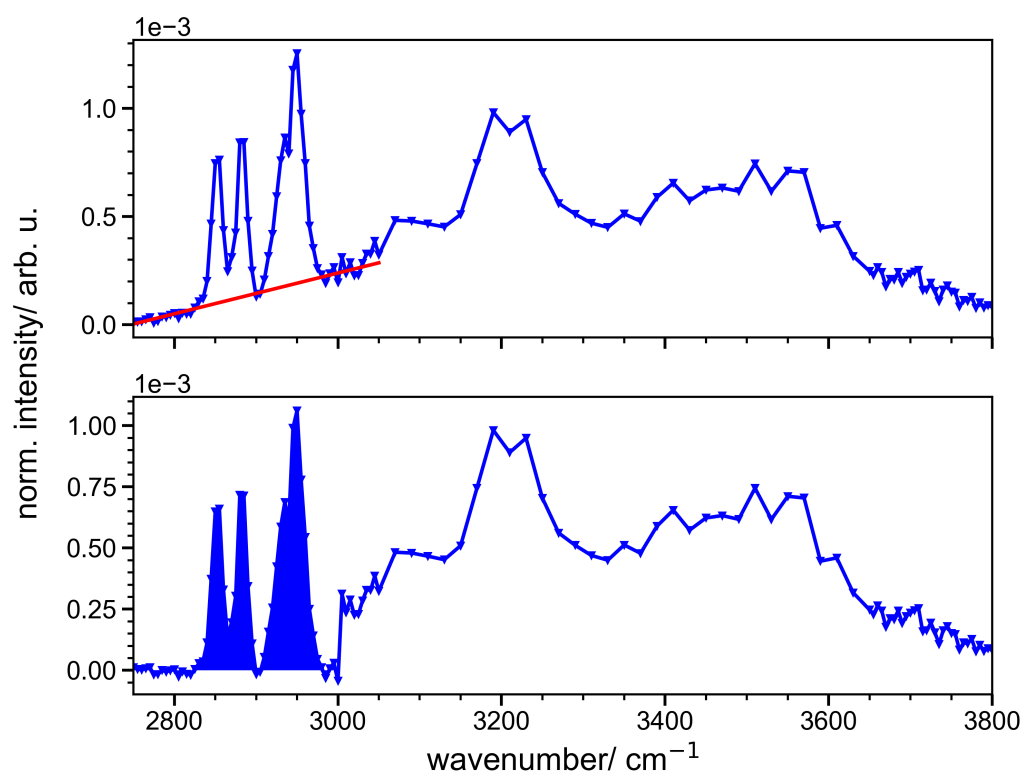


Figure 6.6: SFG spectrum of a natural seawater sample with some signal in the aliphatic CH region. The upper subfigure demonstrates the automatic baseline correction, the lower indicates the region of the spectrum that is integrated to obtain the surface coverage.

As the presence of surfactants lowers the surface tension and therefore increases the surface pressure, a high maximum surface pressure corresponds to a high amount of surfactants. On the other hand, the lift-off point is defined as the point in the isotherm from which the surface pressure starts to increase upon further compression. In a simplified model view it can be assumed that as soon as there is full coverage of the surface with surfactants, the surface pressure starts to increase if the system is compressed further. This qualifies the lift-off point as index for the amount of surfactants on the surface. Both the lift-off point and maximum surface pressure are specified in the example shown in Fig. 6.7. The isotherms selected for this figure were recorded during the analysis of the Baltic GasEx cruise data and therefore are typical examples for natural sea sample isotherms. The isotherm depicted in red shows a step increase in sur-

face pressure after the lift-off point, reaching a relatively high maximum surface pressure above 15 mN m^{-1} . Such a high surface pressure was only observed in few cases and was interpreted as a relatively high amount of surfactants. Much more often, isotherms like the one depicted in green were observed. The lift-off point occurred nearly at the end of the compression range of the trough barriers, meaning that the formed layer was not completely compressed at the end of the measurement, hence not reaching high maximum values. Finally, the blue isotherm indicates a situation with no measurable surfactant concentration. Even at the highest possible compression ratio, no increase in surface pressure could be observed. This occurred typically for water samples taken from higher depths.

Index from surface tension measurements

The salinity-corrected surface tension obtained via tensiometry was used without any further modification as a measure for surfactant abundance since a decrease in surface tension is a direct indicator for surfactant presence. Note that there is a difference in the dynamic range of detectable values for the different techniques whereas a strong effect on surface tension can only be expected if a large part of the surface is already covered by a surfactant layer, VSFG offers sub-monolayer sensitivity but may be somewhat biased at low surface coverages due to the structural effect mentioned above. The LANGMUIR trough, relying on measuring the surface tension as well, makes use of an artificial upconcentration of the surfactants at the surface by the compression. For the trough model used in this work, the maximum compression ratio is sc ,

$$sc = \frac{27 \text{ cm}^2}{190 \text{ cm}^2} = 0.13$$

which is equal to an enhancement of the surface concentration by a factor of 7. This means that even for surfactant concentrations in a magnitude where they are "invisible" for a surface tension measurement in uncompressed state, recording of a compression isotherm may indicate their presence down to a surface coverage of $sc=0.13$.

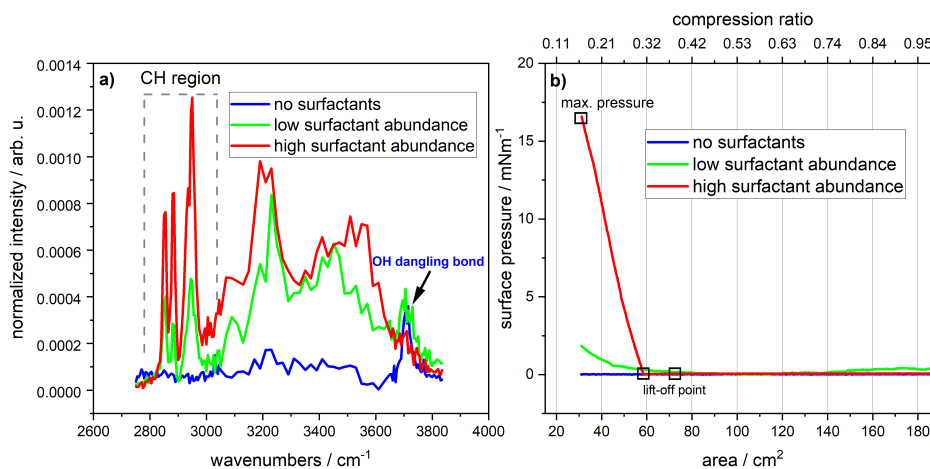


Figure 6.7: Demonstration of the characteristic features of VSFG spectra and compression isotherms that have been employed for the calculation of the SAI at three different levels of surfactant abundance (no surfactants, low concentration, high concentration).

6.5 Cruise data

As the collection of samples took place under various conditions it is useful to carefully examine the differences between and the distribution of the resulting values for the four SAI obtained from different types of samples. The sample category pairs treated in this analysis are the following:

- samples collected by the glass plate and samples collected by the screen
- samples collected from the zodiac and samples collected directly from the research vessel "Alkor"
- bulk water samples and SML samples
- samples collected during cruise 1 and samples collected during cruise 2

An overview about the number of samples present in each category is given in Tab. 6.3. In addition to the total count, numbers how many of the samples have been investigated by the respective techniques are given for each category.

Table 6.3: Overview about the total numbers of samples and measured samples grouped by cruise and sample category. The number of samples which were analyzed by the corresponding techniques are given in the column **n (method)**. In **n (lift-off)** the number of samples with a detectable lift-off point is reported (corresponding to $sc > 0.13$).

cruise	category	total	n (coverage)	n (tension)	n (isotherm)	n (lift-off)
1	plate	54	54	48	33	9
	screen	67	65	59	36	9
	Alkor	29	29	24	4	0
	zodiac	92	90	83	65	18
	bulk	18	18	15	1	0
2	plate	53	52	43	50	11
	screen	59	59	49	54	21
	Alkor	22	22	15	19	6
	zodiac	90	89	77	85	26
	bulk	17	17	15	16	0

To compare those category pairs, two steps of analysis have been performed: The data sets were visualized using a box plot to illustrate the distribution, mean and median of the values side-by-side and a MANN-WHITNEY-U-test¹ test has been utilized to test for the null hypothesis H_0 of equal mean of each of the SAI. With this procedure it was possible to identify similarities and differences between the various sample categories.

6.5.1 Comparison between the cruises

Because preliminary VSFG long-term studies at the Boknis Eck time series station have indicated an annual variation of the surfactant abundance in the microlayer, the two GasEx cruises were scheduled to potentially coincide with different states of the annual surfactant cycle, resulting in a significant difference in SML surfactant concentration.

Fig. 6.8 and 6.9 visualize, on a day-of-the-year x scale, the average data per station calculated from the SML samples (plate and screen samples were combined). The scatter points represent the resulting mean values for each station, the error bars show the standard deviation. As there was only one bulk water sample, no

¹ A statistical test for the null hypothesis of equal mean of two independent sets of values which are not normal-distributed. All data sets have failed the SHAPIRO-WILKS test for normal distribution, so a regular t -test was not suitable

averaging was performed for those and therefore no error bars are provided. Fig. 6.8 illustrates the course of the surface coverage and the surface tension. The values for the surface coverage as determined from VSFG data are in general quite low, typically below 0.2 and the difference between SML and bulk samples does not appear significant. No obvious trend of the surface coverage appeared during the course of the cruise. For the surface tension, the variation between the individual samples collected at one station (indicated by the error bars) are too high to postulate any significant day-to-day variation during the cruise.

The results of the Langmuir trough measurement of the maximum surface pressure and the lift-off compression ratio are shown in Fig. 6.9. In comparison to the surface tension and VSFG coverage measurements, the error bars (and therefore the differences between the samples of a single station) are even more prominent. In many cases, only one or two of the SML samples from one station showed a significant increase in surface pressure upon compression while the others remained close to zero. A significant difference is, however, detectable between the values for bulk samples in comparison to SML samples. As seen from the averaged values (dashed horizontal lines) from the second cruise, the surface pressures are in general much lower. Actually, in no case of a lift-off point was detected for the bulk water samples. This is remarkable because surface tension and VSFG coverage data did not allow for such a clear distinction was found. Note that, however, during the first cruise only one isotherm of bulk water samples was measured (see Tab. 6.3), hence a comparison is only valid for the data from the second cruise.

To further examine if there is any statistical difference between the cruises, the SAI for SML and bulk samples have been examined by visualization in a box plot and a MANN-WHITNEY-U-test for equal mean has been performed. Here, in the data shown in 6.8 and 6.9, no averaging per station was performed but all single data points have been used. The resulting plot is shown in Fig. 6.10. The boxes (representing 50% of the data points, lower and upper quartile) for the surface tension and coverage are small, indicating that the vast majority of the measured value was in this range. However, in particular the SML data for the max. surface pressure contained many data points with significantly higher values, depicted as dots above the box. Because of their relatively small number and their large distance to the median of the distribution, they could be statistically classified as "outliers" and therefore shown beyond the whiskers (identified by

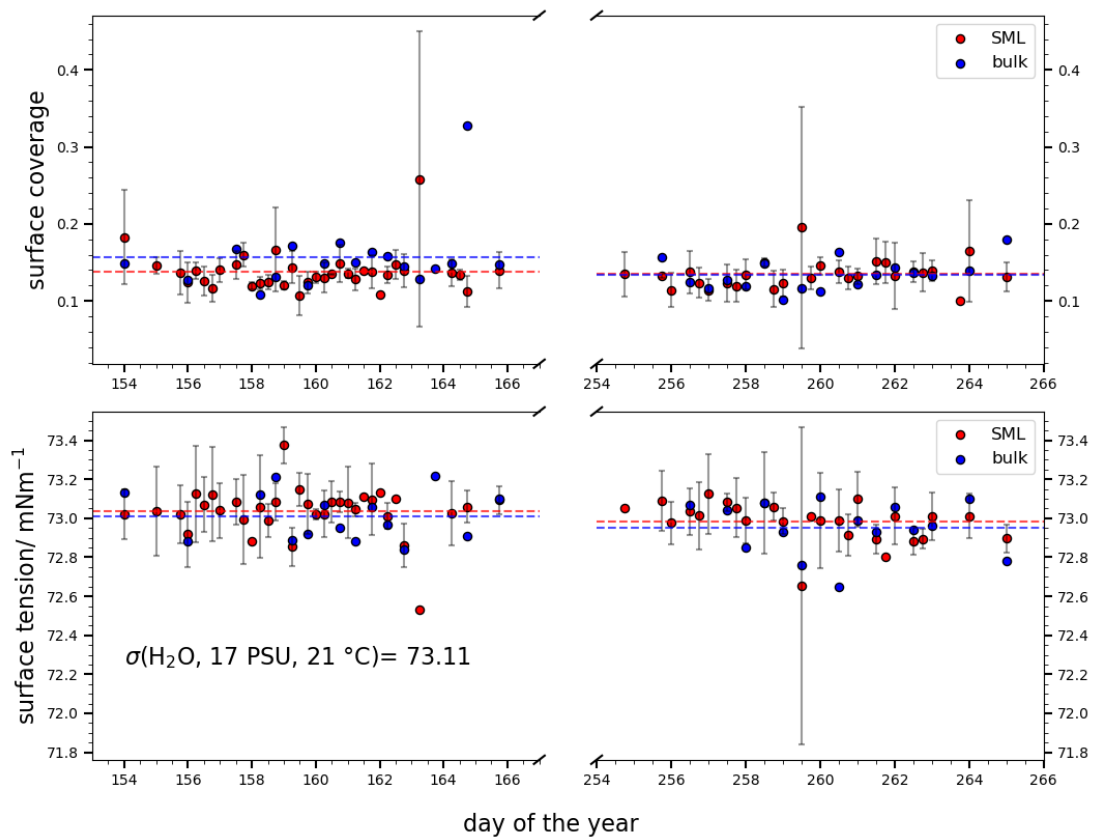


Figure 6.8: Plot of the surface coverage (measured by VSFG) and surface tension as function of the day of the year. The values are calculated as per-station average of all samples of one category (either SML, indicated in red, or bulk, indicated in blue) with the standard deviation of this average shown as error bar. The cruise means are indicated as the thick dashed horizontal lines. The stated theoretical value for the surface tension was calculated from the relations derived by *Nayar et al.*^[110]

the 1.5 inter-quartile range of the data) of the box plot. Here, it is assumed that there is a physical relevance of those measured surface pressures and therefore they were retained for the interpretation of the data. None of the isotherms of any bulk sample had a visible lift-off point, so no boxes for the bulk samples appear in the corresponding subplot. Looking at the difference between both the cruises, at first glance the boxes (C1, SML vs. C2, SML etc.) mostly overlap, indicating that the variation between the values is not significant. This visual impression is actually not confirmed by the results of the MANN-WHITNEY-U presented in Tab. 6.4. Only the p -values for the surface tension indicated that the null hypothesis H_0 of equal mean between the cruises has to be accepted. In the case of the SML, the hypothesis had to be rejected for the surface pressure and

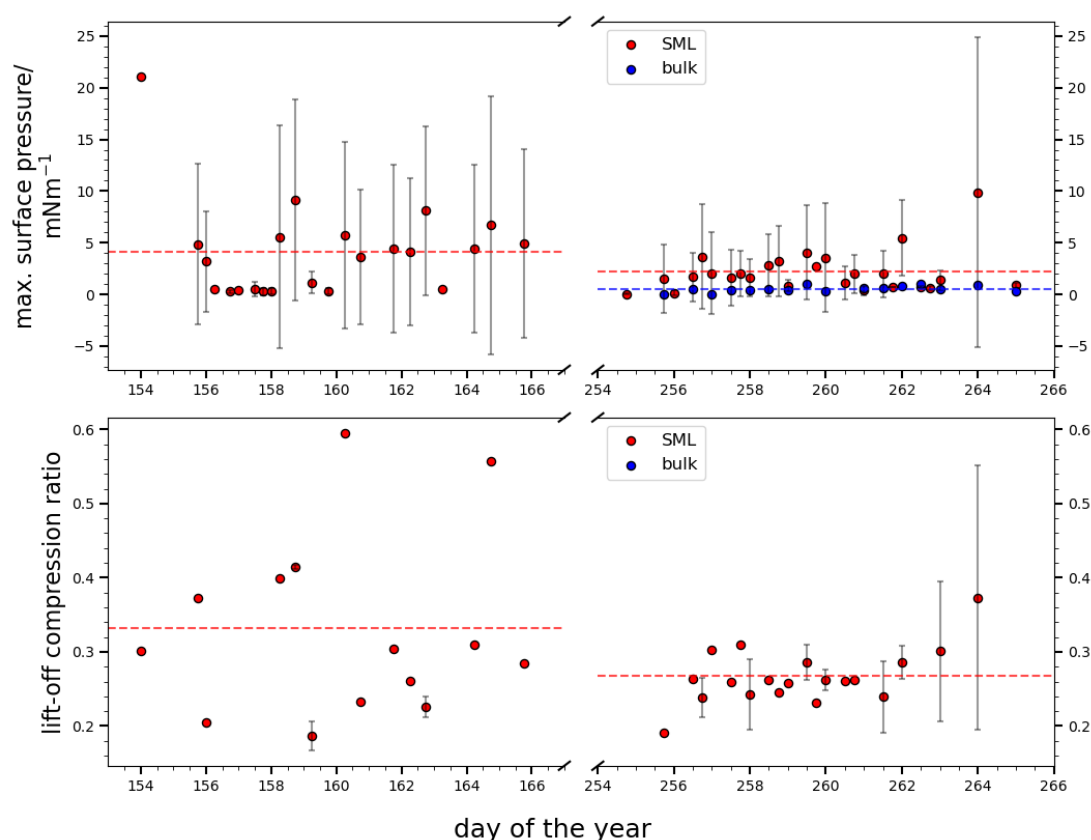


Figure 6.9: Plot of the max. surface pressure and lift-off compression ratio as function of the day of the year. The values are calculated as per-station average of all samples of one category (either SML, indicated in red, or bulk, indicated in blue) with the standard deviation of this average as denoted error bar. The cruise means are indicated as the thick dashed horizontal lines.

lift-off ratio values. For the bulk, this was the case for the surface coverage. Although not all SAI are significantly different, these findings could be taken as an indication for a slight difference in surfactant concentration for both the cruises, with the second cruise being lower in surfactant abundance. Note, however, that this finding of the generally low surfactant abundance during both cruises that was difficult to detect with the employed techniques. It remains to be seen if a detectable correlation of the surfactant abundance and the gas transfer rate (the data is targeting this issue have not yet been evaluated) and if the results of the complementary AC voltammetry measurements conducted by another group (also not made available yet) comply with the result of this work.

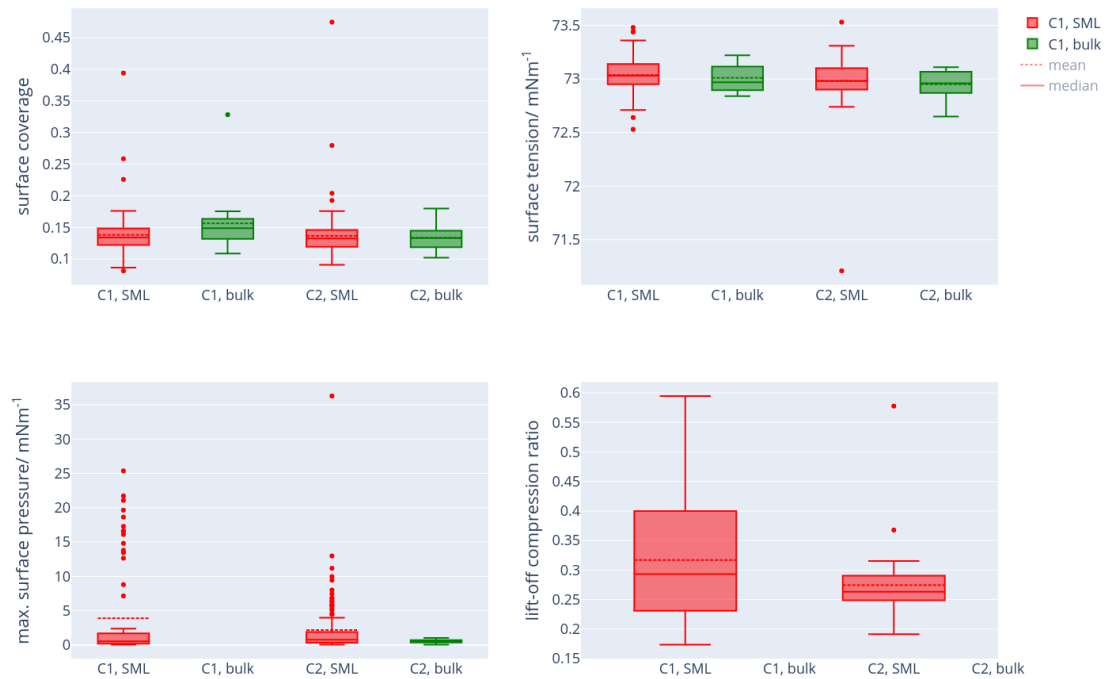


Figure 6.10: Box plots of the four SAI grouped by category (SML and bulk water samples) and cruise. SML samples are indicated in red, bulk samples are indicated in green. The mean and median values are indicated by a dotted and a solid line, respectively.

Table 6.4: Statistical analysis of the SML SAI quantity means by a MANN-WHITNEY-U-test. Comparison between the SML samples from cruise 1 vs. SML samples from cruise 2 and the same comparison for the bulk. H_0 is the null hypothesis, i.e. equal mean of surface tension of SML and bulk water samples.

category	quantity	statistics	p -value	H_0 accepted
SML	surf. tension	6387	0.22	y
	surf. coverage	6321	0.19	y
	max. surf. press.	4625	$1.4 \cdot 10^{-5}$	n
	lift-off ratio	1970	$4.4 \cdot 10^{-5}$	n
bulk	surf. tension	125	0.177	y
	surf. coverage	88	0.02	n
	max. surf press.	-	-	-
	lift-off ratio	-	-	-

6.5.2 Plate and screen sampling comparison

Sampling of the SML with the GARRETT screen and the glass plate are both well-established widely used sampling techniques in sea-surface science. However, because of the physical mechanisms, the chemical characteristics of the sampler surface and the depth up to which the water is sampled there might be differences in the composition and the detected abundance of the surfactants. To examine whether those effects are of relevance in the context of this cruise, samples collected by the screen and glass plate are compared by means of a box plot and MANN-WHITNEY-U-tests for all four SAI. The results of the statistical analysis are described in tab 6.6. For the first cruise, the p - values indicate equal means for all the SAI except for the lift-off compression ratio, indicating that under the conditions of the cruise no significant difference between both sampling techniques was observed. For the second cruise, the means for the parameters of max. surface pressure as well as lift-off compression ratio were found to be of distinct mean on 5 % significance level. This is an interesting finding that could indicate a higher sensitivity for lower surfactant abundances of the LANGMUIR trough since the surface tension and coverage are still of equal mean. How small the differences are is visible from the box plot depicted in Fig. 6.12. The distribution of values looks very similar in the case of the surface tension, coverage and compression ratio, only the boxes for the max. surface pressure of the second cruise appear distinct from each other with the screen samples showing slightly higher pressures.

In SML research, it is very common to express differences in (chemical or biological) observables in terms of the enrichment factor (EF) which is usually defined as the ratio of the SML value of the quantity and the bulk value of the quantity. If the resulting number is greater than one, the corresponding observable (e.g. surfactant concentration) is considered enriched in the SML. To allow a comparison with the results of other SML investigations and see if the SML sampling method leads to a difference in enrichment, for each station the ratios of the SAI obtained from plate and screen sampling have been divided by the corresponding bulk value, in analogy to the EF calculation. The results of this calculation are displayed in Fig. 6.11. As for no bulk sample a measurable lift-off point was detected, the lift-off compression ratios are not evaluated here. For both the surface tension and the coverage obtained by VSFG the resulting

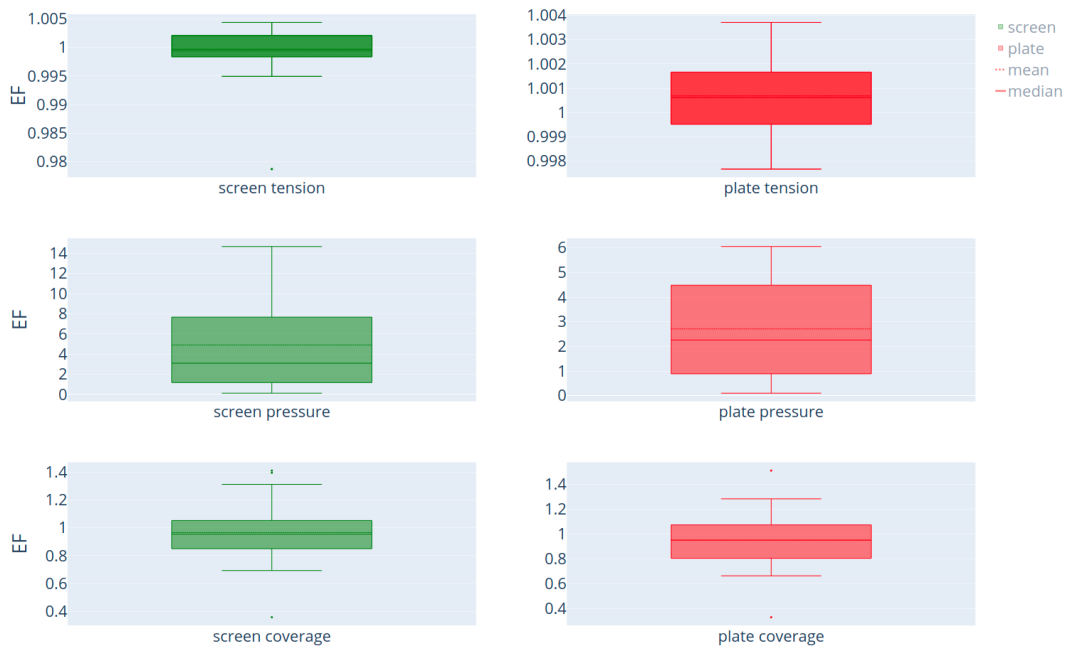


Figure 6.11: Illustration of "enrichment factors" (EF), obtained (per station) i.e. the ratio of the station average SAI values of plate and screen samples and the corresponding bulk water sample values.

enrichment factors are very close to one. For the surface pressure, the variance is much broader with values between 1-8. Plate and screen sampling did not yield a significant EF difference in all three SAI, as confirmed by the MANN-WHITNEY-U test (see Tab. C.1) Note, however, that a calculation of the EF based on surface tension may be not reasonable since the surface tension is not directly proportional to the surfactant concentration. It should be considered in this context only as a simple measure between the difference in surface tension between bulk and SML.

Table 6.5: Results of the MANN-WHITNEY-U test for equal mean for the enrichment factors of plate and screen sampling. The null hypothesis H_0 of equal mean is accepted if the p value is higher than the significance level than 0.05.

enrichment factor 1	enrichment factor 2	statistics	p-value
tension (plate)	tension (screen)	306	0.11
surf. pressure (plate)	surf. pressure (screen)	78	0.12
coverage (plate)	coverage (screen)	500	0.44

This is comparable to the observations made by Guitart *et al.* where the enrichment factor of polycyclic aromatic hydrocarbons (as a proxy for soluble

SML organics in general) has been investigated by applying both screen and plate sampling, yielding no significant EF difference between those techniques.^[159] In addition, the calculated EF values are comparable to enrichment factors of carbohydrates at Boknis Eck reported by Engel *et al.* where the found mean values were slightly greater than one.^[160]

Table 6.6: Statistical analysis of the SML SAI means by a MANN-WHITNEY-U-test: Comparison of plate and screen samples grouped by the cruises.

cruise	quantity	statistics	<i>p</i>-value	H_0 accepted
1	surf. tension	1754	0.39	y
	surf. coverage	1543	0.08	y
	max. surf. press.	1721	0.32	y
	lift-off ratio	831	$1.744 \cdot 10^{-7}$	n
2	surf. tension	1355	0.11	y
	surf. coverage	1431	0.22	y
	max. surf. press.	1215	0.02	n
	lift-off ratio	650	$5.7 \cdot 10^{-8}$	n

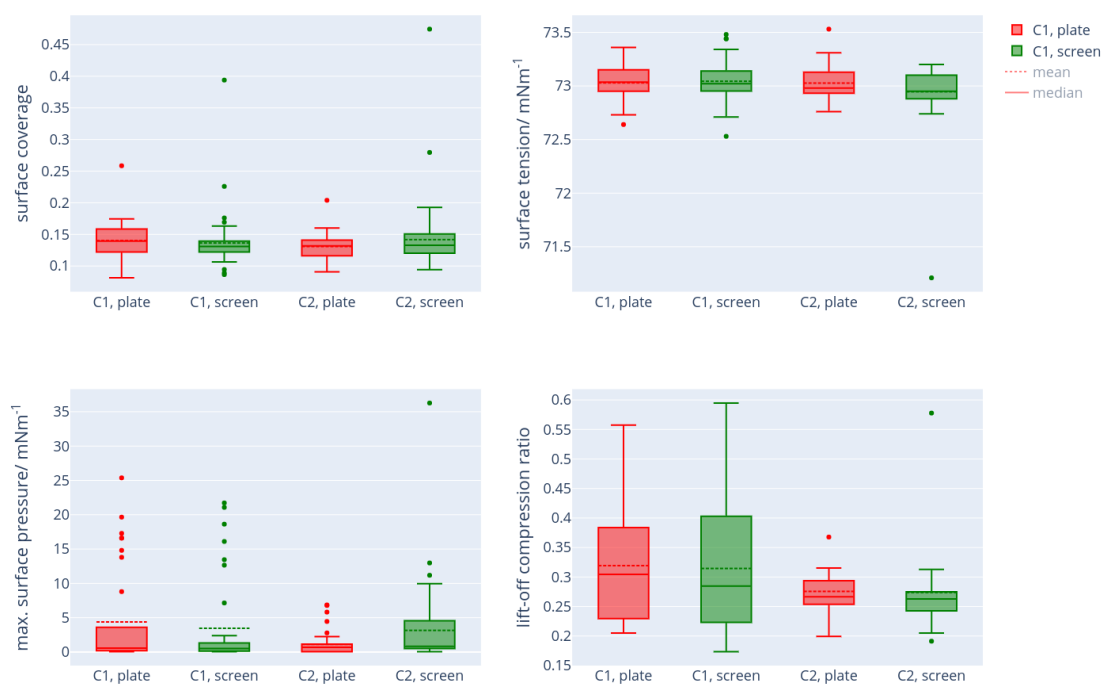


Figure 6.12: Box plots of the four SAI grouped by category (plate and screen SML samples) and cruise. Plate samples are indicated in red, bulk screen are indicated in green. The mean and median values are marked by a dotted and a solid line, respectively.

6.5.3 Comparison between zodiac- and ship-based sampling

It is often considered being problematic to sample the SML directly from ship because of potential contamination caused by the vessel itself (oil, waste...)^[40] Consequently, within this section a comparison of the samples taken from board of the Alkor (as performed during small stations) and the samples taken from the zodiac is drawn. Box plots of the four SAI and grouped by the respective cruise and the location of sampling (Alkor vs. zodiac) are presented in Fig. 6.13. Regarding the surface tension and the surface coverage, the values fall in the same range and, except for some outliers, the box plots appear very similar. With respect to the max. surface pressure and the lift-off compression ratio, the situation is different. During the first cruise, only four isotherms of samples from the Alkor have been collected, so the sample size is too low for a reasonable statistical comparison and the obvious difference in the shape of

the box plot is not meaningful. During the second cruise, however, more Alkor samples have been analyzed by means of the Langmuir trough. Here, the box plots overlap except for some outliers present in the zodiac samples. For the lift-off compression ratio, the same constraints apply: the sample size during the first cruise was extremely small and in addition, none of these four had an observable lift-off point, therefore no box plot could be drawn. Although the boxes of the data from the second cruise do not overlap as clear as in the case of the surface coverage or tension, a MANN-WHITNEY-U-test of the hypothesis of equal means between the lift-off compression ratio of samples taken during cruise 2 from Alkor and the zodiac could not be rejected at the significance level of 5 %. The statistical tests were performed for all pairs of the SAI and the result of this analysis is presented in Tab. 6.7. Except for the surface pressure and coverage during cruise 1 (where the pressure value has to be treated with caution because of the low sample size), and the missing value for lift-off compression ratio during cruise one, the null hypothesis of equal means has to be accepted. From this data it is not clear if there is a difference between the samples taken from the zodiac in comparison with those collected directly from board of the Alkor, especially because of the different results for the first and the second cruise. What can be safely stated is that if there is a difference, it is not a big one-contamination stemming from the ship was not a problem here. In summary, contamination from the ship does not seem to be a relevant problem, although the surfactant presence was very low.

Table 6.7: Statistical analysis of the SML coverage SAI means by a MANN-WHITNEY-U-test: Comparison of samples taken from the ship and samples taken from the zodiac grouped by the cruises.

cruise	quantity	statistics	<i>p</i>-value	H_0 accepted
1	surf. tension	1076	0.06	y
	surf. coverage	1009	0.02	n
	surf. press.	852	0.001	n
	lift-off ratio	-	-	-
2	surf. tension	857	0.17	y
	surf. coverage	811	0.1	y
	surf press.	973	0.45	y
	lift-off ratio	668	0.01	n

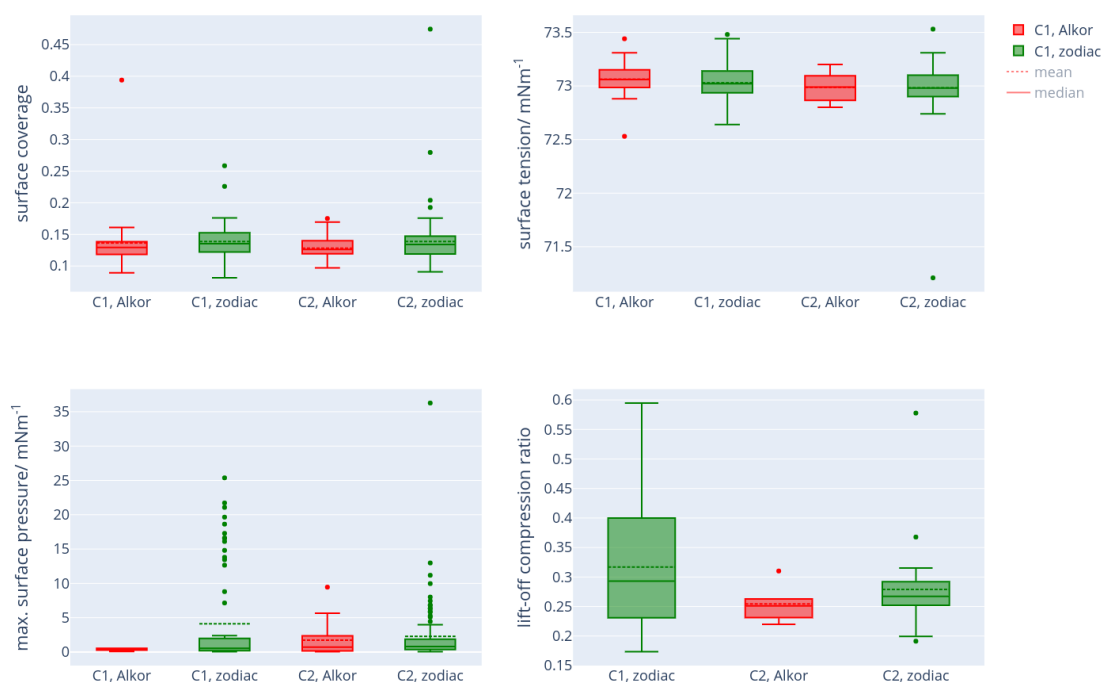


Figure 6.13: Box plots of the four SAI grouped by category (SML samples taken from the zodiac and from the Alkor) and cruise. Samples collected from board of the Alkor are indicated in red, zodiac samples are indicated in green. The mean and median values are visualized by a dotted and a solid line, respectively.

6.5.4 SML and bulk water comparison

As it is assumed that surfactants accumulate at the surface, a difference in the surfactant SAI between SML and bulk water samples would be expected. The intuitive visualization of the value distribution of the two sample categories has already been presented in Fig. 6.10. The corresponding MANN-WHITNEY-U-test analysis of those results are presented in 6.8. For the surface tension, neither during cruise 1 nor cruise 2, a significant difference between the means of bulk water and microlayer samples could be determined. For the second cruise, the difference in the means of max. surface pressure was found to be statistically significant and, as not a single bulk water sample exhibited a measurable lift-off point, although the statistical test could not be performed, but this is an obvious difference between the two sample types. Also, the surface coverage was found to be significantly different between bulk and SML for the first cruise,

but not for the second. Those data gives rise to the assumption that, at surfactant abundances as low as during those cruises, the experimental methods that leave the surface "as it is", hence without artificial concentration at the interface like it is done during isotherm compression, are not well-suited to distinguish between SML and bulk water samples and detect any enrichment. However, with caution, the hypothesis of surfactant enrichment at the sea surface seems to be supported by the fact that none of the bulk water sample showed a significant surface pressure upon compression.

Table 6.8: Statistical analysis of the SML SAI means by a MANN-WHITNEY-U-test: Comparison of SML and bulk water samples grouped by the cruises.

cruise	quantity	statistics	<i>p</i>-value	H_0 accepted
1	surf. tension	1032	0.36	y
	surf. coverage	731	0.01	n
	max. surf. press.	-	-	-
	lift-off ratio	-	-	-
2	surf. tension	778	0.11	y
	surf. coverage	948	0.5	y
	max. surf press.	647	0.02	n
	lift-off ratio	-	-	-

6.6 Inter-comparability of different indices for surfactant abundance

As for each sample multiple independent measurements with complementary methods providing quantitative measures for the amount of surfactants have been performed, it is of interest to analyze the data with respect to a correlation between those parameters. Since those methods target different physical properties it is not guaranteed that the information is translated one to one among them. As mentioned before, the overall low signal makes the analysis difficult and the results have to be interpreted with care. Nevertheless, all data has been analyzed with respect to the four SAI (surface coverage determined by SFG, max. surface pressure and lift-off point determined by Langmuir compression isotherms and surface tension) visually by means of a plot and numerically by employing the PEARSON correlation coefficient. The latter is a statistical measure for the degree of correlation between two datasets and can take values from -1 (strong negative correlation) to 1 (strong positive correlation). All this information is presented in terms of a scatter matrix plot in Fig. 6.14.

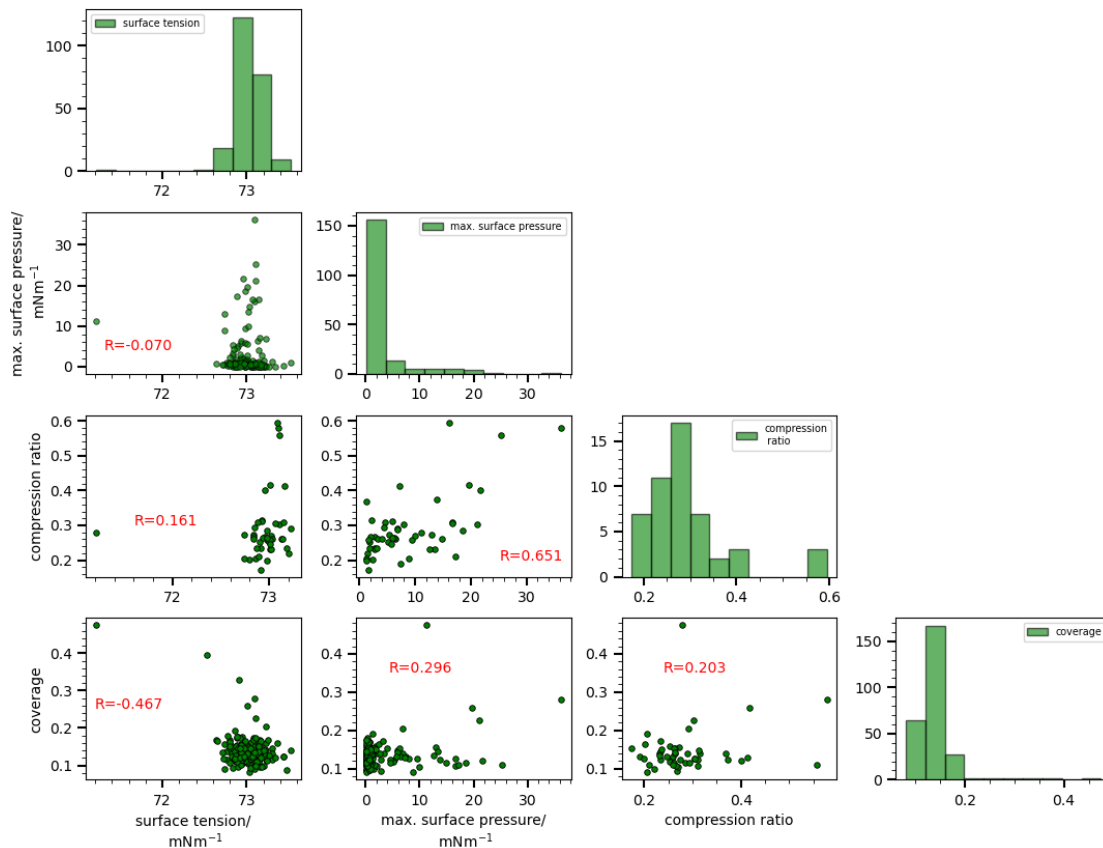


Figure 6.14: Correlation plots of the four SAI. Red indicates the PEARSON correlation coefficient between the displayed quantities which is a measure for the degree of linear correlation.

Distribution of the values (histograms)

The surface tension (first element of the main diagonal) in Fig. 6.14 is distributed within a small window of values between 72.5 and 73.4 mN m^{-1} with few measurements outside this range. The distribution is relatively symmetric with a median of approx. 73- 73.2 mN m^{-1} . The maximum surface pressure (second element) values cluster in the regime of low surface pressure (ca. 0-3 mN m^{-1}) and only few measurements exceed this value significantly, resulting in an asymmetric distribution of values. Measurement results for the lift-off compression ratio are close to a normal distribution around a mean of 0.28. However, it has to be taken into account that only a fraction of the samples exhibited a detectable lift-off point (see Tab. 6.3), so the number of data is lower than in the other histograms. Surprisingly, some values lay out of this range at significantly higher compression ratios of ca. 0.56 which corresponds to a very early lift-off.

Surface coverage values typically fall in the range of 0.06 - 0.19 with a strong accumulation at ca. 0.13, corresponding to a surface coverage of 13 %. Note that such low surface concentrations are hard to detect by VSFG because of the square dependency of the signal level.

Surface coverage vs. surface tension

The correlation between surface coverage as determined from VSFG measurements and the surface tension is relatively weak with a PEARSON coefficient of ca. -0.47. The negative coefficient is consistent with the expectation, where a higher value of the surface coverage leads to a decrease in surface tension.

Surface coverage vs. max. surface pressure

With a coefficient of ca. 0.3, this correlation is weak and the scatter plot exhibits a rather wide, blurry distribution of the points. Based on this data it is not possible to proof an interrelationship between those quantities.

Surface coverage vs. lift-off compression ratio

The scatter plot of this relation is far from being straight and the PEARSON coefficient of 0.2 supports that those two quantities do not correlate.

Surface tension vs. max. surface pressure

With a coefficient of 0.07, this correlation is the weakest of all examined ones which means that there is, from a statistical point of view, no connection between the surface tension and the max. surface pressure as determined by compression isotherm measurements. The scatter plot appears as blurry cloud and is far from showing a linear dependence.

Surface tension vs. lift-off compression ratio

The correlation between the lift-off compression ratio and the surface tension is again a very weak one ($r = 0.161$). As the lift-off point could only be determined for the subset of the samples which show a measurable increase in surface pressure, it is no surprise that those quantities are statistically not linked, since the correlation with the max. surface pressure is extremely weak.

Max. surface pressure vs. lift-off compression ratio

The strongest correlation in this set has been found between the max. surface pressure and the lift-off compression ratio ($r = 0.651$). Despite considerable scatter, this plot is the one closest to a linear relation. This is not unexpected, as only samples with a measurable surface pressure exhibit a lift-off point. In addition, it is reasonable that samples with a high compression ratio ($\hat{=}$ early lift-off point) corresponds to higher mean values of the max. pressure as there is a higher free area range from the appearance of the first increase in surface pressure.

6.7 Conclusion and outlook

It can be stated that during both cruises the amount of surfactants, at least with respect to the detection limit of the applied methods, have been quite low and often close to the detection limit. Only in few cases a concentration was high enough to yield VSFG signal with clear spectral signatures in CH region. Even upon surface compression, in many cases the surface pressure did not show any increase. There is some statistical evidence for a small difference in surfactant abundance between both the cruises with slightly higher values in the first one. What is remarkable is that none of the water samples taken from the depth showed any significant increase in surface tension nor a detectable lift-off point. This finding indicates that the overall surfactant concentration in bulk water samples was even lower than in the SML, which supports the models stating an enrichment in the surface layers. Neither a great differences between plate and screen sampling (except for a deviation of the surface pressure and lift-off compression ratio in the second cruise) nor between a direct sampling from the ship and from a zodiac in a certain distance to the ship could be confirmed. All in all, it seems to be beneficial to apply those complementary techniques resulting in different SAI in order to get a more complete picture of the nature of the complex SML samples. For the purpose of communication with other researches in this highly interdisciplinary research field it is useful to utilize this simple numeric values instead of reporting the complete spectra and isotherms to simplify batch data analysis, correlation with other oceanographic parameters and knowledge transfer. As a future perspective it would be highly desirable to repeat this set of experiments in a situation with significantly higher surfactant abundance to check if the findings from this work hold true under those conditions as

well. Also, a correlation of this results with other complementary SML sampling techniques such as AC voltammetry is necessary to get a broader database and understanding of the sample nature. Finally, it would be reasonable to evaluate numerical relations between the SAI as presented here and gas transfer velocities obtained *in situ* parallel to the SML sampling. If such a relation exists, it could probably be used to advance the phenomenological understanding of the surfactant influence on sea-air gas transfer and parameterize those processes in theoretical models.

Part II

Systems of artificial photosensitizers

CHAPTER 7

Benzoylbenzoic Acid Hydroxyalkyl Esters as a Class of Surface-Active Photosensitizers at the Air-Water Interface

7.1 Abstract

The air-sea interface is one of the largest interfaces on earth. It is a region of active photo-chemical processes due to its direct exposure to the solar radiation and enrichment with tenside-like organic compounds. Because of the significant difference in chemical and physical properties interfacial photochemical reaction mechanisms may differ from the bulk leading to unexpected products. Reactions at the very interface are difficult to study with conventional analytic techniques and therefore little is known about the mechanistic details of the interface photochemistry. In this work, a novel class of surface-active photosensitizers is introduced. The benzoylbenzoic acid hydroxyalkyl esters with long alkyl chains (termed BX compounds) form LANGMUIR-BLODGETT-Films at the air-water interface and as such can be used to initiate photochemistry directly at the interface. BX can be obtained by a simple esterification reaction of a tenside spacer with the well-known photosensitizer moiety benzoylbenzoic acid. Characterization of the surface properties is accomplished by means of surface-selective vibrational sum frequency laser spectroscopy. These measurements reveal remarkably strong signals, indicating a high degree of molecular order in the surfactant monolayer. Moreover, photolysis experiments with visible light revealed the photochemical activity of the substance leading to a complete destruction of the film on a minute timescale. hence ideal for future experiments.

7.2 Introduction

The sea surface microlayer (SML) is defined as the uppermost 1000 micrometers of the sea at the air-water interface.^[3,16] In comparison to the bulk, the SML ex-

hibits very special physical, chemical and biological properties.^[2,24] It is enriched with organic substances like lipids, polysaccharides, proteins and amino acids. The SML changes the viscoelastic properties of the sea surface and influences the gas transfer between the ocean and the atmosphere.^[12,45] Field experiments have shown that a significant part of the world's ocean is covered by this organic film.^[16] Therefore, the question arises to what extent these films impact global-scale environmental processes. Because of the proximity to the very interface the amount of solar radiation the SML is exposed to is higher than within the bulk water. The combination of a relatively high concentration of organic substrates and significant energy uptake by light suggest that photochemistry might play an important role in the chemical fate and dynamics of the SML. Furthermore, understanding those processes is also important when it comes to photochemistry of organic compounds in aerosols. Marine aerosols can contain big fractions of organic surfactants,^[35] exhibit high surface-to-volume ratios and are directly exposed to solar radiation.^[34,161] Besides this, the photosynthetic centers of autotroph organisms often employ membrane-bound chromophors and are therefore interface-dominated systems. Gaining insight in mechanistic details of interface photochemistry may contribute to the understanding of those important biological membrane reactions as well.

Photochemistry at the sea-water interface can be induced by different molecules. The photochemical production of reactive halogen species from dissolved anions at the sea surface has been studied for several years.^[54,162,163] Besides those, a fraction of the organic material enriched in the interface layer is known to absorb sunlight in the visible range and may act as direct photosensitizer. The most important substance classes exhibiting those properties are quinones, phenols, chlorophylls and different kinds of carbonyl compounds.^[49] Especially the photochemistry of aromatic ketones, in particular derivatives of benzophenone, is widely used as a model system to understand the processes occurring in natural systems. They can undergo a variety of different photochemical reactions (see section 2.3.2) such as NORRISH type I and type II reactions, YANG cyclizations and indirect sensitization by production of singlet oxygen.^[49,53,62,164] Recent studies indicate that the occurrence of unusual unsaturated compounds and high molecular weight radical recombination products is the result of interface specific photochemical reaction pathways leading to unique products that are different from the products of the bulk reaction.^[52] The accessibility of the sub-

strates from both the gas and the liquid phase, the weaker interaction with the solvent in comparison to the bulk as well as the high density of molecules in the surface film form a unique reaction system.^[49] In particular, reaction mechanisms involving intermolecular hydrogen abstraction by excited states are more likely to occur if the sensitizer is surrounded by alkyl chains of reactant molecules in contrast to a solvent-separated arrangement.

Interface photochemistry was found to be one of the major sources of volatile organic compounds (VOC) in the atmosphere^[74], even compounds like isoprene^[67] were identified as products of such processes. Besides the primary photochemical processes occurring in the SML, their products are discussed to significantly contribute to the formation of secondary organic aerosol particles.^[165] A comparison of photolysis products of natural surface samples with artificial mixtures resulted in similar composition.^[69]

The general experimental challenge for studying interface photochemistry usually includes the combination of a surfactant not directly susceptible to photolysis and a surface-active photosensitizer absorbing light in the near UV or visible spectral region in order to simulate the interaction with sunlight. Ideally both substances are either directly obtained from natural sources or, in terms of a laboratory model system, include functional groups which are known to be present in naturally occurring organic (and inorganic) molecules.^[68] Next to monitoring the fate of the interfacial organics, a full characterization of the photosensitized reaction could include the analysis of gas and bulk phase reaction products. For example, the gas phase products formed upon irradiation can be analyzed by means of mass spectrometry, but in fact there are only few examples reported where the very interface has been characterized by direct time-resolved methods. This is due to the fact that truly surface-selective techniques are rare.^[53,70,166] One of the few available surface-sensitive spectroscopic techniques is vibrational sum frequency generation (VSFG) spectroscopy.^[79,167] It is surface-selective intrinsically due to the symmetry constraints set by the underlying spectroscopic selection rules that require a break of inversion symmetry, which is fulfilled at interfaces.^[75] As it is based on a nonlinear optical effect, strong light intensities are necessary in order to create detectable signals. In a typical VSFG experiment, short light pulses of a tunable IR laser beam is overlapped temporarily and spatially with a fixed wavelength upconversion beam in the visible or near infrared spectral range. VSFG provides, besides excellent surface selectivity, sub-

monolayer sensitivity and surface-structure information. VSFG spectroscopy yields a (orientation-dependent) vibrational spectrum of interface species in which the signal intensities are proportional to the square of the surface concentration and the degree of molecular order of the analyte. Besides the sensitivity to the film structure in terms of molecular order, the method offers direct access to information about the molecular orientation relative to the surface normal by varying the polarization of the lasers and the detected SFG signal.^[41] In the context of marine chemistry, VSFG has successfully been used to study SML samples from the Baltic Sea. For example, the seasonal variation of the observed surfactant signal intensity can be used as a direct measure for the amount of surface-active material in the sample.^[105,106,168]

Following the successful experimental approach in the work of Ciuraru *et al.*,^[68] we tried to study the nonanoic acid/humic acid system employing VSFG spectroscopy. Unfortunately, both substances are rather soluble surfactants and turned out to be not suitable for our experimental approach. The degree of order or the concentration of nonanoic acid at the interface yielded only weak SFG signals whereas the humic acid was SFG-inactive even at high concentrations. To the best of our knowledge, no surface-active model photosensitizer with the required surfactant properties has been described in the literature as yet, although there exist some studies using similar compounds to study micelle photochemistry^[169] and to label membrane-forming molecules.^[170]

Unfortunately, the molecules used in those works are products of complex synthesis and too hydrophobic to be suitable for air-water interface studies.^[171] In order to overcome this lack of feasible surface active photosensitizers, this study reports the design, synthesis and characterization of a model substance which carries a sensitizer moiety with well-known photochemical properties attached to a tenside scaffold to force the formation of a LANGMUIR-BLODGETT film at the aqueous interface. A suitable sensitizer unit is 4-benzoylbenzoic acid, which was used as a model sensitizer before in the context of interface photochemistry. A straightforward method of transforming this compound into a tenside is the esterification with symmetric diol. This approach offers variable hydrophobicity by adjusting the alkyl spacer length as well as a hydrophilic terminal group that ensures interaction with the water.

7.3 Experimental

7.3.1 Materials

4-benzoylbenzoic acid, 1,6-hexanediol, 1,9-nonanediol, 1,12-dodecanediol, anhydrous chloroform, DMAP were purchased from Sigma-Aldrich. EDC was obtained from Carbolution chemicals. Dichloromethane was purchased from Walter CMP. All chemicals had a purity > 98% and were used without further purification.

7.3.2 Synthesis of the hydroxyalkyl esters

The hydroxyalkyl esters were synthesized according to a variant of the original STEGLICH esterification.^[172-174] *N,N*-Dimethyl-pyridin-4-amine (DMAP) (0.2 mmol,) and the diol (5 mmol) were dissolved in 30 mL of dichloromethane. 4-benzoylbenzoic acid (1 mmol) and *N*-Ethyl-*N'*-(3-dimethylaminopropyl) carbodiimide-hydrochloride (EDC) (1.5 mmol) were dissolved in 20 mL of ice cooled dichloro-methane. This mixture was added to the diol/DMAP solution and stirred for 4 h at room temperature. Afterwards, the reaction was quenched with sat. aqueous NaHCO₃ solution. The phases were separated and the organic phase was washed with brine, dried over anhydrous magnesium sulfate and evaporated. The crude product was purified by column chromatography using pentane/ethyl acetate as mobile phase, where the solvent ratio was depending on the diol chain length (see Tab. D.1 in the Appendix). Analytical data of the esters can be found in the Supplementary (Appendix D). The yields were typically about 30-40 %.

7.3.3 Characterization

CHNS combustion gas analysis was carried out on a vario MICRO CUBE by the manufacturer ELEMENTAR. IR spectra were recorded using a BRUKER ALPHA-P ATR IR-Spektrometer. Raman spectra were measured on a FT-Raman spec-

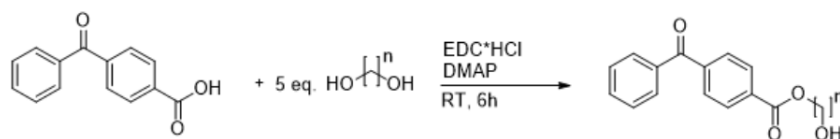


Figure 7.1: Reaction scheme for the synthesis of the surface-active photosensitizers.

trometer FRA 106 by BRUKER. NMR spectra were measured using a BRUKER AVANCE NEO 500 NMR spectrometer. MALDI mass spectra were recorded using a BRUKER MALDI-TOF AUTOFLEX instrument. UV spectra were measured using a SHIMADZU UV-1800 UV/Vis spectrophotometer.

7.3.4 VSFG spectroscopy and photolysis

All SFG experiments were performed with a picosecond VSFG spectrometer based on a commercially available system by EKSPLA. Details of this spectrometer is described elsewhere.^[41] Briefly, the output of a pump laser (Nd:YAG laser) with a repetition rate of 10 Hz, a pulse duration of 30 ps and an output wavelength of 1064 nm was used for pumping an optical parametric generator to generate the tunable infrared pulses and to provide the second harmonic at 532 nm as the visible upconversion beam. The pulse energies of the tunable IR light and the visible pulse were up to 200 μ J and 600 μ J, respectively. The polarization applied in all measurements in this work was ssp, hence s for the SFG and the visible and p for the IR pulse, respectively. Photolysis was performed using a 150 W xenon arc lamp (66907-150XF-R1) by NEWPORT. To block the strong IR lamp radiation, a water filter (Model 61945, NEWPORT) was applied. In some experiments a liquid light guide (transparent in the visible and near UV, Model 7759, NEWPORT) was used in order to feed the photolysis light into a custom-made reaction chamber. A schematic representation of the experimental setup described in the above section is depicted in Fig. 7.2 The samples were prepared in a Teflon dish (5.1 cm diameter). The dish was filled with 10 mL of ultrapure water ($R=18.2$ M Ω) and the surfactant was spread using a stock solution of the compound in anhydrous chloroform. The spreading was accomplished by dropping the stock solution on the water with an EPPENDORF pipette held in a sharp angle. Concentrations of the stock solution were typically in the range of 1-5 mM while spreading 2-20 μ L.

7.3.5 LANGMUIR compression isotherms and VSFG spectra at constant surface pressure

The LANGMUIR compression isotherms have been recorded using a commercially available system by RIEGLER & KIRSTEIN GMBH with two movable Teflon barriers allowing to change the total area from 190 cm² to 27 cm². A WILHEMY film balance equipped with a filter paper and attached to one of the barriers

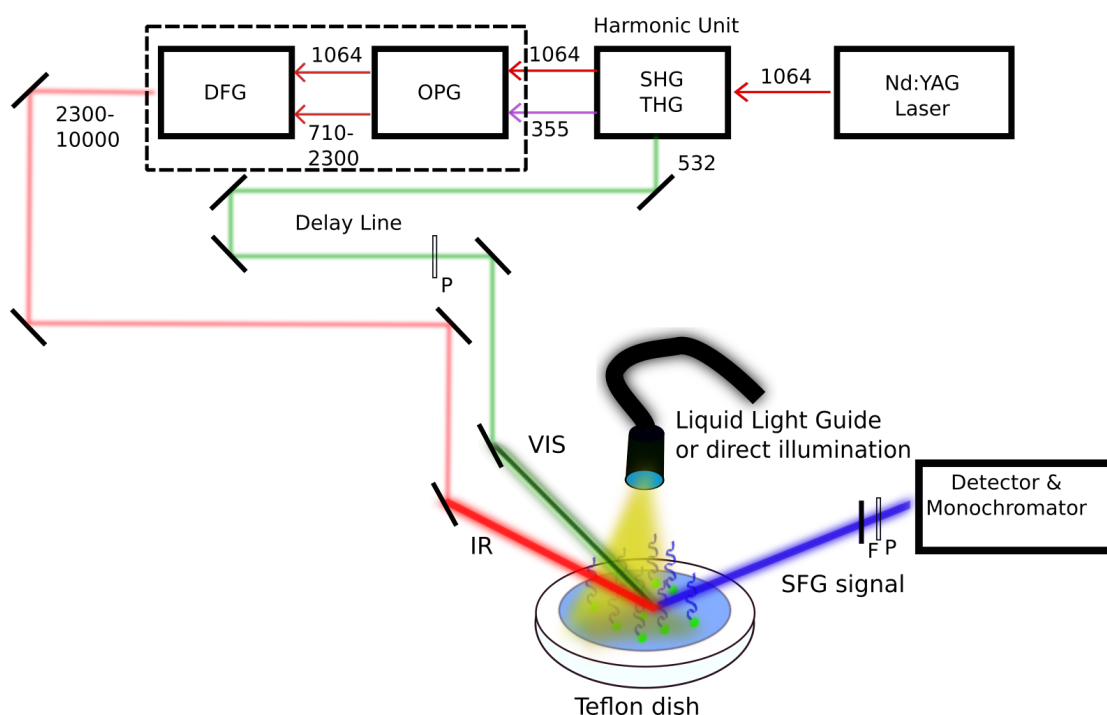


Figure 7.2: Schematic representation of the experimental setup used for the combined VSG and photolysis experiments. The numbers denote the wavelengths in units of nm.

served as the surface pressure probe. Calibration of the system was performed by recording the isotherm of the reference substance arachidic acid and adjusting the surface pressure read to the characteristic 2D phase transition at 24.5 mN m^{-1} . Cleaning of the trough was achieved by adding a few drops of a special cleaning agent (TICKOPUR R 33, DR. H. STAMM GMBH) in the trough followed by consecutive rinsing with hot, then ultrapure water until the surface pressure upon rapid compression remained below 0.8 mN m^{-1} . For all the compression experiments the compression speed was set to $0.35 \text{ cm}^2 \text{ s}^{-1}$. In a typical experiment, the trough was filled with 100 mL of ultrapure water ($R=18.2 \text{ M}\Omega$), ensuring that the trough was completely filled and a convex meniscus formed at the boundaries.

In order to record VSG spectra at a constant surface pressure, the trough was mounted on a height-adjustable stage integrated into the VSG spectrometer's beam path. The trough control unit offers a mode where the barrier position is regulated in a way that a preset value of surface pressure is held constant. The initial adjustment of the VSG spectrometer using DPPC in this setup was

accomplished by spreading a certain amount of DPPC in chloroform (typically about 40 μL of a 1 mM solution) at a surface pressure $> 30 \text{ mN m}^{-1}$ to ensure that the monolayer was in the solid 2D state (see section 2.1.3) with full monolayer coverage.

7.4 Results and Discussion

7.4.1 Preliminary experiments with Humic Acid and Nonanoic Acid

The model system consisting of humic acid as a naturally occurring photosensitizer with a well-studied photochemistry and nonanoic acid as a proxy for natural surfactants has successfully been employed in photochemical experiments by George *et. al.*^[68] In these experiments the formation of unexpected products has been reported which the authors associated with an interface-specific reaction mechanism. Preliminary experiments have been performed to expand the understanding of the system utilized in the previous study by using VSFG spectroscopy. Unfortunately, it turned out that this system is not suitable for this purpose for two reasons: The first problem is the low surface activity of nonanoic acid. In contrast to its higher homologues (e.g. stearic acid), it has a much higher solubility and requires high amounts of substance to be spread on the interface in order to achieve a detectable SFG signal. The necessary amount is so high that a significant fraction of the nonanoic acid dissolves into the bulk and hence interfering bulk photochemistry cannot be ruled out. In Fig. 7.3, the SFG spectra of a sample with nonanoic acid spread upon humic acid solution before and after 15 or 30 min. of photolysis is depicted. In addition, a reference sample was allowed to stand for one hour in the dark to ensure that the observed spectral change was due to photochemical alteration. Actually, it turned out that the spectra of both the dark reference and the photolyzed sample look are more or less the same. The initial spectrum clearly reveals a typical fatty acid spectrum with a small peak at 2850 cm^{-1} , corresponding to the symmetric stretch vibration of the methylene groups (d^+) and a pronounced peak at 2880 cm^{-1} belonging to the symmetric stretch vibration of the terminal methyl group (r^+). Centered at about 2950 cm^{-1} , the spectra show a broad signal which can be assigned to the overlapping FERMI resonances of the d^+ and r^+ modes that are expected at 2935 and 2945 cm^{-1} , respectively.^[86] The spectra after photolysis or resting in the dark both show in comparison with the initial one a

significant decrease in the intensity of the r^+ and d^+ bands. The methylene band nearly disappears whereas the methyl vibration is still visible as a peak. The intensity of the broad band located at 2950 cm^{-1} remains unaltered but a slight shift towards higher wavenumbers is apparent. As the spectral trends were reproducible, it is very likely that upon initial spreading, the system is not in equilibrium and that over time a part of the nonanoic acid slowly dissolves into the subphase, hence leading to an increase in the OH bulk signal and a strong decrease in the CH spectral region. The fact that the broad 2945 cm^{-1} band remains rather strong may indicate a spectral contribution of the humic acid. However, VSFG spectra of humic acid solution (without nonanoic acid) did not exhibit VCSFG signals. Prolonged time of photolysis did not lead to any further alteration of the system. Once in the state of "equilibrium", the VSFG spectra did not change, no matter how long photolysis was performed or the samples were allowed to rest. It might be associated with another, yet unidentified vibration. Because of the instability of the system, the poor surface activity of nonanoic acid and the absence of spectral changes for long equilibration times it was decided to discontinue the experiment. The question remains if the experiments reported in Ref.^[68] by the relatively high solubility of nonanoic acid as well.

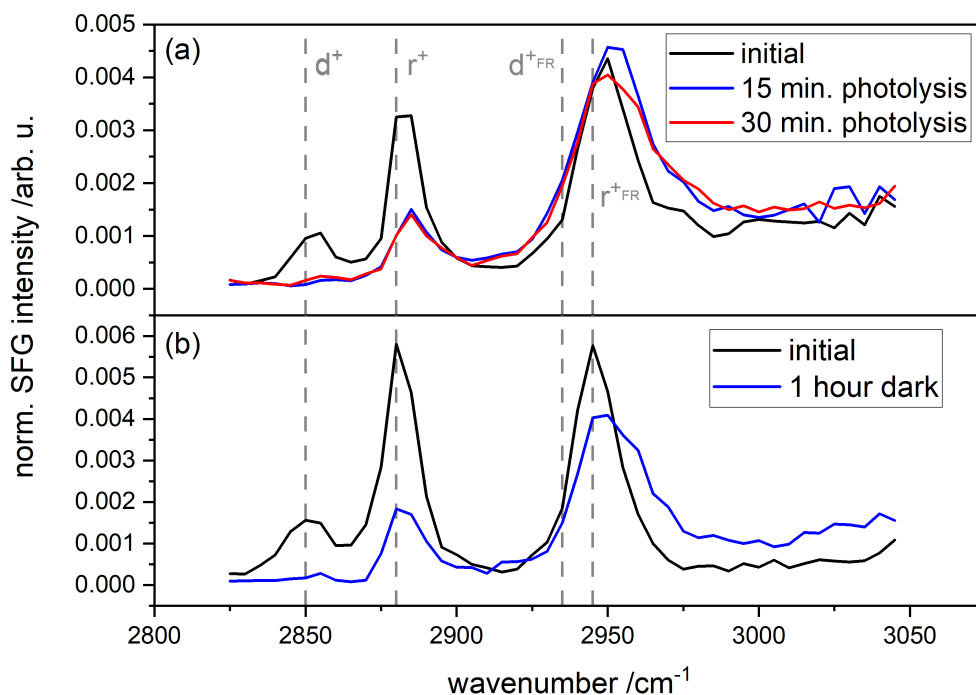


Figure 7.3: Demonstration of the photolysis of a "monolayer" of nonanoic acid (nominal area per molecule = 0.2 \AA^2 , at higher areas no SFG signal was observed) spread on a solution of humic acid probed by VSF SFG spectroscopy in the region of alkyl CH vibrations. For comparison, a spectrum before and after allowing another sample to stand one hour in the dark is shown below. The gray lines indicate the position of the methyl and methylene symmetric stretch vibrations and their corresponding FERMI resonances.

7.4.2 Synthesis and preparation of spreading solutions

As described in the Experimental section 7.3.2, the synthesis of the surface-active BX photosensitizers were carried out as a one-step STEGLICH-type esterification. After several unsuccessful attempts using protection group chemistry to ensure the monoesterification of the diol, this straightforward synthesis approach using a significant excess of the diol compound was chosen and found to yield the monoester in sufficient quantities. The ease of this one-step synthesis in terms of instrumentation and reaction control as well as the reliable removal of byproducts by standard column chromatography made this approach fully suitable for the purposes of this work. In addition, it was easily possible to vary the length of the CH chain by choosing another diol. The spacer length influences the

surface activity of the compound. The synthesized compounds are abbreviated with respect to their chain length n (see Fig. 7.1) with the term BX n where B stands for benzoylbenzoic acid and X $_n$ for the lipid component with n methylene groups in the chain. The systematic names following the IUPAC convention are 6-hydroxyhexyl-4-benzoylbenzoate (BX6), 9-hydroxynonyl-4-benzoylbenzoate (BX9) and 12-hydroxydodecyl-4-benzoylbenzoate (BX12). Because the synthesized compounds are not yet described in the literature, a full analytical characterization is provided in the Supplement. After synthesis, characterization and purification, the solid esters were dissolved in chloroform to prepare a stock solution for spreading it on a water surface to prepare LANGMUIR-BLODGETT films.

7.4.3 VSFG spectroscopy

VSFG spectra of BX compounds with long alkyl chain ($n = 9$ and 12) yielded strong spectral signatures, at least three very intense signals were visible. Interestingly, two very strong vibrations occurred in the carbonyl range of the spectrum. To the best of our knowledge, such strong carbonyl signals are not very common for VSFG spectroscopy and clearly indicate a structural order of the benzoylbenzoic acid moiety in the resulting monolayer. In contrast, the short chain species ($n = 6$) did not show intensive VSFG signals, indicating that the surface-activity of this compound was not sufficient to form stable surface layers.

For SFG can be visualized as a synchronous IR and Raman transition (see Chap. 2), to be SFG-active vibration needs to be both Raman and IR-active.^[75,80] In order to identify and assign the observed SFG signals, combined IR and Raman data can be employed. A comparison of SFG, Raman and IR data of the hydroxyalkyl ester BX9 is shown in Fig. 7.4. Moreover, quantum-chemical vibration frequency calculation have been performed using GAUSSIAN 09 software suite^[175] at the B3LYP/6-31G(d) level of theory. For better comparability, the theoretical wavenumbers determined by the calculation were corrected for the known systematic error of this theoretical method by multiplication with a specific correction factor.^[176] The VSFG signal which was closest to a calculated vibration being both IR and Raman-active can be assigned to the corresponding molecular vibration. According to this, the VSFG signal appearing at 1655 cm^{-1} was assigned to the symmetric stretch vibration of the carbonyl group located

between the two benzene rings whereas the signal at 1720 cm^{-1} belongs to the ester carbonyl group. The intense signal at 3070 cm^{-1} corresponds to a CH-stretch vibration of the benzene rings. By this procedure, it was not possible to make an unambiguous assignment for the aliphatic CH region (peaking at 2955 and 2850 cm^{-1}) yet because many different methylene CH-vibrations of the chain fall in this region. An overview about this peak assignment is presented in 7.1. However, a typical assignment of the two bonds in agreement with the assignment of nonanoic acid (see section 7.4.1) would be a dominating CH_2 group vibration with the symmetric stretch at 2850 cm^{-1} and a corresponding FERMI resonance at 2955 cm^{-1} .

In order to illustrate the molecular shape of those new compounds, a 3D representation of the geometry-optimized gas phase structure of BX9 is shown in Fig. 7.5. Remarkable is the twist between both the aromatic rings, resulting in an arrangement where they lay in different planes, as well as the distinct angle between the aromatic system and the aliphatic tail at the ester group. This gives rise to the assumption that, even in dense layers of those substances, they are not able to form the same stretched long linear-shaped arrangement that is typical for saturated fatty acid monolayers. A comparison of the VSFG spectra of the three different artificial photosensitizers is presented in Fig. 7.6. BX9 and BX12 exhibit very similar spectra with pronounced signals of the carbonyl stretch vibrations at 1655 and 1720 cm^{-1} and the aromatic CH stretch vibration at 3070 cm^{-1} . The signals of the alkyl chain at 2955 and 2850 cm^{-1} are, compared to the other signals, rather small which could be an indicator for ordered alkyl chains where the resulting VSFG signals at least partly cancel out because of

Table 7.1: SFG peak assignment for the BX photosensitizers. DFT frequencies are scaled by a factor of 0.9613 according to Ref.^[176]

ν (SFG) / cm^{-1}	ν (exp. IR/Raman) / cm^{-1}	ν (corr. DFT) / cm^{-1}	assignment
1655	1651	1672	CO symm. stretch, benzoyl
1720	1713	1728	CO symm. stretch, ester
2850	2847	2862	aliphatic CH_2 stretch, d^+
2955	2947	2964	aliphatic CH_2 stretch, d_{FR}^+
3070	3060	3082	aromatic CH stretch

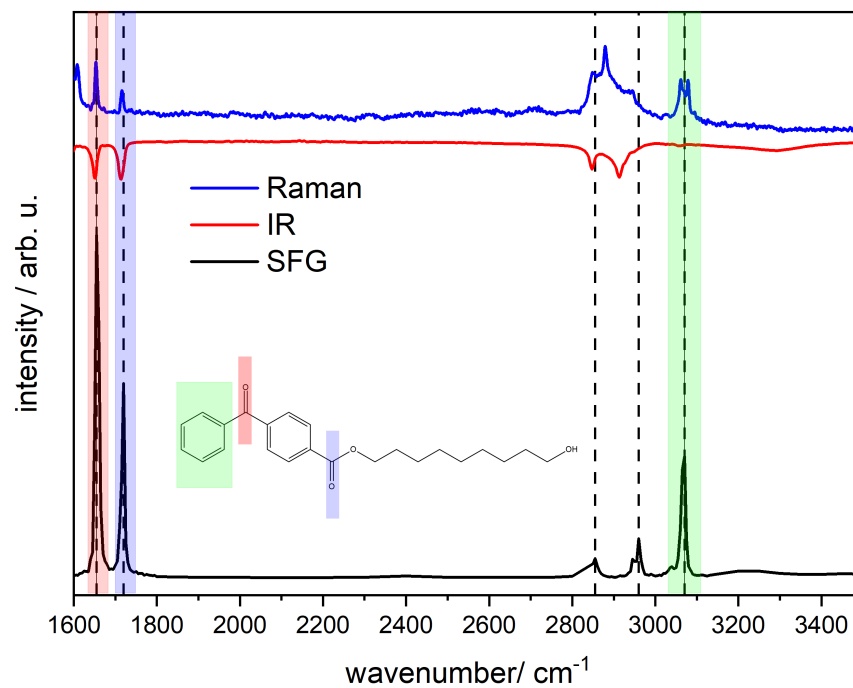


Figure 7.4: Comparison of the VSGF, Raman and IR spectra of the sensitizer BX9. All spectra are normalized and shown in arbitrary units and shifted with respect to each other for clarity.

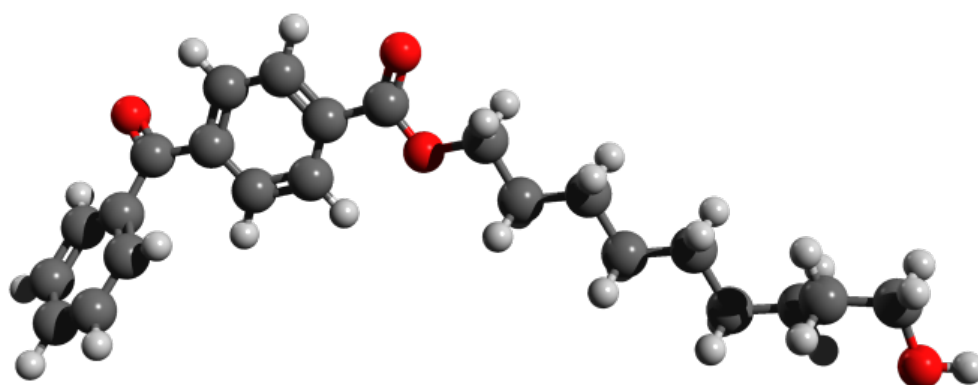


Figure 7.5: 3D representation of the geometry-optimized (B3LYP/6-31G(d) level of theory) BX9 molecule gas phase structure.

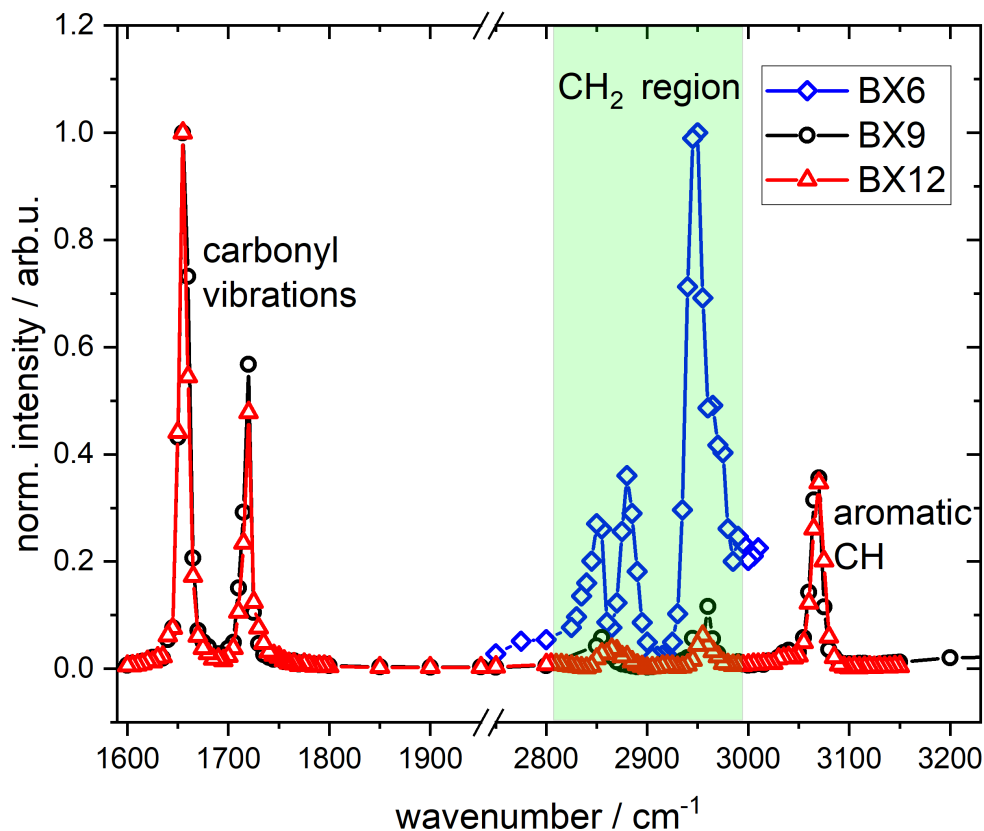


Figure 7.6: Comparison of the VSFG spectra of the three BX sensitizers. Each spectrum has been normalized to its maximum intensity to allow a comparison. Total intensities have been about a factor of nine lower for BX6 compared to BX9 and BX12.

the pseudo-inversion symmetry of two neighboring CH_2 groups in all-trans conformation. Interestingly, the spectrum of BX6 looks very different compared to its longer homologues. Neither the carbonyl vibrations nor the signal of the aromatic group could be detected in any VSFG spectrum of BX6. In order to obtain any SFG intensity at all, much higher surface concentrations of BX6 compared to BX9 and BX12 were necessary, leading to a theoretical surface coverage well above than expected for single monolayer. This is a clear indication that the surface activity of BX6 is significantly lower than the one of its higher homologues, which is, considering the chain length and relative number of polar functional groups, not surprising. The BX6 VSFG spectrum shows only weak signals in the aliphatic region of the spectrum at 2850, 2880 and 2990 cm^{-1} . The

carbonyl vibrations of BX6 have not been detected in any measurement, indicating statistical orientation of the aromatic moieties in the sample. In contrast, a possible explanation for the extraordinary high carbonyl and aromatic CH signals of the higher homologues is a high degree of structural order as a result of energetically favorable $\pi - \pi$ stacking of the aromatic moieties. The importance of this kind of intramolecular interactions within LANGMUIR monolayers has already been reported in the past.^[177]

7.4.4 LANGMUIR trough Experiments

To get a better understanding of the surface film structure and properties, both LANGMUIR compression isotherms of the sensitizers as well as VSFG measurements at constant surface pressure have been performed. Compression isotherms of the three sensitizers are shown in Fig. 7.7. The isotherm of the lowest homologue (BX6) starts to increase approx. at a value of the area per molecule of about 14 \AA^2 . This is a very low value if one considers that the typical space demand for a fatty acid chain is about 27 \AA^2 . This is in agreement with the very low signal intensities observed in the VSFG measurements and supports the hypothesis of a low surface activity. The situation of for the higher homologues is more complex. Here, the reproducibility of single compression isotherms was rather poor, so the depicted data are the result of averaging multiple measurements. As such, the isotherms visualize the general trend rather than allowing for a quantitative comparison. It is obvious that the increase in surface pressure which is caused by structural changes and the resulting from intermolecular interactions in the film (lift-off point) occurs much earlier than for BX6. Considering the dimensions of the molecule, this is not surprising. A rough estimation of the surface space requirements (demonstrated in Appendix D.4) yields a maximum space requirement of 130, 154 and 179 \AA^2 for a flat-lying BX6, BX9 and BX12 molecule. The isotherms of BX9 and BX12 both exhibit roughly three "zones" characterized by their slopes: a zone of relatively steep increase of the surface pressure following the lift-off, a rather flat region reaching from approx. 100 to 50 \AA^2 , and a third zone of very steep increase in surface pressure up to maximum compression or collapse. Visible collapse points appeared in some single measurements of BX12, typically at about 15 \AA^2 . The second zone of low slope in the case of BX12 appeared as a real plateau, whereas in case of BX9 a constant increase of surface pressure was observed. Such regions in

compression isotherms are typically associated with the coexistence of two 2D phases. In many single measurements of BX 12 (see Appendix D), a slight decay in the surface pressure before the plateau was observed, a phenomenon that has been described in the literature as "roll-over collapse" caused by the formation of multilayers.^[178,179] Considering the very high SFG intensity of the carbonyl group signals, this observation could indicate the formation of some type of aggregates driven by π - π stacking interaction, resulting in stable layers even at rather low theoretical area per molecule values. To investigate the surface film characteristics of BX9 and BX12 further, VSFG measurements in the LANGMUIR trough at defined surface pressures have been performed. It was tried to measure the system at two different states: within the plateau/ low slope region in the middle of the isotherm as well as in the zone of high slope at the end. The results of this approach are shown in Fig. 7.8. Sub-figure (a) contains the measurements of BX12, (b) the ones for BX9 and (c) those for BX9 normalized to their corresponding maximum to allow for a better comparison since the absolute intensities are extremely different. BX12 exhibits similar spectra for both surface pressure zones with slightly lower intensities for the lower surface pressure. The most significant difference is a strong increase of the carbonyl signal at 1720 cm^{-1} whereas the other signal only increase moderately. In case of BX9, the difference between the two surface pressure values is much more distinct. The absolute intensity of the spectrum obtained at 6 mN m^{-1} is much lower. In addition, all the signals exhibit comparable intensities (see Fig. 7.8 c). Moreover, the intensity of the two carbonyl signals are almost equal whereas in the high surface pressure measurement the peak at 1655 cm^{-1} is much higher. Note that the apparent splitting of the carbonyl peak in the spectrum at 6 mN m^{-1} was not well reproducible and probably is a spectral artifact from the normalization procedure of the low-intensity spectra caused by very low IR intensities in this spectral region. The weak CH vibrations which are barely visible in the high pressure spectra of both BX9 and BX12 are visible and in the same order of magnitude as the carbonyl signals in the low pressure measurement. Comparing BX9 and BX12, the position of the alkyl signals slightly differ (BX12: 2865 and 2955 cm^{-1} , BX9: 2850 , 2930 cm^{-1}). The relative decrease of CH_2 alkyl intensity is consistent with better aligned alkyl groups at higher surface concentration (see above).

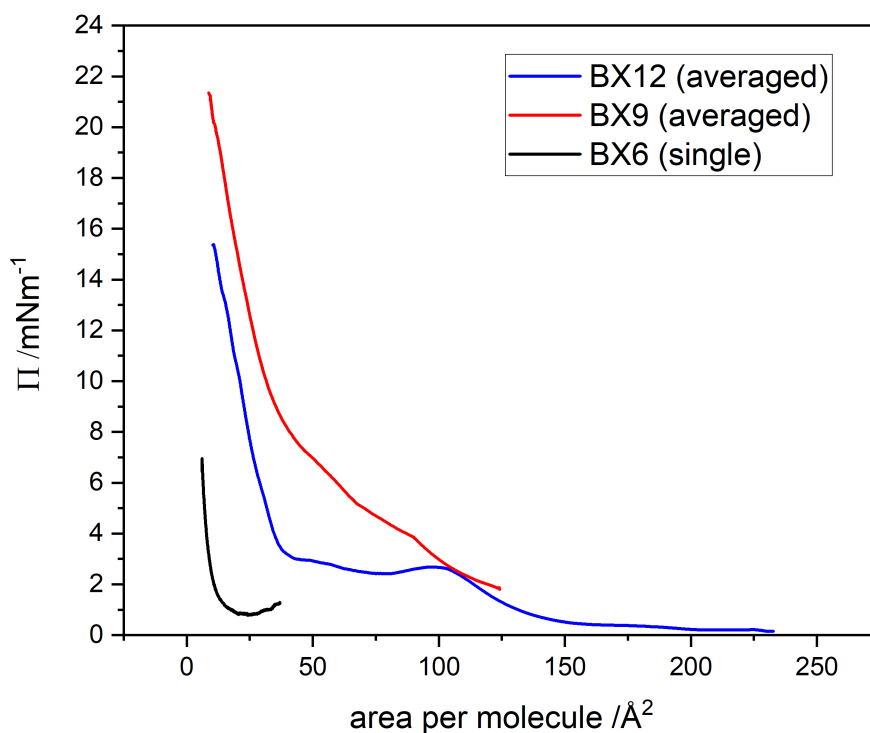


Figure 7.7: LANGMUIRcompression isotherms of the three sensitizers. The BX6 measurement is a single measurement, the other isotherms are averaged from 10 (BX9) and 7 (BX12) single measurements (see Appendix D). The single measurements are shown in Fig. D.13 and D.14, respectively.

7.4.5 Photolysis experiments

Photolysis experiments were performed by exposing the Teflon dish containing the sample to radiation generated by a Xenon arc lamp, simulating solar radiation. VSFG spectra were recorded before and after the photolysis in order to detect changes in the spectrum and therefore changes in the interface characteristics. The results of a typical photolysis experiments are shown in Fig. 7.9. Although at the beginning of the experiment strong signals of the hydroxyalkyl ester are present, after 30 minutes all photosensitizer signals had completely vanished. A blank experiment where a sample was rest without photolysis for more than one hour did not show significant changes in the spectrum before and after at all, so it can be certainly stated that the drastic change of the spectrum is a direct consequence of the irradiation. Assuming a similar photoreactivity

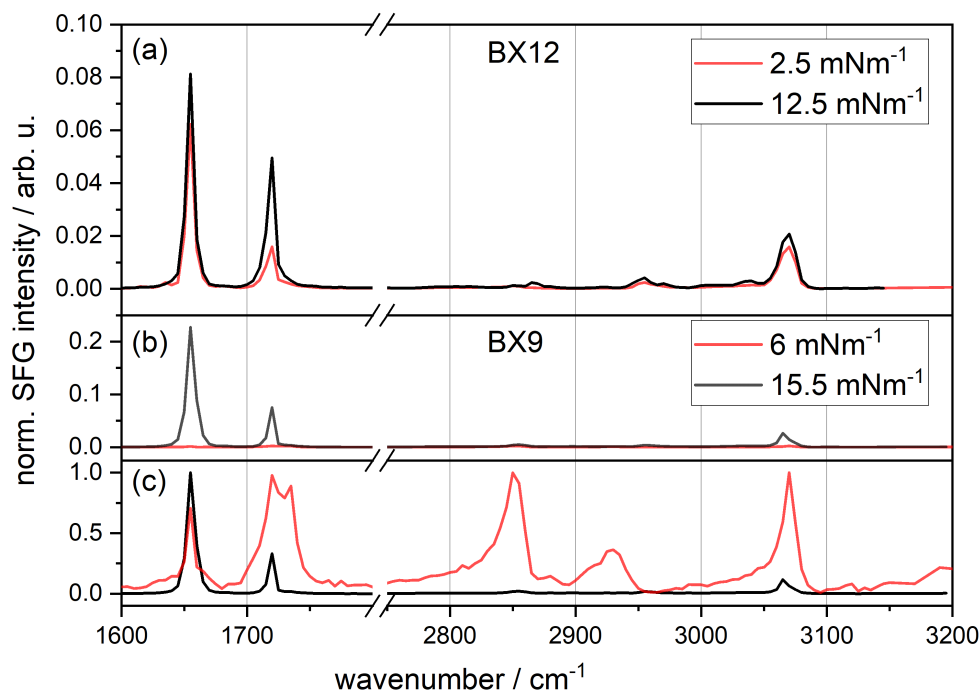


Figure 7.8: VSFG spectra of the sensitizers obtained at low and high surface pressures. The depicted spectra are averaged from 2-3 single measurements. Subfigure (a) shows the measurements for BX12, (b) for BX9 and (c) the BX9 measurements with both spectra normalized to their corresponding maxima for better comparison.

of this species as it is well-known for pure benzoylbenzoic acid and other benzophenones, a likely explanation for this observation is autophotolysis of the substrate.^[63,169] As the intense SFG signals indicate that a dense layer is present, the excited sensitizer moiety has several alkyl chains of the tail of nearby hydroxylalkyl ester molecules around it. Therefore, it is likely that H atom abstraction reactions take place, leading the way to NORRISH-type chemistry. This results in breaking the chains and therefore altering the molecule in a way that it is not longer surface active and leaves the interface. This could either, in case of more hydrophilic products, occur by dissolving into the water subphase, or, in case of volatile species, escape into the gas phase.

The photolysis occurred no matter whether the liquid light guide or the direct lamp radiation was used. Because the lamp setup includes a water filter cutting of the IR part of the Xenon lamp spectrum, the observed effect cannot be explained by heating the sample but indicates that the sensitizer is susceptible

to irradiation of light in the visible and near-UV region of the spectrum. This confirmed that the benzoylbenzoic acid hydroxyesters are suitable candidates as a model systems designed to study surface photochemistry.

Time-resolved photolysis

Time-dependent photolysis experiments have been performed. SFG spectra of the intense carbonyl peak at 1655 cm^{-1} were recorded (with the lamp switched off) after steps of one minute photolysis. The result of this experiment for the sensitizer BX12 is shown in fig. 7.10. Note that the total time of the experiment was about 30 minutes because the spectrum acquisition (with the lamp switched off) took about three minutes each time. The time stated on the x-axis of Fig. 7.10 refers to the photolysis time with the lamp switched on. It can be seen that, after an apparently slower phase at the beginning of the experiment, the decrease in signal intensity is fast and takes place on a timescale of less than 10 minutes. In all systems used in the course of this study the signal decrease took place in a maximum of one hour.

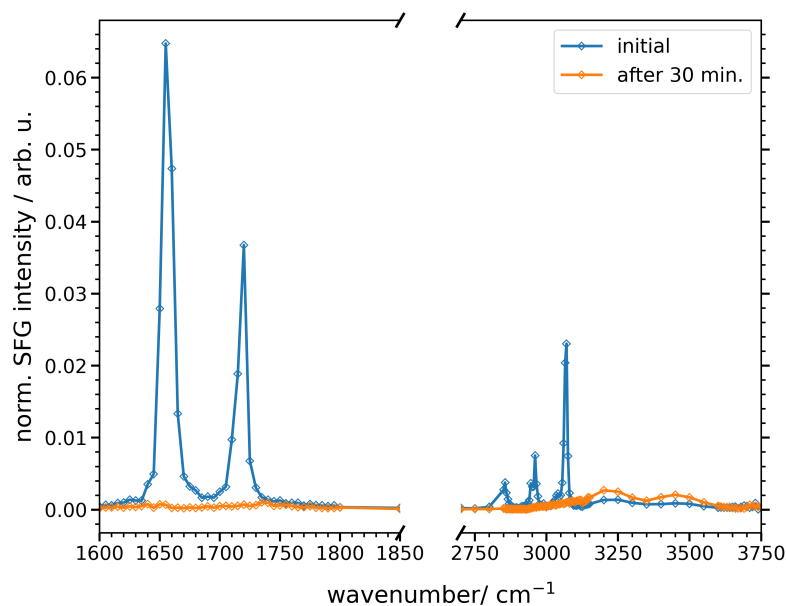


Figure 7.9: SFG spectrum of the sensitizer BX9 before and after 30 minutes of irradiation.

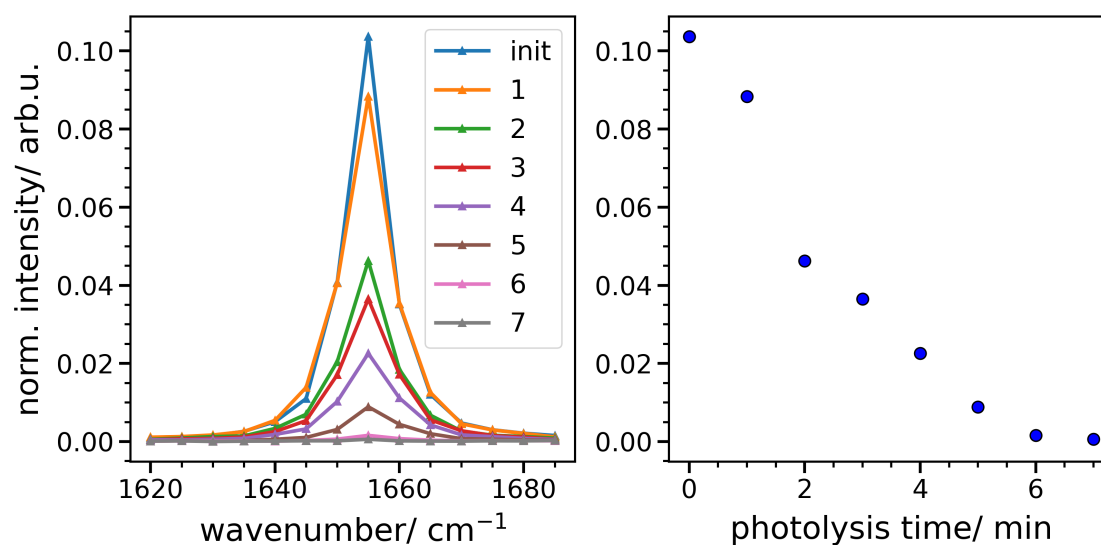


Figure 7.10: Typical result of a time-dependent photolysis measurement. The number in the legend indicates the number of minutes the samples was photolyzed before the spectrum was recorded. Note that because of the square dependency of the SFG signal on the surface concentration, a linear decay with time is not expected.

7.5 Conclusion

A novel class of surface-active photosensitizers forming interfacial well-ordered surface monolayers has been synthesized and characterized by VSFG measurements. The synthesis is reliable, simple in terms of instrumentation and includes only one reaction step. This class of molecules turned out to be highly suitable for VSFG measurements and susceptible to photolysis. It is therefore an excellent model system for photochemical studies at the very interface of an air-water system. The SFG spectra revealed besides the usual aliphatic and aromatic CH vibrations unexpected strong carbonyl vibrations indicating a high degree of order in the layer which could be a result of π - π stacking interaction between the aromatic compartments of the molecules. This observation alone justifies further investigations targeting the surface behavior and detailed structure of the monolayers of this compounds in more detail. Using a standard solar simulation lamp, the photolysis of the sensitizer happens on a time-scale reasonable for lab experiments. Future investigations should focus in the characterization the photolysis kinetics in more detail and head in the direction of the formation of mixed layers between a photo-inert surface-active substance and those photosensitizers to be a more realistic model system for the SML processes. These next steps will be taken in the following chapter of this thesis.

CHAPTER 8

Mixed layers of fatty acids and an artificial photosensitizer

8.1 Introduction

The interfacial zone between sea and air resembles a complex and highly dynamic environment. It is, in many parts of the world's oceans, enriched with a variety of surface-active chemical compounds. The spatial and temporal variability of the composition and concentration of those substances in this so-called Sea Surface Microlayer (SML) contributes to the complexity of this system.^[2,3,16] For instance, a huge variety of chemical compounds like proteins, complex carbohydrates, fatty acids, humic substances and amino acids with distinct chemical properties have been found to be present in this zone with an extension of 1-1000 μm from the surface.^[8,10,180] Those substances stem from a variety of different sources, including anthropogenic and riverine input, atmospheric deposit, biological primary production and degradation of organic matter by microbes and photolysis.

However, it has been shown that the presence of surface-active materials at the interface can alter the chemical and physical properties drastically. One important example is the influence of those compounds on air-sea gas exchange.^[18,45] At higher levels of surfactant enrichment at the interface, the same wind speed leads to the formation of lower waves than for pure water, hence resulting in less turbulence and therefore reduced gas transfer.^[25,32,144,153] As gas transfer is a key step in modeling atmospheric processes on global scale, quantification of those phenomena as well as the implementation of numerical models relies on a profound understanding of the underlying microscopic processes. This includes the consideration of the mechanisms that lead to the formation and alteration of the SML.

One of the processes that has been found to be responsible for alteration of the

SML's chemical composition is photochemistry. As the SML is a zone of the with high exposure to sunlight in combination with a relatively high concentration of organic molecules, it is not surprising that many photophysical and -chemical processes occur. In addition, some substance typical classes present in the SML exhibit high absorption of light in the near UV and visible range of the spectrum.^[49] For example, humic acids are strongly absorbing compounds are able to act as so-called photosensitizers: their excited state reacts with other types of molecules in the direct neighborhood and thus allows for a light-induced transformation of compounds that are usually inert to sunlight.^[53,68] This kind of processes and its role for SML chemistry is not understood in detail yet because it is difficult to directly observe them *in situ*. During the last years several attempts have been made to create suitable model systems of representative model surfactants with suitable behavior to mimic a typical SML photosensitizers. Of special interest for this kind of experiments is the question whether the photochemical mechanisms occurring directly at the interface differ significantly from the somewhat (better-known) ones taking place in surface bulk water. Recent model studies employed a model system of humic acid as a sensitizer and nonanoic acid, as a so-called wet (i.e. partly soluble) surfactant. Irradiated by artificial sunlight, the formation of unexpected unsaturated compounds has been observed that can be associated with surface-enhanced reaction pathways, indicating that the unique combination of surfactant accumulation and solar irradiation in the SML triggers a yet unexplored photochemistry. Of course, such processes will also play a role for other atmospheric processes (such as aerosol aging).^[53,68-70] Recently, (see chapter 7 of this thesis), a novel class of photosensitizers (benzoyl-benzoic acid hydroxyalkyl esters, so-called BX compounds) has been developed. BX compounds with long hydroxyalkyl chain are supposed to show high surface-activity to ensure their presence at the very interface between air and water. Moreover, these compounds yield strong and characteristic spectral features in VFSG spectra, thus allowing surface-specific spectroscopic studies. With such a photosensitizer it should be possible to study interface-specific photochemical processes in a much more direct way than before. First irradiation experiments of BX monolayers with artificial sunlight clearly revealed an effective decomposition at the air-water interface. This autophotolysis is a clear indicator for the photoreactivity of this compounds.

In order to reflect the situation in natural SML more realistically, it is neces-

sary to create well-mixed organic monolayers of photosensitizer and reactant to suppress this autophotolytic process in favor of the cross-reaction between photosensitizer and the reactant of interest. Consequently, the next step towards the study of monolayer photosensitized reactions is the preparation of mixed monolayers with substances that are inert towards photolysis under regular conditions and ideally are present in natural SML systems. If the sensitizing process works as expected upon irradiation of such mixed monolayers, the photosensitizer will induce reactions of the photochemically inert molecules in its proximity.

A pictorial scheme of the desired interfacial mixed layer is shown in Fig. 8.1. A class of molecules suitable for the role as surfactant in this kind of experiments are fatty acids (FA). Their surface-behavior is well-known and has been studied with different analytical techniques.^[43,82,118,181,182] Moreover, fatty acids are typically present in natural systems such as the SML and they are, except for the case of short-wave UV radiation, relatively inert towards photolysis. This work describes the preparation of mixed FA/BX surface monolayers, their physicochemical surface properties, and first photolysis experiments of these mixed systems.

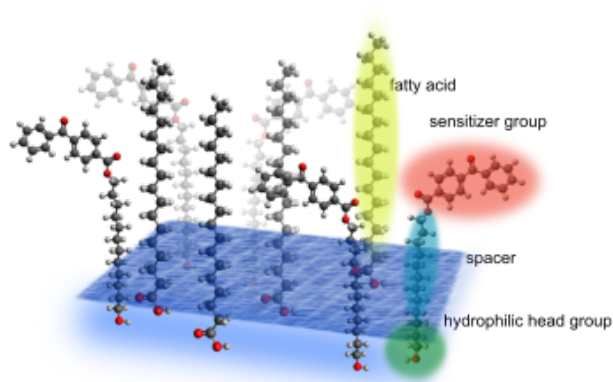


Figure 8.1: Schematic illustration of the structure of a FA/BX monolayer. The benzoylbenzoic acid moiety of BX serves as the sensitizer group, the alkyl spacer induces surface activity with the hydrophilic head group pointing towards the water side.

8.2 Experimental

8.2.1 Preparation of the spreading stock solutions

For the experiments, different mixture ratios of the saturated fatty acids with variable alkyl chain length n , i.e. myristic acid (YA, $n=14$), palmitic acid (PA, $n=16$) and stearic acid (SA, $n=18$), with the two benzoylbenzoic acid hydroxyalkyl ester sensitizers BX9 and BX12 have been prepared. Details of the synthesis of BX9 and BX12 are described in section 7.3.2. The structures of FA and sensitizers are shown in Fig. 8.2. Note that the number in the sensitizer name indicates the count of methylene groups in the alkyl chain. In order to prepare a mixed layer of sensitizer and fatty acid (from here on referred to as "surfactant"), stock solutions of all compounds with an initial concentration of 5 mM in chloroform have been prepared. Directly before the measurement, the desired mixture was obtained by adding the suitable volume of surfactant and sensitizer stock solution to a flask and diluting it with the necessary amount of anhydrous chloroform to yield the desired concentration. If not otherwise stated, the final concentration was 1 mM in total such that a 1 to 1 mixture contained 0.5 mM of the surfactant and 0.5 mM of the sensitizer.

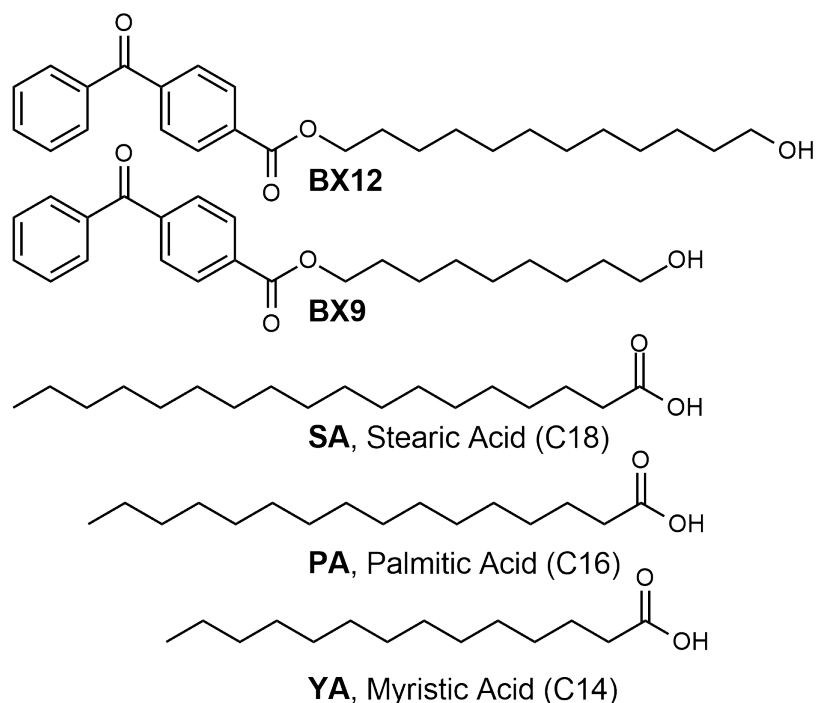


Figure 8.2: Chemical structures of the fatty acids and artificial photosensitizers.

8.2.2 LANGMUIR trough measurements

LANGMUIR compression isotherms have been recorded using a commercially available system by RIEGLER & KIRSTEIN GMBH. The maximum available area of the trough was 190 cm^2 , which could be compressed using two step motor-controlled movable PTFE barriers to a minimum area of 27 cm^2 . The compression speed was set to $0.35 \text{ cm}^2 \text{ s}^{-1}$. The surface pressure Π was recorded by a WILHEMY film balance equipped with a filter paper. The balance was attached to one of the movable barriers. At the beginning of a set of measurements the balance was calibrated by recording the isotherm of the reference substance arachidic acid and by adjusting the surface pressure read with respect to its characteristic 2D phase transition at $\Pi = 24.5 \text{ mN m}^{-1}$. Cleaning of the trough was achieved by adding a few drops of a special cleaning agent (TICKOPUR R 33, DR. H. STAMM GMBH) to the trough followed by consecutive rinsing with hot, then ultrapure water until the surface pressure upon rapid compression remained below 0.8 mN m^{-1} . In a typical experiment, the trough was filled with 100 mL of ultrapure water ($R = 18.2 \text{ M}\Omega$), ensuring that the trough was completely filled and a convex meniscus formed at the boundaries. The substances of interest, dissolved in chloroform, were dropped from an EPPENDORF pipette held at an sharp angle upon the water surface.

8.2.3 VSFG spectroscopy

VSFG spectra have been recorded using a modified, commercially available spectrometer by EKSPLA. This system was based on a ps-Nd:YAG laser with an output wavelength of 1064 nm. This laser pumped a harmonic unit generating the second (532 nm) and third harmonic (355 nm) of the fundamental. The second harmonic was used for upconversion in the SFG process, the third harmonic was used to feed an OPG/DFG unit which generated a coherent tunable infrared beam in the wavenumber range of $1000\text{-}4350 \text{ cm}^{-1}$. The resulting IR beam and the VIS beam from the harmonic unit were overlapped spatially and temporally on the sample surface. The generated SFG response (in reflection geometry) was separated from the reflected incident beams by spatial separation employing an iris diaphragm as well as an optical filter and a monochromator. The SFG signal was measured using a gated photomultiplier tube.

The samples were prepared in a Teflon dish (5.1 cm diameter). The dish was filled with 10 mL of deionized water and the surfactant was spread using the

stock solution of the compounds as described above. To optimize the beam line's optical alignment, at the beginning of each day, a sample of the reference substance DPPC (for details, see section 3.4.2) was measured. In order to check the stability of the spectrometer performance, an additional DPPC spectrum was recorded at the end of each set of measurements.

8.2.4 Combined VSFG and LANGMUIR trough measurements

For combined experiments LANGMUIR trough/VSFG experiments, the trough was mounted on a height-adjustable stage and placed in the beam path of the SFG spectrometer. This step was used to record spectra while holding the system at a constant surface pressure. The spectrometer beam adjustment was performed similar to the setup without the trough using DPPC as reference. A solution of DPPC in chloroform was spread upon water in the trough and, after adjusting the height of the movable stage correctly, compressed until the surface pressure was about 30 mN m^{-1} to ensure that the system was in the solid 2D state (see 2.1.3) with full monolayer coverage.

8.2.5 Photolysis

Photolysis was performed using a 150 W xenon arc lamp (66907-150XF-R1), by NEWPORT. To block the strong IR lamp radiation, a water filter (Model 61945, NEWPORT) was applied. A liquid light guide (transparent in the visible and near UV, Model 7759, NEWPORT) was used to transfer the light to the sample. The samples were located in a Teflon dish, prepared as described in section 8.2.3. The sample was irradiated with the light guide located approx. 1 cm above the sample's surface. Typical photolysis durations were about 15-45 minutes, depending on the decline in VSFG signal intensity.

8.3 Results and Discussion

8.3.1 General concept of the experiments

To investigate the structural properties of the mixed monolayers, complementary experimental approaches have been taken:

- single VSFG measurements at different surfactant/sensitizer ratios to explore the general appearance of the spectra and to identify suitable mixture ratios and surface concentration for a more detailed analysis

- systematic measurement of LANGMUIR compression isotherms of different surfactant/ sensitizer ratios to identify the 2D phase behavior of the resulting surface films which can be either mixed layers or composed of domains of the individual compounds due to phase separation
- combined VSFG and LANGMUIR trough measurements to record spectra at fixed surface pressures to identify potential structural characteristics of different 2D phases of the systems
- the photolysis of selected monolayers to investigate whether it is possible to decompose the (usually photochemically inert) fatty acids in the presence of the photosensitizers

The results of those different approaches are reported in the following sections.

8.3.2 SFG spectra

As a first approach towards the preparation and understanding of the surface characteristics of the monolayers of mixtures of the FA and the sensitizers (BX), various mixtures and FA/BX ratios have been prepared and investigated by means of SFG spectroscopy. The mixtures were chosen based on the criterion of yielding good SFG signals rather than corresponding to a nominal value of the area per molecule. In this way, the resulting area was typically between 24 and 7 Å². Note that at such low area per molecule regimes the coverage can be expected to be above one molecular layer. However, due to the excellent quality of the obtained VSFG spectra at this high surface concentrations that were obtained directly after the successful synthesis of the substance. Especially the strong carbonyl vibrations, most likely a consequence of structural order, indicated low area that a stable layer was present at the interface even at such low nominal areas per molecule. An example for an VSFG spectrum of a mixture of stearic acid and the sensitizer BX12 in the ratio 1:1 is displayed in Fig. 8.3. For comparison, this figure includes spectra of the pure compounds as well and all spectra are normalized to the maximum peak intensities of each spectrum. Clearly the spectrum of the mixture contains all signals of the sensitizer and the fatty acid: the strong carbonyl peaks at 1655 and 1720 cm⁻¹, the strong aromatic CH vibration at 3070 cm⁻¹, the CH vibrations of the sensitizer at 2850 and approx. 2950 cm⁻¹ as well as the strong characteristic d⁺(2850 cm⁻¹) and r⁺(2880 cm⁻¹) fatty acids bands and their corresponding FERMI resonances (2935

and 2945 cm^{-1}). The CH vibrations of both compounds overlap in the final spectrum whereas the aromatic and carbonyl peaks are well-separated. This particular spectrum of a mixture resembles a situation where its appearance is mainly dominated by the photosensitizer compound. This was not the case for all the mixtures. As expected, the FA/BX ratio and the type of surfactants (depending on the chain lengths of both substances) had a strong influence on the overall spectral appearance. An interesting observation was that the position of the peak of the aromatic stretch vibration shifted from 3070 cm^{-1} in for the pure sensitizers to 3065 cm^{-1} in the mixture (compare Fig. 8.3). This was observed for most of the mixed layer spectra. One possible explanation of such a shift is, assuming a well-aligned surface structure of the aromatic rings due to an energetically favorable interaction such as π -stacking (see chapter 7), a disturbance of this alignment due to concurring interaction with the fatty acid molecule. As such, the signal shift could be an indicator for the presence of a mixed layer at the interface. Unfortunately, repeated VSFG spectra of the mixtures yielded quite variable relative peak intensities, hence did not allow for a straightforward, statistically significant evaluation of the peak ratios. An example for this problem of reproducibility is demonstrated in Fig. 8.4. The two spectra show significant different peak patterns. In the spectrum obtained in the first measurement, the aromatic (ar) peak is the highest and both the r^+ and d^+ peaks are of similar intensity but smaller than the carbonyl peaks. For the second measurement two, the r^+ peak is the highest whereas the d^+ peak is only slightly higher than in the first measurement, indicating the presence of well-aligned fatty acid molecules (bearing the terminal methyl group) at the interface. A possible explanation for such a behavior is the presence of domains of different composition at the interface, such that during both measurements, different domains have been probed. If the size of the domains is larger or in the same order of magnitude of the laser spot (ca. 1 mm), consecutive measurement of the same sample could in principle lead to two very different results. Nevertheless, an attempt was undertaken to identify general trends in the spectra. An overview of some characteristics of the measured spectra is compiled in Tab. 8.2. A naming convention for the peaks of the photosensitizer as shown in Tab. 8.1 have been adopted. The overview table lists three peak ratios: $ca1/r^+$, $ca1/d^+$, and r^+/d^+ . These ratios are a measure whether the spectrum is dominated by the surfactant or the sensitizer. On the one hand, the signal of the terminal methyl

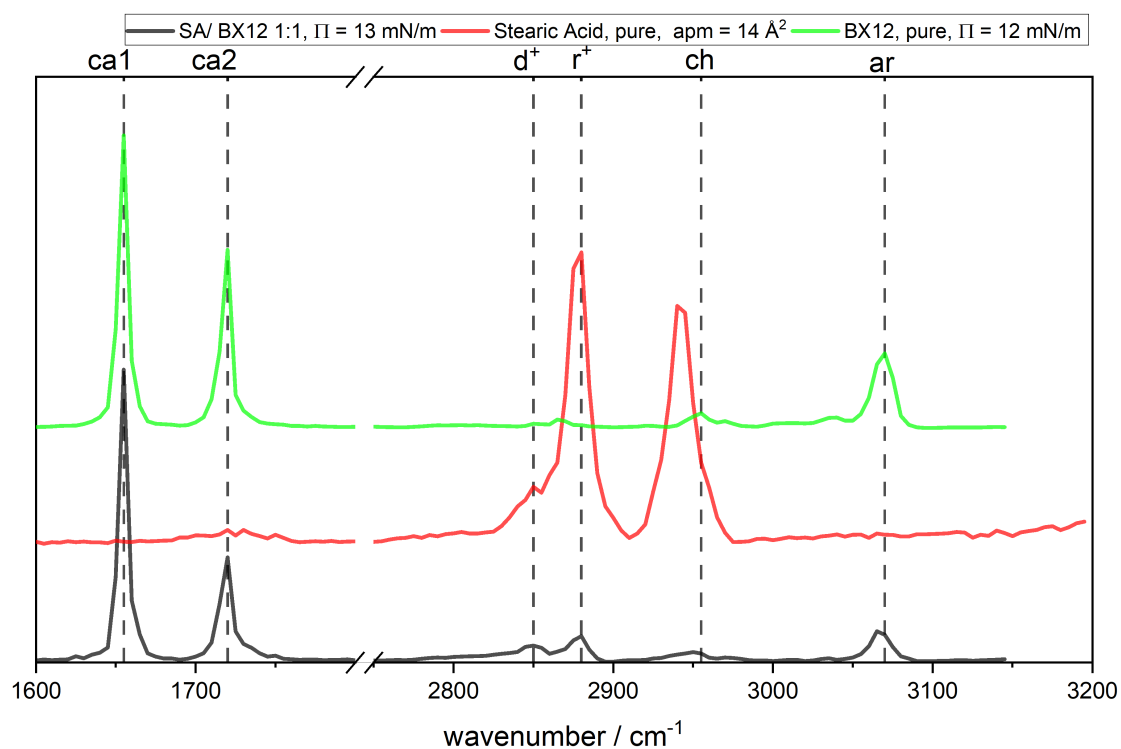


Figure 8.3: SFG spectra of a mixture of stearic acid and the photosensitizer BX12 (black) as well as spectra of the pure substances (red and green). For comparability, all spectra have been normalized to their corresponding maximum. The stated apm values refer to the available area per molecule as evaluated from the number of molecules in the spreading solution.

Table 8.1: Symbols to refer to the characteristic VSFG peaks of the photosensitizers.

peak position / cm^{-1}	naming convention	assignment
1655	ca1	carbonyl CO symm. stretch
1720	ca2	carbonyl CO symm. stretch
3070	ar	aromatic CH symm. stretch
2955	ch	alkyl CH symm. stretch

group (r^+) corresponds to the fatty acid alone and does not overlap with any sensitizer signals and the carbonyl signal (ca1) is usually the strongest sensitizer peak. The r^+/d^+ ratio is often used as an indicator of the degree of order within monolayers consisting of long-chain methylene-terminated surfactants. The higher the order, the higher the relative CH_3 signal and r^+/d^+ peak ratio.^[183] Finally, $ca1/d^+$ is included as additional information. A remarkable finding that in case of the short fatty acid YA and the long-chain sensitizer BX 12 the

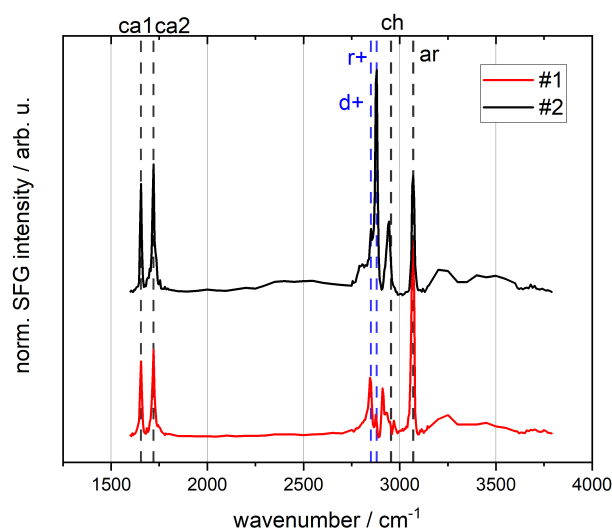


Figure 8.4: Demonstration of the irreproducibility of the VSFG spectra of a mixed layer (SA/BX12 1:2, $\text{apm} = 12 \text{ \AA}^2$), sometimes leading to very different spectra if the same sample is measured two times directly after each other. The peak assignments is indicated by dashed lines, black for the sensitizer, blue for the fatty acid bands.

Table 8.2: Overview about characteristics obtained from VSFG spectra of various fatty acid/photosensitizer mixtures. The apm column reports the area per molecules in \AA^2 . The "no." column reports the number of averaged spectra and the following columns the peak ratios of interest. Numbers marked with a star exhibit a standard deviation on which was in the same order of magnitude or even larger than the actual mean, hence indicating irreproducible spectra.

surfactant	sensitizer	ratio	apm	no.	ca1/ r ⁺	ca1/ d ⁺	r ⁺ / d ⁺
YA	BX12	1:1	35	2	> 200	172	0.2
YA	BX9	1:1	18	2	7.7	0.84	0.12
YA	BX9	1:4	18	2	1.8	0.35	0.2
YA	BX9	4:1	7	4	0.7	0.44	0.8
PA	BX12	1:1	12	3	3	0.7	2
PA	BX12	1:2	24	10	32*	8	1.5*
SA	BX9	1:1	7	2	0.06	0.6	9
SA	BX12	1:2	24	8	3.7*	5.3*	1.5

sensitizer signals completely dominates the spectrum as it is reflected by a very high ratio of $ca1$ to r^+ . In case of YA mixed with the short-chain sensitizer BX9, this ratio is much lower. This is in agreement with the expectation because both the FA and sensitizer are of comparable chain length and presumably exhibit about the same hydrophobicity. At a ratio of 4:1 of the YA/BX9 mixture, the methyl stretch vibration finally is stronger than the carbonyl peak. This trend is even more obvious in case of SA/BX9. Already at a ratio of 1:1, the sensitizer's signals are barely visible and the spectrum is dominated by the fatty acid. In this case, the high ratio r^+/d^+ indicates a well-ordered fatty acid layer. In conclusion, this set of measurements is in agreement with a straightforward interpretation that the more hydrophobic (and/or more abundant) compound is predominant at the interface.

8.3.3 Compression isotherms at variable surfactant/sensitizer ratios

Since the reproducibility of the isotherms of the same mixture was, in many cases, not satisfactory, four isotherms for each surfactant/sensitizer/ratio sample have been measured and averaged in the following way, typical example of this procedure of averaging is demonstrated in Fig. 8.5:

- the isotherms were concatenated to allow averaging even if the area per molecule ranges was not identical
- after concatenation, the samples were reduced to evenly spaced x (area per molecule) intervals
- the resulting noisy curve was smoothed by a moving average, choosing the window size such that the noise mostly disappeared (typically 100-400 points) but the characteristic zones of the underlying isotherms were retained

Multiple combinations of the surfactants YA, PA and SA, the sensitizers BX9 and BX12 mixed in the ratios of 1:1, 1:2, 2:1, 4:1 and 1:4 have been analyzed. The results of this series of measurements are presented in Fig. 8.6 for the ratios 1:1, 2:1 and 1:2 and in Fig. 8.7 for the ratios 1:4 and 4:1. Representative isotherms for pure fatty acid monolayer can be found in the appendix (Fig. E.1). To compare the isotherms with each other and to get a first hint whether they may indicate rather a mixed or a phase-separated layer of the surfactant and the sensitizer, they have been classified according to characteristic features.

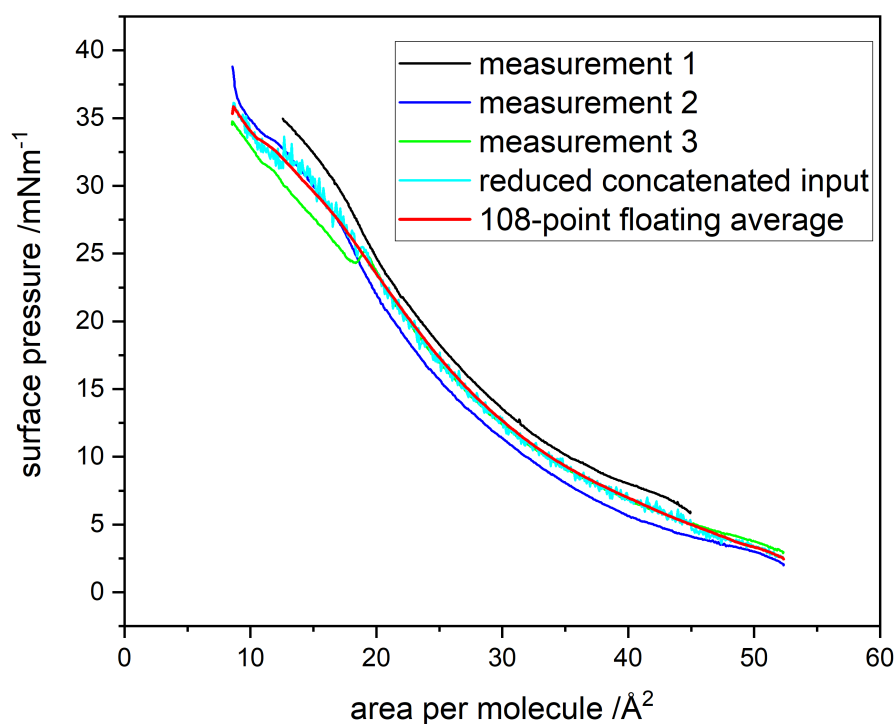


Figure 8.5: Demonstration of the averaging of multiple isotherms (SA/BX9 1:2 in this example). The reduced concatenated average is indicated in turquoise, the final smoothed curve in red.

These are schematically depicted in Fig. E.2 in the Appendix. and consist of the number of zones (parts of the isotherms determined by different slopes) and the number of plateaus (defined as regions with a slope close to 0 or very small). According to the work of KITA *et. al.*, for mixed surface layers it is possible to distinguish between miscible compounds forming true mixed monolayers and such forming separated domains with the help of the compression isotherms.^[184] An isotherm with no obvious steps and plateaus typically indicates miscibility whereas the appearance of such features can be the result of separate 2D phase transitions of the underlying phase-separated compounds. Such isotherms or zones of isotherms of nonlinear increase without plateaus or steps will be called **smooth** in the following discussion. A general overview about the determined features of all measurement, including sparklines and a short statement if the single measurements contained in the average diverged significantly from each

other, is given in Tab. 8.3 and 8.4. The following sections describe the results, subdivided into the different surfactant/sensitizer combinations.

YA/BX9

The isotherms of the 1:1 mixture used for averaging were very similar, indicating a good reproducibility of the measurements. Starting from low compression, the overall isotherm follows a smooth shape up to a molecular area of 20 \AA^2 where it is followed by another zone of rather linear increase (see Fig. 8.6 and Fig. 8.7). In case of the ratios 1:2, 2:1 and 1:4, the single measurements were much more diverging, reflecting a rather bad reproducibility of the measurements. Therefore, the reported zones of the averaged isotherms have to be treated with some caution as they may contain artifacts from the averaging process. Moreover, the overall shapes are similar to the 1:1 isotherm with a mainly smooth curvature, ending at a break point, followed by a second zone of small linear increase. The single measurements of the ratio 4:1 were again very consistent and exhibit a plateau zone between 19 and 12 \AA^2 . The transition between the smooth part and the linear zone is most prominent for the 1:4 and 4:1 ratios. This could indicate that in those cases the system is composed of domains rather than consisting of a mixed layer.

YA/BX12

Single measurements for the ratios 1:1 and 1:2 showed high variability, for the others the reproducibility was better. Although the exact position of the characteristic points of the isotherm somewhat varied, the overall shapes were well reproducible. In comparison with the mixture of YA with the lower homologue BX9, the isotherms typically exhibited multiple zones of different slopes. Note that these are not artifacts caused by the averaging procedure. A typical motif appearing in most of the isotherms were two region of constant, steep slope, separated by a small drop in surface pressure. In case of the 1:4 ratio, a long plateau at a surface pressure around 6 mN m^{-1} was observed. Concluding from the shapes of the isotherms and in comparison with the YA/BX9 system, the occurrence of domains is more likely for the YA/BX12 system.

PA/BX9

For this mixture, measurements were only made for the ratios 1:1 and 4:1. The

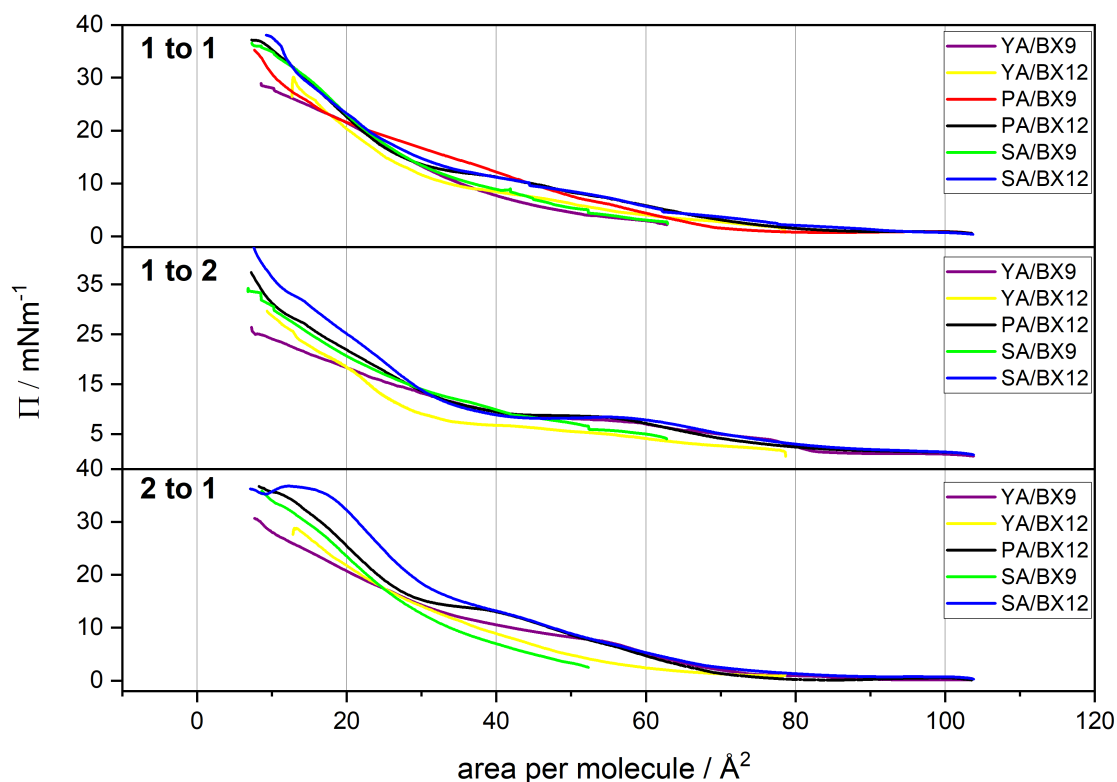


Figure 8.6: Overview of the averaged isotherms for different surfactant/sensitizer/mixture ratio combinations, Part I: ratios 1:1, 2:1, 1:2.

reproducibility in both cases was acceptable. Both systems did show a smooth shape, although for the 1:1 samples revealed a zone of low slope in the beginning and, after a breakpoint at ca. 11.6 \AA^2 , a zone with higher slope at the end of the isotherm. Surprisingly, even in the 4:1 example the isotherm appeared smooth despite the high concentration of fatty acid that may force phase separation. Concluding from the shapes, both isotherms reflect rather mixed layers than domain structure, although this applies more clearly for the 4:1 mixture.

PA/BX12

For the ratios 1:1 and 1:2, the single measurements diverged significantly. For the other samples, the observed shape of the isotherm was similar. Similar to YA, the different zones of the isotherm are much more pronounced. Another similarity is the appearance of a pronounced plateau with a surface pressure above 7 mNm^{-1} in the 1:4 measurement. This observation, since it appears at high sensitizer concentrations, could be an indicator for the formation of some

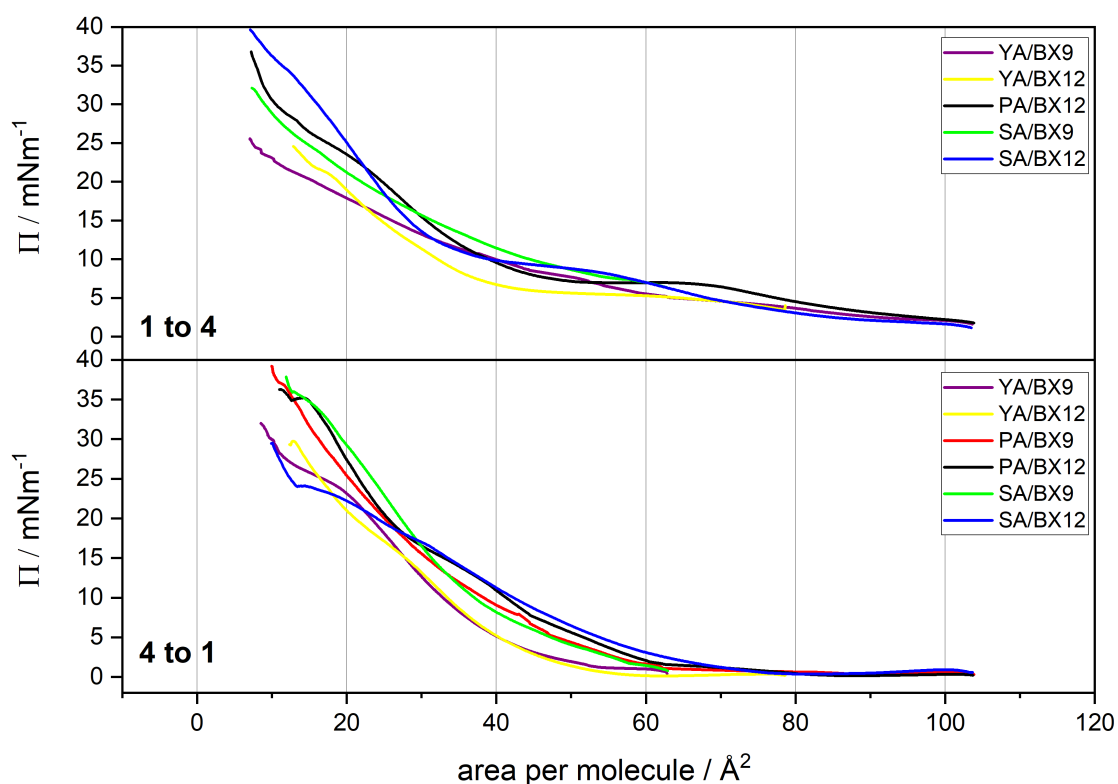


Figure 8.7: Overview of the averaged isotherms for different surfactant/sensitizer/mixture ratio combinations, Part II: ratios 4:1, 1:4.

kind of multilayer structure driven by π - π stacking interactions between the sensitizer molecules. The motif of two regions of constant slope separated by a small drop in surface pressure that was observed in the YA/BX12 isotherms as well in the 2:1 and 4:1 measurements. In general, the isotherms of this surfactant/sensitizer combination again seem to reflect a domain-like structure rather than a mixed layer.

SA/BX9

The mixtures of SA and BX9, showed a good reproducibility for all mixing ratios. For the ratios of 1:1, a pronounced plateau indicates a rather domain-like structure. For the other ratios, more or less distinct zones of slopes have been observed, presumably indicating a better mixing than for the 1:1 ratio.

SA/BX12

The reproducibility of the isotherms in this mixture was good for all ratios (except for 1:1 and 4:1). All isotherms exhibit pronounced zones of different

slope, indicating that for this mixture all ratios should be considered consisting of domains rather than a mixed monolayer.

Table 8.3: Comparison of the characteristics of the LANGMUIR compression isotherms of different surfactant/sensitizer combinations and ratios, part I. The column titled "diverging" states whether the single isotherms contained in the average-differed significantly from each other (t=true, f=false).

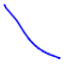


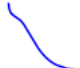

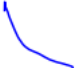


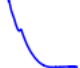
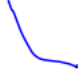
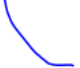




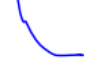
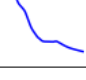

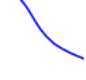

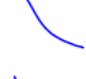
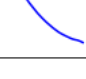





surfactant	sensitizer	ratio	plateaus	zones	diverging	sparkline
YA	BX9	1:1	0	3	f	
		2:1	1	4	t	
		1:2	0	3	t	
		4:1	0	4	f	
		1:4	0	2	t	
YA	BX12	1:1	0	2		
		2:1	0	2	t	
		1:2	0	2	f	
		4:1	0	3		
		1:4	1	3		
PA	BX9	1:1	0	3	f	
		4:1	0	3	f	

Table 8.4: Comparison of the characteristics of the LANGMUIR compression isotherms of different surfactant/sensitizer combinations and ratios, part II.

surfactant	sensitizer	ratio	plateaus	zones	diverging	sparkline
PA	BX12	1:1	0	2	t	
		2:1	1	4	f	
		1:2	1	3	t	
		4:1	0	3	f	
		1:4	1	4	f	
SA	BX9	1:1	0	2	t	
		2:1	0	2	t	
		1:2	0	2	f	
		4:1	0	2	f	
		1:4	0	2	f	
SA	BX12	1:1	0	2	t	
		2:1	1	4	f	
		1:2	1	3	f	
		4:1	0	3	t	
		1:4	1	4	f	

8.3.4 Combined VSFG/LT experiments

To get more insight into of the mixture's properties on a molecular level, VSFG spectra at selected surface pressures have been measured for a different surfactant/sensitizer combinations. For most of the systems, one low and one high surface pressure value was selected with the intention to probe different 2D states of the system. In each case, the surface pressure was kept constant by adjusting the barrier position during the duration of a measurement which was typically about 30 minutes. In case of very low intensities of the sensitizer carbonyl peaks, intensities are less accurate because the procedure of normalization to the IR and Vis intensity may cause the appearance of ghost peaks. This is due to the low IR intensities in the spectral range of the carbonyl peaks. This problem could be partially overcome by applying an additional manual baseline correction to the raw SFG intensity data (see Appendix E.3 for an example). A comparative overview about the most characteristic spectral features including all the peak ratios that will be discussed in the following sections are presented in Tab. 8.5. The results of these measurements of the systems SA/BX9 and YA/BX9 at mixture ratios of 5:1 and 1:5 are shown in 8.8.

SA/BX9, 5:1

In the low surface pressure measurement of this mixture (see Fig. 8.8, $\Pi_{\min} = 10 \text{ mN m}^{-1}$), the ca1 and ca2 signals appear very weak. The spectrum is dominated by the fatty acid signals and the d^+ signal is, as expected for the low pressure system, higher than the r^+ signal ($d^+/r^+ = 0.5$). For the high surface pressure spectrum ($\Pi_{\max} = 26 \text{ mN m}^{-1}$), the situation is inverse. The sensitizer signal remains unchanged whereas the signal of the fatty acid strongly increases. In the spectral region of the FERMI resonance, a new signal at approx. 2965 cm^{-1} is observed. Interestingly, this signal cannot be directly attributed to any of the expected signals of the individual compounds. Thus, this signal might be an indicator for a molecular interaction and within a mixed layer, of the two compounds. Considering the results of the LANGMUIR isotherm measurement of the 4:1 ratio mixture of SA/BX9 (which exhibits two distinct zones), this mixture is probably dominated by the presence of the fatty acid.

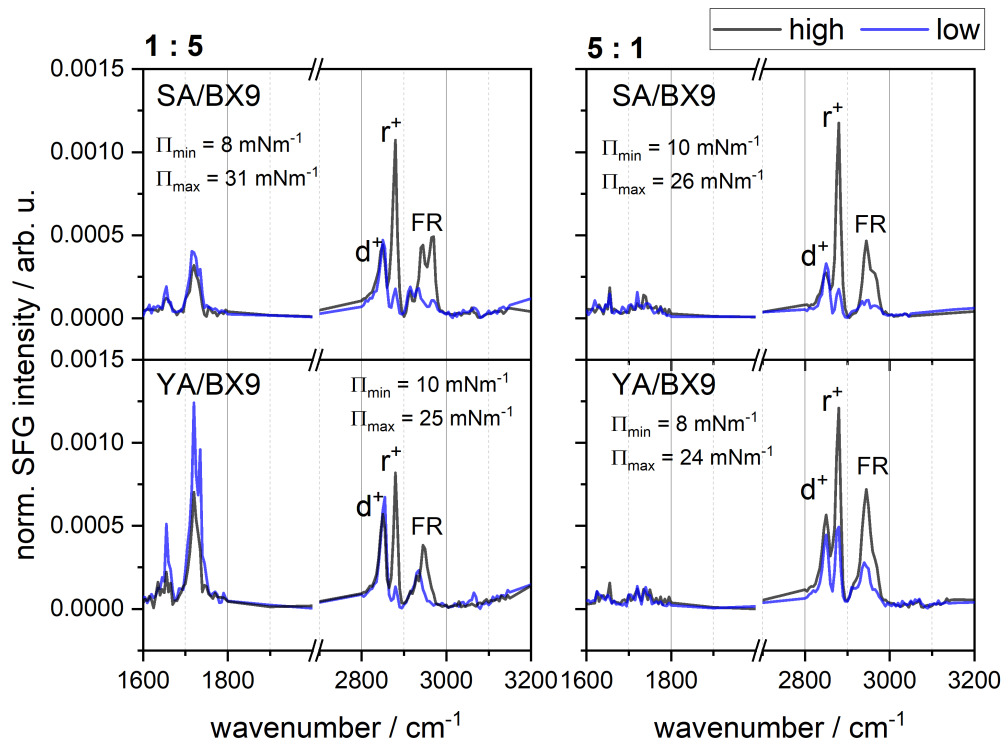


Figure 8.8: VSFG spectra recorded at constant surface pressure for the mixtures YA/BX9 and SA/BX9 with the ratio 1:1.

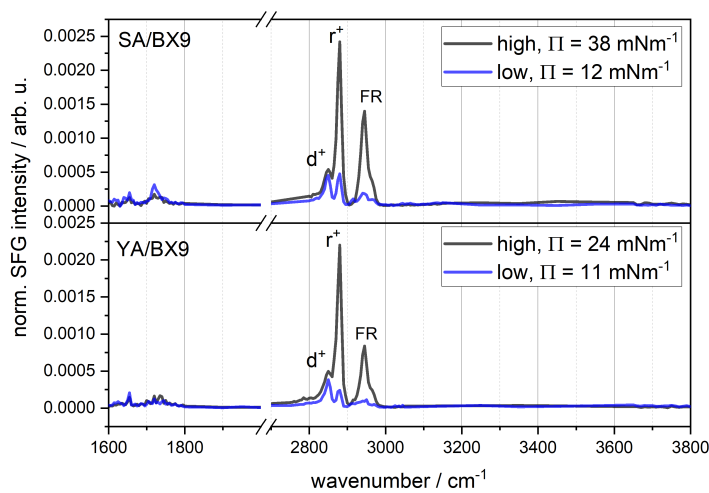


Figure 8.9: VSFG spectra recorded at constant surface pressure for the mixtures YA/BX9 and SA/BX9 with the ratio 1:1.

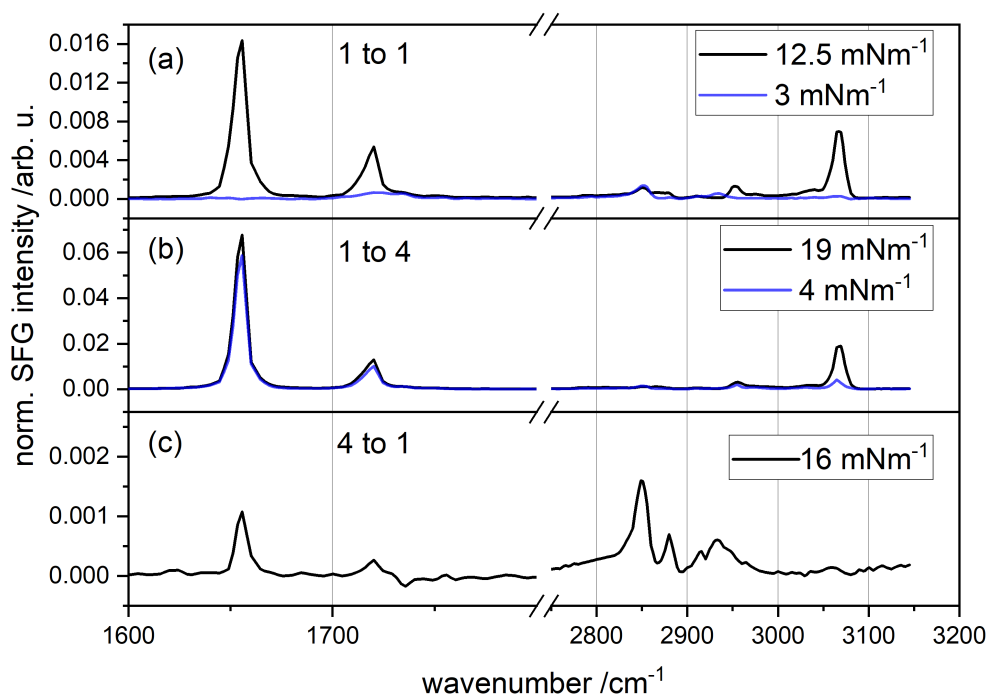


Figure 8.10: VSGF spectra recorded at constant surface pressure for the YA/BX12 mixture with a ratio of 1:1, 1:4 and 4:1.

YA/BX9, 5:1

The spectra of this ratio are shown in Fig. 8.8 ($\Pi_{\min} = 8 \text{ mNm}^{-1}$, $\Pi_{\max} = 24 \text{ mNm}^{-1}$). The low pressure spectrum of this mixture exhibits, like in its SA/BX9 analogue, very weak sensitizer carbonyl signals at Π_{\min} which also do not become much stronger at Π_{\max} measurement. Interestingly, the r^+ signal is slightly higher than the d^+ signal already in the low pressure spectrum ($d^+/r^+ = 1.1$). This is remarkable because the chain length of YA is relatively short. As expected becomes even higher in the high pressure sample. Again at Π_{\max} , the unassigned signal at 2965 cm^{-1} is observed.

The corresponding LANGMUIR isotherm (4:1 ratio, see Fig. 8.7) shows a stepped structure rather than a smooth shape, indicating a film with separate domains. Considering the very low sensitizer intensities, the observations are thus in agreement with a film that is primarily dominated by the fatty acid with minor (if at all) contributions of the sensitizer. Taking into account the extremely low amount of sensitizer in the 5:1 mixture, the degree of order of its aryl groups may

be so low that they do not yield a significant contribution to the VSFG spectrum. This cannot be stated with confidence from these data.

SA/BX9, 1:5

The spectra of this ratio are shown in Fig. 8.8 ($\Pi_{\min} = 8 \text{ mN m}^{-1}$, $\Pi_{\max} = 31 \text{ mN m}^{-1}$). For this sample, the low surface pressure measurement yielded both the ca1 and ca2 peak of the sensitizer with the latter being significantly higher than the other. The d^+ and r^+ peaks of the fatty acid appear but in this case the d^+ band is stronger than the r^+ band ($d^+/r^+ = 0.5$). Interestingly, the shape of the FERMI resonance peak appears as three resolved peaks. Most likely this is caused by an overlap of the signals from the fatty acid and the methylene groups of the sensitizer. At high surface pressure the r^+/d^+ ratio increases as expected while the sensitizer carbonyl signals remain unchanged. However, the shape of the FERMI resonance is again different compared to its appearance in spectra of pure fatty acids. It exhibits two distinct peaks (2935 and 2965 cm^{-1}). The latter is clearly distinct from the expected value of about 2945 cm^{-1} for the r^+ FERMI resonance and could be an indicator for a molecular interaction of both compounds in mixed domains. Indeed, this is in consistence with the corresponding isotherm (ratio 1:4, see Fig. 8.7), that shows two well-separated zones of slope with a rather smooth transition. In summary, the unusual shape of the FERMI resonance region, together with the observed LANGMUIR isotherm, may indicate some degree of mixture between surfactant and sensitizer.

YA/BX9, 1:5

The spectra of this ratio are shown in Fig. 8.8 ($\Pi_{\min} = 10 \text{ mN m}^{-1}$, $\Pi_{\max} = 25 \text{ mN m}^{-1}$). In the low pressure measurement of this mixture, the ca1 and ca2 peaks of the sensitizer are higher in intensity than the signals of the fatty acid, again with ca2 being more intense than ca1. The intensity of the d^+ band is much higher than for the r^+ band ($r^+/d^+ = 0.2$). In comparison to the SA/BX9 sample of the same ratio, the ar vibration of the sensitizer appears weakly at 3065 cm^{-1} but, surprisingly, only in the low pressure measurement. At Π_{\max} , the ca1 and ca2 intensities decrease with respect to the low pressure measurement whereas the intensities of the r^+ and d^+ bands increase. This is a surprising finding at this high abundance of the sensitizer. Contrary to SA/BX9 of the same mixing ratio, the shape of the FERMI resonances band is usual. Together with

the results of the LANGMUIR isotherm measured for the 1:4 ratio, it seems likely that the spectrum resembles a phase-separated domain.

SA/BX9, 1:1

Fig. 8.9 shows the results for SA/BX9 and YA/BX9 at a ratio of 1:1 ($\Pi_{\min} = 12 \text{ mN m}^{-1}$, $\Pi_{\max} = 38 \text{ mN m}^{-1}$). At low surface pressure, the mixture of SA/BX9 reveals the typical sensitizer peaks at 1655 and 1720 cm^{-1} . They appear in similar intensities as the d^+ and r^+ vibration of the fatty acid with a d^+/r^+ ratio of 1.1. The FERMI resonances of the r^+ and d^+ signal are visible as well. All possible other sensitizer SFG signals are absent. For the high surface pressure measurement, the intensity of the fatty acid signals is drastically increased in comparison with the Π_{\min} spectrum. Remarkably, the intensities of the carbonyl bands of the sensitizer remain nearly unchanged. The r^+ band in the high pressure sample is significantly higher than the d^+ band (ratio = 4.3), indicating a well-ordered fatty acid monolayer. The corresponding averaged LANGMUIR isotherm shows distinct slope zones, hence both VSFG and the LANGMUIR trough measurements are most consistent with a domain-like structure of the monolayer.

YA/BX9, 1:1

The spectra for this ratio can be found in Fig 8.9 ($\Pi_{\min} = 11 \text{ mN m}^{-1}$, $\Pi_{\max} = 24 \text{ mN m}^{-1}$). In the low pressure measurement, the signals of the carbonyl vibrations of the sensitizer are very weak. The spectrum is dominated by the peaks of the fatty acids with a r^+/d^+ ratio of 1:1. As observed for SA/BX9, at Π_{\max} the r^+/d^+ ratio strongly increases, indicating a dense layer of fatty acid molecules with well-aligned alkyl chains, whereas the sensitizer signals remain unchanged. The averaged LANGMUIR isotherm recorded for this mixture with distinct zones of slopes does support the assumption that this mixture is strongly dominated by the fatty acid.

YA/BX12 1:1

The results of the VSFG measurements at constant surface pressures are shown in fig. 8.10 ($\Pi_{\min} = 3 \text{ mN m}^{-1}$, $\Pi_{\max} = 12.5 \text{ mN m}^{-1}$). In the low pressure measurement of this sample, overall intensities are quite low. The sensitizer signals are not visible and the only prominent peak is the d^+ peak. This situation changes drastically upon compression: at high surface pressure, the spectrum is

fully dominated by the signals of the sensitizer. The d^+ and r^+ peaks are barely visible in this case, even the ch peak of the sensitizer (2950 cm^{-1}) which was usually only observed as a shoulder of the FERMI resonance region is clearly visible. This spectrum, since the amount of substance is equal for both species, indicates a clear predominance of the sensitizer in this surface layer. This is most likely a consequence of the large difference in chain lengths. Considering the averaged isotherm obtained for this mixture which however showed pronounced separated zones, the combined insight from VSFG and LANGMUIR trough data point in the direction of a film strongly dominated by the sensitizer surrounding some domains of fatty acids which are not sufficiently large to yield significant SFG signal. Another possible explanation would be that, assuming the system was over-compressed, the fatty acid as the less hydrophobic compound was completely displaced from the surface.

YA/BX12 1:4

The results of the measurement of this ratio are shown in Fig. 8.10 ($\Pi_{\min} = 4\text{ mN m}^{-1}$, $\Pi_{\max} = 19\text{ mN m}^{-1}$). Both the high and the low surface pressure measurement of this sample are dominated by the signals of the sensitizer. The fatty acid bands are nearly invisible whereas all characteristic sensitizer signals ($ca1$, $ca2$, ar , ch) are clearly detectable. Interestingly, except for an increase in the intensity of the ar band, the spectra of the low and high surface pressure measurement are very similar. Considering the isotherm for this mixture, which clearly indicate separated zones, it is likely that this system is dominated by the sensitizer.

YA/BX12 4:1

The spectra for this ratio are depicted in Fig. 8.10 ($\Pi_{\min} = 11\text{ mN m}^{-1}$, $\Pi_{\max} = 24\text{ mN m}^{-1}$). Unfortunately, for this sample only one measurement at high surface pressure is available. Interestingly, in this measurement the signals of the sensitizer and the surfactant are similar in intensity despite the fatty acid excess. Although the surface pressure was quite high, the d^+ band is higher in intensity than the r^+ , indicating a rather unordered structure. The $ca1$ peak is significantly higher than the $ca2$ peak (ratio = 3.9). The ar signal is not visible at all, what is kind of unexpected considering the relatively high carbonyl intensity. The isotherm of this mixture shows well-separated zones in the single measurements

although the average curve appears smooth because of mutual compensation of the different slope regions. This mixture is especially interesting. Although the fatty acid is much more abundant, the sensitizer is clearly visible in the SFG spectrum and influences the isotherm. It would be of great interest to investigate the nature of this mixture further since the current data does not allow a clear statement whether this layer is well-mixed or domain-like.

Table 8.5: Compiled overview about the most important characteristics of the VSFG spectra obtained from measurements at constant surface pressure. The column apm reports the area per molecule in \AA^2 , the surface pressure Π is reported in mN m^{-1} .

surfactant	sensitizer	ratio	$\Pi / \text{mN m}^{-1}$	$\text{apm} / \text{\AA}^2$	r^+ / d^+	$\text{ca1} / \text{ca2}$	$\text{ca2} / r^+$	$\text{ca1} / r^+$	$\text{ca1} / d^+$	$\text{ca2} / r^+$
SA	BX12	1:1	12.5	35	0.53	3.00	7.00	21.00	11.05	3.68
SA	BX12	1:1	6	58	0.85	3.29	2.12	6.97	5.93	1.80
YA	BX12	1:1	12.5	29	0.47	3.02	8.26	24.92	11.64	3.86
YA	BX12	1:1	3	66.						
YA	BX12	1:4	19	20		5.23				
YA	BX12	1:4	4	74		5.86			58.60	10.00
YA	BX12	4:1	16	26	0.44	3.85	0.37	1.41	0.63	0.16
SA	BX9	1:5	38	25	2.43	0.39	0.30	0.11	0.28	0.72
SA	BX9	1:5	1	64	0.38	0.48	2.21	1.07	0.41	0.85
SA	BX9	5:1	26	20	4.31	1.34	0.12	0.16	0.69	0.52
SA	BX9	5:1	10	60	0.52	2.03	0.42	0.86	0.45	0.22
SA	BX9	1:1	38	31	4.45	0.69	0.07	0.05	0.23	0.33
SA	BX9	1:1	12	78	1.07	0.61	0.67	0.40	0.43	0.71
YA	BX9	1:5	25	26	1.47	0.31	0.86	0.27	0.39	1.27
YA	BX9	1:5	10	74	0.21	0.43	8.99	3.91	0.81	1.86
YA	BX9	5:1	24	24	2.13	1.34	0.10	0.13	0.28	0.21
YA	BX9	5:1	8	84	1.09	0.65	0.29	0.19	0.20	0.31
YA	BX9	1:1	26	25	4.31	1.00		0.07	0.29	0.29
YA	BX9	1:1	11	72	0.64	1.27		0.85	0.54	0.43

8.3.5 Photolysis experiments

First photolysis measurements have been performed utilizing selected FA/BX combinations by irradiating the sample dish with light from a Xe lamp. A typical result of this kind of experiment is depicted in Fig. 8.11. For comparison, the figure also shows the photolysis of a monolayer of pure palmitic acid, demonstrating the inertness of this compound to radiation at this wavelength. The black curve represents the initial measurement before any photolysis, the blue after 15 min. and the red after 45 minutes of photolysis. Note that in between the continued photolysis of the samples some time elapsed because each SFG measurement took approx. 20 minutes. Comparing those curves, it is obvious that the signals associated with the sensitizer (the two carbony bands and the aromatic vibration) which are the most prominent peaks in the initial measurement, disappear almost completely already after 15 minutes. The same applies for the ν^+ band (symmetric stretch vibration of the terminal methyl group of the fatty acid). In contrast, the ν^+ of the fatty acid at 2850 cm^{-1} shows only a small decrease in intensity. Comparing the measurements after 15 and 45 minutes of photolysis, only small changes in the CH region are visible. In particular the intensity of the ν^+ band of the PA declined, which can be interpreted as the equilibration of the remaining PA to a steady state after the photolysis is complete, most likely occurring after all sensitizer molecules already disappeared. If the photolysis induced some cross-reactivity between the photosensitizer and the fatty acid, can not be answered from from this experiment. Although the ν^+ band of the fatty acid significantly decreases, this might be an effect of the total decrease in surface concentration alone. Neglecting all effects of structure and assuming that the photosensitizer (i.e. the photolysis product) completely disappeared from the interface, the of the fatty acid signal would decrease with the square of the concentration (see chapter 2.2.2). This would result in an expected decrease in fatty acid signal of a factor of about nine. Although the ν^+ band disappears completely, the nearly unchanged methylene signal may indicate that photolysis products remain at the surface and/or the structural order of the alkyl chains is reduced. Actually, the results are more compatible with a sole photodecomposition of the sensitizer. Keeping in mind that at the studied mixing ratio of 1:2 the FA and the sensitizer form separate domains (as it is indicated by the LANGMUIR isotherm measurements), this may not be fully

surprising.

Multiple experiments of this kind employing different sensitizer/surfactant combinations and ratios have been performed. In these experiments the changes in the r^+ and d^+ bands were analyzed and compared with the expected change of signal intensity if only the sensitizer would be degraded. These results are compiled in Tab. 8.6. Again, the expected change was calculated under the assumption of full removal of the photosensitizer but leaving the FA unchanged. For example, in the case of a 1:4 mixture, the expected ratio r_e is calculated as follows:

$$r_e = \left(1 - \frac{4}{5}\right)^2 = \left(\frac{1}{5}\right)^2 = 0.04 \quad (8.1)$$

Table 8.6: Overview of the observed changes in SFG peak ratios following photolysis of various FA/BX mixtures. The column "expected" shows the expected ratio under the assumption of complete removal of the sensitizer from the surface and negligible structural changes of the FA molecules. The "dev" columns illustrate the deviation of the observed from the expected value.

surf- tant	sensi- tizer	ratio	apm/ mN m ⁻¹	t _{photolysis} / min.	r _{expected}	r _{before} ⁺ / r _{after} ⁺	d _{before} ⁺ / d _{after} ⁺	deviation r ratio	deviation d ratio
PA	BX12	1to1	24	30	0.25	0.51	1.84	2.0	7.3
PA	BX12	1to1	24	45	0.25	0.36	0.07	1.5	0.3
PA	BX12	1to2	24	15	0.11	0.50	0.04	4.5	0.3
PA	BX12	1to2	24	45	0.11	0.69	0.10	6.2	0.9
PA	BX12	1to2	24	45	0.11	0.68	0.07	6.1	0.6
SA	BX9	1to1	7	56	0.25	0.60	0.52	2.4	2.1
SA	BX9	1to1	7	24	0.25	0.43	0.83	1.7	3.3
SA	BX12	1to2	24	60	0.11	0.83	0.19	7.5	1.7
SA	BX12	1to2	12	45	0.11	0.58	0.39	5.3	3.5
SA	BX12	1to2	24	75	0.11	1.33	0.31	11.9	2.8
YA	BX9	1to1	7	25	0.25	0.12	0.12	0.5	0.5
YA	BX9	1to1	7	90	0.25	0.22	0.06	0.9	0.2
YA	BX9	1to1	18	28	0.25	0.24	0.99	0.9	3.9
YA	BX9	1to1	18	28	0.25	0.20	0.47	0.8	1.9
YA	BX9	4to1	7	48	0.64	0.73	0.29	1.1	0.5
YA	BX9	4to1	7	27	0.64	0.12	0.14	0.2	0.2
YA	BX9	4to1	7	27	0.64	0.16	0.10	0.2	0.2
YA	BX9	1to4	18	38	0.04	0.31	0.74	7.8	18.4
YA	BX9	1to4	18	27	0.04	0.12	0.25	3.0	6.3

In nearly all of the photolysis experiments, the VSFG signals of the sensitizer disappeared completely within approx. 30 minutes. In almost all of the cases, the change of either the r^+ or d^+ band was equal to or lower than the expected one determined by the sensitizer degradation. The only notable exception was the mixture of YA/BX9 with a ratio of 4:1 (hence a high percentage of the fatty acid). In 2 of 3 measurements, the decrease in both CH signals was much higher than expected. The same held true for two measurements of YA/BX9 in the ratio 1:1. Before coming to conclusions from these promising results, it should be stated that in most of the measurements the initial area per molecule was chosen rather high, so it is well possible that one of the species was displaced from the surface, making the interpretation of the results even more challenging. Considering the situation in a natural system with few sensitizer molecules surrounded by an excess of photoinert material, the experimental composition is not desirable for mimicking natural systems. Therefore, future experiments should focus on mixtures with a lower sensitizer concentration, especially to avoid the autophotolysis. Note that the reaction mechanisms of the photochemical processes as well resulting products remain unclear. In principle, three options (or a combination of them) are possible:

- Formation of soluble reaction products followed by dissolution into the bulk water, thus disappearing from the interface.
- Formation of insoluble reaction products that remain at the interface.
- Formation of volatile, gas phase products that evaporate from the surface.

To determine which of this scenarios applies, further investigation is necessary.

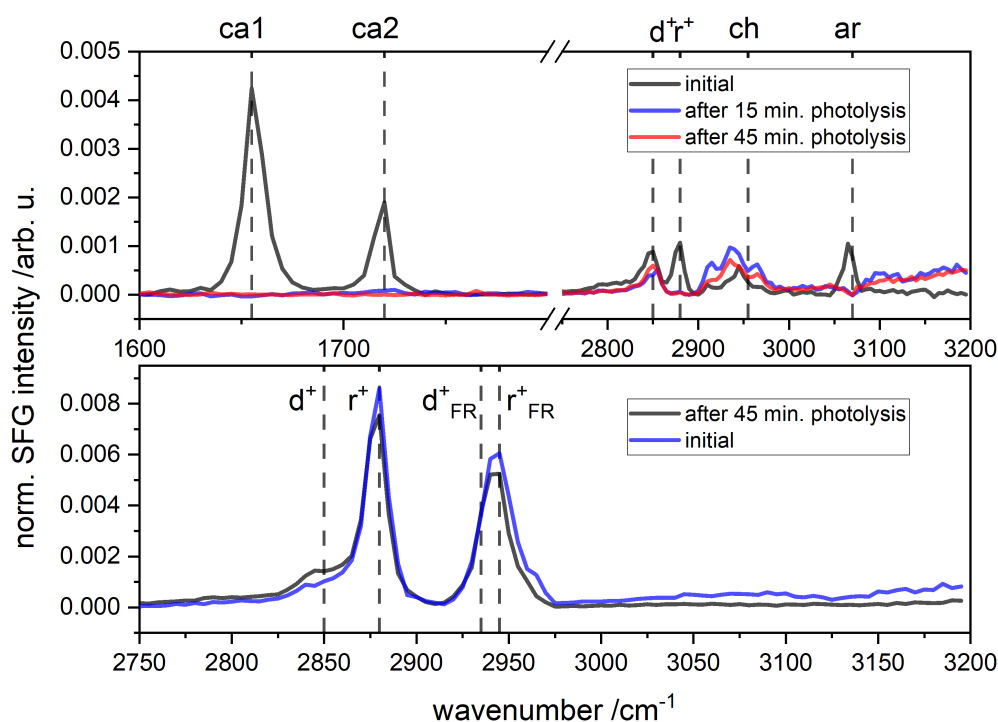


Figure 8.11: SFG spectra before and after photolysis of monolayers of palmitic acid (PA) and a mixture with the sensitizer BX12 with a ratio of 1:2. Below, the photolysis of a monolayer of pure palmitic acid is demonstrated.

8.4 Summary and Outlook

All in all, this systematic investigation of mixed monolayer composed of the novel surface photosensitizers and fatty acids, both with variable alkyl chain lengths, using complementary surface-sensitive techniques yielded valuable insight. Data about the molecular and, in particular, surface properties of the BX photosensitizer and their behavior when incorporated into mixed surface layers was not available beforehand. This made it necessary to choose a more systematic-explorative experimental approach for this work, heading towards a basic understanding of those interfacial systems. Summarizing all the insights gained throughout the various analysis approaches, some preliminary conclusions may be drawn. In general, the mixtures based on BX12 yielded data indicating the presence of domain structures rather than mixed layers. In compression isotherm measurements, the determined number of distinct slope regions and the overall quality of the isotherms was not well reproducible for BX12. More consistent results were obtained with BX9. In VSFG experiments,

the BX12 signals often dominated the spectrum, especially at high surface concentrations. In addition, the difference in molecule size (or, more precisely, hydrophobicity induced by the variable chain lengths) lead to the dominance of the respective larger molecule. In extreme cases spectra have been obtained where only the signals of the smaller species was present. Note that this observation could also be the result of overcompression of the system, leading to a collapse of the layer with only one compound (the more surface-active) remaining at the interface. Based on the insights gained from the systematic LANGMUIR isotherm measurements and supported by the additional VSFG measurements, a tentative assessment mixed layers or separated domains of the compounds are present in surface layers of the corresponding FA/BX mixtures was possible. The results are summarized in Tab. 8.7. Although those results have to be interpreted with caution because of the aforementioned issues with reproducibility and the current lack of deep molecular-level understanding of this systems. The most promising candidate for the preparation of a SML photochemistry model system without well-mixed monolayer is the mixture of SA and BX9 system. This could indicate that, in principle, mixtures of short sensitizers and long fatty acids tend do form mixed layers instead of domains. Upon photolysis, the sensitizers were reliably degraded, but whether the fatty acid reacted as can not be concluded from these experiments alone. As the used mixture's sensitizer ratio was always high, the complete degradation of the sensitizer caused a strong reduction of molecule density at the surface. Therefore, a strong decrease of SFG signal intensity was expected anyway. Besides that, the general very high surface concentrations that were applied in these set of experiments for the sake of good signal quality are not optimal for thermodynamically equilibrated and well-defined mixed layers. For those reasons, in future experiments it is highly desirable to utilize much lower amounts of the sensitizer and apply overall lower surface concentrations. Moreover, complementary analytical techniques to determine the nature of the surface layers (mixed layers or domains) are required since the SFG/LT data do not yield enough information. A suitable method for this purpose would be BREWSTER angle microscopy, a technique that has been applied successfully to investigate domain formation upon phase transition in LANGMUIR films. Another interesting approach for future experiments would be the alteration of the photochemical reactivity of the surfactants component within the mixtures. This could be achieved by modifying the chem-

Table 8.7: Estimation if the experimental results indicate rather mixed layers (m) or separated domains (d).

surfac- tant	sensi- tizer	ratio	layer type	surfac- tant	sensi- tizer	ratio	layer type
YA	BX9	1:1	m	PA	BX12	1:1	d
		2:1	d			2:1	d
		1:2	d			1:2	d
		4:1	d			4:1	d
		1:4	d			1:4	d
YA	BX12	1:1	m	SA	BX9	1:1	d
		2:1	d			2:1	m
		1:2	d			1:2	m
		4:1	d			4:1	m
		1:4	d			1:4	m
PA	BX9	1:1	d	SA	BX12	1:1	d
		2:1	-			2:1	d
		1:2	-			1:2	d
		4:1	m			4:1	d
		1:4	-			1:4	d

ical composition in a way that the formation of mixed layers with BX is more favorable. A possible modification to achieve this could be to place an aromatic moiety within the surfactant's chain, trying to induce energetically favorable π - π stacking interaction with the photosensitizer BX.

CHAPTER 9

Summary

The focus of this work was the systematic investigation of natural sea surface nanolayer samples and a first step towards the systematic study of the surface nanolayer photochemistry by means of modern surface-sensitive analytical techniques. The project was structured in complementary subtasks. First, a software tool set to support handling, systematic storage and automatized batch analysis of analytical data has been implemented as open source code. Second, these tools have been employed to analyze the SML abundance data in terms of newly established surfactant indices based on vibrational sum frequency generation spectroscopic and LANGMUIR trough compression isotherms. Monthly samples from the Boknis Eck Time series and from the Baltic GasEx cruise in 2018 served as examples. Third, a novel class of surface-active photosensitizers as a model system for photochemistry taking place at the very interface between air and water was created. This covered design, synthesis and characterization of the new class of surface active photosensitizers (so-called BX) with respect to its interfacial behavior and photochemical properties. As next step towards better mimicking natural systems, mixed surface layers of the sensitizers with fatty acids have been prepared, characterized and photolyzed.

Implementation of software tools to support analytical data handling and visualization
The efficient management of experimental data as they are typically obtained in scientific studies is a challenge. Keeping track of metadata such as environmental conditions, performing (unbiased) analytical tasks upon massive amounts of data and sharing them among co-working researcher can be simplified by applying the knowledge and tools of modern software engineering. Such tools are also required to comply with the **FAIR** (Findability, Accessibility, Interoperability, and Reusability) guide principles of digital data management. In this work, a

collection of tools to support the handling and analysis of the experimental data measured in its course have been implemented using Python. The features of those tools include systematic storage of the data and metadata in a relational database, functionality for automatic baseline correction, integration and averaging of multiple VSFG spectra and visualization tool chains for several different measurement data. The database organization allows efficient grouping and statistical evaluation of related measurements, e.g. comparing samples obtained during the same month or automatically normalizing a spectrum to the reference that was measured on the same day. Those tools have been published as open source code on the GitHub platform.

Investigation of natural SML/NL surfactants

Those tools have been applied to analyze the VSFG spectra (carrying information about the surfactant abundance) of sea surface water samples obtained during the monthly cruise to the Boknis Eck time series station. Besides the collection of new samples in 2017 and 2018, the old data (obtained 2009-2015) were re-evaluated using the new routines (sorting, automatic baseline correction, averaging and normalization). The enrichment of surfactants in the Sea Surface Microlayer (SML) with respect to the underlying bulk water as well as the higher VSFG intensity occurring in the middle of the year compared to early spring and winter as found in the first analysis published 2013 could be confirmed by the new results. In addition, also using the new procedures no coincidence of the annual VSFG signal maximum with the annual chlorophyll maximum was found, supporting the hypothesis of sloppy feeding and organic matter transformation as prerequisite for nanolayer abundance. However, the larger amount of data as well as a generally lower surfactant abundance in the later years of the analysis lead to a less pronounced seasonal trend of the signal in the course of the year than could be expected from the previously published work. In 2018, the Baltic GasEx campaign with the goal to investigate the influence of surfactant abundance on the gas transfer velocity was conducted. During both cruises of the campaign, sea surface water samples have been collected several times a day using both GARRETT screen and glass plate SML sampling. It was sampled from both a zodiac and from board of the cruise vessel. The samples have been analyzed by means of VSFG spectroscopy and, complementary, LANGMUIR compression isotherm and surface tension measurements to

characterize the surfactant abundance. A set of simple numeric indices for surfactant abundance were extracted as the most relevant core information from the rather complex measurement data. Such simple to use surfactant indices facilitate interdisciplinary data exchange and communication. Unfortunately, The surfactant abundances measured during the campaign were generally very low. No significant differences in the resulting surfactant abundance indices in between plate and screen sampling or between sampling from the ship and from the zodiac were found. The difference in surfactant abundance between the cruises of the campaign was very low, with slightly higher values for the first cruise. For future investigations, this kind of study should be repeated at higher surfactant concentrations to ensure the reliability of the proposed surfactant abundance indices.

Artificial photosensitizers at the air/water interface

The physicochemical investigation of the photochemistry occurring at the direct interface between the ocean and air is, because of the small lateral dimension of this zone, very challenging. Ideally, it requires model systems that form stable surface layers and are active as photosensitizers. In this work, a novel class of photosensitizers (so-called BX sensitizers) with those properties has been designed, synthesized and characterized. The three new molecules were obtained by a one-step esterification of the well-known photosensitizer benzoylbenzoic acid with three symmetric diols of different chain length (6, 9 and 12 C atoms). The resulting sensitizers, especially BX9 and BX12, turned out to form well-ordered monolayers and are susceptible to photolysis initiated by the light of a solar simulator. In addition, they yielded VSFG spectra of excellent quality with two untypically pronounced carbonyl signals and a strong aromatic CH vibration. This finding indicates a dense monolayer with high structural order, probably induced by $\pi - \pi$ -stacking of the aromatic systems.

As in the SML typically only a small amount of the organic material is photochemically active, instead of using monolayers of the pure sensitizers, the next step towards a more realistic model system was the preparation of mixed layers of BX9 and BX12 with naturally-occurring, surface-active fatty acids with different chain length (myristic acid (C14), palmitic acid (C16), arachidic acid (C18)) at five different ratios (1:1, 1:2, 2:1, 5:1, 1:5). Using VSFG analysis combined with LANGMUIR compression isotherm measurements, these mea-

surements were designed to find hints whether the resulting surface layers were rather separated domains of the single compounds or well-mixed layers. Mixed layers can be considered the better SML photochemistry model system. Based on the obtained data, the combination stearic acid/BX9 (sensitizer with chain length=9) was identified as the most promising candidate for future studies on SML photochemistry.

Bibliography

- [1] K. A. HUNTER, 'Chemistry of the sea-surface microlayer' *Sea Surf. Glob. Chang.* Cambridge University Press, **Mar. 1997**, pp. 287–320, DOI 10.1017/CB09780511525025.010 (cit. on pp. 1, 91).
- [2] M. CUNLIFFE, A. ENGEL, S. FRKA, B. Ž. GAŠPAROVIĆ, C. GUITART, J. C. MURRELL, M. SALTER, C. STOLLE, R. UPSTILL-GODDARD, O. WURL, 'Sea surface microlayers: A unified physicochemical and biological perspective of the air-ocean interface', *Prog. Oceanogr.* **2013**, *109*, 104–116, DOI 10.1016/j.pocean.2012.08.004 (cit. on pp. 1, 73, 91, 128, 147).
- [3] A. ENGEL et al., 'The ocean's vital skin: Toward an integrated understanding of the sea surface microlayer', *Front. Mar. Sci.* **2017**, *4*, 1–14, DOI 10.3389/fmars.2017.00165 (cit. on pp. 1–3, 73, 74, 91, 127, 147).
- [4] O. WURL, W. EKAU, W. M. LANDING, C. J. ZAPPA, 'Sea surface microlayer in a changing ocean – A perspective', *Elem Sci Anth* **June 2017**, *5*, 31, DOI 10.1525/elementa.228 (cit. on pp. 1, 4, 73, 91).
- [5] J. M. I. SIEBURTH, 'Microbiological and organic-chemical processes in the surface and mixed layers' *Air–Sea Exch. Gases Part.* (Eds.: P. LISS, W. SLINN), Springer Netherlands, Dordrecht, **1983**, pp. 121–172, DOI 10.1007/978-94-009-7169-1 (cit. on p. 1).
- [6] V. ŽUTIC, B. ĆOSOVIĆ, E. MARĆENKO, N. BIHARI, 'Surfactant production by marine phytoplankton', *Mar. Chem.* **1981**, *10*, 505–520, DOI 10.1016/0304-4203(81)90004-9 (cit. on pp. 1, 91).
- [7] MYKLESTA.S, 'Production of Carbohydrates By Marine Planktonic Diatoms .1. Comparison of 9 Different Species in Culture', *J. Exp. Mar. Bio. Ecol.* **1974**, *15*, 261–274, DOI 10.1016/0022-0981(74)90049-5 (cit. on p. 1).

- [8] W. D. GARRETT, 'The organic chemical composition of the ocean surface', *Deep. Res. Oceanogr. Abstr.* **1967**, *14*, DOI 10.1016/0011-7471(67)90007-1 (cit. on pp. 1, 147).
- [9] L. A. COPEMAN, C. C. PARRISH, 'Marine lipids in a cold coastal ecosystem: Gilbert Bay, Labrador', *Mar. Biol.* **2003**, *143*, 1213–1227, DOI 10.1007/s00227-003-1156-y (cit. on p. 1).
- [10] S. M. HENRICHS, P. M. WILLIAMS, 'Dissolved and particulate amino acids and carbohydrates in the sea surface microlayer', *Mar. Chem.* **1985**, *17*, 141–163, DOI 10.1016/0304-4203(85)90070-2 (cit. on pp. 1, 91, 147).
- [11] M. KUZNETSOVA, C. LEE, J. ALLER, N. FREW, 'Enrichment of amino acids in the sea surface microlayer at coastal and open ocean sites in the North Atlantic Ocean', *Limnol. Oceanogr.* **2004**, *49*, 1605–1619, DOI 10.4319/10.2004.49.5.1605 (cit. on p. 1).
- [12] K. A. HUNTER, P. S. LISS, 'The input of organic material to the oceans: air-sea interactions and the organic chemical composition of the sea surface', *Mar. Chem.* **1977**, *5*, 361–379, DOI 10.1016/0304-4203(77)90029-9 (cit. on pp. 1, 91, 128).
- [13] U. PASSOW, Formation of transparent exopolymer particles, TEP, from dissolved precursor material, **2000**, DOI 10.3354/meps192001 (cit. on pp. 1, 91).
- [14] U. PASSOW, 'Transparent Exopolymer Particles in Aquatic Environments', *Prog. Oceanogr.* **2002**, *55*, 287–333, DOI 10.1016/S0079-6611(02)00138-6 (cit. on p. 1).
- [15] K. AZETSU-SCOTT, U. PASSOW, 'Ascending marine particles: Significance of transparent exopolymer particles (TEP) in the upper ocean', *Limnol. Oceanogr.* **2004**, *49*, 741–748, DOI 10.4319/10.2004.49.3.0741 (cit. on p. 1).
- [16] O. WURL, E. WURL, L. MILLER, K. JOHNSON, S. VAGLE, 'Formation and global distribution of sea-surface microlayers', *Biogeosciences* **2011**, *8*, 121–135, DOI 10.5194/bg-8-121-2011 (cit. on pp. 1, 73, 91, 127, 128, 147).

-
- [17] D. C. O. THORNTON, S. D. BROOKS, J. CHEN, 'Protein and Carbohydrate Exopolymer Particles in the Sea Surface Microlayer (SML)', *Front. Mar. Sci.* **2016**, *3*, 1–14, DOI 10.3389/fmars.2016.00135 (cit. on pp. 1, 91).
- [18] O. WURL, C. STOLLE, C. VAN THUOC, P. THE THU, X. MARI, 'Biofilm-like properties of the sea surface and predicted effects on air-sea CO₂ exchange', *Prog. Oceanogr.* **2016**, *144*, 15–24, DOI 10.1016/j.pocean.2016.03.002 (cit. on pp. 1, 73, 92, 147).
- [19] O. WURL, M. HOLMES, 'The gelatinous nature of the sea-surface microlayer', *Mar. Chem.* **2008**, *110*, 89–97, DOI 10.1016/j.marchem.2008.02.009 (cit. on pp. 1, 91).
- [20] L. GALGANI, J. PIONTEK, A. ENGEL, 'Biopolymers form a gelatinous microlayer at the air-sea interface when Arctic sea ice melts', *Sci. Rep.* **2016**, *6*, 1–10, DOI 10.1038/srep29465 (cit. on p. 1).
- [21] M. van PINXTEREN, C. MÜLLER, Y. IINUMA, C. STOLLE, H. HERRMANN, 'Chemical Characterization of Dissolved Organic Compounds from Coastal Sea Surface Microlayers (Baltic Sea, Germany)', *Environ. Sci. Technol.* **2012**, *46*, 10455–10462, DOI 10.1021/es204492b (cit. on p. 1).
- [22] D. J. CARLSON, 'Dissolved organic materials in surface microlayers: Temporal and spatial variability and relation to sea state', *Limnol. Oceanogr.* **1983**, *28*, 415–431, DOI 10.4319/lo.1983.28.3.0415 (cit. on p. 2).
- [23] R. SCHMIDT, B. SCHNEIDER, 'The effect of surface films on the air-sea gas exchange in the Baltic Sea', *Mar. Chem.* **2011**, *126*, 56–62, DOI 10.1016/j.marchem.2011.03.007 (cit. on p. 2).
- [24] Z. ZHANG, L. LIU, C. LIU, W. CAI, 'Studies on the sea surface microlayer: II. The layer of sudden change of physical and chemical properties', *J. Colloid Interface Sci.* **Aug. 2003**, *264*, 148–159, DOI 10.1016/S0021-9797(03)00390-4 (cit. on pp. 2, 128).
- [25] N. M. FREW, E. J. BOCK, U. SCHIMPF, T. HARA, H. HAUSSECKER, J. B. EDSON, W. R. MCGILLIS, R. K. NELSON, S. P. MCKENNA, B. M. UZ, B. JÄHNE, 'Air-sea gas transfer: Its dependence on wind stress, small-scale roughness, and surface films', *J. Geophys. Res. Ocean.* **2004**, *109*, n/a–n/a, DOI 10.1029/2003JC002131 (cit. on pp. 2, 147).

- [26] H. HÜHNERFUSS, W. ALPERS, W. D. GARRETT, P. A. LANGE, S. STOLTE, 'Attenuation of Capillary and Gravity Waves At Sea By Monomolecular Organic Surface Films.', *J. Geophys. Res.* **1983**, *88*, 9809–9816, DOI 10.1029/jc088ic14p09809 (cit. on pp. 2, 73, 92).
- [27] H. HÜHNERFUSS, P. LANGE, W. WALTER, 'Wave damping by monomolecular surface films and their chemical structure. Part II: Variation of the hydrophilic part of the film molecules including natural substances', *J. Mar. Res.* **Aug. 1984**, *42*, 737–759, DOI 10.1357/002224084788506059 (cit. on pp. 2, 73, 92).
- [28] H. HÜHNERFUSS, P. A. LANGE, W. WALTER, 'Wave damping by monomolecular surface films and their chemical structure. Part I: Variation of the hydrophobic part of carboxylic acid esters', *J. Mar. Res.* **1982**, *40*, 209–225 (cit. on p. 2).
- [29] S. MCKENNA, W. MCGILLIS, 'The role of free-surface turbulence and surfactants in air–water gas transfer', *Int. J. Heat Mass Transf.* **Jan. 2004**, *47*, 539–553, DOI 10.1016/j.ijheatmasstransfer.2003.06.001 (cit. on p. 2).
- [30] E. MESARCHAKI, C. KRÄUTER, K. E. KRALL, M. BOPP, F. HELLEIS, J. WILLIAMS, B. JÄHNE, 'Measuring air-sea gas-exchange velocities in a large-scale annular wind-wave tank', *Ocean Sci.* **2015**, *11*, 121–138, DOI 10.5194/os-11-121-2015 (cit. on p. 2).
- [31] M. E. SALTER, R. C. UPSTILL-GODDARD, P. D. NIGHTINGALE, S. D. ARCHER, B. BLOMQUIST, D. T. HO, B. HUEBERT, P. SCHLOSSER, M. YANG, 'Impact of an artificial surfactant release on air-sea gas fluxes during Deep Ocean Gas Exchange Experiment II', *J. Geophys. Res. Ocean.* **2011**, *116*, 1–9, DOI 10.1029/2011JC007023 (cit. on p. 2).
- [32] R. PEREIRA, K. SCHNEIDER-ZAPP, R. C. UPSTILL-GODDARD, 'Surfactant control of gas transfer velocity along an offshore coastal transect: Results from a laboratory gas exchange tank', *Biogeosciences* **2016**, *13*, 3981–3989, DOI 10.5194/bg-13-3981-2016 (cit. on pp. 2, 73, 92, 147).
- [33] D. K. WOOLF, 'Bubbles and their role in gas exchange' *Sea Surf. Glob. Chang.* Cambridge University Press, **Mar. 1997**, pp. 173–206, DOI 10.1017/CB09780511525025.007 (cit. on p. 2).

-
- [34] P. K. QUINN, T. S. BATES, K. S. SCHULZ, D. J. COFFMAN, A. A. FROSSARD, L. M. RUSSELL, W. C. KEENE, D. J. KIEBER, 'Contribution of sea surface carbon pool to organic matter enrichment in sea spray aerosol', *Nat. Geosci.* **2014**, *7*, 228–232, DOI 10.1038/ngeo2092 (cit. on pp. 2, 128).
- [35] R. E. COCHRAN, O. S. RYDER, V. H. GRASSIAN, K. A. PRATHER, 'Sea spray aerosol: The chemical link between the oceans, atmosphere, and climate', *Acc. Chem. Res.* **2017**, *50*, 599–604, DOI 10.1021/acs.accounts.6b00603 (cit. on pp. 2, 128).
- [36] P. SCHMITT-KOPPLIN, G. LIGER-BELAIR, B. P. KOCH, R. FLERUS, G. KATTNER, M. HARIR, B. KANAWATI, M. LUCIO, D. TZIOTIS, N. HERTKORN, 'Dissolved organic matter in sea spray: A transfer study from marine surface water to aerosols', *Biogeosciences* **2012**, *9*, 1571–1582, DOI 10.5194/bg-9-1571-2012 (cit. on p. 2).
- [37] A. J. KWAN, J. D. CROUNSE, A. D. CLARKE, Y. SHINOZUKA, B. E. ANDERSON, J. H. CRAWFORD, M. A. AVERY, C. S. MCNAUGHTON, W. H. BRUNE, H. B. SINGH, P. O. WENNERBERG, 'On the flux of oxygenated volatile organic compounds from organic aerosol oxidation', *Geophys. Res. Lett.* **2006**, *33*, 1–5, DOI 10.1029/2006GL026144 (cit. on p. 2).
- [38] H. TERVAHATTU, J. JUHANOJA, K. KUPIAINEN, 'Identification of an organic coating on marine aerosol particles by TOF-SIMS', *J. Geophys. Res. Atmos.* **2002**, *107*, 1–7, DOI 10.1029/2001JD001403 (cit. on pp. 2, 3).
- [39] L. M. RUSSELL, L. N. HAWKINS, A. A. FROSSARD, P. K. QUINN, T. S. BATES, 'Carbohydrate-like composition of submicron atmospheric particles and their production from ocean bubble bursting', *Proc. Natl. Acad. Sci.* **2010**, *107*, 6652–6657, DOI 10.1073/pnas.0908905107 (cit. on p. 2).
- [40] M. CUNLIFFE, O. WURL, 'Guide to best practices to study the ocean's surface', *Occas. Publ. Mar. Biol. Assoc. United Kingdom* **2014**, 118 (cit. on pp. 3, 44, 76, 115).
- [41] K. LASS, J. KLEBER, G. FRIEDRICHS, K. LAß, J. KLEBER, G. FRIEDRICHS, 'Vibrational sum-frequency generation as a probe for composition, chemical reactivity, and film formation dynamics of the sea surface nanolayer', *Limnol. Oceanogr. Methods* **May 2010**, *8*, 216–228, DOI 10.4319/1om.2010.8.216 (cit. on pp. 3, 9, 74, 75, 78, 92, 96, 130, 132).

- [42] B. ĆOSOVIĆ, V. VOJVODIĆ, 'Voltammetric Analysis of Surface Active Substances in Natural Seawater', *Electroanalysis* **1998**, *10*, 429–434, DOI 10.1002/(SICI)1521-4109(199805)10:6<429::AID-ELAN429>3.0.CO;2-7 (cit. on pp. 3, 74, 92).
- [43] D. HÖNIG, D. MÖBIUS, 'Direct visualization of monolayers at the air-water interface by Brewster angle microscopy', *J. Phys. Chem.* **1991**, *95*, 4590–4592, DOI 10.1021/j100165a003 (cit. on pp. 3, 74, 149).
- [44] N. HERTKORN, M. HARIR, B. P. KOCH, B. MICHALKE, P. SCHMITT-KOPPLIN, 'High-field NMR spectroscopy and FTICR mass spectrometry: Powerful discovery tools for the molecular level characterization of marine dissolved organic matter', *Biogeosciences* **2013**, *10*, 1583–1624, DOI 10.5194/bg-10-1583-2013 (cit. on p. 3).
- [45] L. J. CARPENTER, P. D. NIGHTINGALE, 'Chemistry and Release of Gases from the Surface Ocean', *Chem. Rev.* **2015**, *115*, 4015–4034, DOI 10.1021/cr5007123 (cit. on pp. 3, 73, 91, 128, 147).
- [46] N. V. BLOUGH, 'Photochemistry in the sea-surface microlayer' *Sea Surf. Glob. Chang.* (Eds.: P. S. LISS, R. DUCE), Cambridge University Press, Cambridge (UK), **Mar. 1997**, pp. 383–424, DOI 10.1017/CB09780511525025.014 (cit. on pp. 4, 91).
- [47] X.-Y. ZHU, 'Surface Photochemistry', *Annu. Rev. Phys. Chem.* **Oct. 1994**, *45*, 113–144, DOI 10.1146/annurev.pc.45.100194.000553 (cit. on p. 4).
- [48] C. GEORGE, B. D'ANNA, H. HERRMANN, C. WELLER, V. VAIDA, D. J. DONALDSON, T. BARTELS-RAUSCH, M. AMMANN, 'Emerging Areas in Atmospheric Photochemistry', *Top. Curr. Chem.* **2014**, *339*, 1–54, DOI 10.1007/128 (cit. on p. 4).
- [49] C. GEORGE, M. BRÜGGEMANN, N. HAYECK, L. TINEL, J. DONALDSON, *Interfacial Photochemistry*, 1st ed., (Eds.: J. E. F. JENNIFER A., HOUSE), Elsevier, **2018**, pp. 435–457, DOI 10.1016/B978-0-12-813641-6.00014-5 (cit. on pp. 4, 7, 128, 129, 148).
- [50] L. J. RICHTER, R. R. CAVANAGH, Mechanistic studies of photoinduced reactions at semiconductor surfaces, **1992**, DOI 10.1016/0079-6816(92)90022-A (cit. on p. 4).

-
- [51] X. L. ZHOU, X. Y. ZHU, J. M. WHITE, 'Photochemistry at adsorbate/metal interfaces', *Surf. Sci. Rep.* **1991**, *13*, 73–220, DOI 10.1016/0167-5729(91)90009-M (cit. on p. 4).
- [52] H. FU, R. CIURARU, Y. DUPART, M. PASSANANTI, L. TINEL, S. ROSSIGNOL, S. PERRIER, D. J. DONALDSON, J. CHEN, C. GEORGE, 'Photosensitized Production of Atmospherically Reactive Organic Compounds at the Air/Aqueous Interface', *J. Am. Chem. Soc.* **2015**, *137*, 8348–8351, DOI 10.1021/jacs.5b04051 (cit. on pp. 5, 6, 128).
- [53] L. TINEL, S. ROSSIGNOL, A. BIANCO, M. PASSANANTI, S. PERRIER, X. WANG, M. BRIGANTE, D. J. DONALDSON, C. GEORGE, 'Mechanistic Insights on the Photosensitized Chemistry of a Fatty Acid at the Air/Water Interface', *Environ. Sci. Technol.* **Oct. 2016**, *50*, 11041–11048, DOI 10.1021/acs.est.6b03165 (cit. on pp. 5–7, 128, 129, 148).
- [54] O. C. ZAFIRIOU, J. JOUSSOT-DUBIEN, R. G. ZEPP, R. G. ZIKA, 'Photochemistry of natural waters', *Environ. Sci. Technol.* **Dec. 1984**, *18*, 358A–371A, DOI 10.1021/es00130a001 (cit. on pp. 5, 128).
- [55] F. AL HOUSARI, D. VIONE, S. CHIRON, S. BARBATI, 'Reactive photoinduced species in estuarine waters. Characterization of hydroxyl radical, singlet oxygen and dissolved organic matter triplet state in natural oxidation processes', *Photochem. Photobiol. Sci.* **2010**, *9*, 78–86, DOI 10.1039/b9pp00030e (cit. on p. 5).
- [56] C. M. SHARPLESS, N. V. BLOUGH, 'The importance of charge-transfer interactions in determining chromophoric dissolved organic matter (CDOM) optical and photochemical properties.', *Environ. Sci. Process. Impacts* **2014**, *16*, 654–71, DOI 10.1039/c3em00573a (cit. on p. 5).
- [57] K. MCNEILL, S. CANONICA, 'Triplet state dissolved organic matter in aquatic photochemistry: Reaction mechanisms, substrate scope, and photophysical properties', *Environ. Sci. Process. Impacts* **2016**, *18*, 1381–1399, DOI 10.1039/c6em00408c (cit. on p. 5).
- [58] J. P. AGUER, C. RICHARD, F. ANDREUX, 'Effect of light on humic substances: Production of reactive species', *Analisis* **1999**, *27*, 387–390, DOI 10.1051/analisis:1999270387 (cit. on p. 5).

- [59] D. CLIFFORD, D. J. DONALDSON, M. BRIGANTE, B. D'ANNA, C. GEORGE, 'Reactive uptake of ozone by chlorophyll at aqueous surfaces', *Environ. Sci. Technol.* **2008**, *42*, 1138–1143, DOI 10.1021/es0718220 (cit. on p. 5).
- [60] D. I. REESER, A. JAMMOUL, D. CLIFFORD, M. BRIGANTE, B. D'ANNA, C. GEORGE, D. J. DONALDSON, 'Photoenhanced reaction of ozone with chlorophyll at the seawater surface', *J. Phys. Chem. C* **2009**, *113*, 2071–2077, DOI 10.1021/jp805167d (cit. on p. 5).
- [61] D. I. REESER, C. GEORGE, D. J. DONALDSON, 'Photooxidation of Halides by Chlorophyll at the Air - Salt Water Interface', **2009**, 0–4 (cit. on p. 5).
- [62] S. CANONICA, U. JANS, K. STEMMLER, J. HOIGNE, 'Transformation Kinetics of Phenols in Water: Photosensitization by Dissolved Natural Organic Material and Aromatic Ketones', *Environ. Sci. Technol.* **1995**, *29*, 1822–1831, DOI 10.1021/es00007a020 (cit. on pp. 5, 39, 128).
- [63] S. CANONICA, 'Oxidation of Aquatic Organic Contaminants Induced by Excited Triplet States', *Chimia (Aarau)*. **2007**, *61*, 641 (cit. on pp. 5, 144).
- [64] M. EHRHARDT, G. PETRICK, 'On the sensitized photo-oxidation of alkylbenzenes in seawater', *Mar. Chem.* **1984**, *15*, 47–58, DOI 10.1016/0304-4203(84)90037-9 (cit. on p. 6).
- [65] M. EHRHARDT, G. PETRICK, 'The sensitized photo-oxidation of n-pentadecane as a model for abiotic decomposition of aliphatic hydrocarbons in seawater', *Mar. Chem.* **June 1985**, *16*, 227–238, DOI 10.1016/0304-4203(85)90063-5 (cit. on p. 6).
- [66] M. EHRHARDT, R. R. WEBER, 'Formation of low molecular weight carbonyl compounds by sensitized photochemical decomposition of aliphatic hydrocarbons in seawater', *Fresenius. J. Anal. Chem.* **1991**, *339*, 772–776, DOI 10.1007/BF00321742 (cit. on p. 6).
- [67] R. CIURARU, L. FINE, M. V. PINXTEREN, B. D'ANNA, H. HERRMANN, C. GEORGE, B. D'ANNA, H. HERRMANN, C. GEORGE, 'Unravelling New Processes at Interfaces: Photochemical Isoprene Production at the Sea Surface', *Environ. Sci. Technol.* **Nov. 2015**, *49*, 13199–13205, DOI 10.1021/acs.est.5b02388 (cit. on pp. 6, 129).

-
- [68] R. CIURARU, L. FINE, M. van PINXTEREN, B. D'ANNA, H. HERRMANN, C. GEORGE, 'Photosensitized production of functionalized and unsaturated organic compounds at the air-sea interface', *Sci. Rep.* **2015**, *5*, 12741, DOI 10.1038/srep12741 (cit. on pp. 6, 129, 130, 134, 135, 148).
- [69] M. BRÜGGEMANN, N. HAYECK, C. BONNINEAU, S. PESCE, P. A. ALPERT, S. PERRIER, C. ZUTH, T. HOFFMANN, J. CHEN, C. GEORGE, 'Interfacial photochemistry of biogenic surfactants: a major source of abiotic volatile organic compounds', *Faraday Discuss.* **2017**, DOI 10.1039/C7FD00022G (cit. on pp. 6, 8, 129, 148).
- [70] M. SHRESTHA, M. LUO, Y. LI, B. XIANG, W. XIONG, V. H. GRASSIAN, 'Let there be light: stability of palmitic acid monolayers at the air/salt water interface in the presence and absence of simulated solar light and a photosensitizer', *Chem. Sci.* **2018**, *9*, 5716–5723, DOI 10.1039/C8SC01957F (cit. on pp. 6, 129, 148).
- [71] J. V. TRUEBLOOD, M. R. ALVES, D. POWER, M. V. SANTANDER, R. E. COCHRAN, K. A. PRATHER, V. H. GRASSIAN, 'Shedding Light on Photosensitized Reactions within Marine-Relevant Organic Thin Films', *ACS Earth Sp. Chem.* **2019**, *3*, 1614–1623, DOI 10.1021/acsearthspacechem.9b00066 (cit. on p. 6).
- [72] P. XIAO, Q. WANG, W. H. FANG, G. CUI, 'Quantum Chemical Investigation on Photochemical Reactions of Nonanoic Acids at Air-Water Interface', *J. Phys. Chem. A* **2017**, *121*, 4253–4262, DOI 10.1021/acs.jpca.7b03123 (cit. on p. 6).
- [73] M. C. DEROSA, R. J. CRUTCHLEY, 'Photosensitized singlet oxygen and its applications', *Coord. Chem. Rev.* **2002**, 233-234, 351–371, DOI 10.1016/S0010-8545(02)00034-6 (cit. on p. 7).
- [74] M. BRÜGGEMANN, N. HAYECK, C. GEORGE, 'Interfacial photochemistry at the ocean surface is a global source of organic vapors and aerosols', *Nat. Commun.* **Dec. 2018**, *9*, 2101, DOI 10.1038/s41467-018-04528-7 (cit. on pp. 8, 129).
- [75] Y. R. SHEN, 'Basic Theory of Surface Sum-Frequency Generation', *J. Phys. Chem. C* **July 2012**, *116*, 15505–15509, DOI 10.1021/jp305539v (cit. on pp. 8, 129, 137).

- [76] J. F. MCGILP, 'A review of optical second-harmonic and sum-frequency generation at surfaces and interfaces', *J. Phys. D. Appl. Phys.* **1999**, *29*, 1812–1821, DOI 10.1088/0022-3727/29/7/016 (cit. on p. 8).
- [77] K. B. EISENTHAL, 'Liquid Interfaces Probed by Second-Harmonic and Sum-Frequency Spectroscopy', *Chem. Rev.* **1996**, *96*, 1343–1360, DOI 10.1021/cr9502211 (cit. on p. 8).
- [78] F. VIDAL, A. TADJEDDINE, 'Sum-frequency generation spectroscopy of interfaces', *Reports Prog. Phys.* **2005**, *68*, 1095–1127, DOI 10.1088/0034-4885/68/5/R03 (cit. on p. 8).
- [79] M. BUCK, M. HIMMELHAUS, 'Vibrational spectroscopy of interfaces by infrared–visible sum frequency generation', *J. Vac. Sci. Technol. A Vacuum Surfaces Film.* **2001**, *19*, 2717, DOI 10.1116/1.1414120 (cit. on pp. 8, 24, 129).
- [80] Y. R. SHEN, Surface properties probed by second-harmonic and sum-frequency generation, **Feb. 1989**, DOI 10.1038/337519a0 (cit. on pp. 9, 137).
- [81] Y. R. SHEN, 'Surfaces probed by nonlinear optics', *Surf. Sci.* **1994**, *299*, 551–562 (cit. on p. 9).
- [82] W. SUNG, D. KIM, Y. SHEN, 'Sum-frequency vibrational spectroscopic studies of Langmuir monolayers', *Curr. Appl. Phys.* **June 2013**, *13*, 619–632, DOI 10.1016/j.cap.2012.12.002 (cit. on pp. 9, 149).
- [83] Y. R. SHEN, V. OSTROVERKHOV, 'Sum-Frequency Vibrational Spectroscopy on Water Interfaces: Polar Orientation of Water Molecules at Interfaces', *Chem. Rev.* **Apr. 2006**, *106*, 1140–1154, DOI 10.1021/cr040377d (cit. on p. 9).
- [84] N. WATANABE, H. YAMAMOTO, A. WADA, K. DOMEN, C. HIROSE, T. OHTAKE, N. MINO, 'Vibrational sum-frequency generation (VSFG) spectra of n-alkyltrichlorosilanes chemisorbed on quartz plate', *Spectrochim. Acta Part A Mol. Spectrosc.* **1994**, *50*, 1529–1537, DOI 10.1016/0584-8539(94)E0064-H (cit. on p. 9).
- [85] J. F. D. LILJEBLAD, *Biomimetic Membranes : Molecular Structure and Stability Studies by Vibrational Sum Frequency Spectroscopy*, **2010** (cit. on p. 9).

-
- [86] G. MA, H. C. ALLEN, 'DPPC Langmuir Monolayer at the Air - Water Interface : Probing the Tail and Head Groups by Vibrational Sum Frequency Generation Spectroscopy', *Langmuir* **2006**, *22*, 5341–5349, DOI 10.1021/1a0535227 (cit. on pp. 9, 134).
- [87] R. YAM, G. BERKOVIC, 'Linear and nonlinear spectroscopy of a monolayer', *Langmuir* **1993**, *9*, 2109–2111 (cit. on p. 9).
- [88] L. FU, Z. WANG, V. S. BATISTA, E. C. Y. YAN, 'New Insights from Sum Frequency Generation Vibrational Spectroscopy into the Interactions of Islet Amyloid Polypeptides with Lipid Membranes', *J. Diabetes Res.* **2016**, *2016*, DOI 10.1155/2016/7293063 (cit. on p. 9).
- [89] X. CHEN, M. L. CLARKE, J. WANG, Z. CHEN, 'Sum Frequency Generation Vibrational Spectroscopy Studies on Molecular Conformation and Orientation of Biological Molecules at Interfaces', *Int. J. Mod. Phys. B* **Feb. 2005**, *19*, 691–713, DOI 10.1142/S0217979205029341 (cit. on p. 9).
- [90] S. ROKE, J. SCHINS, M. MÜLLER, M. BONN, 'Vibrational Spectroscopic Investigation of the Phase Diagram of a Biomimetic Lipid Monolayer', *Phys. Rev. Lett.* **2003**, *90*, 128101, DOI 10.1103/PhysRevLett.90.128101 (cit. on p. 9).
- [91] R. A. LIVINGSTONE, Y. NAGATA, M. BONN, E. H. BACKUS, 'Two Types of Water at the Water-Surfactant Interface Revealed by Time-Resolved Vibrational Spectroscopy', *J. Am. Chem. Soc.* **2015**, *137*, 14912–14919, DOI 10.1021/jacs.5b07845 (cit. on p. 9).
- [92] W. GAN, D. WU, Z. ZHANG, R.-R. FENG, H.-F. WANG, 'Polarization and Experimental Configuration Analysis of Sum Frequency Generation Vibrational Spectra of Air/Water Interface', *J. Chem. Phys.* **2005**, *124*, 114705, DOI 10.1063/1.2179794 (cit. on p. 9).
- [93] C. Y. TANG, H. C. ALLEN, 'Ionic binding of Na + versus K + to the carboxylic acid headgroup of palmitic acid monolayers studied by vibrational sum frequency generation spectroscopy', *J. Phys. Chem. A* **2009**, *113*, 7383–7393, DOI 10.1021/jp9000434 (cit. on p. 9).

- [94] C. Y. TANG, Z. HUANG, H. C. ALLEN, 'Binding of Mg²⁺ and Ca²⁺ to palmitic acid and deprotonation of the cooh headgroup studied by vibrational sum frequency generation spectroscopy', *J. Phys. Chem. B* **2010**, *114*, 17068–17076, DOI 10.1021/jp105472e (cit. on p. 9).
- [95] M. BONN, Y. NAGATA, E. H. G. BACKUS, 'Molecular Structure and Dynamics of Water at the Water-Air Interface Studied with Surface-Specific Vibrational Spectroscopy', *Angew. Chemie Int. Ed.* **May 2015**, *54*, 5560–5576, DOI 10.1002/anie.201411188 (cit. on p. 9).
- [96] S. NIHONYANAGI, S. YAMAGUCHI, T. TAHARA, Ultrafast Dynamics at Water Interfaces Studied by Vibrational Sum Frequency Generation Spectroscopy, **2017**, DOI 10.1021/acs.chemrev.6b00728 (cit. on p. 9).
- [97] D. ZHANG, J. GUTOW, K. B. EISENTHAL, 'Vibrational spectra, orientations, and phase transitions in long-chain amphiphiles at the air/water interface: Probing the head and tail groups by sum frequency generation', *J. Phys. Chem.* **1994**, *98*, 13729–13734, DOI 10.1021/j100102a045 (cit. on p. 9).
- [98] G. RICHMOND, 'Structure and bonding of molecules at aqueous surfaces', *Annu. Rev. Phys. Chem.* **Oct. 2001**, *52*, 357–389, DOI 10.1146/annurev.physchem.52.1.357 (cit. on p. 9).
- [99] C. S. TIAN, Y. R. SHEN, 'Comment on "vibrational response of hydrogen-bonded interfacial water is dominated by intramolecular coupling"', *Phys. Rev. Lett.* **2008**, *101*, 1–4, DOI 10.1103/PhysRevLett.101.139401 (cit. on p. 9).
- [100] C. J. EBBEN, A. P. AULT, M. J. RUPPEL, O. S. RYDER, T. H. BERTRAM, V. H. GRASSIAN, K. A. PRATHER, F. M. GEIGER, 'Size-resolved sea spray aerosol particles studied by vibrational sum frequency generation', *J. Phys. Chem. A* **2013**, *117*, 6589–6601, DOI 10.1021/jp401957k (cit. on p. 9).
- [101] A. B. VOGES, G. Y. STOKES, J. M. GIBBS-DAVIS, R. B. LETTAN, P. A. BERTIN, R. C. PIKE, S. T. NGUYEN, K. A. SCHEIDT, F. M. GEIGER, 'Insights into Heterogeneous Atmospheric Oxidation Chemistry: Development of a Tailor-Made Synthetic Model for Studying Tropospheric

-
- Surface Chemistry', *J. Phys. Chem. C* **Feb. 2007**, *111*, 1567–1578, DOI 10.1021/jp0652771 (cit. on p. 9).
- [102] F. M. GEIGER, 'Second Harmonic Generation, Sum Frequency Generation, and χ (3) : Dissecting Environmental Interfaces with a Nonlinear Optical Swiss Army Knife', *Annu. Rev. Phys. Chem.* **May 2009**, *60*, 61–83, DOI 10.1146/annurev.physchem.59.032607.093651 (cit. on p. 9).
- [103] G. Y. STOKES, E. H. CHEN, S. R. WALTER, F. M. GEIGER, 'Two Reactivity Modes in the Heterogeneous Cyclohexene Ozonolysis under Tropospherically Relevant Ozone-Rich and Ozone-Limited Conditions', *J. Phys. Chem. A* **Aug. 2009**, *113*, 8985–8993, DOI 10.1021/jp904104s (cit. on p. 9).
- [104] A. M. JUBB, W. HUA, H. C. ALLEN, 'Environmental Chemistry at Vapor/Water Interfaces: Insights from Vibrational Sum Frequency Generation Spectroscopy', *Annu. Rev. Phys. Chem.* **May 2012**, *63*, 107–130, DOI 10.1146/annurev-physchem-032511-143811 (cit. on p. 9).
- [105] K. LASS, G. FRIEDRICHS, 'Revealing structural properties of the marine nanolayer from vibrational sum frequency generation spectra', *J. Geophys. Res. Ocean.* **2011**, *116*, 1–15, DOI 10.1029/2010JC006609 (cit. on pp. 9, 48, 75, 77, 88, 92, 96, 103, 130).
- [106] K. LASS, H. W. BANGE, G. FRIEDRICHS, 'Seasonal signatures in SFG vibrational spectra of the sea surface nanolayer at Boknis Eck Time Series Station (SW Baltic Sea)', *Biogeosciences* **2013**, *10*, 5325–5334, DOI 10.5194/bg-10-5325-2013 (cit. on pp. 10, 75–77, 81–83, 86, 88–90, 92, 93, 130).
- [107] H. Y. ERBIL, *Surface Chemistry*, Blackwell Publishing Ltd., Oxford, UK, **June 2006**, DOI 10.1002/9781444305401 (cit. on p. 13).
- [108] R. EÖTVÖS, 'Ueber den Zusammenhang der Oberflächenspannung der Flüssigkeiten mit ihrem Molecularvolumen', *Ann. der Phys. und Chemie* **1886**, *263*, 448–459, DOI 10.1002/andp.18862630309 (cit. on p. 15).
- [109] W. RAMSAY, J. SHIELDS, 'The variation of molecular surface-energy with temperature', *Philos. Trans. R. Soc. London.* **Dec. 1893**, *184*, 647–673, DOI 10.1098/rsta.1893.0013 (cit. on p. 15).

- [110] K. G. NAYAR, D. PANCHANATHAN, G. H. MCKINLEY, J. H. LIENHARD, 'Surface Tension of Seawater', *J. Phys. Chem. Ref. Data* **2014**, *43*, DOI 10.1063/1.4899037 (cit. on pp. 16, 97, 109).
- [111] G. J. LAUTH, J. KOWALCZYK, *Einführung in die Physik und Chemie der Grenzflächen und Kolloide*, Springer Berlin Heidelberg, Berlin, Heidelberg, **2016**, DOI 10.1007/978-3-662-47018-3 (cit. on p. 16).
- [112] J. F. PADDAY, A. R. PITT, R. M. PASHLEY, 'Menisci at a free liquid surface: surface tension from the maximum pull on a rod', *J. Chem. Soc. Faraday Trans. 1 Phys. Chem. Condens. Phases* **1975**, *71*, 1919, DOI 10.1039/f19757101919 (cit. on p. 17).
- [113] D. HARKINS, 'a Method for the Determination of Surface and', **1930**, 399, 1751–1772 (cit. on p. 17).
- [114] B. B. FREUD, H. Z. FREUD, 'A theory of the ring method for the determination of surface tension', *Science (80-.)*. **1930**, *71*, 345–346, DOI 10.1126/science.71.1839.345 (cit. on p. 17).
- [115] A. C. MITROPOULOS, 'What is a surface excess?', *J. Eng. Sci. Technol. Rev.* **2008**, *1*, 1–3, DOI 10.25103/jestr.011.01 (cit. on p. 18).
- [116] H. BUTT, K. GRAF, M. KAPPL, *Physics and Chemistry of Interfaces*, Wiley, **Sept. 2003**, DOI 10.1002/3527602313 (cit. on p. 20).
- [117] W. D. HARKINS, T. F. YOUNG, E. BOYD, 'The thermodynamics of films: Energy and entropy of extension and spreading of insoluble monolayers', *J. Chem. Phys.* **1940**, *8*, 954–965, DOI 10.1063/1.1750610 (cit. on pp. 21–23).
- [118] V. M. KAGANER, 'Kaganer, Möhwald, Dutta - 1999 - Structure and phase transitions in Langmuir monolayers.pdf', **1999**, *71*, 779–819 (cit. on pp. 23, 149).
- [119] R. W. BOYD, 'The Nonlinear Optical Susceptibility' *Nonlinear Opt. Vol. 30*, 1, Elsevier, **2008**, pp. 1–67, DOI 10.1016/B978-0-12-369470-6.00001-0 (cit. on p. 24).

-
- [120] A. G. LAMBERT, P. B. DAVIES, D. J. NEIVANDT, 'Implementing the Theory of Sum Frequency Generation Vibrational Spectroscopy: A Tutorial Review', *Appl. Spectrosc. Rev.* **2005**, *40*, 103–145, DOI 10.1081/ASR-200038326 (cit. on pp. 26, 28, 29, 78).
- [121] C. HIROSE, N. AKAMATSU, K. DOMEN, 'Formulas for the Analysis of the Surface SFG Spectrum and Transformation Coefficients of Cartesian SFG Tensor Components', *Appl. Spectrosc.* **June 1992**, *46*, 1051–1072, DOI 10.1366/0003702924124385 (cit. on p. 28).
- [122] F. CECCHET, D. LIS, J. GUTHMULLER, B. CHAMPAGNE, Y. CAUDANO, C. SILIEN, A. A. MANI, P. A. THIRY, A. PEREMANS, 'Orientational analysis of dodecanethiol and p-nitrothiophenol SAMs on metals with polarisationdependent SFG spectroscopy', *ChemPhysChem* **2010**, *11*, 607–615, DOI 10.1002/cphc.200900733 (cit. on p. 29).
- [123] P. E. OHNO, H. F. WANG, F. M. GEIGER, 'Second-order spectral line-shapes from charged interfaces', *Nat. Commun.* **2017**, *8*, 1–9, DOI 10.1038/s41467-017-01088-0 (cit. on p. 30).
- [124] T. ISHIYAMA, T. IMAMURA, A. MORITA, 'Theoretical Studies of Structures and Vibrational Sum Frequency Generation Spectra at Aqueous Interfaces', *Chem. Rev.* **2014**, *114*, 8447, DOI 10.1021/cr4004133 (cit. on p. 32).
- [125] X. ZHUANG, P. B. MIRANDA, D. KIM, Y. R. SHEN, 'Mapping molecular orientation and conformation at interfaces by surface nonlinear optics', *Phys. Rev. B* **May 1999**, *59*, 12632–12640, DOI 10.1103/PhysRevB.59.12632 (cit. on p. 33).
- [126] H. F. WANG, W. GAN, R. LU, Y. RAO, B. H. WU, 'Quantitative spectral and orientational analysis in surface sum frequency generation vibrational spectroscopy (SFG-VS)', *Int. Rev. Phys. Chem.* **2005**, *24*, 191–256, DOI 10.1080/01442350500225894 (cit. on p. 33).
- [127] C. HIROSE, N. AKAMATSU, K. DOMEN, 'Formulas for the analysis of surface sum-frequency generation spectrum by CH stretching modes of methyl and methylene groups', *J. Chem. Phys.* **1992**, *96*, 997–1004, DOI 10.1063/1.462120 (cit. on p. 33).

- [128] G. R. BELL, C. D. BAIN, R. N. WARD, 'Sum-frequency vibrational spectroscopy of soluble surfactants at the air/water interface', *J. Chem. Soc. - Faraday Trans.* **1996**, *92*, 515–523, DOI 10.1039/ft9969200515 (cit. on p. 33).
- [129] A. MORITA, T. ISHIYAMA, 'Recent progress in theoretical analysis of vibrational sum frequency generation spectroscopy', *Phys. Chem. Chem. Phys.* **2008**, *10*, 5801, DOI 10.1039/b808110g (cit. on p. 33).
- [130] L. VELARDE, H. F. WANG, 'Unique determination of the -CN group tilt angle in Langmuir monolayers using sum-frequency polarization null angle and phase', *Chem. Phys. Lett.* **2013**, *585*, 42–48, DOI 10.1016/j.cplett.2013.07.052 (cit. on p. 33).
- [131] J. KLEBER, 'VSFG-Spektroskopische Untersuchungen von organischen Filmen und ihrer Oxidationskinetik an der Luft-Wasser-Grenzfläche', PhD thesis, CAU Kiel, **2015** (cit. on pp. 33, 50).
- [132] *IUPAC Compendium of Chemical Terminology*, (Eds.: M. NIČ, J. JIRÁT, B. KOŠATA, A. JENKINS, A. MCNAUGHT), IUPAC, Research Triangle Park, NC, **June 2009**, DOI 10.1351/goldbook (cit. on p. 35).
- [133] J. D. COYLE, H. A. CARLESS, 'Selected aspects of photochemistry: I - Photochemistry of carbonyl compounds', *Chem. Soc. Rev.* **1972**, *1*, 465–480, DOI 10.1039/CS9720100465 (cit. on p. 37).
- [134] M. S. ISLAM, 'Analytical modeling of organic solar cells including monomolecular recombination and carrier generation calculated by optical transfer matrix method', *Org. Electron.* **2017**, *41*, 143–156, DOI 10.1016/j.orgel.2016.10.040 (cit. on p. 52).
- [135] P. CARBONNELLE, *PYPL PopularitY of Programming Language*, **2018** (cit. on p. 57).
- [136] H. P. LANGTANGEN, *A Primer on Scientific Programming with Python*, Springer Berlin Heidelberg, Berlin, Heidelberg, **2016**, DOI 10.1007/978-3-662-49887-3 (cit. on p. 57).
- [137] S. van der WALT, S. C. COLBERT, G. VAROQUAUX, 'The NumPy Array: A Structure for Efficient Numerical Computation', *Comput. Sci. Eng.* **Mar. 2011**, *13*, 22–30, DOI 10.1109/MCSE.2011.37 (cit. on p. 57).

-
- [138] J. D. HUNTER, 'Matplotlib: A 2D Graphics Environment', *Comput. Sci. Eng.* **2007**, 9, 90–95, DOI 10.1109/MCSE.2007.55 (cit. on p. 57).
- [139] T. pandas development TEAM, pandas, **2020**, DOI 10.5281/zenodo.3509134 (cit. on p. 57).
- [140] M. BAYER, 'SQLAlchemy' *Archit. Open Source Appl. Vol. II Struct. Scale, a Few More Fearless Hacks*, (Eds.: A. BROWN, G. WILSON), aosabook.org, **2012** (cit. on p. 58).
- [141] F. MACINTYRE, 'The Top Millimeter of the Ocean', *Sci. Am.* **May 1974**, 230, 62–77, DOI 10.1038/scientificamerican0574-62 (cit. on p. 73).
- [142] J. C. GOLDMAN, M. R. DENNETT, N. M. FREW, 'Surfactant effects on air-sea gas exchange under turbulent conditions', *Deep Sea Res. Part A Oceanogr. Res. Pap.* **1988**, 35, 1953–1970, DOI 10.1016/0198-0149(88)90119-7 (cit. on pp. 73, 92).
- [143] M. RIBAS-RIBAS, F. HELLEIS, J. RAHLFF, O. WURL, 'Air-Sea CO₂-Exchange in a Large Annular Wind-Wave Tank and the Effects of Surfactants', *Front. Mar. Sci.* **2018**, 5, 1–16, DOI 10.3389/fmars.2018.00457 (cit. on pp. 73, 92).
- [144] A. ENGEL, M. SPERLING, C. SUN, J. GROSSE, G. FRIEDRICHS, 'Organic matter in the surface microlayer: Insights from a wind wave channel experiment', *Front. Mar. Sci.* **June 2018**, 5, DOI 10.3389/fmars.2018.00182 (cit. on pp. 73, 92, 147).
- [145] N. I. H. MUSTAFFA, T. H. BADEWIEN, M. RIBAS-RIBAS, O. WURL, 'High-resolution observations on enrichment processes in the sea-surface microlayer', *Sci. Rep.* **2018**, 8, 1–12, DOI 10.1038/s41598-018-31465-8 (cit. on pp. 73, 92).
- [146] W.-T. TSAI, 'An assessment of the effect of sea surface surfactant on global atmosphere-ocean CO₂ flux', *J. Geophys. Res.* **2003**, 108, 3127, DOI 10.1029/2000JC000740 (cit. on pp. 73, 92).
- [147] S. T. LENNARTZ, A. LEHMANN, J. HERRFORD, F. MALIEN, H. P. HANSEN, H. BIESTER, H. W. BANGE, 'Long-term trends at the Boknis Eck time series station (Baltic Sea), 1957-2013: Does climate change counteract

- the decline in eutrophication?', *Biogeosciences* **2014**, *11*, 6323–6339, DOI 10.5194/bg-11-6323-2014 (cit. on pp. 74, 84, 93).
- [148] Y. R. SHEN, V. OSTROVERKHOV, 'Sum-frequency vibrational spectroscopy on water interfaces: Polar orientation of water molecules at interfaces', *Chem. Rev.* **2006**, *106*, 1140–1154, DOI 10.1021/cr040377d (cit. on pp. 75, 81, 87).
- [149] P. S. LISS, R. A. DUCE, *The Sea Surface and Global Change*, Cambridge (UK), **2005** (cit. on pp. 83, 91).
- [150] J. R. WHEELER, 'Formation and collapse of surface films', **1975**, *20*, 338–342 (cit. on p. 91).
- [151] A. BRINIS, L. M??JANELLE, A. MOMZIKOFF, G. GONDRY, J. FILLAUX, V. POINT, A. SALIOT, 'Phospholipid ester-linked fatty acids composition of size-fractionated particles at the top ocean surface', *Org. Geochem.* **2004**, *35*, 1275–1287, DOI 10.1016/j.orggeochem.2004.04.009 (cit. on p. 91).
- [152] Z. ZHENGBIN, L. LIANSHENG, W. ZHIJIAN, L. JUN, D. HAIBING, 'Physicochemical Studies of the Sea Surface Microlayer: I. Thickness of the Sea Surface Microlayer and Its Experimental Determination Zhang', *J. Colloid Interface Sci.* **Aug. 1998**, *204*, 294–299, DOI 10.1006/jcis.1998.5538 (cit. on p. 91).
- [153] R. PEREIRA, I. ASHTON, B. SABBAGHZADEH, J. D. SHUTLER, R. C. UPSTILL-GODDARD, 'Reduced air-sea CO₂ exchange in the Atlantic Ocean due to biological surfactants', *Nat. Geosci.* **2018**, *11*, 492–496, DOI 10.1038/s41561-018-0136-2 (cit. on pp. 92, 147).
- [154] H. W. BANGE, A. DALE, H. P. HANSEN, J. KARSTENSEN, F. MALIEN, C. PETEREIT, K. LASS, G. FRIEDRICHS, 'LOICZ-Affiliated Activities Boknis Eck Time Series Station (SW Baltic Sea): Measurements from 1957 to 2010', *Inprint 2011/1* **2011**, 16–22 (cit. on p. 93).
- [155] MET OFFICE, Cartopy: a cartographic python library with a matplotlib interface (cit. on p. 94).
- [156] W. D. GARRETT, 'Collection of Slick-forming materials from the sea surface', *Limnol. Oceanogr.* **Apr. 1965**, *10*, 602–605, DOI 10.4319/lo.1965.10.4.0602 (cit. on p. 95).

-
- [157] P. VIRTANEN et al., 'SciPy 1.0: fundamental algorithms for scientific computing in Python', *Nat. Methods* **Mar. 2020**, *17*, 261–272, DOI 10.1038/s41592-019-0686-2 (cit. on p. 97).
- [158] N.-T. TON-NU, 'Verhalten natürlicher und artifizierter Mischungen löslicher und unlöslicher oberflächenaktiver Stoffe an der Wasser-Luft-Grenzfläche Nhat-Thao Ton-Nu', Bachelor Thesis, CAU Kiel, **2018** (cit. on pp. 97, 100).
- [159] C. GUITART, N. GARCÍA-FLOR, J. DACHS, J. M. BAYONA, J. ALBAIGÉS, 'Evaluation of sampling devices for the determination of polycyclic aromatic hydrocarbons in surface microlayer coastal waters', *Mar. Pollut. Bull.* **2004**, *48*, 961–968, DOI 10.1016/j.marpolbul.2003.12.002 (cit. on p. 114).
- [160] A. DRESHCHINSKII, A. ENGEL, 'Seasonal variations of the sea surface microlayer at the Boknis Eck Times Series Station (Baltic Sea)', *J. Plankton Res.* **2017**, *39*, 943–961, DOI 10.1093/plankt/fbx055 (cit. on p. 114).
- [161] S. A. MANG, D. K. HENRICKSEN, A. E. BATEMAN, M. P. ANDERSEN, D. R. BLAKE, S. A. NIZKORODOV, 'Contribution of carbonyl photochemistry to aging of atmospheric secondary organic aerosol', *J. Phys. Chem. A* **2008**, *112*, 8337–8344, DOI 10.1021/jp804376c (cit. on p. 128).
- [162] N. K. RICHARDS, B. J. FINLAYSON-PITTS, 'Production of gas phase NO₂ and halogens from the photochemical oxidation of aqueous mixtures of sea salt and nitrate ions at room temperature', *Environ. Sci. Technol.* **2012**, *46*, 10447–10454, DOI 10.1021/es300607c (cit. on p. 128).
- [163] N. K. RICHARDS-HENDERSON, K. M. CALLAHAN, P. NISSENSON, N. NISHINO, D. J. TOBIAS, B. J. FINLAYSON-PITTS, 'Production of gas phase NO₂ and halogens from the photolysis of thin water films containing nitrate, chloride and bromide ions at room temperature.', *Phys. Chem. Chem. Phys.* **2013**, *15*, 17636–46, DOI 10.1039/c3cp52956h (cit. on p. 128).
- [164] S. CANONICA, B. HELLRUNG, J. WIRZ, 'Oxidation of phenols by triplet aromatic ketones in aqueous solution', *J. Phys. Chem. A* **2000**, *104*, 1226–1232, DOI 10.1021/jp9930550 (cit. on p. 128).

- [165] P. A. ALPERT, R. CIURARU, S. ROSSIGNOL, M. PASSANANTI, L. TINEL, S. PERRIER, Y. DUPART, S. S. STEIMER, M. AMMANN, D. J. DONALDSON, C. GEORGE, 'Fatty Acid Surfactant Photochemistry Results in New Particle Formation', *Sci. Rep.* **2017**, *7*, 1–11, DOI 10.1038/s41598-017-12601-2 (cit. on p. 129).
- [166] L. CAPPELLIN, T. KARL, M. PROBST, O. ISMAILOVA, P. M. WINKLER, C. SOUKOULIS, E. APREA, T. D. MÄRK, F. GASPERI, F. BIASIOLI, 'On quantitative determination of volatile organic compound concentrations using proton transfer reaction time-of-flight mass spectrometry.', *Environ. Sci. Technol.* **2012**, *46*, 2283–90, DOI 10.1021/es203985t (cit. on p. 129).
- [167] Y. R. SHEN, 'Optical Second Harmonic Generation at Interfaces', *Annu. Rev. Phys. Chem.* **Oct. 1989**, *40*, 327–350, DOI 10.1146/annurev.pc.40.100189.001551 (cit. on p. 129).
- [168] J. KLEBER, K. LASS, G. FRIEDRICHS, 'Quantitative time-resolved vibrational sum frequency generation spectroscopy as a tool for thin film kinetic studies: New insights into oleic acid monolayer oxidation', *J. Phys. Chem. A* **2013**, *117*, 7863–7875, DOI 10.1021/jp404087s (cit. on p. 130).
- [169] D. Z. MARKOVIC, T. DURAND, L. K. PATTERSON, 'Hydrogen Abstraction From Lipids By Triplet States of Derivatized Benzophenone Photosensitizers', *Photochem. Photobiol.* **1990**, *51*, 389–394, DOI 10.1111/j.1751-1097.1990.tb01729.x (cit. on pp. 130, 144).
- [170] B. HILBOLD, M. PERRAULT, C. EHRET, S. L. NIU, B. FRISCH, E. I. PÉCHEUR, L. BOUREL-BONNET, 'Benzophenone-containing fatty acids and their related photosensitive fluorescent new probes: Design, physicochemical properties and preliminary functional investigations', *Bioorganic Med. Chem.* **2011**, *19*, 7464–7473, DOI 10.1016/j.bmc.2011.10.043 (cit. on p. 130).
- [171] Y. GAN, P. WANG, T. A. SPENCER, 'Synthesis of benzophenone-containing fatty acids', *J. Org. Chem.* **2006**, *71*, 9487–9490, DOI 10.1021/jo061617n (cit. on p. 130).
- [172] B. NEISES, W. STEGLICH, 'Einfaches Verfahren zur Veresterung von Carbonsäuren', *Angew. Chemie* **1978**, *90*, 556–557, DOI 10.1002/ange.19780900718 (cit. on p. 131).

- [173] P. B. JONES, M. P. POLLASTRI, N. A. PORTER, '2-benzoylbenzoic acid: A photolabile mask for alcohols and thiols', *J. Org. Chem.* **1996**, *61*, 9455–9461, DOI 10.1021/jo961638p (cit. on p. 131).
- [174] L. BALAS, J. BERTRAND-MICHEL, F. VIARS, J. FAUGERE, C. LEFORT, S. CASPAR-BAUGUIL, D. LANGIN, T. DURAND, 'Regiocontrolled syntheses of FAHFAs and LC-MS/MS differentiation of regioisomers', *Org. Biomol. Chem.* **2016**, *14*, 9012–9020, DOI 10.1039/c6ob01597b (cit. on p. 131).
- [175] M. J. FRISCH et al., 'Gaussian 09 A.02', **2009**, DOI 111 (cit. on p. 137).
- [176] J. P. MERRICK, D. MORAN, L. RADOM, 'An evaluation of harmonic vibrational frequency scale factors', *J. Phys. Chem. A* **2007**, *111*, 11683–11700, DOI 10.1021/jp073974n (cit. on pp. 137, 138).
- [177] Z. TANG, M. S. JOHAL, P. SCUDDER, N. CACULITAN, R. J. MAGYAR, S. TRETIAK, H. L. WANG, 'Study of the non-covalent interactions in Langmuir-Blodgett films: An interplay between π - π and dipole-dipole interactions', *Thin Solid Films* **2007**, *516*, 58–66, DOI 10.1016/j.tsf.2007.04.149 (cit. on p. 141).
- [178] J. A. SCHRÖTER, R. PLEHNERT, G. TSCHERSKE, S. KATHOLY, D. JANITZ, F. PENACORADA, L. BREHMER, 'Monolayer properties of a new family of amphiphiles with an unusual head-group topology', *Langmuir* **1997**, *13*, 796–800, DOI 10.1021/1a960809i (cit. on p. 142).
- [179] H. LI, R. SACHSENHOFER, W. H. BINDER, T. HENZE, T. THURN-ALBRECHT, K. BUSSE, J. KRESSLER, 'Hierarchical organization of poly(ethylene oxide)-block-poly(isobutylene) and hydrophobically modified fe₂o₃ nanoparticles at the air/water interface and on solid supports', *Langmuir* **2009**, *25*, 8320–8329, DOI 10.1021/1a900549h (cit. on p. 142).
- [180] B. GAŠPAROVIĆ, M. PLAVŠIĆ, B. ČOSOVIĆ, A. SALIOT, 'Organic matter characterization in the sea surface microlayers in the subarctic Norwegian fjords region', *Mar. Chem.* **2007**, *105*, 1–14, DOI 10.1016/j.marchem.2006.12.010 (cit. on p. 147).
- [181] K. KJAER, J. ALS-NIELSEN, C. A. HELM, P. TIPPMAN-KRAYER, H. MOEHWALD, 'Synchrotron x-ray diffraction and reflection studies of arachidic acid monolayers at the air-water interface', *J. Phys. Chem.* **1989**, *93*, 3200–3206, DOI 10.1021/j100345a063 (cit. on p. 149).

- [182] L. F. VOSS, C. M. HADAD, H. C. ALLEN, 'Competition between atmospherically relevant fatty acid monolayers at the air/water interface', *J. Phys. Chem. B* **2006**, *110*, 19487–19490, DOI 10.1021/jp062595b (cit. on p. 149).
- [183] E. TYRODE, P. NIGA, M. JOHNSON, M. W. RUTLAND, 'Molecular structure upon compression and stability toward oxidation of langmuir films of unsaturated fatty acids: A vibrational sum frequency spectroscopy study', *Langmuir* **2010**, *26*, 14024–14031, DOI 10.1021/1a102189z (cit. on p. 155).
- [184] P. DYNAROWICZ-ŁATKA, K. KITA, 'Molecular interaction in mixed monolayers at the air/water interface', *Adv. Colloid Interface Sci.* **1999**, *79*, 1–17, DOI 10.1016/S0001-8686(98)00064-5 (cit. on p. 158).
- [185] J. JACOBSEN, B. ACHENBACH, H. REINSCH, S. SMOLDERS, F.-D. LANGE, G. FRIEDRICHS, D. DE VOS, N. STOCK, 'The first water-based synthesis of Ce(IV)-MOFs with saturated chiral and achiral C4-dicarboxylate linkers', *Dalton Trans.* **2019**, *48*, 8433–8441, DOI 10.1039/C9DT01542F (cit. on p. 239).

List of Figures

1.1	Schematic representation of the SML	3
1.2	Photochemistry bulk vs surface	7
2.1	Salinity vs surface tension	16
2.2	Wilhemy plate	16
2.3	2D phases of an ideal isotherm	23
2.4	SFG coordinate system	27
2.5	SFG calculation steps	29
2.6	SFG resonant/non-resonant	31
2.7	Jablonksi diagram	35
2.8	Examples for sensitizers	37
2.9	Excitated state of carbonyls	38
2.10	Carbonyl photochemistry	39
2.11	Hydroperoxide reaction	39
3.1	VSFG setup	46
3.2	Combination of LT and SFg	49
3.3	Lamp assembly	50
3.4	Transmission curves with filter and LLG	52
4.1	SFG package organization	59
4.2	Program usage demonstration	65
4.3	GasEx database scheme	67
4.4	Framework extension demo	70
5.1	Demonstration sampling day analysis	80
5.2	Old BE/ all BE comparison	83
5.3	SML time series	84
5.4	SML time series	84

5.5	Correlation SML/bulk/ 1m	86
5.6	Quarter SFG average	88
5.7	Monthly average boxplot	89
6.1	GasEx-Stations	94
6.2	Dry and wet surfactants	98
6.3	Different surfactant isotherms	100
6.4	Surfactant strucutres	100
6.5	Preliminary experiment results	101
6.6	SFG spectrum of a natural seawater sample	104
6.7	SAI LT/SFG	106
6.8	Day of year vs. tension/coverage	109
6.9	Day of year vs. pressure/lift-off	110
6.10	Comparison Cruise1-Cruise1	111
6.11	Enrichment factors	113
6.12	Comparison Plate-Screen	115
6.13	Comparison zodiac-Alkor	117
6.14	Correlation plots	120
7.1	Synthesis	131
7.2	experimental	133
7.3	Humic Acid/Nonanoic Acid photolysis	136
7.4	SFG, Raman and IR	139
7.5	Optimized BX9 structure	139
7.6	Sensitizer SFG comparison	140
7.7	Sensitizer LT isotherms	143
7.8	Combined VSFG/LT BX9/BX12	144
7.9	before after	145
7.10	Time-dependent photolysis	146
8.1	Mixed layers	149
8.2	Structure BXn/ fatty acids	150
8.3	SFG spectra mixture SA/BX12	155
8.4	Demo SFG not reproducible	156
8.5	Demonstration LT averaging	158
8.6	Comparison of isotherms, Part I	160

8.7	Comparison of isotherms, Part I	161
8.8	Combined VSFG/LT YA/SA/BX9 1:1	166
8.9	Combined VSFG/LT YA/SA/BX9 1:1	166
8.10	Combined VSFG/LT YA/BX12	167
8.11	SFG before and after mixed layer photolysis	177
B.1	Demo integral variation	219
B.2	Root averaging	220
D.1	UV/Vis spectra	226
D.2	Sensitizer IR spectra	226
D.3	Sensitizer Raman spectra	227
D.4	BX6 NMR	227
D.5	¹ H BX6	228
D.6	¹³ C NMR BX6	229
D.7	BX9 NMR	229
D.8	¹ H BX9	230
D.9	¹³ C NMR BX6	231
D.10	BX6 NMR	231
D.11	¹ H BX9	232
D.12	¹³ C NMR BX6	233
D.13	Demo average LT BX9	234
D.14	Demo average LT BX12	234
D.15	measurements	235
E.1	LT isotherms of fatty acids	237
E.2	Demo isotherm characteristics	237
E.3	Ghost peak demonstration	238

List of Tables

2.1	Comparison saturated and conjugated carbonyls	37
3.1	List of used reagents and chemicals.	42
3.2	Standard analytical techniques.	43
3.3	SFG spectral regions	48
3.4	List of accessories for the photolysis setup.	52
3.5	Lamp output power	53
5.1	MWU test SML vs bulk	87
6.1	GasEx sample overview	94
6.2	SFG spectral regions	97
6.3	Sample count	107
6.4	MWU test cruise 1 vs. cruise 2	111
6.5	MWU test enrichment	113
6.6	MWU-test plate vs. screen	114
6.7	MWU-test zodiac vs. ship	116
6.8	MWU SML vs. bulk	118
7.1	Peak assignment	138
8.1	Sensitizer peak symbols	155
8.2	peak ratio analysis (SFG)	156
8.3	LT isotherm comparison	163
8.4	LT isotherm comparison	164
8.5	Characteristics VSFG/LT	172
8.6	Photolysis overview	175
8.7	Domain vs mixed	179
B.1	Shapiro Test coverage	221

C.1	MWU test enrichment	223
D.1	Chromatography solvent ratios	225
D.2	Elemental analysis	225
D.3	Space requirement	235

List of Listings

- 4.1 Demonstration of MetaSpectrum 60
- 4.2 Framework usage demonstration 69

A Python script usage

A.1 General remarks and prerequisites

The application and usage of the **SFG** Python package. In its current state it still requires Python programming skills are necessary. To use this package it is necessary to install *specsna* and all of its dependencies as well as the dependencies of this module by using an appropriate Python package manager (usually *pip*). The installation of *specsna* is described here: <https://specsna.readthedocs.io/en/latest/>. The SFG package itself should be downloaded or checked from GitHub (<https://github.com/Darkskald/SFG>). The dependencies may be installed by running

```
pip install -r requirements.txt
```

from the command line while being in the root directory of the project.

A.2 Import

A script (`import_interface.py`) to intended simplify the file import can be found in the SFG directory in the project root directory. In general, the import routine relies on a strict directory organization with a directory called "newport" inside the same directory as the `import_interface` script is located. This folder must contain the following subdirectories:

- boknis (for the Boknis Eck SFG spectra)
- gasex_1t (for the GasEx Langmuir trough measurements)
- gasex_sfg (for the GasEx SFG trough measurements)
- IR (for infrared spectra)
- 1t (for regular Langmuir trough measurements)
- Raman (for Raman spectra)
- regular (for regular SFG spectra)

- UV (for UV/Vis spectra)

The SFG directories and the one for regular IR must contain one directory for each day of measurement named by the date and an abbreviation for the person measuring (e.g. 20190111 FL). In case of `gasex_1t`, all isotherm raw data are located in the subdirectory "all" inside `gasex_1t`. At the moment, the import routine is not customized and adjusted to the specific needs of this work, so using it is not recommended. Running the import script using the Python interpreter

```
python import_interface.py
```

yields a file called "orm.db" as output which is the *sqlite* database containing all the data.

A.3 Usage

The import and working with the data is completely decoupled. Once the database is generated, it is possible to use all analysis and visualization functionality without dealing with a particular import directory layout. The most convenient way is to run

```
pip install .
```

while being in the project root directory. This makes the library available as import in the local python directory. Now, a new Python script or Jupyter Notebook should be created and placed, together with the database file, in a directory. The class to interact with the database is the **DbInteractor** from the **interact** module. This class can be used to establish a connection to the database and allow to access it conveniently. The class is used as follows:

```
from SFG.orm import interact

itc = interact.DbInteractor()
# get an SFG spectrum from the database by its name
spec = itc.get_spectrum_by_name("BX6_6_x1_#1_20mM.sfg")
# calculate the integral of the aliphatic region of the
# spectrum and output it
print(spec.calculate_ch_integral())
```

Most of functions to interact with the database are documented in the package source code but especially the interaction with the database in a non-standard way requires understanding of the *sqlalchemy* library. As a general remark, the **DbInteractor** has a "session" attribute which corresponds to an **sqlalchemy** session, allowing to perform SQL operations on the database. The database models are located in the **orm** submodule within the files containing "dto (for data transfer object)". The general syntax of querying the database follows the scheme

```
spectra = itc.session.query(<object>).filter(<object> \
    .<property> == <value>).all()
```

and should be understandable for someone familiar with **sqlalchemy** syntax. In this example, <object> is the underlying database model and <property> one of its class attributes.

B Boknis Eck Time Series

B.1 Baseline correction

The baseline correction is performed following this scheme:

- The wavenumber/VSFG intensity arrays were splitted into two parts: from the lowest wavenumber until 3030 cm^{-1} and from there to the highest wavenumber value
- for each of the halves, the (linear) baseline was calculated using the *baseline* function of the *peakutils* package
- the calculated baselines was subtracted from the data
- the two halves were concatenated to obtain the full spectrum again

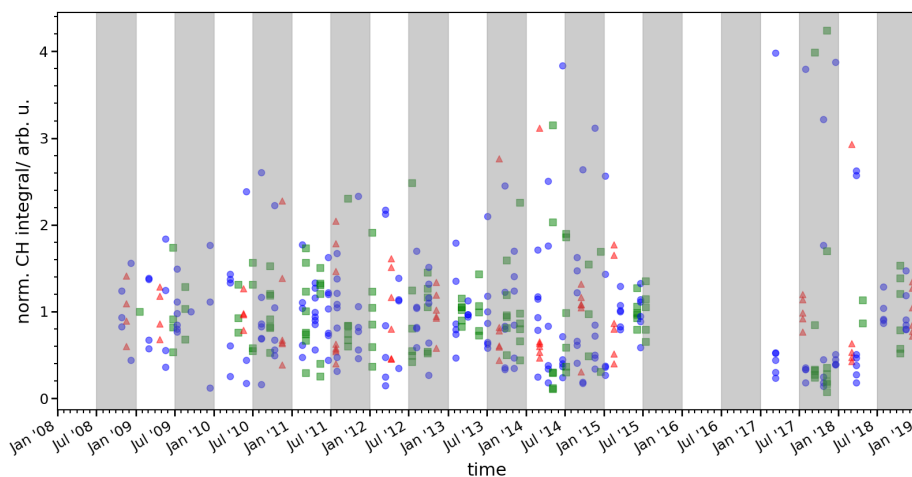


Figure B.1: Visualization of variability of the calculated CH integral values. For this plot all samples measured during one day have been normalized by the respective mean value of that day. In this way the plot depicts the relative variabilities of the VSFG signal.

$$sc = \sqrt{\frac{\int_{2750}^{3000} \left(\sqrt{I_{\text{Sample}}(\tilde{\nu})} - \sqrt{I_{\text{H}_2\text{O, sample}}(\tilde{\nu})} \right)^2 d\tilde{\nu}}{\int_{2750}^{3000} \left(\sqrt{I_{\text{Reference}}(\tilde{\nu})} - \sqrt{I_{\text{H}_2\text{O, reference}}(\tilde{\nu})} \right)^2 d\tilde{\nu}}} \quad (\text{B.1})$$

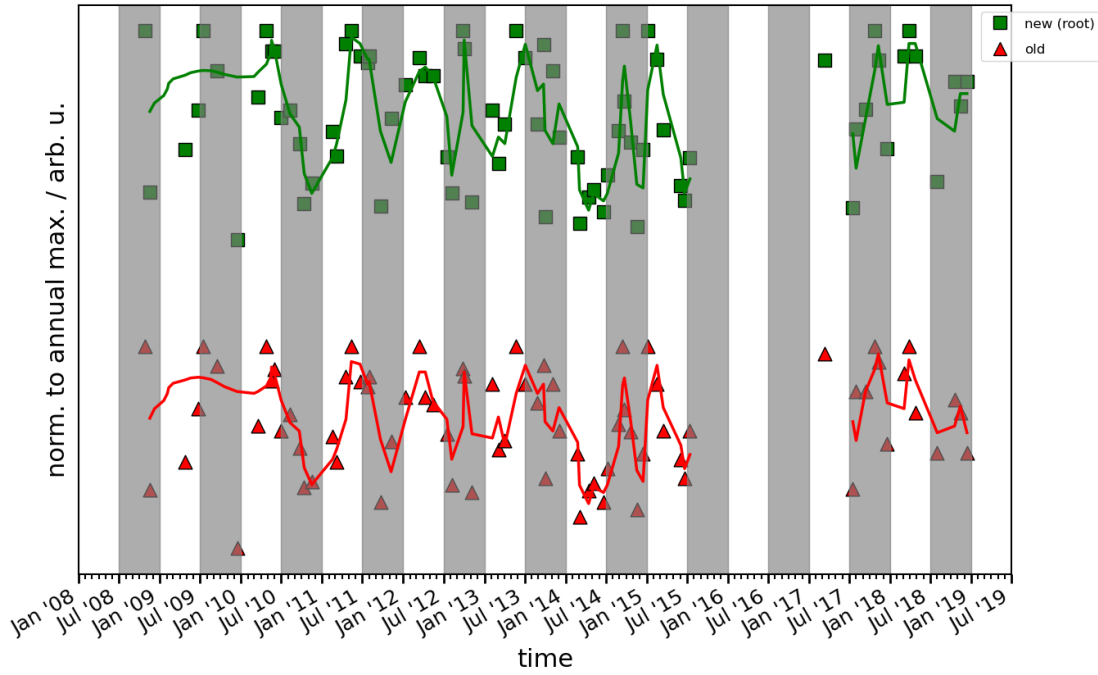


Figure B.2: Comparison of the results obtained for the seasonal variation of the SML surface coverage obtained by the "normal" baseline correction (red) as described in the text (see eq. 5.1) and an alternative baseline correction (according to eq. B.1, green) assuming a purely constructive interference of surfactant and water background signal.

Table B.1: Shapiro test for normal distribution among the surface coverages of samples from the SML, one meter depth, greater than one meter depth and bulk (one + greater one). The statistics column contains the numerical value that is calculated by the test, commonly referred to as the so-called *test statistics W*. The null hypothesis H_0 of normal distribution of the coverage values is accepted if the p value is higher than the significance level than 0.05.

category	statistics (W)	p-value
SML	0.912	$2.7 \cdot 10^{-17}$
bulk	0.72	$9.5 \cdot 10^{-18}$
1 m	0.84	$7.7 \cdot 10^{-7}$
> 1 m	0.63	$3.8 \cdot 10^{-16}$

C GasEx cruise

C.1 Statistical tests

C.1.1 Results of the MANN-WHITNEY-U test for the enrichment factor

Before performing the test, it was confirmed that the data was not normal distributed by employing the SHAPIRO-WILK test.

Table C.1: Results of the MANN-WHITNEY-U test for equal mean for the enrichment factors of plate and screen sampling. The null hypothesis H_0 of equal mean is accepted if the p value is higher than the significance level than 0.05.

enrichment factor 1	enrichment factor 2	statistics	p-value
tension (plate)	tension (screen)	306	0.11
surf. pressure (plate)	surf. pressure (screen)	78	0.12
coverage (plate)	coverage (screen)	500	0.44

D Sensitizers

D.1 Analytical data and Synthesis

Table D.1: Solvent ratios used for the different BX compounds in the chromatographic purification.

compound	Pentane	Ethyle acetate
BX6	1	1
BX9	3	1
BX12	4	1

Table D.2: Elemental analysis

compound	element	found/ %	calculated/ %	deviation/ %
BX6	N	0.021	0	+0.021
	C	72.32	73.6	-1.28
	H	6.95	6.79	+0.19
BX9	N	0.003	0	+0.003
	C	74.63	74.97	-0.34
	H	7.6	8.03	-0.43
BX12	N	0.002	0	+0.002
	C	76.44	76.06	+0.38
	H	8.44	8.35	-0.09

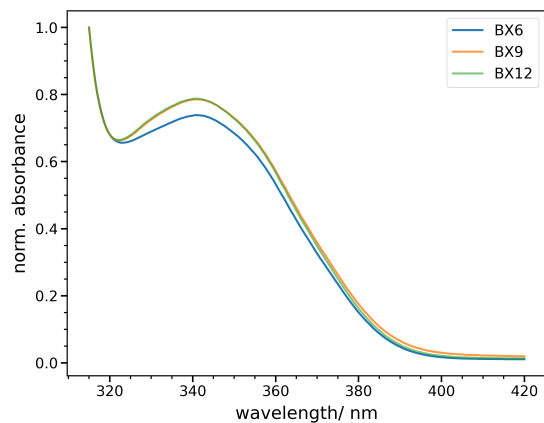


Figure D.1: UV/Vis spectra of the three BX sensitizers BX6, BX9 and BX12.

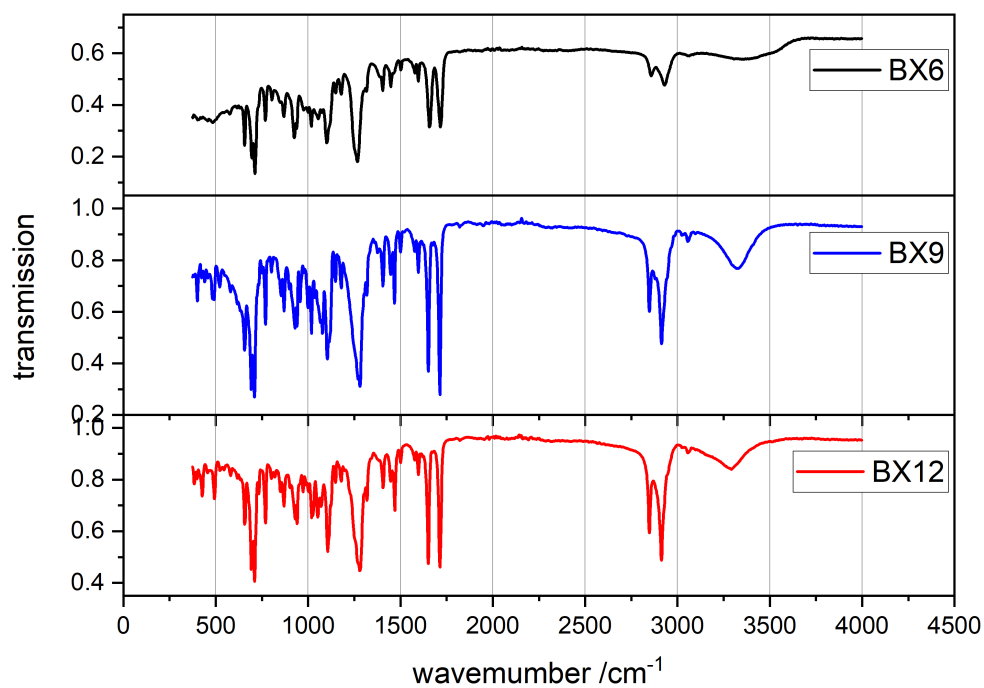


Figure D.2: Infrared spectra of the three BX sensitizers BX6, BX9 and BX12.

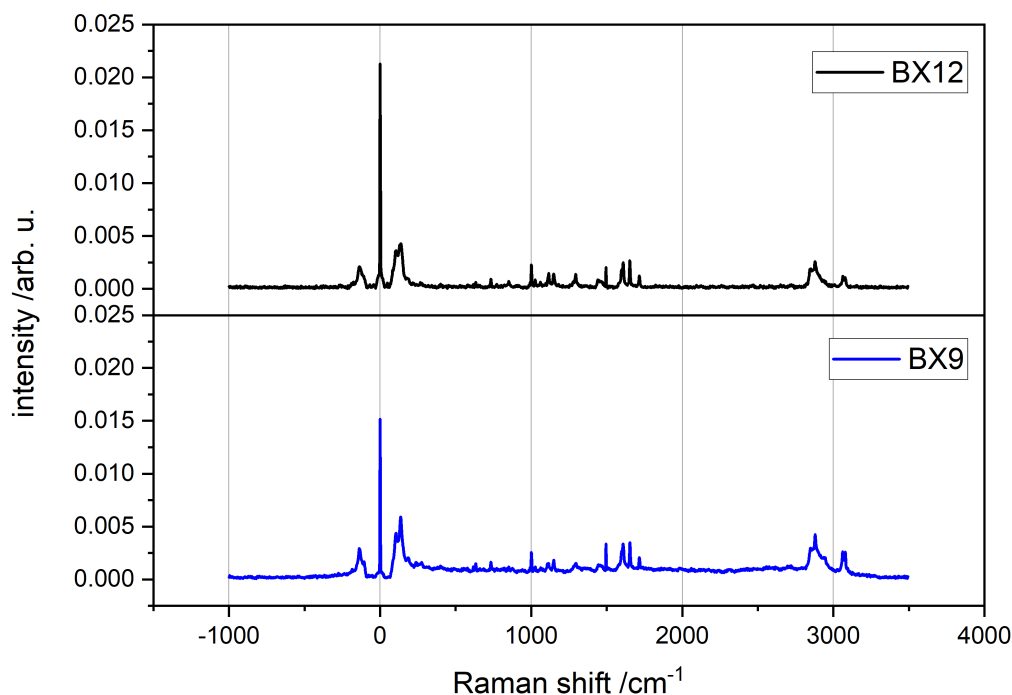
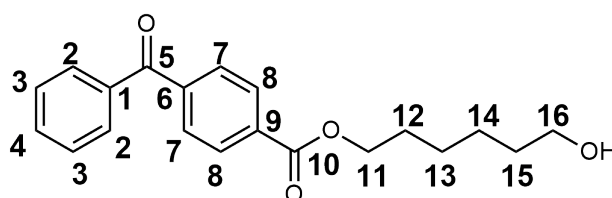


Figure D.3: Raman spectra of the artificial sensitizers BX9 and BX12. The BX6 spectrum has not been measured.

D.2 NMR

BX6



BX6

Figure D.4: Numbering of the C atoms for NMR peak assignment for BX6.

^1H NMR: (600 MHz, CDCl_3) δ = 8.17 – 8.12 (m, 2H, C8), 7.85 – 7.82 (m, 2H, C7), 7.81-7.78 (m, 2H, C2), 7.65-7.59 (m, 1H, C4), 7.53 – 7.47 (m, 2H, C3), 4.37 (t, J = 6.6 Hz, 2H, C11), 3.67 (t, J = 6.5 Hz, 2H, C16), 1.85 – 1.76 (m, 1H, C12), 1.65 – 1.58 (m, 1H, C15), 1.54 – 1.42 (m, 4H, C13 and C14).

^{13}C NMR: (151 MHz, CDCl_3) δ = 196.10 (C5), 165.91 (C10), 141.27 (C9), 136.98

(C1), 133.55 (C6), 132.96 (C4), 130.13 (C8), 129.79 (C7), 129.47 (C2), 128.48 (C3), 65.43 (C11), 62.84 (C16), 32.62 (C15), 28.69 (C12), 25.8 (C13), 25.44 (C14).

BX9

$^1\text{H NMR}$: (600 MHz, CDCl_3) δ = 8.17 – 8.12 (m, 2H, C8), 7.86 – 7.83 (m, 2H, C7), 7.82 – 7.79 (m, 2H, C2), 7.65 – 7.59 (m, 1H, C4), 7.53 – 7.47 (m, 2H, C3), 4.36 (t, J = 6.7 Hz, 2H, C11), 3.64 (t, J = 6.6 Hz, 2H, C19), 1.83 – 1.75 (m, 2H, C12), 1.56 (dt, J = 7.9, 6.3 Hz, 2H, C18), 1.50 – 1.31 (m, 10H, C13-C17).

$^{13}\text{C NMR}$: (151 MHz, CDCl_3) δ = 196.11 (C5), 165.92 (C10), 141.24 (C9), 136.98 (C1), 133.62 (C6), 132.96 (C4), 130.13 (C8), 129.77 (C7), 129.47 (C2), 128.47 (C3), 65.59 (C11), 63.05 (C19), 32.77 (C18), 29.46 (C16), 29.34 (C16), 29.19 (C14), 28.67 (C12), 26.01 (C17), 25.71 (C13).

BX12

$^1\text{H NMR}$: (500 MHz, CDCl_3) δ = 8.18 – 8.12 (m, 2H, C8), 7.87 – 7.82 (m, 2H, C7), 7.82 – 7.78 (m, 2H, C2), 7.66 – 7.59 (m, 1H, C4), 7.54 – 7.47 (m, 2H, C3), 4.36 (t, J =

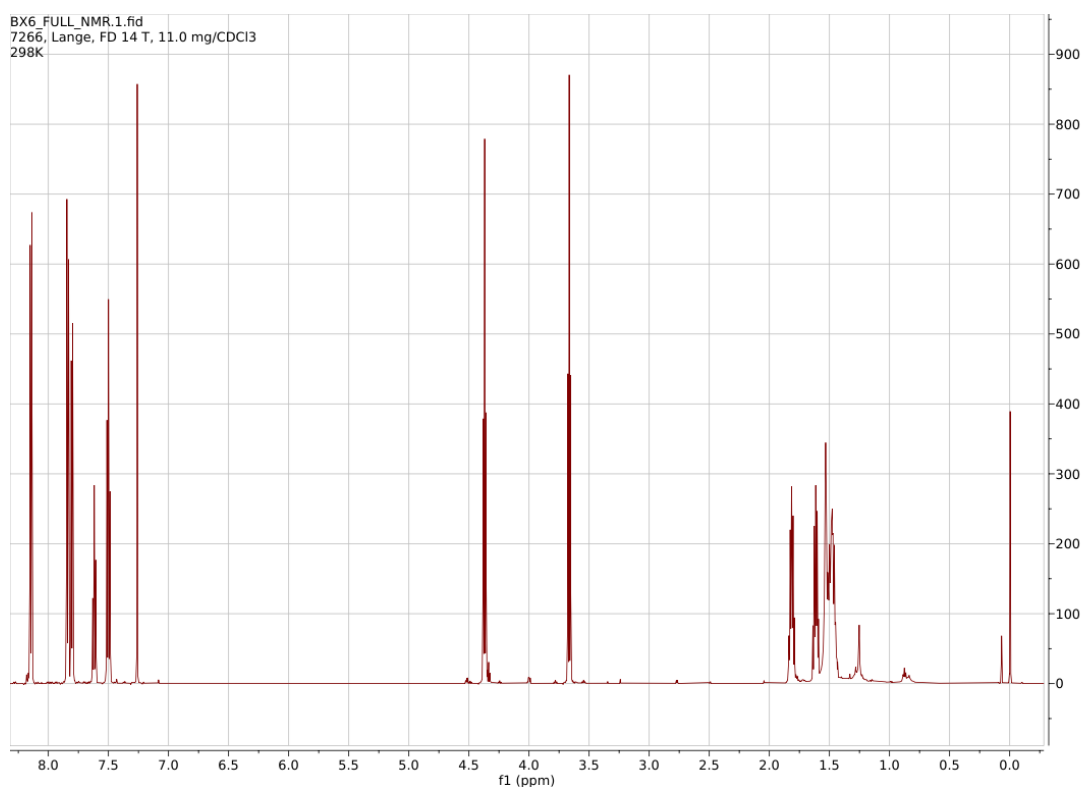


Figure D.5: $^1\text{H-NMR}$ Spectrum of BX6.

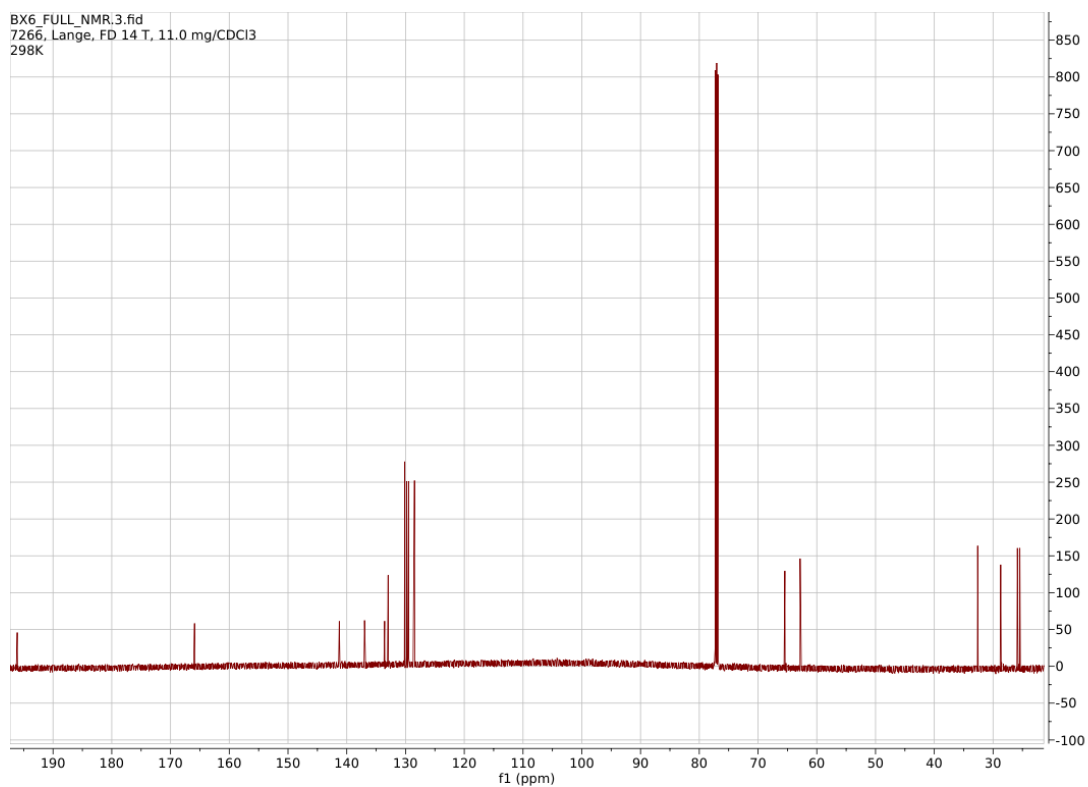


Figure D.6: ¹³C NMR spectrum of BX6.

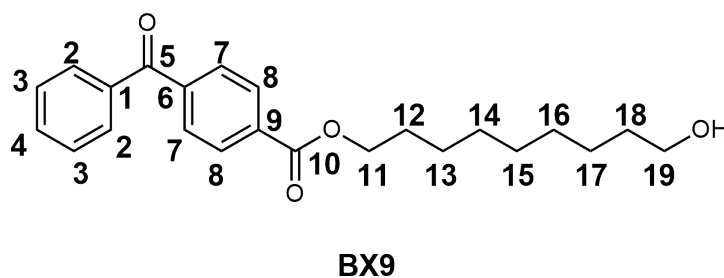


Figure D.7: Numbering of the C atoms for NMR peak assignment for BX9.

6.7 Hz, 2H, C11), 3.64 (t, $J = 6.6$ Hz, 2H, C22), 1.84 – 1.74 (m, 2H, C12), 1.56 (m, 2H, C21), 1.50 – 1.11 (m, 16H, C13-C20).

¹³C NMR: (126 MHz, CDCl₃) $\delta = 196.09$ (C5), 165.91 (C10), 141.22 (C9), 136.99 (C1), 133.63 (C6), 132.94 (C4), 130.12 (C8), 129.77 (C7), 129.46 (C2), 128.46 (C3), 65.62 (C11), 63.10 (C22), 32.81 (C21), C13-C20: 29.59, 29.54, 29.50, 29.42, 29.25, 28.67, 26.02, 25.74.

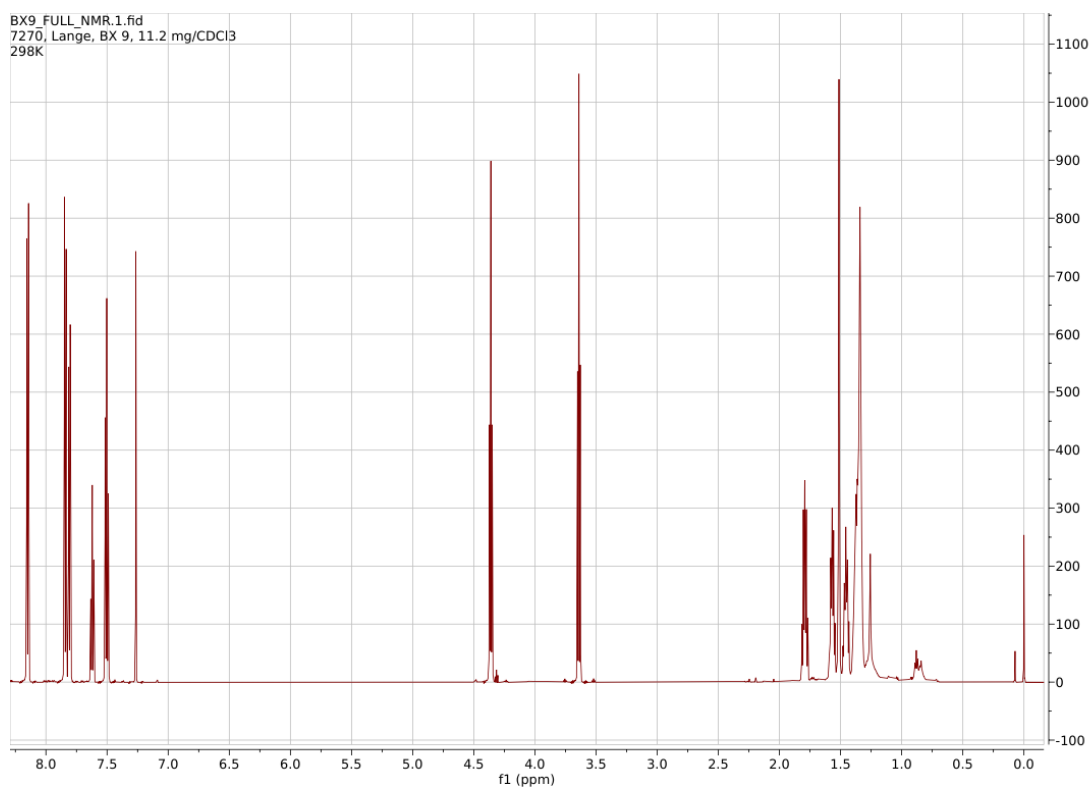


Figure D.8: ¹H-NMR Spectrum of BX6.

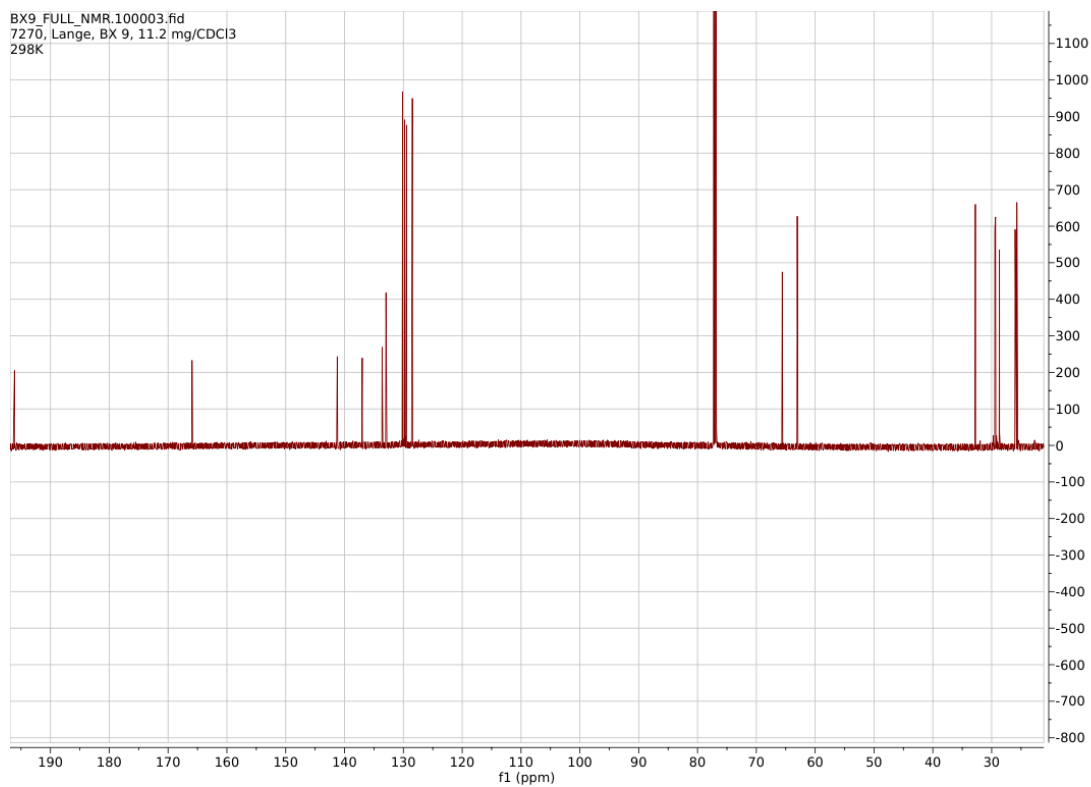
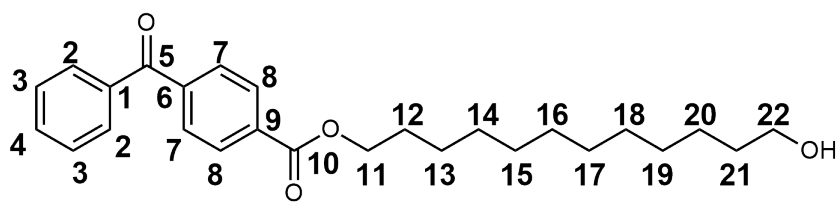


Figure D.9: ^{13}C NMR spectrum of BX9.



BX12

Figure D.10: Numbering of the C atoms for NMR peak assignment for BX12.

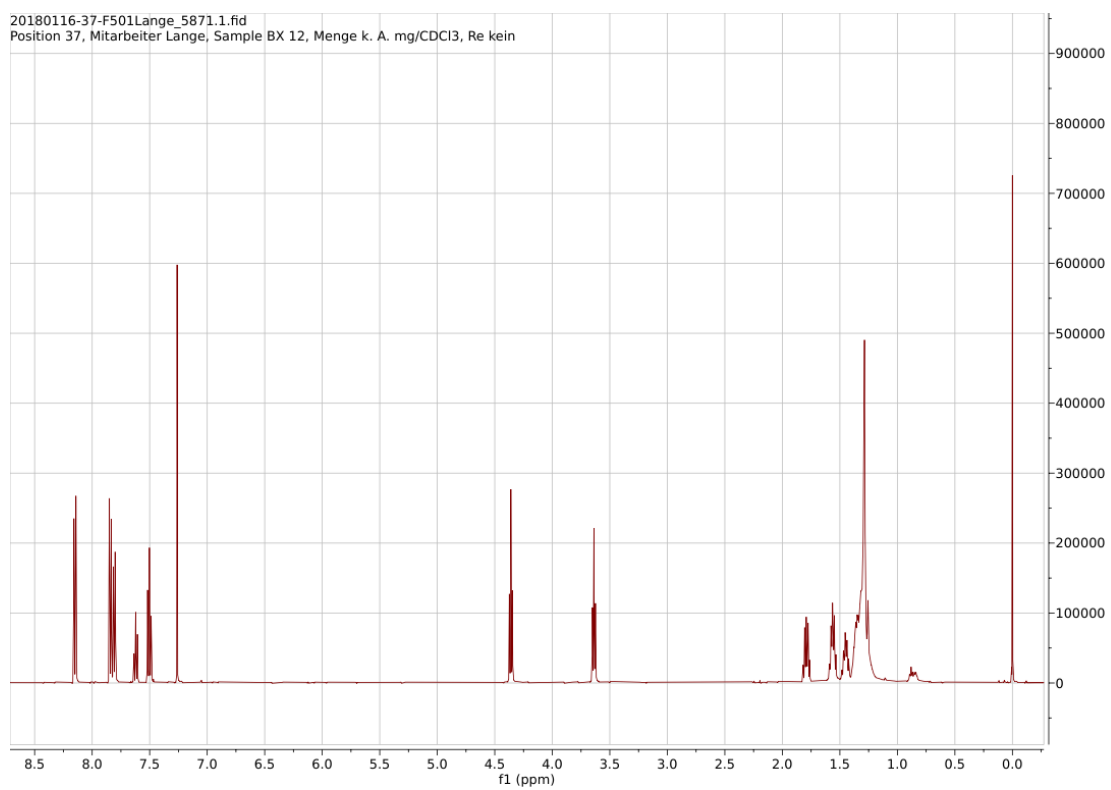


Figure D.11: ¹H-NMR Spectrum of BX12.

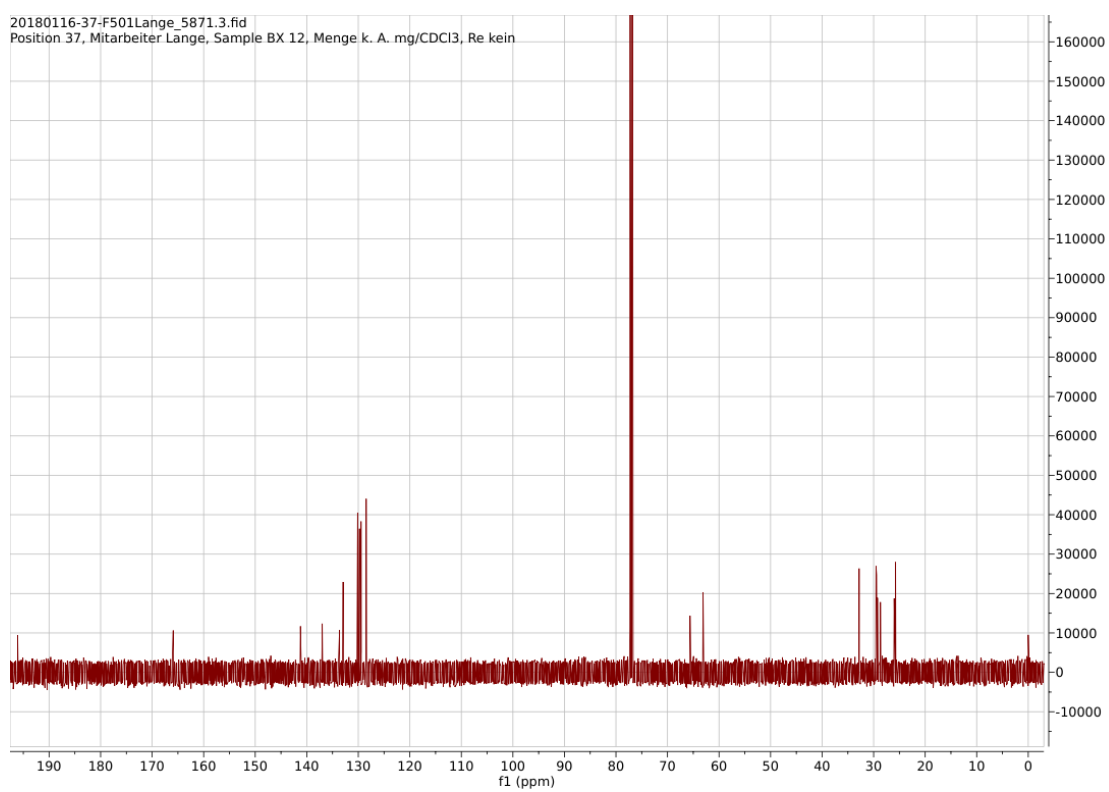


Figure D.12: ¹³C NMR spectrum of BX12.

D.3 Langmuir compression isotherms

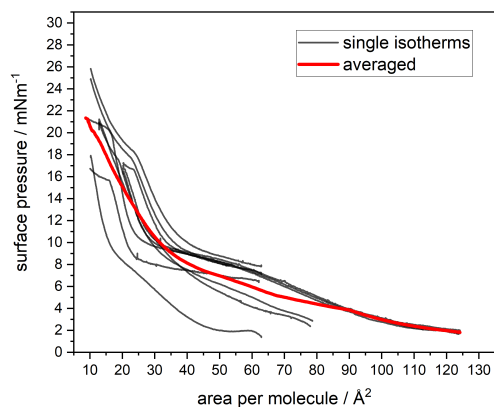


Figure D.13: Demonstration of the high variability of compression isotherms obtained for BX9.

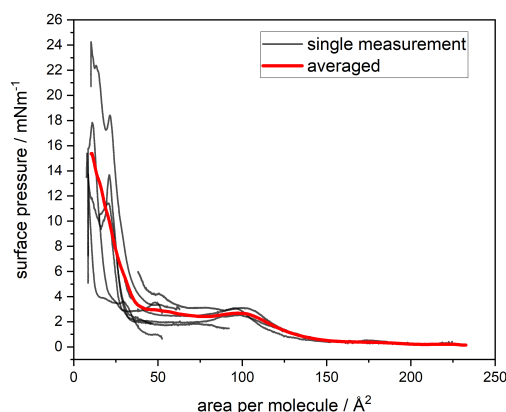


Figure D.14: Demonstration of the high variability of compression isotherms obtained for BX12.

D.4 Space requirement

A rough estimate of the space requirement of the sensitizer molecules lying flat on the surface is calculated as follows: a rectangular shape of the molecule as depicted in Fig. D.15 is used to approximate the molecular area. To account for some space between two adjacent molecules, 1.5 \AA are added to each dimension. The results of this calculations are presented in Tab. D.3. Note that this represents the extreme maximum space requirement because it assumes a completely stretched and plain orientation of the molecule on the surface. At high surface

concentrations, the BX molecules are expected to form monolayers with upright position of the alkyl chains (see text).

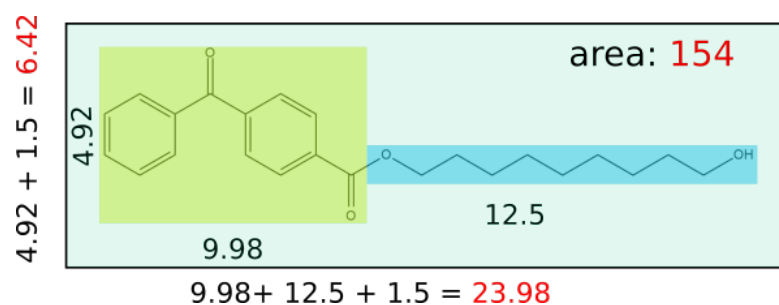


Figure D.15: Demonstration of the simple estimate for the molecule's space maximal space requirement. All numbers are reported in units of Å.

Table D.3: Space requirements of the sensitizers. All numbers are reported in units of Å for the lengths and Å² for the areas.

compound	chain length	ring length	ring height	max. total area
BX6	8.8	10	4.9	130
BX9	12.5	10	4.9	154
BX12	16.4	10	4.9	179

E Mixed layers

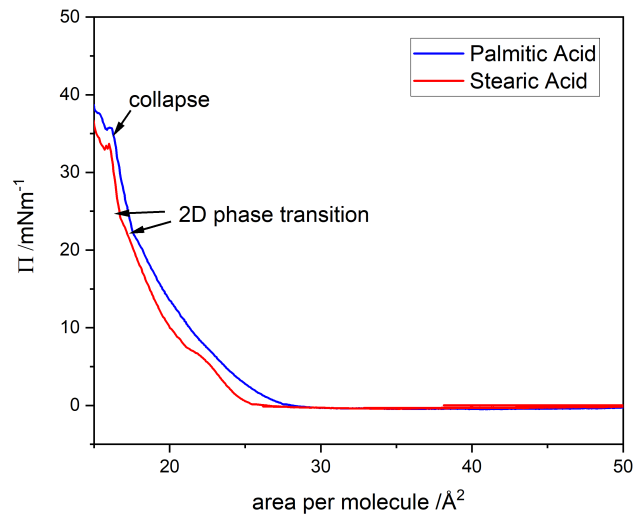


Figure E.1: Langmuir compression isotherms of the pure fatty acids.

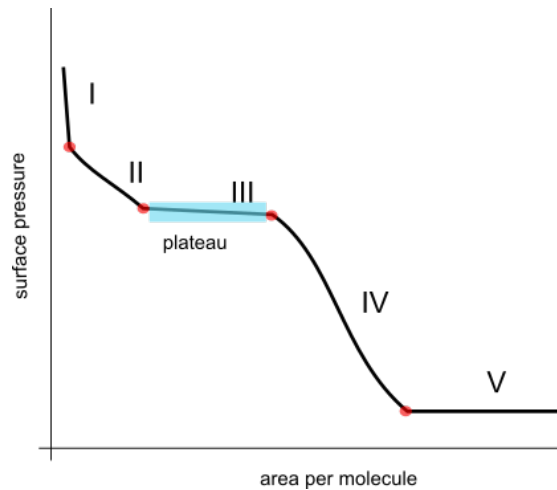


Figure E.2: Schematic representation of the different characteristics derived from an isotherm to allow a comparison of different isotherms in a systematic manner. Here, the roman numbers depict typical zones of different slopes appearing in isotherms.

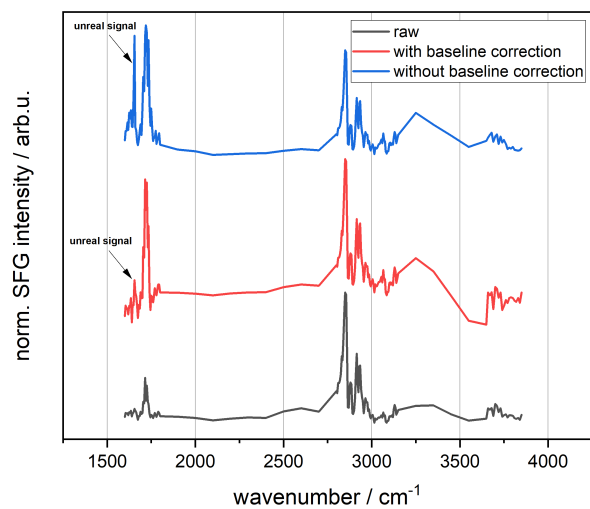


Figure E.3: Demonstration of the occurrence of spectral artifacts ("ghost peaks") caused by the low IR intensity in the carbonyl region of the spectrum.

Scientific contributions

Publications and software releases

1. **Specsnake**: Python package for handling, processing and analysis of spectrum data. GitHub repository: <https://github.com/Darkskald/specsnake>, initial release: Oct. 2020.
2. **SFG**: Python package with utilities for Vibrational Sum Frequency Generation Spectra, Langmuir compression isotherms, Surface Tension measurements for Sea Surface Microlayer (SML) research. GitHub repository: <https://github.com/Darkskald/SFG>, initial release: Oct. 2020.
3. J. JACOBSEN, B. ACHENBACH, H. REINSCH, S. SMOLDERS, F.-D. LANGE, G. FRIEDRICHS, D. DE VOS, N. STOCK, 'The first water-based synthesis of Ce(IV)-MOFs with saturated chiral and achiral C4-dicarboxylate linkers', *Dalton Trans.* **2019**, 48, 8433–8441, DOI 10.1039/C9DT01542F.
Contribution to the paper
Second Harmonic Generation (SHG) analysis of the chiral MOF substrates.

Conferences and Workshops

1. F.-D. Lange, Nhat-Thao Ton-Nu, G. Friedrichs, "Surface-Sensitive Methods for Marine Nanolayer Time-Series Studies", European Geosciences Union General Assembly (EGU), held online, May 4–8 2020, **Talk**.
2. D. Ho, C. A. Marandino, G. Friedrichs, A. Engel, D. Booge, H. Bange, T. Barthelmess, T. Fischer, T. Koffman, F.-D. Lange, B. Quack, M. Paulsen, L. Zhou, "Baltic Sea Gas Exchange Experiment (Baltic GasEx)", SOLAS Open Science Conference, Sapporo, Japan, April 2019, **Poster**.
3. F.-D. Lange, G. Friedrichs, "Surface active 4-Benzoylbenzoic acid ω -hydroxy-alkyl esters as photosensitizers for air-water interface photochemical studies", Tagung der Bunsen-Gesellschaft für physikalische Chemie, Hannover May 10-12 2018, **Poster**.

4. HOSST Summer School – “Multi-use conflicts in an industrialized coastal zone”, Kiel June 6 - 16, 2017.
5. TOSST Summer School – “Ocean Technologies and Observations”, Halifax (Canada) September 26 - October 7, 2016.

Acknowledgments

I am deeply grateful to my supervisor Prof. Dr. Gernot Friedrichs for providing me the opportunity to work on this dissertation project, for his valuable scientific advise, interesting and motivating discussions and especially for giving me the freedom to go my way, although it guided me in a different direction than I initially expected. I thank Prof. Dr. Douglas Wallace for taking the responsibility of being my co-supervisor for this project.

I have greatly benefited from the friendly support of the Friedrichs working group and I would like to thank them all for the pleasant work atmosphere. I would particularly like to thank Alexandra for her kind practical introduction to the SFG lab as well as for her support in scientific and technical questions and problems. I also want to thank Michael, my office colleague, for the nice atmosphere and especially for countless rich off-topic discussions about a variety of issues like history and philosophy- I will miss these inspiring conversations. I want to thank the HOSST responsables and coordinators as well as all members of my HOSST cohort for a wonderful time: inspiring talks, fantastic summer schools and retreats and, last but not least, financial support.

I would like to express my gratitude to student apprentices and bachelor candidates, maely Falko, Thao and Ludwig for their help as well as the interesting and fruitful scientific collaboration. In particular, would like to thank the teams from the institute's workshops, the secretaries and technical staff for their help and support in all infrastructural and organization issues. My special thanks go to my friends from the Department of Inorganic Chemistry, Sebastian, Philipp and Michael for great times, relaxing coffee breaks and for being open for all my questions, doubts and thoughts. For making my time in Kiel really memorable, I would like to thank all my friends here.

For going the first part of my way with me, for always helping me with scientific and other questions and issues and for keeping up my motivation, I want to gratefully thank my chemistry team from Marburg (Fabian, Lars and Markus). I am in debt to my dear friend Roman for the countless intellectual and not-

so-intellectual discussions, scientific advise, motivation, proofreading of this work and all the great times we had. My family, as a steady source of joy, shelter and inspiration and motivation, standing with me even when I completely lost my drive and focus, I want to express my deepest gratitude. I would not have finished this work without you.

Finally, I want to thank my dearest Ricarda for taking all my stress, frustration and doubts, being at my side throughout all those turbulent times and supporting me in each and every aspect. You inspired me, believed in me and gave me the strength to stand the struggle and finalize this project.